Grating Technology and System Development for High-Resolution X-Ray Phase-Contrast Imaging

by

Abdollah Pil-Ali

A thesis
presented to the University of Waterloo
in fulfillment of the
thesis requirement for the degree of
Doctor of Philosophy
in
Electrical and Computer Engineering

Waterloo, Ontario, Canada, 2023

© Abdollah Pil-Ali 2023

Examining Committee Membership

The following served on the Examining Committee for this thesis. The decision of the Examining Committee is by majority vote.

External Examiner:	Guang-Hong Chen Professor, Dept. of Medical Physics and Radiology, University of Wisconsin-Madison
Supervisor:	Karim S. Karim Professor, Dept. of Electrical and Computer Engineering, University of Waterloo
Internal Member:	Bo Cui Professor, Dept. of Electrical and Computer Engineering, University of Waterloo
Internal Member:	Simarjeet Saini Associate Professor, Dept. of Electrical and Computer Engineering, University of Waterloo
Internal-External Member:	Alexander Wong Professor, Dept. of System Design Engineering, University of Waterloo

Author's Declaration

I hereby declare that I am the sole author of this thesis. This is a true copy of the thesis, including any required final revisions, as accepted by my examiners.

I understand that my thesis may be made electronically available to the public.

Abstract

X-ray imaging is a workhorse of medical imaging, and in particular, high-resolution X-ray imaging is used in the detection of carcinomas and micro-calcifications in the breast, small fractures, and early stages of cancerous tumors. In addition, high-resolution X-ray imaging is essential for material characterization, material differentiation, and minute crack detection in industrial imaging. Although high-resolution X-ray imaging has traditionally been performed using X-ray attenuation-contrast imaging, X-ray phase-contrast imaging is nascent. X-ray phase-contrast (XPCi) imaging can visualize and image materials that are transparent to X-ray attenuation methods with higher sensitivity and contrast, and even highlight sub-pixel resolution features. XPCi methods in medical imaging have been demonstrated to provide significantly better soft tissue contrast and could potentially offer a viable high-speed X-ray imaging alternative to slower high-resolution MRI scans in particular use cases such as stroke imaging.

Grating-based XPCi techniques provide three images for each single X-ray exposure: transmission (absorption), refraction (phase-shift), and dark-field (ultra-small angle scattering). These images help quantify an object of interest. X-ray absorption gratings play a central role in grating-based XPCi systems as they directly determine the quality of imaging and enable the acquisition of the transmission, refraction, and dark-field images in a single X-ray exposure. An impediment to commercial development and adoption of XPCi systems is the lack of scalable manufacturing technology for large area, high-resolution, high aspect ratio X-ray absorption gratings. Grating technology development, primarily due to technological limitations, has lagged system development and today prevents the scaling up of the XPCi system into a footprint and price point acceptable for the medical market.

Towards that end, we investigate the fabrication of high-resolution high aspect ratio X-ray absorption gratings. We present the first bridge-assisted high-resolution high aspect ratio silicon-micropillar design for X-ray absorption grating fabrication in silicon wafers. Furthermore, we report on a novel fabrication process that relies on a self-aligned single-sided multilayer grating fabrication technique based on a conventional UV-LIGA lithography process to fabricate scalable high aspect ratio micron-scale feature X-ray absorption gratings. The process we invented and developed does not require any specialized processing steps or equipment such as access to synchrotron facilities for X-ray LIGA, deep reactive ion etching (DRIE), or even atomic layer deposition (ALD) commonly seen in silicon-based fabrication processes. By stacking multiple layers of the same grating design (i.e., multi-layer structures) through a backside self-aligned UV flood exposure technique, larger area X-ray gratings can be realized in an established and mature large-area thin-film

electronics processing facility. We demonstrate the first prototype grating with an absorption thickness of 40 μm with SU-8 micropillars of 4 μm in diameter and 16.2 μm period (with three layers), with an average visibility of 28% at 60 kV_p, all fabricated in a university lab with no specialized equipment. The development of such a grating creates new opportunities for translation of grating-based XPCi into clinical imaging applications where contrast, resolution, and dose efficiency are important, such as screening and diagnostic mammography.

We also present the design of an unoptimized single-mask edge-illumination (EI) XPCi system employing an in-house high-resolution prototype X-ray detector alongside the high-resolution prototype X-ray absorption gratings reported in this work. The compact single-mask high-resolution EI-XPCi system developed in this thesis is demonstrated to image various test samples including nano-scale powders. The imaging is performed using only a single X-ray exposure and subsequently results in dose reduction compared to two-exposure approaches. Moreover, our 2D X-ray grating system design is beneficial because it eliminates the object orientation dependency associated with line grating systems. We also briefly explore three previously reported algorithms to retrieve the three established contrast modalities, namely transmission, phase-shift, and dark-field images, and present first, unoptimized results with our in-house high-resolution grating.

The large area fabrication process for X-ray gratings and results demonstrated can potentially expedite the development of commercial, single-grating, high-resolution, X-ray phase contrast systems, especially for mammography medical imaging.

Acknowledgements

I am truly grateful to Allah for blessing me with the opportunity to work with Professor Karim S. Karim. I would like to express my sincere gratitude to my supervisor, Prof. Karim, who has been a great mentor throughout my Ph.D. journey. All the accomplishments achieved in this Ph.D. journey would not have been possible without him. His unwavering belief in me, positive attitude towards challenges, and openness to new ideas have been a constant source of inspiration. Through his guidance, I have gained a deeper appreciation of the importance of building strong relationships and rapport with colleagues. He has shown me how being passionate, optimistic, and positive about solving a challenge can change our perspective on the journey we take so that we can enjoy the moments. Beyond academic supervision, his mentorship has taught me invaluable lessons that have expanded my horizons in life. Thank you for all the memories and experiences you shared with us in our meetings.

I would like to express my appreciation to my supervisor, Prof. Karim S. Karim, and my examining committee, Prof. Guang-Hong Chen, Prof. Bo Cui, Prof. Alexander Wong, and Prof. Simarjeet Saini, for reviewing my work. I am also highly grateful to Prof. Alessandro Olivo from University College London, who provided invaluable guidance and discussion on the edge-illumination X-ray phase-contrast imaging method and provided me with the X-ray line grating.

It is an honor to work alongside many talented and diverse colleagues: Dr. Christopher Scott for assisting me with X-ray phase-contrast imaging; Sahar Adnani for helping me with all the software development and support in testing, measurement, and fabrication; Dr. Celal Con for assisting with X-ray detector fabrication; and Dr. Mohammad Soltani for all the talks we had about the challenges I faced in my device fabrication.

Special thanks go to Richard Barber and Dr. Czang-Ho Lee for assisting with G2N lab maintenance and tools training. I would also like to thank Dr. Lino Eugene, Dr. Greg Holloway, Dr. Sandra Gibson, Dr. Nathan Nelson-Fitzpatrick, Rodello Salandanan, and Matt Scott for training me on multiple tools at the quantum-nano fabrication and characterization facility (QNFCF). Additionally, I am thankful to thank Prof. Raafat Mansour for granting me access to the centre for integrated RF engineering (CIRFE) to conduct gold electroplating for my grating fabrication. I am also grateful to Dr. Diako Mardanbegi for his assistance with the X-ray phase-contrast information retrieval algorithm. I would also like to thank my colleagues at KA Imaging Inc. for their instrumental collaboration that contributed to the success of this work. I want to thank Jane Russwurm from the Writing and Communication Centre for assisting me in editing my thesis.

I would like to express my appreciation to everyone who made this thesis possible.

Lastly and most importantly, I am deeply indebted to my parents, Mrs. Mahboubeh Elyaszadeh and Mr. Alireza Pil-Ali, my brother, Ebrahim Pil-Ali, and my lovely wife, Razieh Khalili, who supported me immensely and unconditionally and provided much-needed encouragement and prayers for success throughout my journey in all these years. Alhamdulillah.

Early in my Ph.D. journey, I faced major challenges that made me need help I couldn't find then. The one thing that enlightened my path and gave me strength throughout my program was a Hadith by Amir Al Momenin, Ali bin Abi Talib (peace be upon him):

> "*When you become afraid of the difficulty of a task, show firmness in the face of it, and it will become easy for you...*"
>
> *(Ghurar al-Hikam, Hadith 4108)*

This Hadith was my torch in challenges, my strength in difficulties, and my hope in all moments of my Ph.D. journey.

Dedication

To

Al-Abbas ibn Ali ibn Abi Talib *(peace be upon him)*

and his mother,

lady Fatima bint Hazam–Umm ul-Banin *(peace be upon her)...*

Table of Contents

Author's Declaration iii

Abstract iv

Acknowledgements vi

Dedication viii

List of Tables xiii

List of Figures xiv

1 Introduction 1

1.1 Background on X-ray Phase-Contrast Imaging 1

1.2 X-ray Grating 2

1.3 Thesis Purpose and Objectives 4

1.4 Thesis Organization 5

2 High-Resolution X-ray Phase Contrast Imaging 6

2.1 Introduction 7

2.2 Theory and Model 8

2.3 Simulation and Verification 12

2.4 Comparison Metrics for High-Resolution PB-XPCi and EI-XPCi 16

2.5 Direct vs. Indirect Conversion Detector . . . 17
2.6 Investigation of X-ray Phase-Contrast Imaging System Performance . . . 21
2.6.1 PB-XPCi . . . 21
2.6.2 EI-XPCi . . . 22
2.7 Effect of Absorption Mask Thickness Variation in a High-Resolution EI-XPCi System . . . 25
2.8 Effect of Mechanical Vibration in a High-Resolution EI-XPCi System . . . 30
2.9 Current XPCi Technologies . . . 33
2.9.1 Propagation-Based X-ray Phase-Contrast Imaging System . . . 33
2.9.2 Edge-Illumination X-ray Phase-Contrast Imaging System . . . 39
2.10 Conclusion . . . 41

3 Silicon-based X-ray Absorption Grating Fabrication 43
3.1 Introduction . . . 44
3.2 Determining Grating Specifications . . . 46
3.3 Hard-Mask for DRIE Etching . . . 47
3.3.1 Metal/Oxide Hard-Mask . . . 48
3.3.2 Photoresist Hard-Mask . . . 54
3.4 Bridge-Assisted structures . . . 55
3.5 High Aspect Ratio Silicon-based X-ray Absorption Grating . . . 63
3.5.1 Etching High Aspect Ratio Structures . . . 63
3.5.2 Seed Layer Deposition for Electroplating . . . 65
3.5.3 Sputtering of Gold . . . 66
3.5.4 Gold Electroplating . . . 68
3.6 Results and Discussion . . . 70
3.6.1 Fabricated Prototype Gratings . . . 70
3.6.2 X-ray Projection Image . . . 74
3.6.3 Visibility, Transmission, and Absorption Characteristics of the Prototype Gratings . . . 78
3.7 Conclusion . . . 80

4 Self-Aligned Multi-Layer Grating Fabrication **81**
4.1 Introduction . . . 82
4.2 Adhesion of SU-8 to Gold Thin Film . . . 84
4.2.1 Investigating the Adhesion Quality . . . 84
4.3 Multi-Layer Fabrication of X-ray Absorption Grating . . . 92
4.3.1 Fabrication Process Flow . . . 93
4.3.2 Alignment Issue for Micron-Scale Features . . . 95
4.3.3 Effect of Exposure Energy and Optimization . . . 97
4.4 Self-Aligned Multi-Layer Fabrication process . . . 98
4.4.1 Fabrication Process Flow . . . 98
4.4.2 Effect of Exposure Energy and Optimization . . . 100
4.4.3 Effect of Feature Size . . . 103
4.4.4 Electroplating and Optimization . . . 106
4.4.5 Multi-Layer Backside UV Lithography . . . 109
4.4.6 Results and Discussion . . . 112
4.5 Conclusion . . . 121

5 Application of High-Resolution X-ray Phase-Contrast Imaging **123**
5.1 Introduction . . . 123
5.2 Propagation-Based X-ray Phase-Contrast Imaging . . . 126
5.2.1 Intraoral Tomosynthesis . . . 129
5.2.2 Mammography . . . 131
5.2.3 Microscopy . . . 133
5.3 Edge-Illumination X-ray Phase-Contrast Imaging . . . 137
5.3.1 Line Grating . . . 138
5.3.2 2D Grating . . . 152
5.4 Speckle-tracking X-ray Phase-Contrast Imaging . . . 157
5.4.1 Silicon-based 2D Grating . . . 159
5.4.2 Self-Aligned Multi-Layer SU-8 2D Grating . . . 164
5.5 Conclusion . . . 168

6 Conclusions and Contributions **170**

6.1 Conclusions 170

6.2 Contributions 172

6.3 Future Works 176

References **177**

APPENDICES **194**

A MATLAB® Algorithm for Simulating PB and EI-XPCi **194**

B Python Algorithm for Single-Mask EI-XPCi Information Retrieval **207**

B.1 1D Grating Information Retrieval 207

B.2 2D Grating Information Retrieval 215

List of Tables

2.1 Algorithm used for simulating the model in MATLAB® for both PB-XPCi and EI-XPCi. 14

2.2 List of today's EI-XPCi systems with source, setup size (source to detector), masks, and detector information. 39

3.1 PECVD deposition process condition for SiO_2 and Si_3N_4 based on two different tools. 49

3.2 AJA Sputtering properties for chromium (Cr) and gold (Au) film deposition. 66

4.1 List of various adhesion promoters—and their combinations—and the result of adhesion quality during the developing process, through tape test, and under a harsh acidic electroplating process condition. 89

4.2 A summary of limitations and potentials of various X-ray grating fabrication process methods. 122

List of Figures

2.1 Components and geometry of the EI-XPCi (as well as PB-XPCi) system model. In this figure, a line grating is shown; however, a 2D grating could be substituted as required. 9

2.2 setup-model 12

2.4 Comparison between the simulation result and experimental data extracted from [71] for (**a**) a PEEK wire, and (**b**) a Titanium wire. The solid blue line represents the simulation result, and the red circles demonstrate experimental data. 15

2.5 X-ray spectrum of the tungsten target employed from the *spektr* toolset in MATLAB® for simulation. The spectrum is filtered by 0.5 mm aluminum (Al). 16

2.6 The effect of detector modulation transfer function (MTF_d) on the image quality. (**a**) Represents a direct conversion detector with a pixel size equal to 7.8 μm. (**b**) Represents a direct conversion detector with a pixel size equal to 23.4 μm. (**c**) Represents a direct conversion detector with a pixel size equal to 46.8 μm. (**d**) Represents a direct conversion detector with a pixel size equal to 70.2 μm. Simulation is done for a PEEK wire with 585 μm in diameter using a polychromatic microfocus X-ray source working at 60 kV_p with a spot size equal to 2 μm to only study and highlight the effect of MTF_d on the system performance. 18

2.7 The effect of detector modulation transfer function (MTF_d) on the relative intensity of the same images shown in Figure 2.6. (**a**) Represents a direct conversion detector with a pixel size equal to 7.8 μm. (**b**) Represents a direct conversion detector with a pixel size equal to 23.4 μm. (**c**) Represents a direct conversion detector with a pixel size equal to 46.8 μm. (**d**) Represents a direct conversion detector with a pixel size equal to 70.2 μm. Simulation is done for a PEEK wire with 585 μm in diameter using a polychromatic microfocus X-ray source working at 60 kV_p with a spot size equal to 2 μm to only study and highlight the effect of MTF_d on the system performance. 19

2.8 (**a**–**c**) Simulation results of contrast, edge-enhancement, and visibility for a PB-XPCi system carried out for a PEEK wire with 585 μm in diameter as a function of different detector modulation transfer function values (MTF_d). 20

2.9 Simulation results of the behavior of (**a**) contrast and (**b**) edge-enhancement of a PB-XPCi system versus the object-to-detector distance, carried out for a PEEK wire with 585 μm in diameter. 21

2.10 Simulation results of the behavior of visibility of a PB-XPCi system versus the object-to-detector distance, carried out for a PEEK wire with 585 μm in diameter. 22

2.11 Simulation results of the behavior of (**a**) contrast and (**b**) edge-enhancement of an EI-XPCi system versus mask misalignment carried out for a PEEK wire with 585 μm in diameter. 23

2.12 Simulation results of the behavior of visibility of an EI-XPCi system versus mask misalignment carried out for a PEEK wire with 585 μm in diameter. 24

2.13 The effect of detector mask thickness variation on the performance of a high-resolution EI-XPCi system with 10% transmission of X-ray through the absorption mask. The vertical green bars highlight the working regions with the highest performance, and the vertical red bar represents the region where the detector mask fully absorbs X-rays in the dark image. 26

2.14 The effect of detector mask thickness variation on the performance of a high-resolution EI-XPCi system with 30% transmission of X-ray through the absorption mask. The vertical green bars highlight the working regions with the highest performance, and the vertical red bar represents the region where the detector mask fully absorbs X-rays in the dark image. 27

2.15 The effect of detector mask thickness variation on the performance of a high-resolution EI-XPCi system with 70% transmission of X-ray through the absorption mask. The vertical green bars highlight the working regions with the highest performance, and the vertical red bar represents the region where the detector mask fully absorbs X-rays in the dark image. 28

2.16 The effect of detector mask thickness variation on the performance of a high-resolution EI-XPCi system with 90% transmission of X-ray through the absorption mask. The vertical green bars highlight the working regions with the highest performance, and the vertical red bar represents the region where the detector mask fully absorbs X-rays in the dark image. 29

2.17 Environmental vibration modelled through mechanical displacement which causes misalignment between pre-sample and detector mask in an EI-XPCi system for high-resolution imaging application. 30

2.18 Illustration of simulation results of the effect of environmental vibration in the range of 2 μm on the performance of an EI-XPCi system with pixel size equal to 39 μm $\times$ 39 μm. 31

2.19 (**a**–**d**) Illustration of simulation results of the effect of environmental vibration on the performance of an EI-XPCi system with pixel size equal to 7.8 μm $\times$ 7.8 μm. The behavior of the system dramatically changes even with less than one micrometre shift in the mask misalignment. 32

2.20 Illustration of X-ray projections (phase-contrast images) highlighting the edge-enhancement effect of PB-XPCi for a 0.7 mm PTFE rod at different magnifications of (**a**) 1.11, (**b**) 2, (**c**) 3, and (**d**) 4. 34

2.21 Cross-sectional view of the relative intensity profile across the object in Figure 2.20 highlighting the edge-enhancement effect of PB-XPCi for a 0.7 mm PTFE rod at different magnifications of (**a**) 1.11, (**b**) 2, (**c**) 3, and (**d**) 4. 35

2.22 The experimental setup used for PB-XPCi imaging with the tungsten target Thermo Scientific™ PXS5-927 Microfocus X-ray Source, sample stage, and a prototype version of the BrillianSe™ X-ray detector. 36

2.23 Demonstration of the tungsten target Thermo Scientific™ PXS5-927 Microfocus X-ray source spectrum used for imaging—both the unfiltered and 0.5 mm Al filtered spectrum. 37

2.24 (**a**) Phase-contrast image of a dried bay leaf using a prototype version of the BrillianSe™ X-ray detector and a microfocus source at 60 kV_p, z_{so} = 18 cm, and z_{od} = 8 cm; (**b**) profile of relative intensity along the vertical cross-section (blue line). 38

3.1 Schematic of an X-ray absorption grating specifications in the single-mask EI-XPCi technique. 46
3.2 A metal/oxide hard mask is defined for Bosch DIRE process by using a negative photoresist in the liftoff process. 47
3.3 A metal/oxide hard mask is defined for Bosch DIRE process by using a positive photoresist in the liftoff process. 47
3.4 Photoresist as the hard mask for Bosch DIRE process. 48
3.5 Thickness profile map of (**a**) a 2.2 μm thick SiO_2 film, (**b**) a 1.2 μm thick Si_3N_4 film, and (**c**) a 0.3 μm thick Si_3N_4 film, all measured using the Woollam M-2000DI spectroscopic ellipsometer. 50
3.6 Optical microscope images of line patterns lithographed on the substrate (**a**) without, and (**b**) with the HMDS application as the adhesion promoter. HMDS increases the bonding strength between the photoresist and the substrate. 51
3.7 (**a**) S1805 spin coated at 6000 RPM and baked at 115°C ,(**b**) S1805 spin coated at 3000 RPM and baked at 115°C, (**c**) S1811 spin coated at 6000 RPM and baked at 115°C, (**d**) S1811 spin coated at 5000 RPM and baked at 115°C. 52
3.8 (**a**) Lamellae with 8.6 μm width and 32 μm period, and (**b**) micropillars with 4.5 μm width and 27 μm period. All samples were etched for 40 μm into the silicon using a metal/oxide hard mask. 53
3.9 Lamellae with 330 nm width and 10.5 μm period. The sample was etched for 40 μm into the silicon using a metal/oxide hard mask. 54
3.10 SEM image of high aspect ratio micropillars fabricated on a silicon wafer through Bosch DRIE process. Micropillars are broken or collapsed due to plasma-induced forces and partial higher horizontal etching rate at some part of their base. 56
3.11 SEM image of patterns on a silicon wafer with different periodicity values etched through the Bosch DRIE process. 57
3.12 Schematic illustration of high aspect ratio micropillars (**a**) without and (**b**) with auxiliary supporting bridge structures. 58
3.13 Illustration of CAD design of micropillars without and with bridge structures along with the SEM images of the same micropillar designs etched on a silicon wafer. 59

3.14 Illustration of an SEM image where micropillars became thinned at their base before the end of the Bosch DRIE process. 60
3.15 Illustration of CAD design of micropillars with 1 μm, 1.5 μm, 2 μm, and 2.5 μm thick bridges along with their SEM images of patterned structures on a silicon wafer coated with photoresist. 61
3.16 SEM images of micropillars with bridge structures. (**a**) Side view of the sample where bridges still exist in the middle of the etching process, (**b**) top view with an angle of the same sample, and (**c**) top view with an angle of micropillars with bridges about to become etched toward the end of the etching process. 62
3.17 Schematic illustration of the process flow for fabricating a high aspect ratio high-resolution X-ray absorption grating on a silicon wafer. (**a**) Obtaining a silicon wafer, (**b**) coating a thick photoresist as the etching hard mask and transferring the pattern onto the photoresist through UV exposure lithography, (**c**) performing Bosch deep reactive ion etching (DRIE), (**d**) stripping the remaining photoresist, (**e**) deposition of a thin layer of gold through atomic layer deposition (ALD), and (**f**) to (**h**) conducting intermittent gold electroplating to form the absorption part of the grating. 63
3.18 Illustration of SEM images of (**a**) line grating with 5 μm width and 21.6 μm period; (**b**) line grating with 4 μm width and 12.2 μm period. 64
3.19 Illustration of SEM images of (**a**) micropillar grating with 4 μm in diameter and 12.2 μm period, and (**b**) micropillar grating with 3 μm in diameter and 16.3 μm period. 65
3.20 Schematic illustration of the process flow for deposition of seed layer onto high aspect ratio gratings using a sputtering tool. (**a**) Depiction of the sputtering process, (**b**) gold particles deposited through sputtering only cover the top part of high aspect ratio structures, and (**c**)-(**e**) conducting intermittent gold electroplating to form the absorption part of the grating. 67
3.21 Schematic illustration of a high aspect ratio micropillar sputtered with gold. Multiple SEM images at various locations of the micropillar were taken, highlighting the sidewall quality and presence of the sputtered gold film. . 68
3.22 Illustration of SEM images of the fabricated micropillar-based X-ray absorption grating. (**a** and **b**) At the beginning of the electroplating, and (**c** and **d**) when the top parts of micropillars are sufficiently electroplated with gold. 69
3.23 (**a** and **b**) Illustration of SEM images of the fabricated micropillar-based X-ray absorption grating with micropillars being overplated. 70

3.24 Illustration of SEM images of the fabricated micropillar-based X-ray absorption grating. (**a**) After performing the Bosch DRIE, and (**b**) after conducting a short gold electroplating. 71

3.25 Illustration of SEM images of the fabricated micropillar-based X-ray absorption grating. (**a**) After longer gold electroplating, (**b**) when the top part of micropillars is almost overplated with gold, and (**c** and **d**) when micropillars are completely overplated. 72

3.26 Illustration of SEM images of the fabricated line X-ray absorption grating. (**a**) After performing the Bosch DRIE, (**b**) after conducting a short gold electroplating, (**c**) after longer gold electroplating, and (**d**) the top view with the top part of line structures fully electroplated with gold. 73

3.27 Photo of the fabricated silicon-based X-ray absorption gratings mounted on an aluminum holder. 74

3.28 Schematic illustration of the X-ray projection setup consisting of a microfocus X-ray source, the prototype silicon-based X-ray absorption grating, a high-resolution X-ray detector, and a post-processing unit to demonstrate the X-ray image. 75

3.29 Illustration of the X-ray projection of the micropillar-based X-ray grating with a magnified image inset to show the resolution of micropillars' projection on the detector. 75

3.30 A full X-ray transmission image of the fabricated silicon-grating. 76

3.31 Transmission map of (**a**) a line and (**b**) a micropillar-based X-ray absorption grating. The transmission value across the blue dashed line is also presented under each transmission map. 77

3.32 Illustration of the visibility maps of the fabricated silicon-based micropillar X-ray grating using a polychromatic microfocus X-ray source with the current of 200 μA and working potential of (**a**) 40 kV_p, and (**b**) 50 kV_p; all the insets are visibility histograms with their peaks representing the grating visibility of the X-ray source energy at the source working potential. The 3D X-ray Microscope, inCiTe™ (from KA Imaging, Waterloo, ON, CA) was employed for this measurement. 78

3.33 Illustration of the visibility maps of the fabricated silicon-based micropillar X-ray grating using a polychromatic microfocus X-ray source with the current of 200 μA and working potential of (**a**) 60 kV_p, (**b**) 70 kV_p, (**c**) 80 kV_p, and (**d**) 90 kV_p; all the insets are visibility histograms with their peaks representing the grating visibility of the X-ray source energy at the source working potential. The 3D X-ray Microscope, inCiTe™ (from KA Imaging, Waterloo, ON, CA) was employed for this measurement. 79

3.34 Visibility, transmission, and absorption characteristics of the silicon-based micropillar X-ray grating versus various X-ray source potentials. 80

4.1 A general process flow for fabricating X-ray absorption gratings: (**a**) cleaning the Si wafer, (**b**) deposition of Cr/Au thin films, (**c**) definition of an adhesion layer, (**d**) spin coating the thick SU-8 layer,(**e**) lithography and pattern transfer through a photomask, (**f**) post exposure baking, (**g**) developing uncrosslinked SU-8 regions, and (**h**) Au electroplating to fill the gaps. . . . 85

4.2 (**a**) Schematic illustration of a delaminated SU-8 film with an ineffective adhesion layer application. (**b**) SU-8 film delaminated from the HMDS-treated gold-coated silicon substrate. 87

4.3 Demonstration of an SEM image of a delaminated SU-8 film from a gold substrate – without any adhesion layer. 89

4.4 Demonstration of adhesive tape test to investigate the quality of adhesion promoter employed between SU-8 film and gold thin film with (**a**) the sample being fixed, (**b**) a strip of adhesive tape applied across the sample onto the SU-8 film, and (**c**) tape peeled off. (**d**) Illustration of SU-8 film delaminated from the substrate during the developing step. 90

4.5 The developed process flow for fabricating an X-ray absorption grating with a strong adhesion layer between SU-8 and gold thin film. (**a**) Cleaning the Si wafer, (**b**) thermal deposition of Cr/Au/Cr thin films, (**c**) definition of a mono-layer of MPTS, (**d**) spin coating a thin SU-8 layer,(**e**) spin coating the thick SU-8 layer, (**f**) lithography and pattern transfer through a photomask, (**g**) post-exposure baking, (**h**) developing uncrosslinked SU-8 parts, (**i**) etching the thin SU-8 layer, (**j**) etching top Cr thin film to open Au thin film, and (**k**) Au electroplating to fill the gaps. 91

4.6 Schematic illustration of the process flow for fabricating multi-layer high aspect ratio X-ray absorption gratings. (**a**) Cleaning the Si wafer substrate, (**b**) deposition of Cr/Au/Cr thin films, (**c**) definition of a mono-layer MPTS, (**d**) definition of the SU-8 base layer, (**e**) spin coating the first SU-8 layer, (**f**) lithography and pattern transfer through a photomask, (**g**) post-exposure bake, (**h**) repeating steps (**e**) to (**g**) until the desired thickness is achieved, (**i**) developing uncrosslinked SU-8 regions, (**j**) removing the SU-8 base layer through an RIE process, (**k**) wet etching the top Cr thin film, and (**l**) gold electroplating to fill the gaps and form the absorption region. 94

4.7 (**a**) Schematic illustration of the inaccuracy in aligning multiple layers (three layers) of SU-8 films—during fabrication of each layer—which compromises the high aspect ratio structures integrity. (**b**) An optical microscope image of a misaligned two-layer fabricated SU-8 mold with misalignment for approximately 5 μm in X direction and 4 μm in Y direction. 95

4.8 SEM images of alignment accuracy for various feature sizes of SU-8 structures. Alignment inaccuracy compromises the integrity of multi-layer micron-scale feature sizes in (**a**) and (**b**); however, it does not affect the structural integrity of greater feature sizes significantly, as demonstrated in (**c**). . . . 96

4.9 (**a**) An optical microscope image of SU-8 based micropillars underexposed in the UV lithography and delaminated during the developing process. (**b**) SEM image of overexposed SU-8 based micropillars. 97

4.10 Process flow for fabricating multi-layer self-aligned high aspect ratio gratings. This graph illustrates the fabrication steps for two layers, where repeating steps (**l**) to (**n**) results in a multi-layer structure: (**a**) cleaning the ITO-on-glass substrate, (**b**) thermal deposition of Cr/Au/Cr thin films, (**c**) spin coating a positive photoresist and patterning it through a photomask, (**d**) etching uncovered Cr/Au/Cr parts, (**e**) cleaning the sample and removing the photoresist,(**f**) definition of a mono-layer MPTS film, (**g**) definition of the SU-8 base layer and performing a flood exposure from top, (**h**) spin coating the first SU-8 layer and performing a backside exposure, (**i**) developing the uncrosslinked SU-8, (**j**) performing an RIE to remove base SU-8 layer and etching the top Cr film, (**k**) gold electroplating to fill the gaps, (**l**) spin coating the second SU-8 layer and performing a backside exposure, (**m**) developing the uncrosslinked SU-8 parts, (**n**) gold electroplating to fill the gaps and so on. 99

4.11 SEM images of the effect of exposure dose on the quality of pattern transfer in the self-aligned backside UV lithography. (**a**) Insufficient UV exposure dose results in unstable SU-8 features and incomplete pattern transfer. (**b**) An optimized UV exposure dose transfers the patterns onto the SU-8 layer successfully. (**c**) Higher exposure dose leads to resolution loss in features and SU-8 cross-linking in unwanted areas. 101

4.12 SEM images of a quality pattern transfer: (**a**) over a large area, and (**b**) a closer view of the features. 102

4.13 SEM images of pattern transfer of various feature sizes through the self-aligned backside UV lithography. Periodic lines with thicknesses of (**a**) 1 μm, (**b**) 2 μm, (**c**) 3 μm, and (**d**) 4 μm. The thickness of the SU-8 was around 10 μm for all features as there were all fabricated simultaneously on the same die. 104

4.14 SEM images of pattern transfer of various feature sizes through the self-aligned backside UV lithography. Periodic micropillars with diameters of (**a**) 1 μm, (**b**) 2 μm, (**c**) 3 μm, and (**d**) 4 μm. The thickness of the SU-8 was around 10 μm for all features as there were all fabricated simultaneously on the same die. 105

4.15 SEM images of gold electroplating. (**a**) An overplated sample where SU-8 features are buried under excessive gold plating. (**b**) Sample has undergone a short gold wet etching process. (**c**) A longer gold wet etching starts opening the SU-8 features. (**d**) SU-8 features are open and excessive plated gold is completely etched. (**e**) A side view of released Su-8 features. 107

4.16 SEM images of indium electroplated samples. (**a**) Underplated sample, (**b**) sufficiently plated sample and ready for subsequent SU-8 layer coating, (**c**) overplated sample where features are buried under excessive indium electroplated regions, and (**d**) a closer view of a sufficiently plated sample. 108

4.17 SEM images of the second SU-8 layer in various feature sizes of micropillar-based gratings. A successful pattern transfer from the first SU-8 layer to the second one is evident in all samples with (**a**) and (**b**) being the micropillars sufficiently electroplated with indium, as well as (**c**) and (**d**) being the micropillars underplated with gold. 110

4.18 SEM images of micropillar and line gratings through the self-aligned multi-layer fabrication process. (**a**) Demonstration of micropillars before the definition of the second SU-8 layer, and (**b**) the same micropillars after the second SU-8 layer is fabricated. (**c**) Illustration of a line grating with two SU-8 layers. 111

4.19 SEM images of micropillar-based grating with the second layer of SU-8 (**a**) before and (**b**) after being electroplated with indium. 112
4.20 Demonstration of a prototype large-area 70 mm×70 mm grating fabricated on a 4-inch glass substrate. 113
4.21 Schematic representation of the laser point source setup for testing the electroplating quality. 114
4.22 (a) Illustration of the test setup, with two Fourier transform images acquired from (b) a line grating and (c) a micropillar grating. 114
4.23 Demonstration of the 3D X-ray Microscope – inCiTe™ – and the test setup we used for taking X-ray projection of the prototype version of our grating. 115
4.24 (**a**) X-ray projection of the micropillar-based X-ray grating with three layers and the X-ray source working at 60 kV_p and 200 μA (focal spot of 12 μm); a magnification of 4.5 was used in this X-ray projection. (**b**) A closer view of grids in the X-ray projection image (top), and the cross-sectional profiles of normalized transmission of grids across four rows of grids (bottom). . . . 116
4.25 Transmission map of (**a**) a two-layer and (**b**) a three-layer 70 mm×70 mm prototype X-ray absorption grating. The three-layer grating exhibits a few visible blemishes stemming from the third layer electroplating. 117
4.26 (**a**) Gain map of the prototype 4K×4K high-resolution X-ray detector, showing detector defects and artifacts; the top right quarter of the detector is defective. (**b**) Transmission image for part of the prototype fabricated grating at 60 kV_p. 118
4.27 Illustration of the visibility maps of the fabricated silicon-based micropillar X-ray grating using a polychromatic microfocus X-ray source with the current of 200 μA and working potential of (**a**) 40 kV_p, (**b**) 50 kV_p, (**c**) 60 kV_p, and (**d**) 70 kV_p; all the insets are visibility histograms with their peaks representing the grating visibility at the corresponding X-ray source potential. The 3D X-ray Microscope, inCiTe™ (from KA Imaging, Waterloo, ON, CA) was employed for this measurement. 119
4.28 Illustration of the visibility maps of the fabricated silicon-based micropillar X-ray grating using a polychromatic microfocus X-ray source with the current of 200 μA and working potential of (**a**) 80 kV_p and (**b**) 90 kV_p; all the insets are visibility histograms with their peaks representing the grating visibility at the corresponding X-ray source potential. The 3D X-ray Microscope, inCiTe™ (from KA Imaging, Waterloo, ON, CA) was employed for this measurement. 120

4.29 Visibility, transmission, and absorption characteristics of the silicon-based micropillar X-ray grating versus various X-ray source potentials. 121

5.1 Demonstration of a prototype 1K×1K resolution X-ray detector soldered on its daughterboard, (**a**) before, and (**b**) after encapsulation. 126

5.2 Demonstration of the PB-XPCi: (**a**) Schematic illustration of the system, and (**b**) the prototype version of the system setup mounted on an optical rail in the X-ray cabinet. 127

5.3 Demonstration of the prototype 4K×4K resolution X-ray detector soldered on its daughterboard. 128

5.4 Illustration of the inCiTe™—a 3D X-ray Microscope—used for PB-XPCi in this work. 128

5.5 (**a**) Illustration of the X-ray system model used for IOT. (**b**) The extracted tooth is covered with a piece of meat to resemble the real scenario in IOT. 129

5.6 (**a**) Schematic illustration of a tooth [151] and (**b**) the X-ray projection of the tooth covered with a piece of meat, imaged at 60 kV_p and 199 μA. . . . 130

5.7 The zoomed-in view of the red dashed line region of Figure 5.6b clearly shows the root canals completely. 131

5.8 (**a**) Phase-contrast X-ray image of a tissue equivalent mammography phantom using the prototype 4K×4K resolution X-ray detector and a microfocus X-ray source at 60 kV_p, z_{so}=18 cm, and z_{od}=8 cm; (**b**) and (**c**) illustration of profiles of relative intensity along the vertical cross-section lines of AA′ and BB′, respectively. Microcalcifications as small as 250 μm are visible using the high-resolution detector and the phase contrast X-ray imaging setup. . 132

5.9 Demonstration of attenuation images of acrylic plastic beads (**a**) without, and (**b**) with a void defect—although attenuation images include some edge enhancements thanks to the high-resolution X-ray detector used in this work. Illustration of X-ray phase-contrast images of the same beads (**c**) without, and (**d**) with the void defect. Images were taken using the Thermo Scientific™ PXS5-927 microfocus X-ray source working at 40 kV_p and 180 μA—9 μm focal spot size; with the source-to-sample distance of 18 cm; as well as the sample-to-detector distance of 1 cm and 9 cm for transmission and phase-contrast images, respectively. 134

5.10 (**a**) Phase-contrast image and (**b**) thickness map image—retrieved using *ANKAphase* software—of an acrylic plastic bead, imaged at 40 kV_p and 180 μA with the source-to-sample distance of 18 cm and the sample-to-detector distance 8 cm. (**c**) A cross-sectional profile of the object thickness (red solid line) and the edge-enhancement (blue solid line) across the corresponding dashed lines. 135

5.11 Illustration of (**a**) X-ray attenuation image of a bee head imaged at 60 kV_p, $z_{so} = 18$ cm, and $z_{od} = 1$ cm; and (**b**) X-ray phase-contrast image of the same bee head imaged at 60 kV_p and 120 μA, $z_{so} = 18$ cm, and $z_{od} = 8$ cm, using the prototype version of the 1K×1K high-resolution X-ray detector and the Thermo Scientific™ PXS5-927 microfocus X-ray source. 136

5.12 Illustration of the EI-XPCi: (**a**) Schematic view of the system, and (**b**) the prototype version of the system setup mounted on an optical rail in the X-ray cabinet; where the z_{sg} is the source-to-grating distance, the z_{go} is the grating-to-object distance, and the z_{od} is the object-to-detector distance. . 137

5.13 Illustration of the inCiTe™ system–that employs the BrillianSe™ X-ray detector–modified to include the X-ray absorption grating and perform EI-XPCi in this work. 138

5.14 Demonstration of a line X-ray absorption grating with 10 μm-wide apertures and 79 μm period. Vertical line apertures—SU-8 molds—are separated by 30 μm bridges. 139

5.15 Illustration of the single-mask EI-XPCi system model used for simulation. The Gaussian profiles on the detector are the intensity profile distribution of beamlets before (solid blue line) and after (dashed purple line) definition of the object. 140

5.16 Simulation result of relative intensity profile clearly highlights the beamlet's profile (the Gaussian pattern) detected by groups of pixels. 141

5.17 Experimental data of relative intensity profile registered at the detector shows the beamlets' profile (the Gaussian pattern) obtained from groups of pixels. 142

5.18 The agreement between beamlet shape from experimental data and simulation result. The higher value of lower left and right tails of experimental data is related to pre-sample mask imperfection and detector PSF. 142

5.19 Illustration of the (**a**) reference and (**b**) sample images of the PTFE rod imaged at 40 kV_p and 180 μm using the prototype 1K×1K high-resolution X-ray detector. 143

5.20 Preliminary qualitative results of (**a**) transmission, (**b**) phase shift, and (**c**) scattering of a PTFE rod imaged at 40 kV_p and 180 μA with source-to-grating, grating-to-sample, and sample-to-detector distances of 18 cm, 1 cm, and 7 cm, respectively. 144

5.21 Representation of the EI-XPCi system highlighting the sensitivity to X-ray scattering by α angle for one beamlet. 146

5.22 Illustration of the optical image of (**a**) acrylic beads, and (**b**) dry sponge. The X-ray projections using the line grating in the EI-XPCi system are illustrated in (**c**) and (**d**) for acrylic beads and dry sponge, respectively. The source-to-grating, grating-to-object, and object-to-grating distances were 32 cm, 1 cm, and 12 cm, respectively. The line grating had 10 μm-wide apertures and 79 μm period. The Hamamatsu L12531 microfocus X-ray source was working at 40 kV_p and 200 μA, and we used the prototype 4K×4K high-resolution 8 μm pixel size X-ray detector. 147

5.23 Illustration of (**a**) transmission, (**b**) phase, and (**c**) scattering images of the acrylic beads sample retrieved through the Gaussian fitting method; (**d**), (**e**), and (**f**) also represent the transmission, phase, and scattering images, respectively, of the same sample using the moment analysis method. 148

5.24 Illustration of (**a**) transmission, (**b**) phase, and (**c**) scattering images of the dry sponge sample retrieved through the Gaussian fitting method; (**d**), (**e**), and (**f**) also represent the transmission, phase, and scattering images, respectively, of the same sample using the moment analysis method. 149

5.25 Illustration of the line grating direction dependency in imaging multi-direction oriented objects. Features perpendicular to grating septa—i.e., horizontal cylinder in (**a**) and vertical cylinder in (**b**)—become invisible in the X-ray phase-contrast image. 150

5.26 (**a**) Photo of the acrylic phantom with line grooves. (**b**) Illustration of the phase image of the acrylic phantom using the setup depicted in Figure 5.25a with the phantom oriented with line grooves almost perpendicular to grating septa. (**c**) Illustration of the phase image of the same phantom using the setup depicted in Figure 5.25a with the phantom oriented with line grooves almost parallel to the grating septa; the edges of line grooves appear in the phase images. 151

5.27 Schematic illustration of a system with an X-ray source, a single X-ray aperture, and a high-resolution X-ray detector to register the X-ray beamlet. The detector pixel size is smaller than the beamlet size. 152

5.28 Demonstration of the two-dimensional Gaussian distribution—IC profile—of a single pencil-shape beamlet. 153

5.29 Schematic illustration of a single-mask EI-XPCi system with a 2D grating, representing the pencil-shape beamlets. The detector pixel size is smaller than the beamlets', enabling the high-resolution X-ray detector to register IC profiles with groups of pixels. 154

5.30 Demonstration of the two-dimensional Gaussian distribution—IC profile—of a 3×3 pencil-shape beamlets' intensity profile detected by the prototype 4K×4K high-resolution X-ray detector. 154

5.31 Schematic illustration of the X-ray setup used to perform XPCi using a single X-ray absorption grating. 155

5.32 (**a**) A centrifuge tube filled with sugar powder as the sample of interest, although the sugar powders are not in the same position as when the EI-XPCi was taken. (**b**) Transmission, (**c**) refraction, and (**d**) scattering images retrieved from a single-exposure X-ray phase-contrast image taken at 60 kV_p of the sample. X-ray phase-contrast images are represented based on a false color tone for better representation. 156

5.33 Schematic illustration of the speckle-tracking XPCi system with a reference interference pattern (blue solid line) and a sample interference pattern (red dashed line). The random interference pattern created by a sandpaper diffuser distorts after passing through an inhomogeneous sample—due to scattering effects. 157

5.34 Schematic illustration of the speckle-tracking XPCi system with a reference interference pattern (blue solid line) and a sample interference pattern (red dashed line). The structured interference pattern created by a 2D grating distorts after passing through an inhomogeneous sample—due to scattering effects. 158

5.35 Image of object used for speckle-tracking XPCi: (**a**) acrylic beads, (**b**) sugar powder, (**c**) titanium oxide powder with 10 μm×100 nm size particles, (**d**) titanium oxide powder with 25 nm size particles, (**e**) dry solder sponge, and (**f**) wet solder sponge. The red dashed squares represent the region of interest (ROI) in X-ray phase-contrast images. 160

5.36 Illustration of (**a**) transmission and (**b**) dark-field images of the acrylic beads, imaged in the speckle-tracking XPCi system using the silicon micropillar 2D grating. The dark-field image does not reveal the semi-homogeneous acrylic beads and the centrifuge tube container. 161

5.37 Illustration of (**a**) transmission and (**b**) dark-field images of the sugar powder sample, imaged in the speckle-tracking XPCi system using the silicon micropillar 2D grating. The dark-field image reveals the inhomogeneous sugar powder with particle sizes well below the system resolution (i.e., defined by the grating aperture size). 161

5.38 Illustration of (**a**) transmission and (**b**) dark-field images of the titanium oxide powder sample with 10 μm$\times$100 nm size particles, and (**c**) transmission and (**d**) dark-field images of the titanium oxide powder sample with 25 nm size particles; both samples were imaged in the speckle-tracking XPCi system using the silicon micropillar 2D grating. The finer particle size sample indicates a higher dark-field signal. 162

5.39 Illustration of (**a**) transmission and (**b**) dark-field images of the wet sponge sample, and (**c**) transmission and (**d**) dark-field images of the dry sponge sample; both samples were imaged in the speckle-tracking XPCi system using the silicon micropillar 2D grating. Water weakens the dark-field signal as evident in the wet sponge dark-field image. 163

5.40 Illustration of (**a**) transmission and (**b**) dark-field images of the acrylic beads, imaged in the speckle-tracking XPCi system using the prototype three-layer SU-8 2D grating. The dark-field image reveals the weak scattering signal from the acrylic beads in the centrifuge tube container. 165

5.41 Illustration of (**a**) transmission and (**b**) dark-field images of the sugar powder sample, imaged in the speckle-tracking XPCi system using the prototype three-layer SU-8 2D grating. The dark-field image reveals the inhomogeneous sugar powder with particle sizes well below the system resolution (i.e., defined by the grating aperture size). 165

5.42 Illustration of (**a**) transmission and (**b**) dark-field images of the titanium oxide powder sample with 10 μm$\times$100 nm size particles, and (**c**) transmission and (**d**) dark-field images of the titanium oxide powder sample with 25 nm size particles; both samples were imaged in the speckle-tracking XPCi system using the prototype three-layer SU-8 2D grating. The finer particle size sample indicates a higher dark-field signal. 166

5.43 Illustration of (**a**) transmission and (**b**) dark-field images of the wet sponge sample, and (**c**) transmission and (**d**) dark-field images of the dry sponge sample; both samples were imaged in the speckle-tracking XPCi system the prototype three-layer SU-8 2D grating. Water weakens the dark-field signal, as evident in the wet sponge dark-field image. 167

Chapter 1

Introduction

1.1 Background on X-ray Phase-Contrast Imaging

X-ray imaging has become an inevitable part of our life with its benefits in many fields, such as medical diagnosis, industry, research, and security. Today's X-ray imaging systems—although with an improvement in image quality—primarily work based on the same concept Röntgen used in the late 19th century. X-ray imaging systems operate based on X-ray photons—generated by an X-ray source—passing through an object and being detected on a screen downstream of the object. In conventional X-ray imaging systems, the main factor in creating X-ray images has been the attenuation of X-ray photons after exiting the object. The attenuation of X-ray photons in an object leads to an intensity change on the screen (detector), resulting in the so-called transmission (attenuation) contrast image. X-ray radiographs present the variation of X-ray photons transmission passing through objects, which provides us with some quantitative—but primarily qualitative—data to analyze the internal structure of objects. Conventional attenuation-contrast X-ray imaging methods do not effectively reveal the internal structure of objects comprised of materials with non-absorbing or poor-absorbing X-ray characteristics. Objects such as soft tissues in medical imaging and diagnosis applications; low atomic number materials in industrial and security inspections; and sub-pixel size features in all applications become invisible to conventional X-ray imaging methods. Furthermore, it is challenging to distinguish between materials with identical X-ray absorption characteristics using attenuation-contrast imaging.

X-ray photons not only attenuate passing through an object, but also refract and scatter, which has been under study in X-ray imaging for the past three decades. X-ray phase-contrast imaging (XPCi) is a method of imaging with a focus on the change in phase

properties of X-rays to create new images and reveal information unseen by conventional attenuation-contrast methods [1, 2]. Although the detection of the amplitude of X-rays is well known, the phase coefficient of X-rays has not yet been measured directly using an X-ray detector. X-ray phase coefficient, however, can be detected indirectly with the phase information encoded in the intensity profile of an X-ray projection. X-ray imaging based on phase-contrast has demonstrated to be as high as three orders of magnitude more sensitive to density variations in an object than attenuation-contrast imaging. Applications that are enabled by XPCi span many fields, from industry and science to medicine and biology [3–11]. XPCi methods provide multi-modal information about the internal properties of objects through three distinct images, transmission (absorption), phase (refraction), and dark-filed (ultra-small angle scattering) [12–15]. The additional information about an object provided by XPCi—phase and scattering images—complements the quantitative data to study the object's internal structure. The phase image emphasizes light materials in an object that hardly create an absorption contrast, which is required in detecting soft tissues, low atomic number materials, and articular cartilage, to name a few. The dark-field image is also valuable as it highlights an object's microstructure particles with features well below the detector pixel size. The scattering information in the dark-field image is of paramount importance in applications such as mammography, lung imaging, and imaging porous material where objects' microstructure features are invisible in transmission or phase images.

1.2 X-ray Grating

Different methods have been developed to perform multi-modal X-ray imaging, which mainly vary based on their optical apparatus requirements. Gratings are among the optical components that can alter the course of an incoming wave. Absorption gratings are periodic structures of an X-ray absorber material that, if placed in front of an X-ray source, translate the incoming X-ray beam into an array of beamlets. Gratings are employed in various applications, such as spectrometers, monochromators, and imaging.

Grating-based XPCi techniques work based on the translation of the incoming X-rays into new patterns, consequently facilitating the detection of an object's transmission, phase, and scattering information simultaneously. Talbot-Lau (Talbot) [16–18], coded-aperture (edge-illumination) [19–23], and speckle-tracking [24–28] are among XPCi methods that employ X-ray absorption gratings to provide multi-modal imaging feasibility. These techniques—reliant on X-ray absorption gratings—possess higher contrast and sensitivity compared to non-grating-based XPCi methods. Absorption gratings are integral to defining the quality of imaging; therefore, any imperfection in their fabrication process

directly affects the final image quality, leading to image artifacts or loss of image quality and details information [29, 30].

There are two main approaches in fabricating X-ray gratings: etching (top to bottom) and molding (bottom to top). The former is usually conducted on silicon wafers through anisotropic etching techniques such as metal-assisted chemical etching [31–33], plasma etching [34–38], or wet etching [39–41]. The latter, however, is performed based on LIGA process–lithographie, galvanoformung, abformung or alternately lithography, electroplating, and molding [42–44]. In spite of the fact that silicon-based etching processes can achieve high aspect ratio structures, fabrication methods reliant on them are limited to standard-size wafers.

In the last two decades, high-resolution X-ray imaging has gained more attention in applications such as clinical diagnostics, material science, and industrial inspections [45–53]. High-resolution XPCi methods are on the verge of becoming an alternative to conventional attenuation-only X-ray imaging systems. However, for high-resolution imaging employing high-resolution detectors, challenges in absorption grating fabrication have impeded the technology translation into the market. These challenges involve the fabrication of high-resolution absorption gratings with high aspect ratio periodic structures in the micron-scale range. Fabrication of gratings for compact systems or higher energy imaging applications becomes even more problematic due to the stringent requirements on the grating feature sizes and aspect ratio. Moreover, the need for a larger field-of-view (FOV) imaging is on the rise with the development of XPCi methods. Applications with larger FOV demand large-area (e.g., 30 cm $\times$ 30 cm) or flexible absorption gratings, such as in clinical diagnostic and whole-body imaging, as well as industrial and security inspections [54–58].

1.3 Thesis Purpose and Objectives

This thesis focuses on the development of high-resolution X-ray phase-contrast imaging systems at both the device and system levels. The research objectives are as follows:

1. To compare the performance of X-ray phase-contrast propagation and grating-based imaging systems that leverage an in-house developed world first 8 μm pixel size direct conversion X-ray detector.

2. To develop a scalable, large-area, fabrication process for a high-resolution, high aspect ratio X-ray grating for large area X-ray imaging applications.

3. To examine and improve XPCi systems performance, particularly single-mask edge-illumination X-ray phase-contrast imaging systems based on the in-house developed detector and the in-house developed high-resolution grating.

At the device level, high-resolution, high aspect ratio X-ray absorption gratings are studied and fabricated. A direct conversion high-resolution X-ray detector with micron-scale pixel pitch is also investigated in this thesis for its application in XPCi. At the system level, various XPCi systems are investigated through propagation-based (PB), double-mask edge-illumination (EI), single-mask EI, and speckle-tracking XPCi techniques. Although the PB-XPCi method—alongside a high-resolution X-ray detector—can potentially provide salient transmission – and, to some extent, phase – images, it is not as powerful as grating-based methods with non-synchrotron facility X-ray sources. The major obstacle to realizing high-resolution grating-based XPCi methods has been the technological challenges in the grating fabrication processes. This work is an endeavor toward addressing the need for high-resolution grating-based XPCi systems for medical and non-medical applications. Having mentioned that, the significant contribution of this thesis—at the device level—is the development of a process to enable the fabrication of scalable high-resolution large-area X-ray absorption gratings with low cost and high throughput. At the system level, however, the main contribution of this work is the realization of grating-based XPCi systems employing low-power polychromatic microfocus X-ray sources with high-resolution X-ray absorption gratings, all in a compact benchtop setup. Finally, by applying a micron-scale pixel pitch X-ray detector and high-resolution X-ray absorption grating developments achieved in the previous research phases, improvements in imaging applications such as mammography, dental tomosynthesis, and material characterization are obtained.

1.4 Thesis Organization

The balance of this thesis is organized as follows:

- Chapter 2 begins with modeling PB and EI-XPCi, reviewing system-level performance metrics, and continues with an investigation on the potential of employing micro-scale high-resolution X-ray detectors in PB and EI-XPCi. This chapter finishes with major challenges concerning using micron-scale X-ray detectors in a compact EI-XPCi setup which opens the way to address them in the following chapters.

- Chapter 3 explores one solution—the first attempt—to address the fabrication of high-resolution X-ray absorption grating via silicon technology. The requirement of an atomic layer deposition (ALD) tool and not having access to this tool made us shift our focus to addressing the fabrication process from etching silicon wafers to an innovative LIGA process.

- Chapter 4 elaborates on a novel UV LIGA process to address the fabrication of high-resolution high aspect ratio large-area X-ray absorption gratings at low cost and high throughput. This chapter, in particular, enables the realization of high-resolution EI-XPCi systems in a compact setup.

- Chapter 5 covers the application of a prototype micron-scale high-resolution X-ray detector in PB and EI-XPCi. The main focus of this chapter is to demonstrate the potential of single-mask EI-XPCi systems employing the high-resolution grating fabricated in this work in providing multi-modal information—transmission, phase, and dark-field images—about a sample, all through a single-exposure compact setup.

- Chapter 6 provides the main conclusions as well as contributions of this work to X-ray grating fabrication development and grating-based XPCi.

All research objectives are fulfilled in this thesis throughout the aforementioned chapters.

Chapter 2

High-Resolution X-ray Phase Contrast Imaging

In this chapter, the first objective of the thesis is addressed, which is to compare the performance of X-ray phase-contrast propagation and grating-based imaging systems considering the existing technological limitations and challenges. Specifically, we investigate the potential of employing a direct conversion integration mode X-ray detector with micron-scale pixels in two different XPCi configurations, PB and EI. Both PB-XPCi and EI-XPCi implementations are evaluated through a wave optics model—numerically simulated in MATLAB—and are compared based on their contrast, edge-enhancement, visibility, and dose efficiency characteristics. The EI-XPCi configuration, in general, demonstrates higher performance compared to PB-XPCi, considering a setup with the same X-ray source and detector. However, absorption masks quality (thickness of X-ray absorption material) and environmental vibration effect are two potential challenges for EI-XPCi employing a detector with micron-scale pixels. Simulation results confirm that the behavior of an EI-XPCi system employing a high-resolution detector is susceptible to its absorption masks thickness and also to misalignment.

The contributions in this chapter, i.e., to compare the performance of X-ray phase-contrast propagation and grating-based imaging systems, highlight the advantages and challenges of leveraging an in-house developed world first 8 μm pixel size direct conversion X-ray detector in XPCi systems and, in particular, compact XPCi setups.

2.1 Introduction

X-ray Phase-Contrast Imaging (XPCi), an emerging modality, has demonstrated early results that are superior to conventional attenuation-based X-ray imaging due to its ability to improve visualization of low-contrast objects. It offers an attractive lower cost and potentially higher throughput, and higher spatial resolution alternative to magnetic resonance imaging (MRI) and other imaging methods in some clinical scenarios. This modality has been clinically evaluated to image breast tissue, cancer specimens, and brain tissue, in addition to characterizing multi-material samples [2, 9, 59].

Among different techniques developed to realize the XPCi modality, propagation-based (PB), and edge-illumination (EI) can be scaled in a relatively straightforward manner to large-area imaging systems, which gives them an advantage over other approaches [1, 19]. EI-XPCi, in particular, can provide excellent detail from various objects, which makes it a promising candidate for next-generation commercial X-ray imaging benchtop systems [60]. In spite of the fact that PB-XPCi offers a less complex setup compared to EI-XPCi—which requires at least one or a set of two absorption gratings—PB-XPCi requires mathematically intensive methods and approximations to retrieve phase and attenuation information. Although many PB-XPCi information retrieval methods are reported, they vary based on different assumptions and approximations made, and the complexity of the required input data for different materials makes them hard to use. Moreover, not all of these information retrieval methods can be applied to applications where polychromatic X-ray sources are employed [61–64]. On the other hand, information retrieval in EI-XPCi can be performed in a less computationally intensive manner with fewer approximations due to simpler imaging physics [65]. In both PB and EI-XPCi, however, employing a high-resolution X-ray detector can potentially improve the detectability of small feature sizes in objects [66].

High spatial resolution imaging is important for certain medical and non-medical applications. The span of its application varies from microtomography (μ-CT) and mammography—where detecting more details and identifying objects with small feature sizes, such as carcinoma, calcification, or cancerous tumor are crucial and vital, especially at their early stages—to emerging applications in the industry such as semiconductor inspection, machine vision, and material science [45–51]. Extensive research has been conducted in our group, in particular, to improve spatial resolution in compact X-ray detectors for energies above 20 keV using a combination of amorphous selenium (a-Se) photoconductors and complementary metal-oxide semiconductor (CMOS) readout technology with micron-scale pixels [52, 67, 68].

Imaging at higher resolutions, higher X-ray energies, and lower exposures are three

main and highly interdependent criteria for enhancing XPCi systems with absorption mask gratings. In principle, employing high-resolution absorption gratings along with a high-resolution detector with a compatible microfocus X-ray source should improve EI-XPCi performance. However, such a high-performance EI-XPCi system has not yet been reported due to technological challenges. Two main bottlenecks that impede the realization of such a high-resolution EI-XPCi system are [69]:

1. Fabrication of high-resolution (fine pitch) absorption gratings compatible with the small pixel size of such high-resolution detectors,

2. Mechanical vibration sensitivity of a high-resolution EI-XPCi system.

In this chapter, we first introduce a framework by which both PB-XPCi and EI-XPCi can be modelled and numerically simulated; we verify the numerical simulation results using experimental data to validate the model. This model, at a system level, takes into account the effect of source, detector, and pixel blurring and, in addition, the thickness and mechanical vibration of the absorption gratings in the final image. By utilizing this model, we analyze PB-XPCi and EI-XPCi methods and evaluate their performance in terms of contrast, edge-enhancement, visibility, and dose efficiency characteristics to explain how EI-XPCi can outperform PB-XPCi with the same X-ray source and detector. This higher performance is a result of EI-XPCi containing less background attenuation signal compared to PB-XPCi—which can be interpreted as an unwanted signal; thus, EI-XPCi produces a phase image with higher contrast compared to PB-XPCi. Despite EI-XPCi's superiority over PB-XPCi, simulation results reveal that the absorption masks thickness variation and mechanical vibration can significantly affect the behavior of a high-resolution EI-XPCi system. Next, we present existing PB-XPCi and EI-XPCi systems and demonstrate what type of technology is currently being used in each system. A 1K×1K direct conversion a-Se/CMOS-based high-resolution integration mode X-ray area detector with a pixel pitch equal to 7.8 μm [70] is introduced in this work. Ultimately, we show how the X-ray absorption grating fabrication industry is one step behind the high-resolution detector technology, particularly in EI-XPCi systems.

2.2 Theory and Model

Both PB-XPCi and EI-XPCi systems can be mathematically modelled based on electromagnetic wave transmission through objects and propagation in free-space. Figure 2.1 illustrates the components and geometry of an EI-XPCi system model. It consists of an X-ray source, a pre-sample absorption mask, an object, a detector absorption mask, and

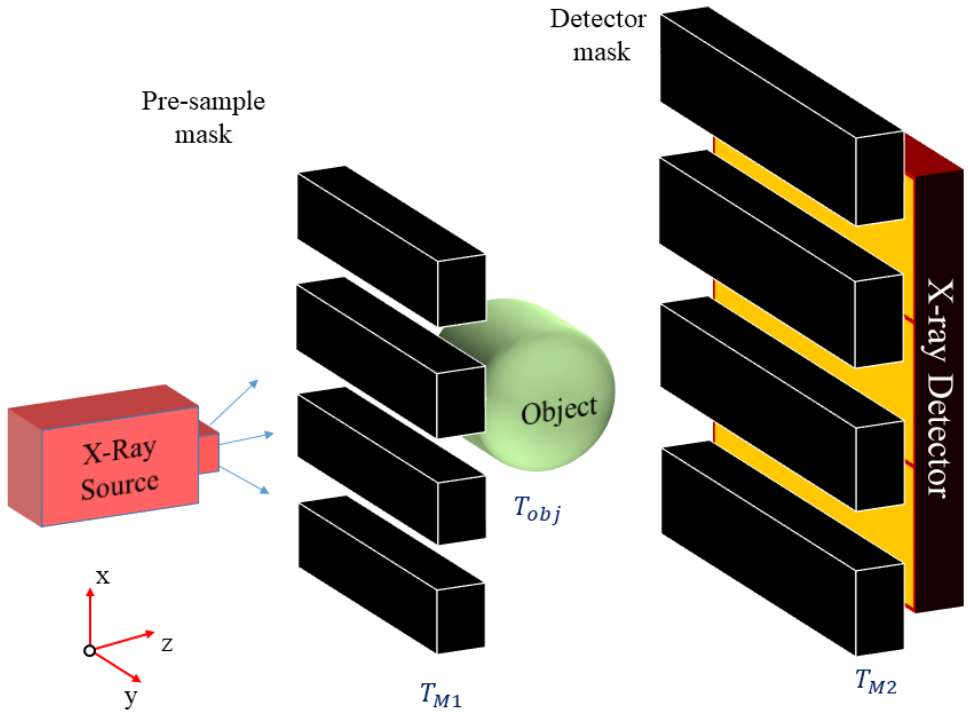


Figure 2.1: Components and geometry of the EI-XPCi (as well as PB-XPCi) system model. In this figure, a line grating is shown; however, a 2D grating could be substituted as required.

an X-ray detector. It is assumed that the pre-sample mask and detector mask are placed at the object plane and detector plane, respectively. Following the Fresnel–Kirchhoff integral to describe the propagation of X-rays between source and object, as well as object and detector, the expected signal intensity at position (x, y) registered at the detector plane—$I_d(x, y)$—can be expressed through Equations (2.1)–(2.6):

$$I_d(x,y) = \int\int EgN(x,y,E)\times$$
$$\mathcal{F}^{-1}\left\{MTF \times \mathcal{F}\left\{\mathcal{F}^{-1}\left\{\mathcal{F}\{S_r(x,y)\} \times \mathcal{F}\{I_p(x,y,E)\}\right\} \times \left|T_{M2}(x,y)\right|^2\right\}\right\} dEdxdy\,, \quad (2.1)$$

$$N(x,y,E) = \Phi(E)tw^2\eta_d(E)\,, \quad (2.2)$$

$$MTF = MTF_s \times MTF_d \times MTF_p\,, \tag{2.3}$$

$$I_p = \left| \mathcal{F}^{-1}\Big\{ \mathcal{F}\big\{ H_1(x,y,E) \times T_{M1}(x,y) \times T_{obj}(x,y,E) \big\} \times \mathcal{F}\big\{ H_2(x,y,E) \big\} \Big\} \right|^2, \tag{2.4}$$

$$H(x,y,E) = \frac{e^{ikz}}{i\lambda z} e^{(ik\frac{x^2+y^2}{2z})}\,, \tag{2.5}$$

$$T_{\text{obj}}(x,y,E) = e^{\left(i\phi(x,y,E) - M(x,y,E)\right)}\,, \tag{2.6}$$

where E is the photon energy; g is the detector gain; $N(x,y,E)$ is the number of X-ray photons; MTF is the combined modulation transfer function of source (MTF_s), detector (MTF_d), and pixel (MTF_p); $S_r(x,y)$ is the re-scaled source intensity distribution on the detector plane; $I_p(x,y,E)$ is the intensity measured at a pixel; $\Phi(E)$ is the photon flux (photons per time and area) in the detector plane when no object is present; t is the duration of exposure time; w^2 is the pixel area; $\eta_d(E)$ is the detector absorption efficiency; $H_1(x,y,E)$ is the Fresnel propagator between source and object plane; $H_2(x,y,E)$ is the Fresnel propagator between the object plane and detector plane; T_{M1} is the pre-sample mask transmission function and T_{M2} is the detector mask transmission function, where both are equal to one within the apertures and are equal to zero in the absorbing septa; T_{obj} is the object transmission function; λ is the wavelength of a monochromatic wave; k is the wave number in the z-propagation-direction; as well as $\phi(x,y,E)$ is the phase shift and $M(x,y,E)$ is the linear amplitude attenuation, both calculated from the complex refractive index of the object [71, 72].

Considering that the object of interest is described by its complex refractive index through Equation (2.7):

$$n(x,y,z) = 1 - \delta(x,y,z) + i\beta(x,y,z), \tag{2.7}$$

where δ (phase coefficient) and β (absorption coefficient) are related to the refraction and absorption of the object, respectively. If the material composition of the object is known, one can calculate δ and β using Equations (2.8) and (2.9):

$$\delta = \frac{r_0 h^2 c^2}{2\pi E^2} \sum_Z n_Z f^0_{1Z}(E), \tag{2.8}$$

$$\beta = \mu \frac{hc}{4\pi E}, \tag{2.9}$$

with r_0 being the Thomson scattering length or the classical electron radius, h the Planck's constant, c the speed of light, and E the photon energy; n_Z is the atomic density, Z is the atomic number with a summation over all present elements in the object material composition, f_{1Z}^0 is the forward scattering factor that can be considered equal to Z in this case, and μ is the linear attenuation coefficient [72]. Using Equations (2.8) and (2.9), we can calculate $\phi(x, y, E)$ and $M(x, y, E)$ through Equations (2.10) and (2.11):

$$\phi(x, y, E) = k \int_{-\infty}^{z} \delta(x, y, z) dz, \tag{2.10}$$

$$M(x, y, E) = 2k \int_{-\infty}^{z} \beta(x, y, z) dz. \tag{2.11}$$

The required thickness of a material to stop an X-ray photon can be calculated using exponential attenuation law through Equation (2.12):

$$\frac{I}{I_0} = e^{-(\frac{\mu}{\rho})x}. \tag{2.12}$$

It is worth mentioning that x, mass thickness, is defined as the mass per unit area, and is obtained by multiplying the thickness x_t by the density ρ, i.e., $x = \rho x_t$. Gold is selected as the X-ray absorber for absorption masks design since it is widely used in X-ray mask fabrication. Figure 2.2 illustrates the required thickness of gold (for an absorption mask) versus X-ray energy so the X-ray can be stopped in an absorption mask.

Environmental vibration has a negative effect on the EI-XPCi system. In this chapter, environmental vibration is translated into mechanical displacement in the mask misalignment. It should be noted that, for the sake of simplicity, this vibration is modelled through mechanical displacement along only the x-direction of the pre-sample mask, since line gratings (Figure 2.1) are assumed for this study. It is assumed that mask misalignment associated with mechanical vibration is within a range of two micrometres. We have simulated different scenarios in which mask misalignment varies within this range for both a high resolution EI-XPCi (pixel size equal to 7.8 μm to match the prototype detector) and an EI-XPCi system with a bigger pixel pitch (39 μm, i.e., 5×5 pixel binning) to highlight the effect of vibration on a high-resolution EI-XPCi system.

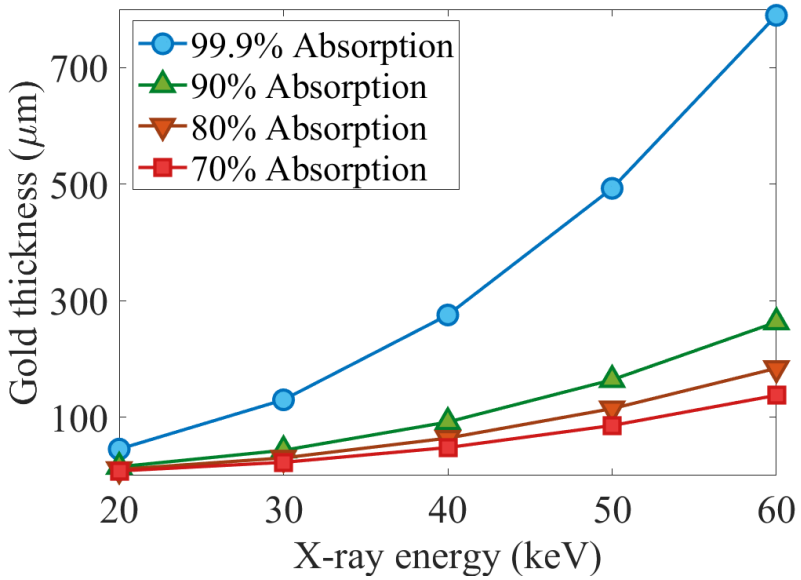


Figure 2.2: Required mask thickness (thickness of absorption part, which is gold here) to stop the X-ray energy.

2.3 Simulation and Verification

The model explained here works well for both monochromatic as well as polychromatic X-ray sources, where, in the latter scenario, the intensity registered at the detector is calculated by integration over each individual X-ray energy component contributed to the polychromatic source energy spectrum. This model is numerically simulated in MATLAB® following the algorithm schematically shown in Figure 2.3 and written in Table 2.1 (Appendix A). It should be noted that we employed the *spektr* toolset to simulate the X-ray spectrum and mass-energy attenuation coefficient—the data for which were retrieved from NIST [73].

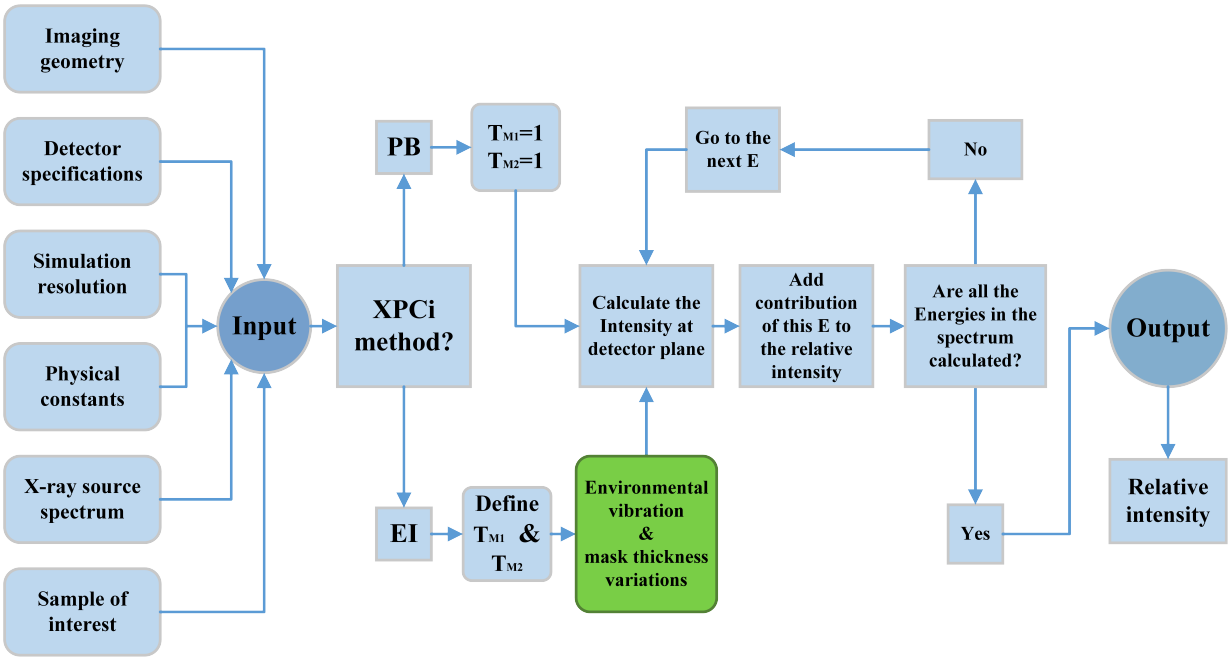


Figure 2.3: Schematic demonstration of the algorithm used to simulate the model for both PB-XPCi and EI-XPCi configurations in MATLAB®. The green block represents where absorption mask thickness variation and mechanical vibration are defined in the model.

The algorithm takes into account the following parameter as the input:

- Imaging geometry: usually equal to the detector size
- Detector specifications: including pixel size and pixel pitch, materials used either as the scintillator or X-ray converter
- Resolution of the simulation: usually at least ten times greater than the pixel size
- Physical constants: those defined in Equations (2.1)–(2.12)
- The X-ray source spectrum: according to the *spektr* toolset
- Physical and geometrical characteristics of the sample of interest.

Absorption masks are defined according to the XPCi modality–PB or EI. The Equation (2.1) is then calculated and integrated over the individual energy components, based on the polychromatic X-ray source spectrum, or single energy component, for the monochromatic X-ray source, in two scenarios: the dark image–with no object present–and the object image–when an object is introduced to the system. Finally, the simulation outputs–the dark image and the object image–help characterize and evaluate the system for both modalities–PB and EI.

Table 2.1: Algorithm used for simulating the model in MATLAB® for both PB-XPCi and EI-XPCi.

Algorithm for simulating the model in MATLAB

Input:

Imaging geometry, source to object distance z_{so}, and object to detector distance z_{od}
Detector's specifications (pixel size w^2, gain g, etc.)
Simulation resolution, field of view, and spatial frequencies
Physical constants
X-ray source spectrum
Sample refractive index data, $\boldsymbol{\mu}$ and $\boldsymbol{\delta}$
Pre-sample and detector absorption masks, $\boldsymbol{T_{M1}}$ and $\boldsymbol{T_{M2}}$:

$$\boldsymbol{T_M(x,y)} = \begin{cases} \mathbf{1} & \text{within the apertures} \\ \mathbf{0} & \text{within the absorbing spectra} \end{cases}$$

Output:

Simulating the intensity at detector plane for all X-ray energies:
for E in energy spectrum
if PB-XPCi
$\boldsymbol{T_{M1}} = 1$
$\boldsymbol{T_{M2}} = 1$
elseif EI-XPCi
consider $\boldsymbol{T_{M1}}$ and $\boldsymbol{T_{M2}}$
end if
Calculate $\boldsymbol{I_d}$ when no object is present = $\boldsymbol{I_{dark}}$ from Equation (2.1)
Calculate $\boldsymbol{I_d}$ with the object in place = $\boldsymbol{I_{object}}$ from Equation (2.1)
end for
Calculating the Contrast, Edge-Enhancement, and Visibility

To verify the model, simulation results are compared with experimental data from [71] (using a quasi-monochromatic X-ray beam with an energy of 20 keV), which are illustrated in Figure 2.4. Simulation is done assuming a quasi-monochromatic Gaussian distributed X-ray source with FWHM = 80 μm at 40 kV_p (equal to 20 keV); source to sample distance of 20 m and sample to detector distance of 0.55 m; as well as 50% illumination fraction (for EI-XPCi setup) for two different samples: polyetheretherketone (PEEK) wire with a diameter equal to 460 μm, and titanium wire with a diameter equal to 250 μm. PEEK is selected as an almost transparent object to the X-ray energy considered for this comparison, hence it reveals an intensity profile that is mainly due to phase shift rather than attenuation contrast; and Titanium is chosen as an object which presents a strong absorption, thus a wide range of conditions is covered to verify the model.

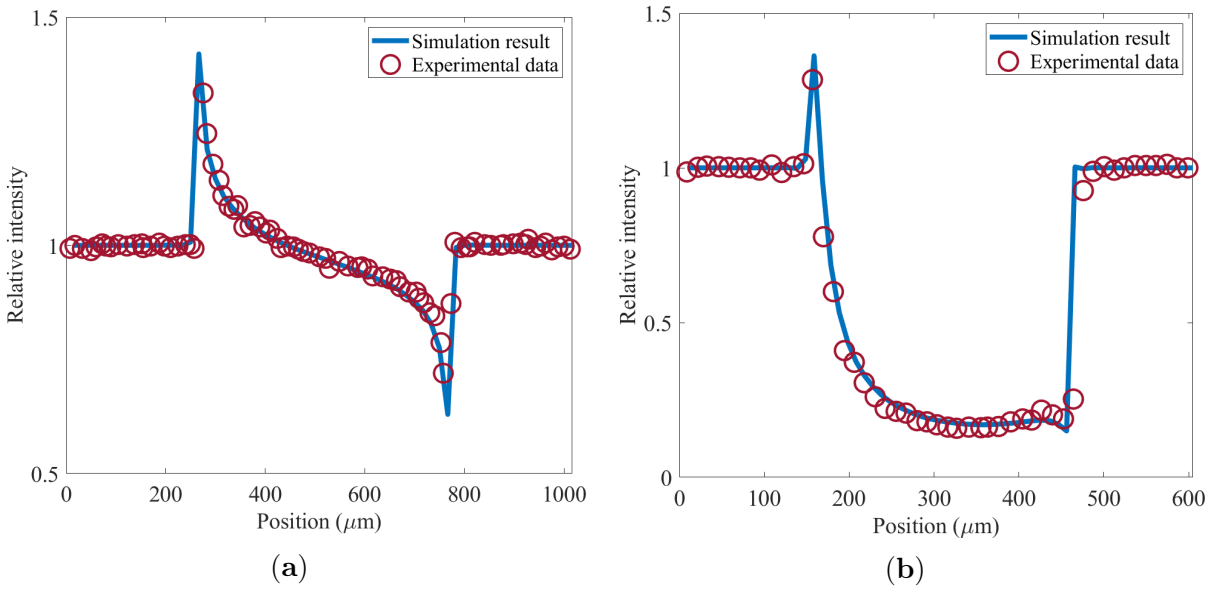


Figure 2.4: Comparison between the simulation result and experimental data extracted from [71] for (**a**) a PEEK wire, and (**b**) a Titanium wire. The solid blue line represents the simulation result, and the red circles demonstrate experimental data.

2.4 Comparison Metrics for High-Resolution PB-XPCi and EI-XPCi

The model explained in the previous section is employed to investigate the PB-XPCi and EI-XPCi systems and to evaluate them, where we have considered a polychromatic micro-focus X-ray source working at 60 kV_p with a spot size equal to 9 μm (except for studying the effect of MTF_d on the imaging performance where we consider a spot size equal to 2 μm) and a detector with pixel size and pitch equal to 7.8 μm for a PEEK wire with a diameter equal to 585 μm as the object of interest. The results of this comparison are studied in the following sections. Figure 2.5 illustrates the X-ray spectrum (of a tungsten target) employed for this study to simulate the model.

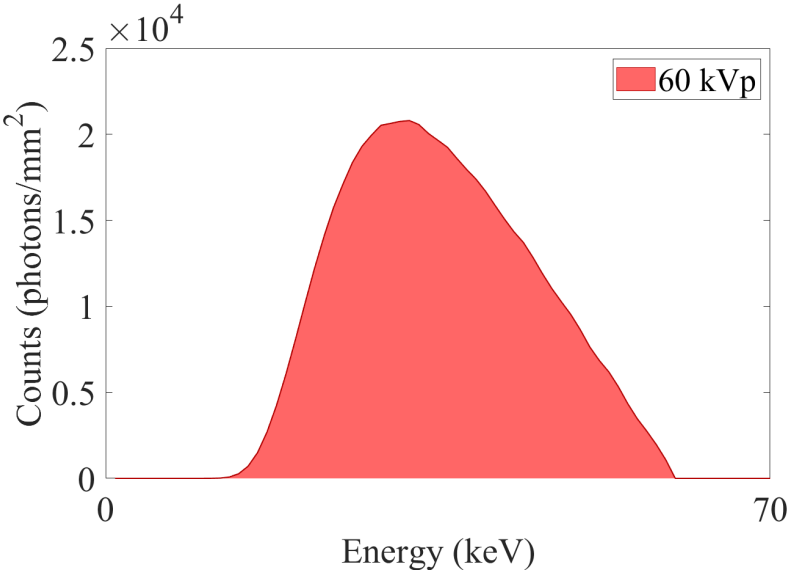


Figure 2.5: X-ray spectrum of the tungsten target employed from the *spektr* toolset in MATLAB® for simulation. The spectrum is filtered by 0.5 mm aluminum (Al).

Contrast, edge-enhancement, and visibility characteristics [74] of PB-XPCi and EI-XPCi are evaluated and compared using Equations (2.13)–(2.15):

$$Contrast = \frac{I_{max} - I_{min}}{I_{background}}, \tag{2.13}$$

$$Edge\text{-}Enhancement\ (\%) = \frac{I_{max} - I_{background}}{I_{background}} \times 100, \tag{2.14}$$

$$Visibility = \frac{I_{max} - I_{min}}{I_{max} + I_{min}}, \tag{2.15}$$

where I_{max}, I_{min}, and $I_{background}$ are the maximum, minimum, and background signals registered at the detector, respectively. Dose efficiency, however, is considered as a relative measure to compare how much of the incident X-ray is registered at the object.

2.5 Direct vs. Indirect Conversion Detector

To highlight the advantage of employing a high-resolution direct conversion detector and its effect on image quality, we simulated and compared a direct conversion detector with an indirect conversion detector. The indirect conversion detector is modelled by modifying its MTF_d. To study only the effect of MTF_d on the imaging performance, simulation is performed considering MTF_p and MTF_s with smaller point spread function (PSF) values than the MTF_d. Simulation is done for different values of full width at half maximum ($FWHM$) of a detector PSF to illustrate the effect of MTF_d on the image quality. Figure 2.6 and Figure 2.7 demonstrate the impact of MTF_d, which is represented here as different values of the $FWHM$ of the detector PSF. As the detector PSF increases, the imaging resolution decreases, leading to losing the object information in the registered image. For the same detector pixel size, indirect conversion detectors suffer from a larger detector PSF, which leads to resolution degradation. However, direct conversion detectors benefit from smaller PSF, making them superior for high-resolution imaging tasks [70].

From a qualitative imaging perspective [75], direct conversion detectors can reveal more details, which is beneficial for XPCi applications where the edge enhancement of a pure phase object plays a critical role (Figure 2.6a), compared to indirect conversion detectors where details are lost (Figure 2.6d). Moreover, for quantitative studies, direct conversion detectors make it easier to extract more information from an image when phase-contrast properties are present (compare Figure 2.7a with Figure 2.7d).

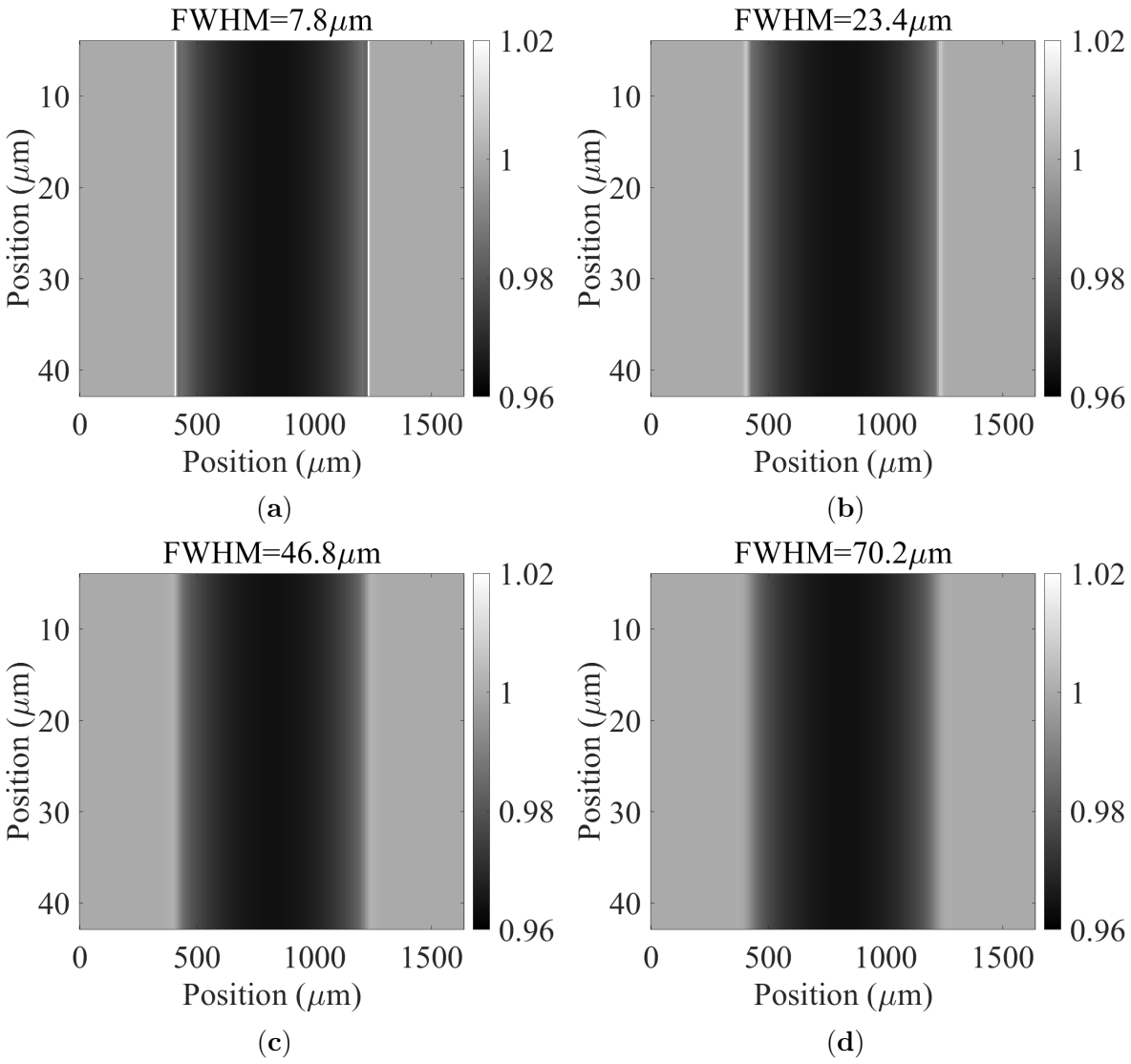


Figure 2.6: The effect of detector modulation transfer function (MTF_d) on the image quality. (**a**) Represents a direct conversion detector with a pixel size equal to 7.8 μm. (**b**) Represents a direct conversion detector with a pixel size equal to 23.4 μm. (**c**) Represents a direct conversion detector with a pixel size equal to 46.8 μm. (**d**) Represents a direct conversion detector with a pixel size equal to 70.2 μm. Simulation is done for a PEEK wire with 585 μm in diameter using a polychromatic microfocus X-ray source working at 60 kV_p with a spot size equal to 2 μm to only study and highlight the effect of MTF_d on the system performance.

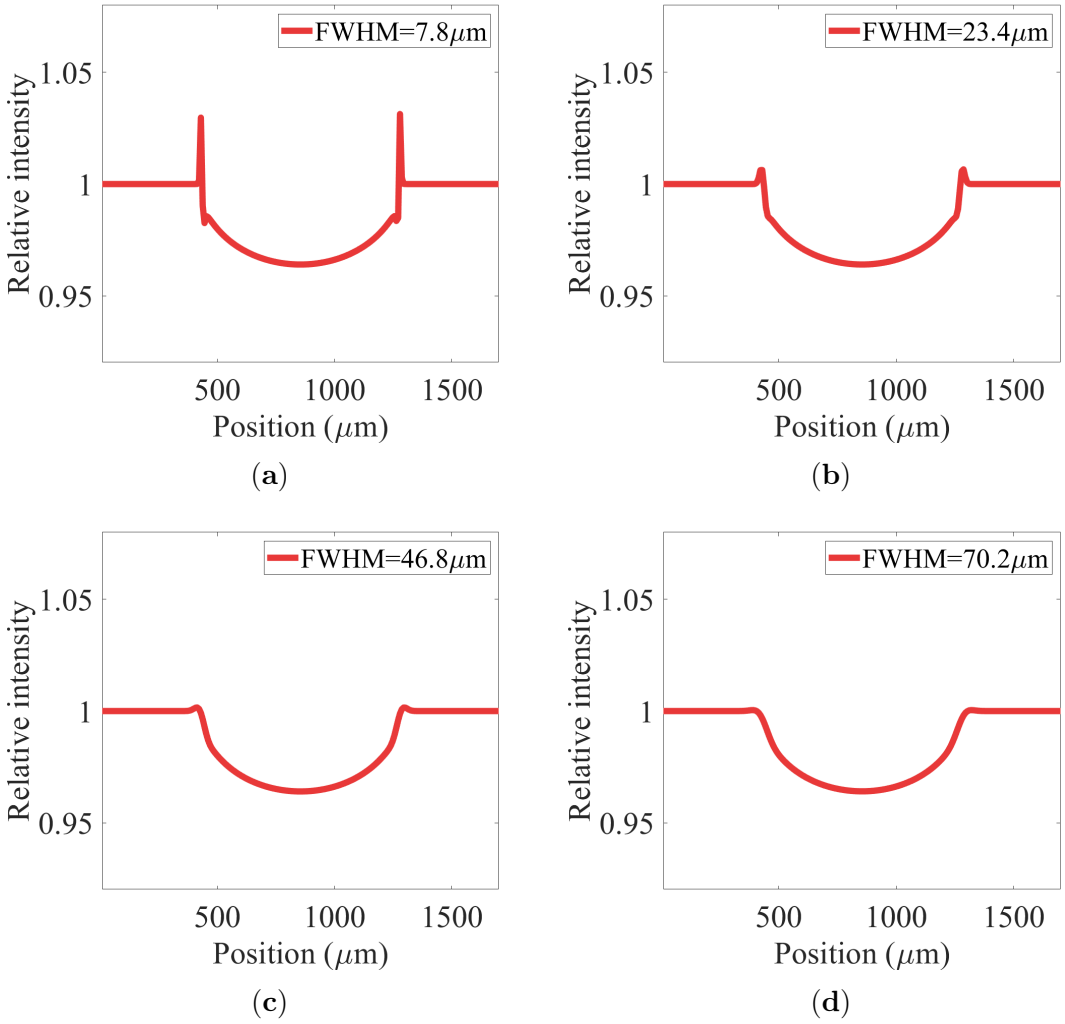


Figure 2.7: The effect of detector modulation transfer function (MTF_d) on the relative intensity of the same images shown in Figure 2.6. (**a**) Represents a direct conversion detector with a pixel size equal to 7.8 μm. (**b**) Represents a direct conversion detector with a pixel size equal to 23.4 μm. (**c**) Represents a direct conversion detector with a pixel size equal to 46.8 μm. (**d**) Represents a direct conversion detector with a pixel size equal to 70.2 μm. Simulation is done for a PEEK wire with 585 μm in diameter using a polychromatic microfocus X-ray source working at 60 kV_p with a spot size equal to 2 μm to only study and highlight the effect of MTF_d on the system performance.

Simulation results confirm that increasing the $FWHM$ of the detector PSF lowers the contrast, edge-enhancement, and visibility of a PB-XPCi system (the same results can be expected for an EI-XPCi system), as illustrated in Figure 2.8. The highest value in the three graphs in Figure 2.8 (at $FWHM = 7.8$ μm) corresponds to a direct conversion detector with a pixel size equal to 7.8 μm, and higher $FWHM$ values in Figure 2.8 represent an indirect conversion detector (with the same pixel size).

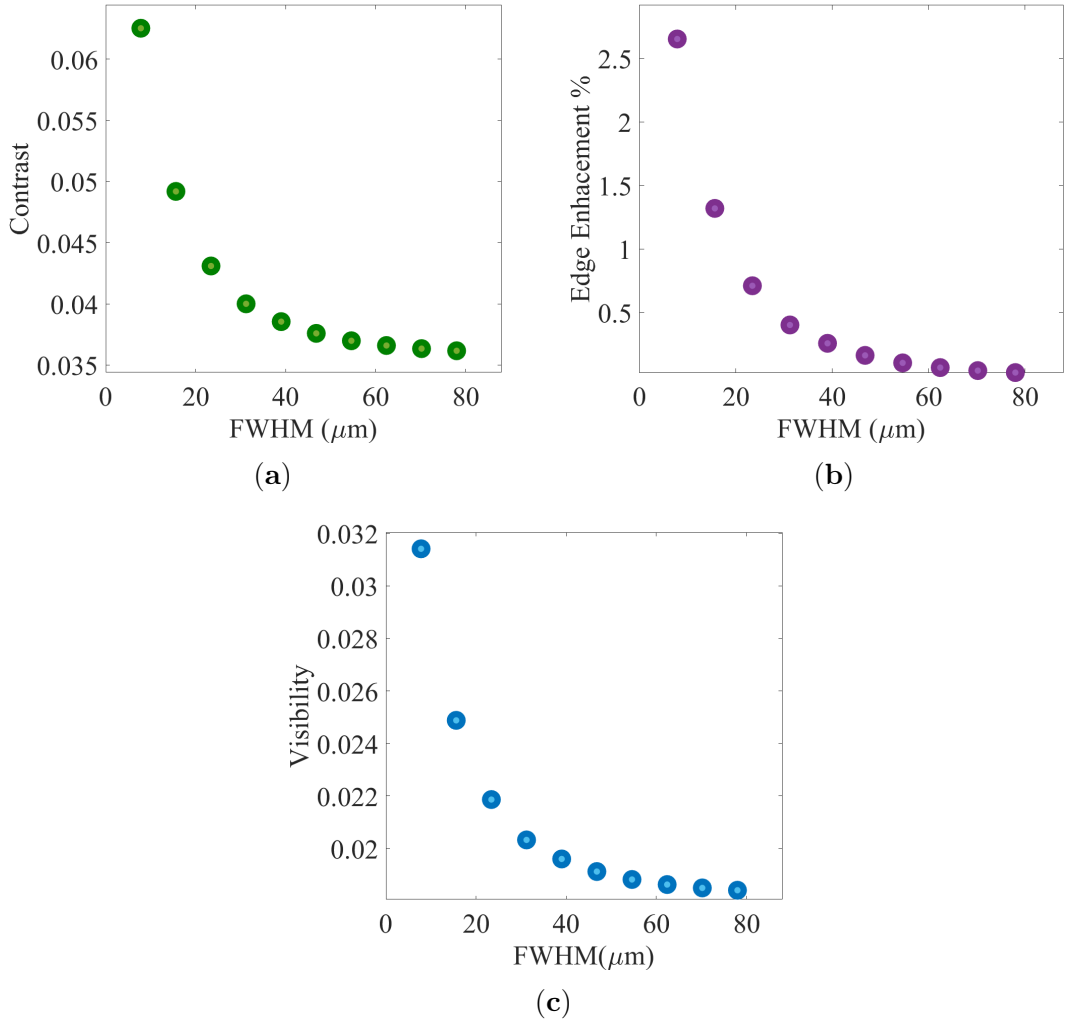


Figure 2.8: (**a**–**c**) Simulation results of contrast, edge-enhancement, and visibility for a PB-XPCi system carried out for a PEEK wire with 585 μm in diameter as a function of different detector modulation transfer function values (MTF_d).

2.6 Investigation of X-ray Phase-Contrast Imaging System Performance

2.6.1 PB-XPCi

With z_{so}, z_{od}, and z_{sd} being the source-to-object, object-to-detector, and source-to-detector distances, investigation of contrast, edge-enhancement, and visibility characteristics are carried out for PB-XPCi as a function of z_{od}, considering the fact that z_{sd} is kept constant—105 cm. In other words, PB-XPCi is evaluated at different magnification scenarios (between 1.05 to 21) when z_{od} is changing between 5 cm to 100 cm, and z_{sd} is always kept constant—equal to 105 cm. Figure 2.9 and Figure 2.10 illustrate the contrast, edge-enhancement, and visibility for a PB-XPCi system. In order to highlight the role of a high-resolution detector in the imaging performance, three different pixel sizes of 7.8 μm, 23.4 μm, and 39 μm are simulated all through the same imaging system condition. Reducing the pixel size results in an enhancement in the detected signal, which leads to higher contrast, edge enhancement, and visibility. Since PB-XPCi systems require high spatial coherence X-ray sources to reveal the phase-contrast effect, phase shift drops for lower spatial coherence components. This is noticeable in Figure 2.9 and Figure 2.10, where increasing in z_{od}—in other words higher magnifications—results in lower contrast, less edge-enhancement, and less visibility.

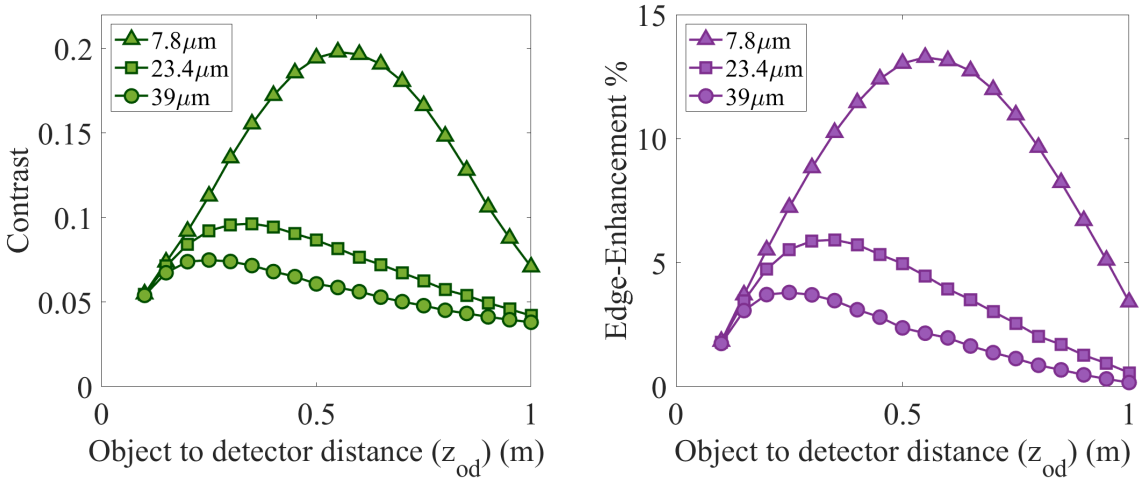
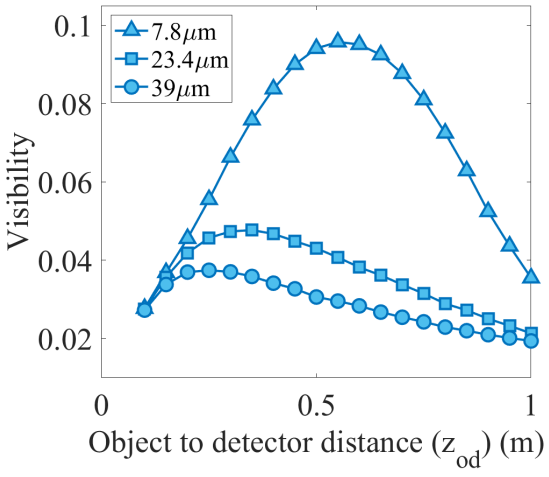


Figure 2.9: Simulation results of the behavior of (**a**) contrast and (**b**) edge-enhancement of a PB-XPCi system versus the object-to-detector distance, carried out for a PEEK wire with 585 μm in diameter.



(**a**)

Figure 2.10: Simulation results of the behavior of visibility of a PB-XPCi system versus the object-to-detector distance, carried out for a PEEK wire with 585 μm in diameter.

Unsurprisingly, contrast, edge-enhancement, and visibility experience lower values when the object is close to the detector—at lower z_{od}, since the phase effect has been suppressed due to a lower propagation distance between the object and detector.

2.6.2 EI-XPCi

An EI-XPCi system performance relies on parameters such as its masks dimensions, detector pixel size, as well as X-ray source energy; thus, z_{so} and z_{od} should be selected and optimized based on the system configuration, and they should be kept fixed, since altering their values affect the system behavior. As a result of that, contrast, edge-enhancement, and visibility are investigated as a function of mask misalignment—which results in different illumination fractions—for the EI-XPCi system. Investigation of the EI-XPCi system is done based on a 7.8 μm pixel size detector; a pre-sample mask with 1.56 μm aperture and 6.24 μm period; a detector mask with 1.17 μm aperture and 7.8 μm period; z_{so} of 18 cm; and z_{od} equal to 4.5 cm. The aperture and period of pre-sample and detector masks are designed based on the X-ray source specifications, distances, and pixel size. Although the detector mask aperture can be greater than the aperture of the pre-sample mask, we designed it to be smaller to minimize the effect of source blurring and to cover different scenarios in changing the mask misalignment. An EI-XPCi system behavior highly depends on where

the beamlets, which exit the pre-sample mask, land on the detector mask. Considering a beamlet to exemplify the situation, three different scenarios could occur: (1) the whole beamlet impinges upon the absorption part of the detector mask (Figure 2.1), therefore nothing is detected; (2) a portion of the beamlet is absorbed by detector mask and the rest is registered by the pixel—this is the definition of edge-illumination; (3) the beamlet is fully landed within the detector mask aperture. Since only the second scenario leads to edge-illumination behavior, note that for mask misalignment, there is a point (or a number of points) at which the system operates to its highest potential for image acquisition. Figure 2.11 and Figure 2.12 illustrate the contrast, edge-enhancement, and visibility of the EI-XPCi system when masks are misaligned over the span of one pre-sample mask period to demonstrate the behavior of the system. The two vertical green bars in Figure 2.11 and Figure 2.12 highlight the regions where the EI-XPCi system reveals the highest contrast (also edge-enhancement and visibility). The middle vertical red bar in Figure 2.11 and Figure 2.12 represent the first scenario where the beamlets of X-ray are fully absorbed by the detector mask, and no signal is detected (without any object present). On the contrary, the far left and far right plateaus are where approximately all of the X-rays are registered by the detector (without any object present).

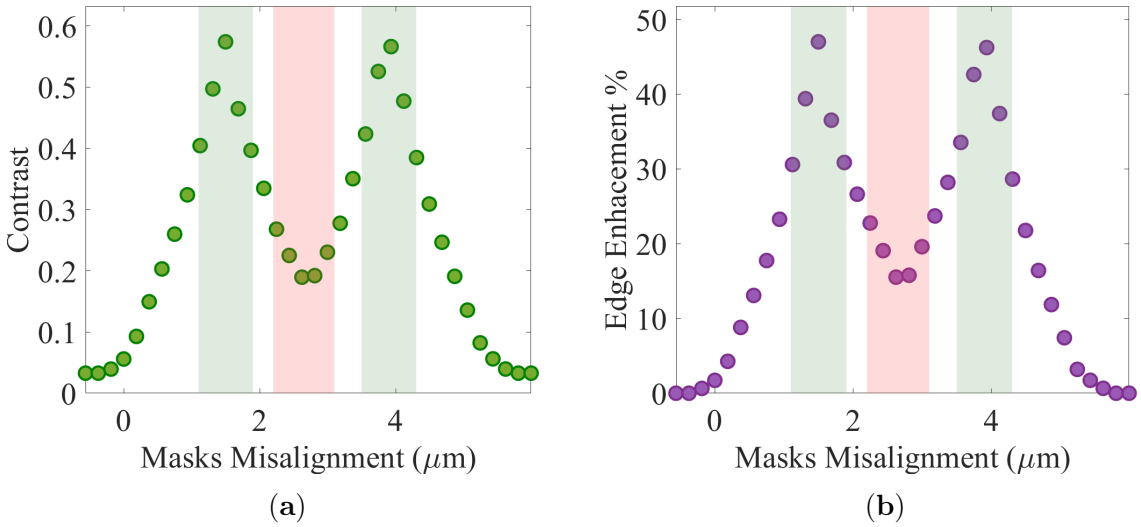
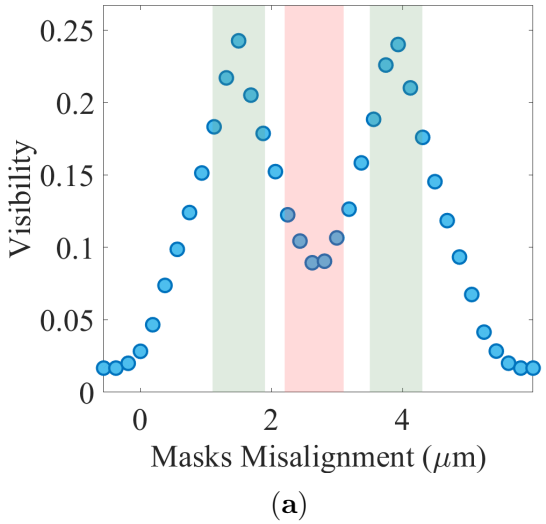


Figure 2.11: Simulation results of the behavior of (**a**) contrast and (**b**) edge-enhancement of an EI-XPCi system versus mask misalignment carried out for a PEEK wire with 585 μm in diameter.



(**a**)

Figure 2.12: Simulation results of the behavior of visibility of an EI-XPCi system versus mask misalignment carried out for a PEEK wire with 585 μm in diameter.

Object dose efficiency, in this investigation, is defined through the amount of X-ray dose the object receives, where a higher object dose efficiency is representative of the lower delivered X-ray dose at the object. The optimum condition would be illuminating the object at the lowest possible dose (i.e., low photon fluence and short exposures) and still achieving the highest contrast in the image. In the PB-XPCi system, nothing blocks the incident X-ray when it propagates toward the object, thus the object is fully illuminated. This is the highest amount of radiation dose an object can receive in any X-ray imaging system. On the other hand, in the EI-XPCi approach, there is an absorption mask right before the object (pre-sample mask), which translates the incident X-ray into smaller beamlets. This translation decreases the delivered X-ray dose at the object. Considering a pre-sample mask with 1.56 μm aperture and 6.24 μm period, only 25% of the incident X-ray will be employed for image acquisition, which is a higher dose efficiency—less delivered radiation dose by the object—compared to the PB-XPCi system. However, it should be mentioned that reducing the dose exposure results in a lower signal-to-noise (SNR) ratio, which in some cases can be later compensated by longer imaging time (or more powerful X-ray sources) to have more X-ray photons. A reduction in the delivered dose at the object can be achieved through the EI-XPCi system [9] because of its higher inherent phase contrast, and the SNR could be compensated by increasing the exposure time. It is worth

mentioning that, from an image perspective, contrast is more important than SNR since that is how features can be distinguished in the image. In the EI-XPCi system, for the same dose efficiency or as defined in this work, dose absorbed by the object (achieved by increasing exposure time to compensate for signal loss in the pre-sample mask), one would expect higher contrast when compared to PB-XPCi using the system described in this manuscript.

The best system, comprehensively, is the one in which contrast, edge-enhance-ment, visibility, and dose efficiency are high. Per the simulation carried out, the EI-XPCi system outperforms the PB-XPCi one, in contrast, edge-enhancement, visibility, and dose efficiency characteristics by a factor of $\times 3$, $\times 3$, $\times 2.5$, and $\times 4$, respectively.

2.7 Effect of Absorption Mask Thickness Variation in a High-Resolution EI-XPCi System

Figure 2.13 to 2.16 illustrate simulation results of the impact of detector mask thickness variation on the behavior of a high-resolution direct conversion detector (with 7.8 μm pixel size) for an EI-XPCi system. It shows that transmissions up to 30% of the incident X-ray through absorption masks will not considerably change the behavior of the EI-XPCi system (Figure 2.13a–2.14d). However, transmissions of more than 40% of the incident X-ray through absorption masks result in the EI-XPCi system experiencing a slight change in its behavior—shifting from EI to PB behavior. Transmissions of more than 70% of the incident X-ray through absorption masks highlight the behavior of a PB-XPCi system rather than an EI-XPCi one (Figure 2.15a–2.16d). The gradual shift from EI to PB behavior, as detector mask thickness decreases, is associated with the increased background signal. The detector mask blocks a portion of incoming beamlets to realize an EI-XPCi system, where any imperfections with the detector mask would result in the EI-XPCi system performance loss. The same shift in behavior, from EI to PB, exists for imperfections in the pre-sample mask, where, in this scenario, impure beamlets generated from an imperfect pre-sample mask result in losing the EI behavior, which is detecting individual beamlet changes.

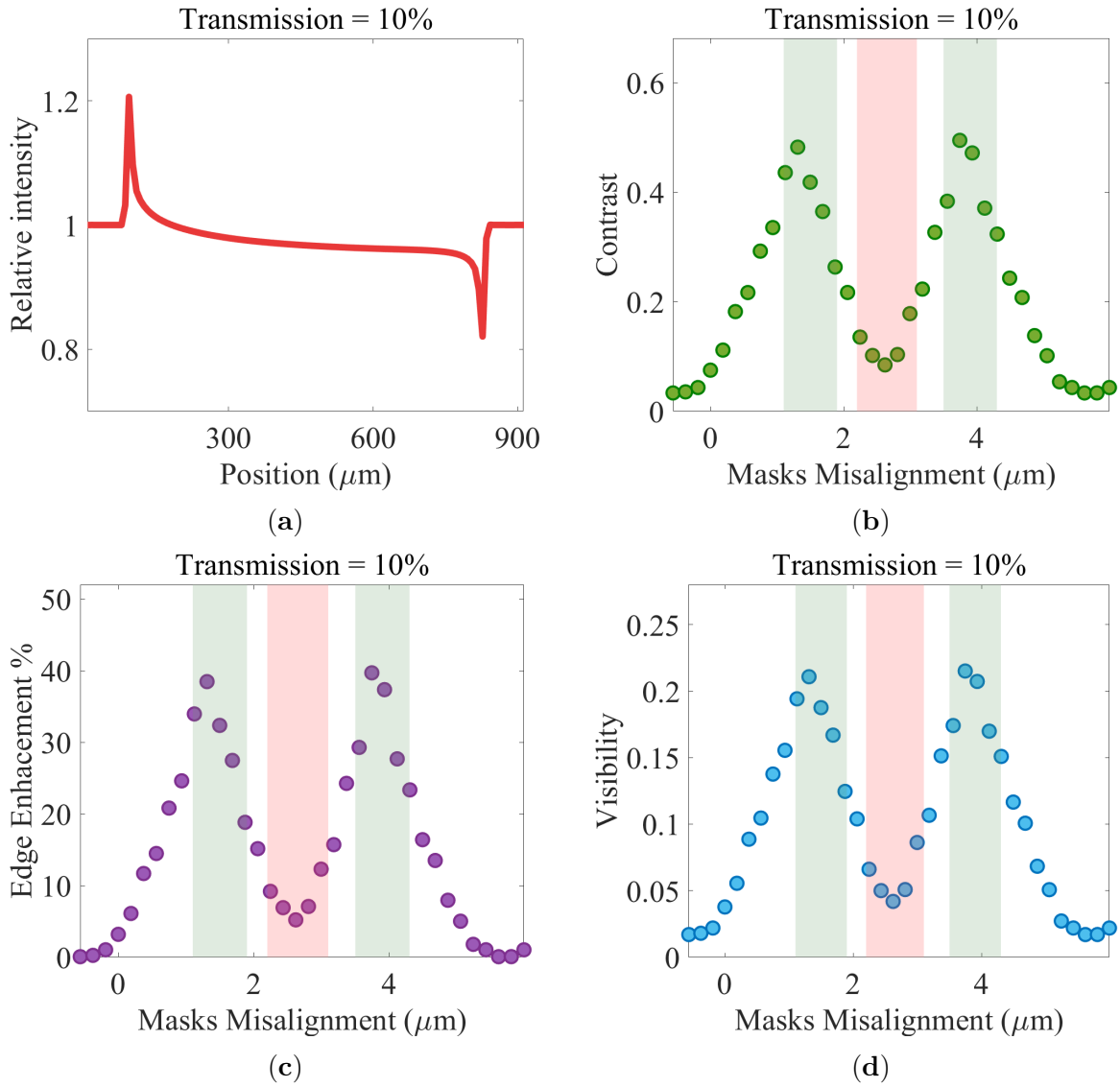


Figure 2.13: The effect of detector mask thickness variation on the performance of a high-resolution EI-XPCi system with 10% transmission of X-ray through the absorption mask. The vertical green bars highlight the working regions with the highest performance, and the vertical red bar represents the region where the detector mask fully absorbs X-rays in the dark image.

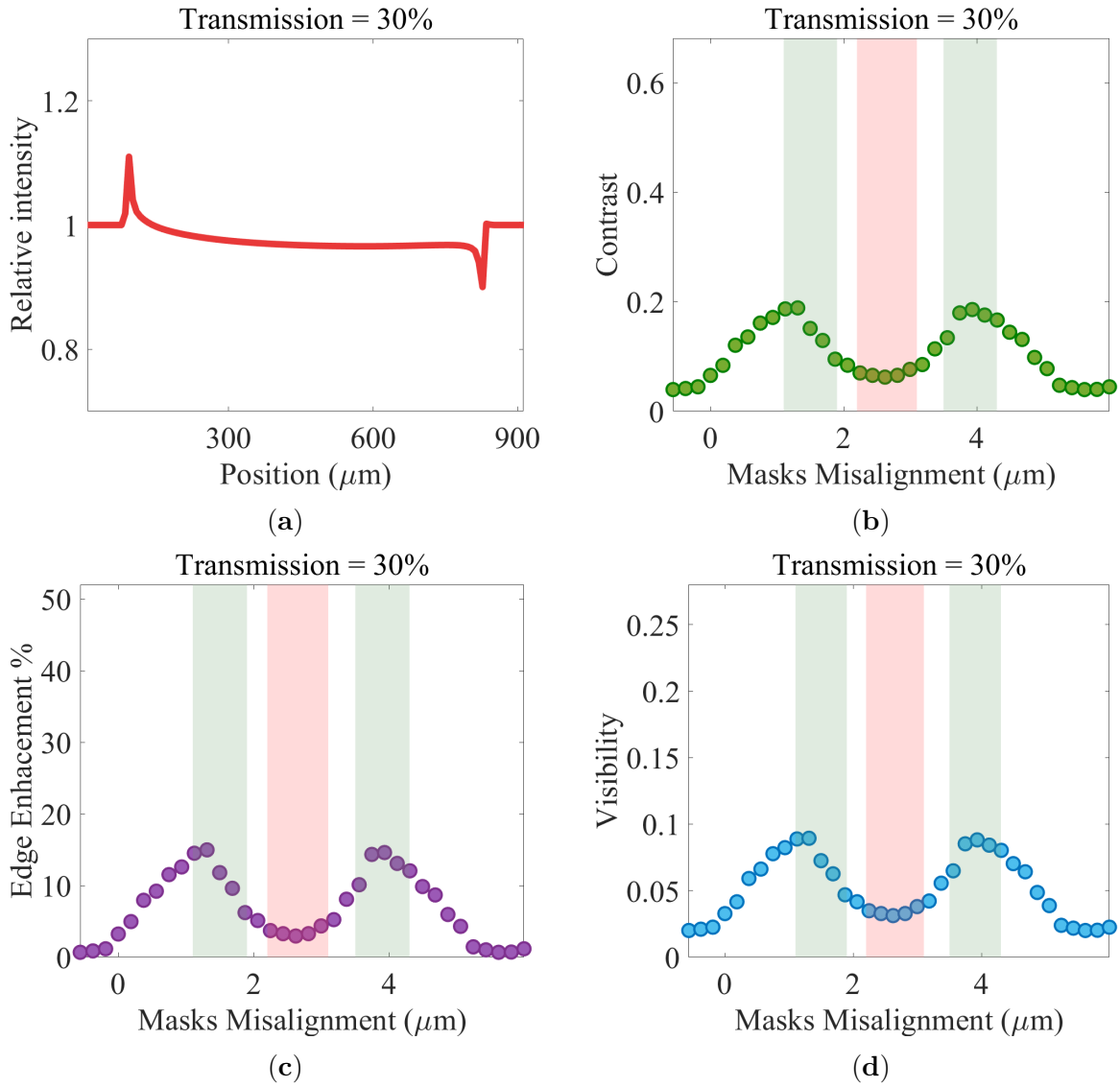


Figure 2.14: The effect of detector mask thickness variation on the performance of a high-resolution EI-XPCi system with 30% transmission of X-ray through the absorption mask. The vertical green bars highlight the working regions with the highest performance, and the vertical red bar represents the region where the detector mask fully absorbs X-rays in the dark image.

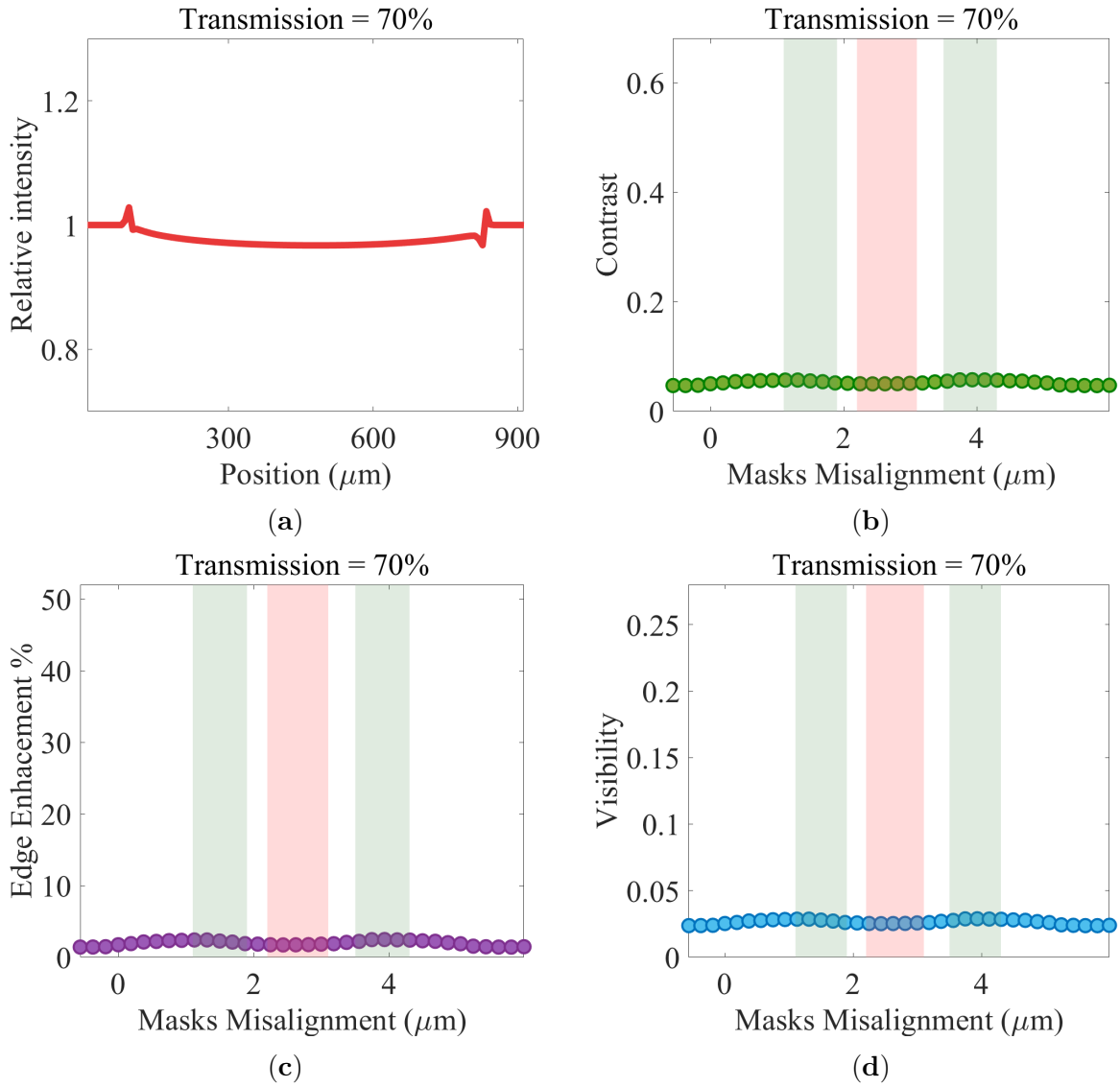


Figure 2.15: The effect of detector mask thickness variation on the performance of a high-resolution EI-XPCi system with 70% transmission of X-ray through the absorption mask. The vertical green bars highlight the working regions with the highest performance, and the vertical red bar represents the region where the detector mask fully absorbs X-rays in the dark image.

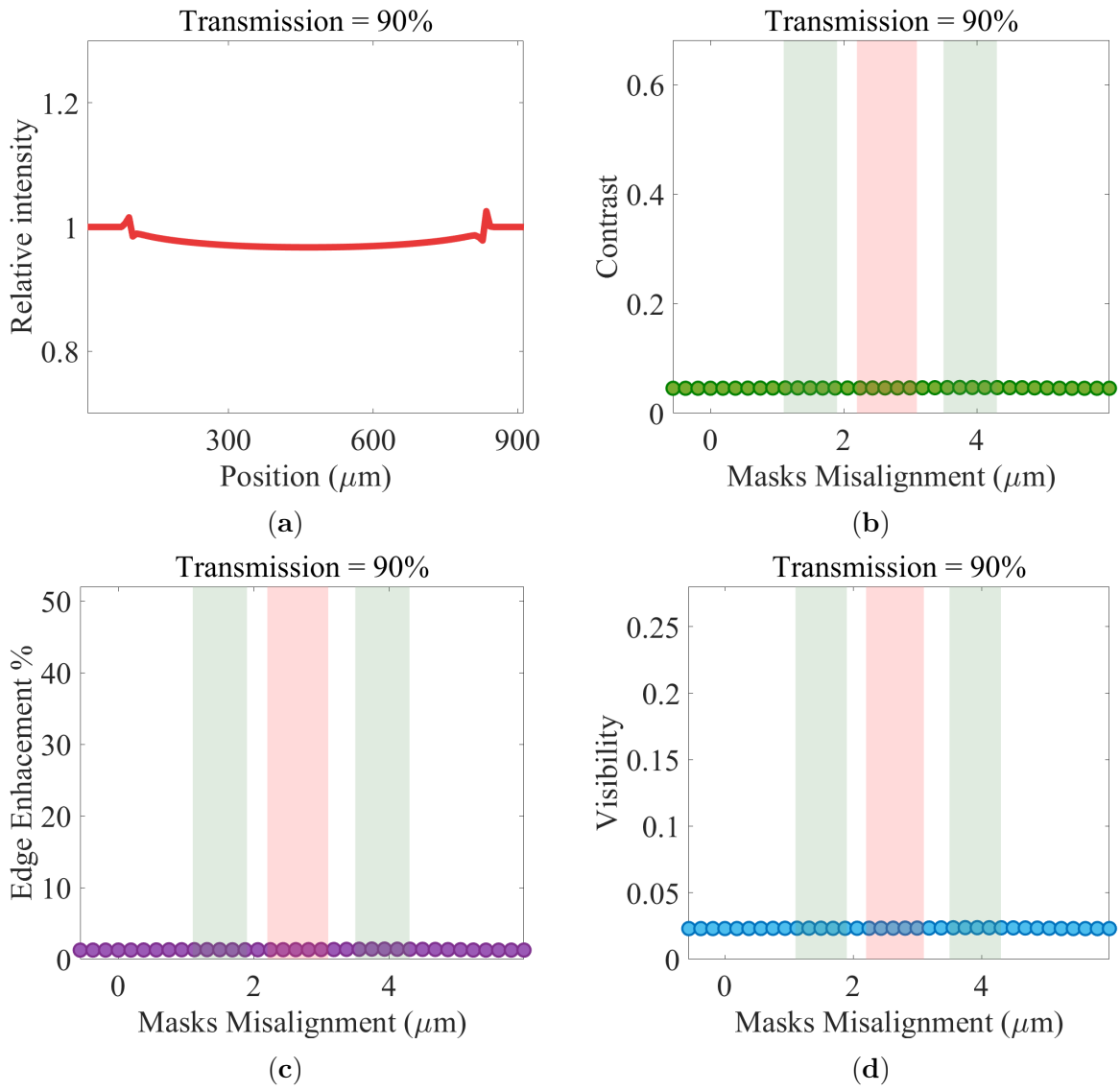


Figure 2.16: The effect of detector mask thickness variation on the performance of a high-resolution EI-XPCi system with 90% transmission of X-ray through the absorption mask. The vertical green bars highlight the working regions with the highest performance, and the vertical red bar represents the region where the detector mask fully absorbs X-rays in the dark image.

2.8 Effect of Mechanical Vibration in a High-Resolution EI-XPCi System

Figure 2.17 displays how environmental vibration is modelled through mechanical displacement. For the sake of simplicity, we only considered the pre-sample mask displacement along the x-direction. Displacements along the y-direction do not change the signal intensity as they are parallel with line gratings. In addition, any displacement along the z-direction does not change the signal intensity significantly as it hardly changes the shape of beamlets (considering the 2 micrometres range of displacement). The red beamlets (in Figure 2.17) illustrate the situation in which the pre-sample mask is shifted due to environmental vibration, where the beamlets' position impinging upon the detector is changed. To study the effect of mechanical vibration on the performance of an EI-XPCi system, we considered two different systems:

1. A 39 μm pixel size system with a pre-sample mask with 4.68 μm and 31.2 μm aperture and period; a detector mask with 9.75 μm and 39 μm aperture and period; z_{so} of 160 cm; and z_{od} equal to 40 cm.

2. A 7.8 μm pixel size system with a pre-sample mask with 1.56 μm and 6.24 μm aperture and period; a detector mask with 1.17 μm and 7.8 μm aperture and period; z_{so} of 18 cm; and z_{od} equal of 4.5 cm.

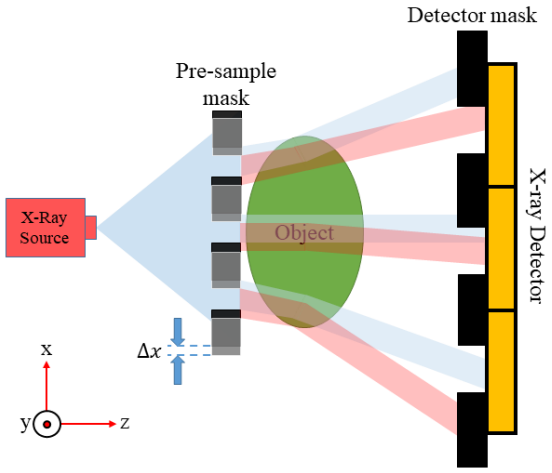


Figure 2.17: Environmental vibration modelled through mechanical displacement which causes misalignment between pre-sample and detector mask in an EI-XPCi system for high-resolution imaging application.

Simulation results confirm that high-resolution EI-XPCi systems are sensitive to environmental vibration, where their behavior changes dramatically when mask misalignment swings even in the range of 2 micrometres. However, EI-XPCi systems with bigger pixel sizes are not influenced noticeably by this misalignment. Figure 2.18 illustrates how environmental vibration within the range of two micrometres does not have a noticeable effect on the behavior of the system with 39 μm pixel size. On the other hand, as Figure 2.19 shows, the same environmental vibration in higher resolution detectors (in this case, a system with 7.8 μm pixel size) significantly swings the system behavior between PB and EI modes.

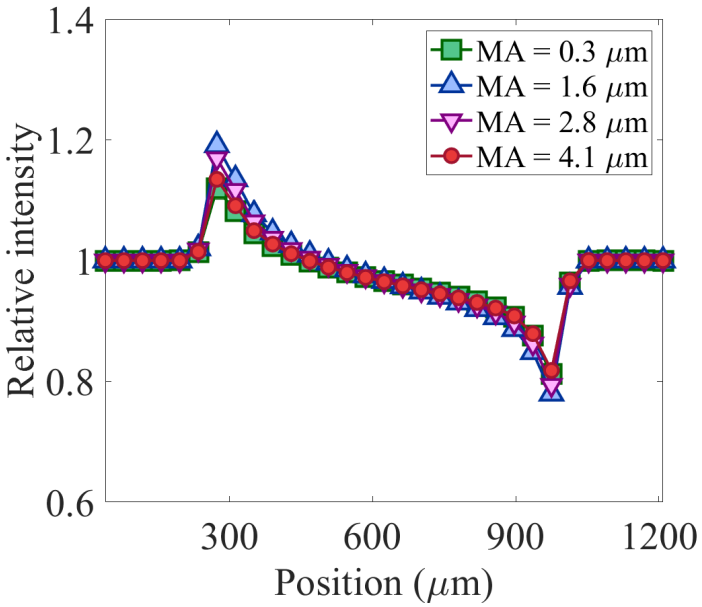


Figure 2.18: Illustration of simulation results of the effect of environmental vibration in the range of 2 μm on the performance of an EI-XPCi system with pixel size equal to 39 μm $\times$ 39 μm.

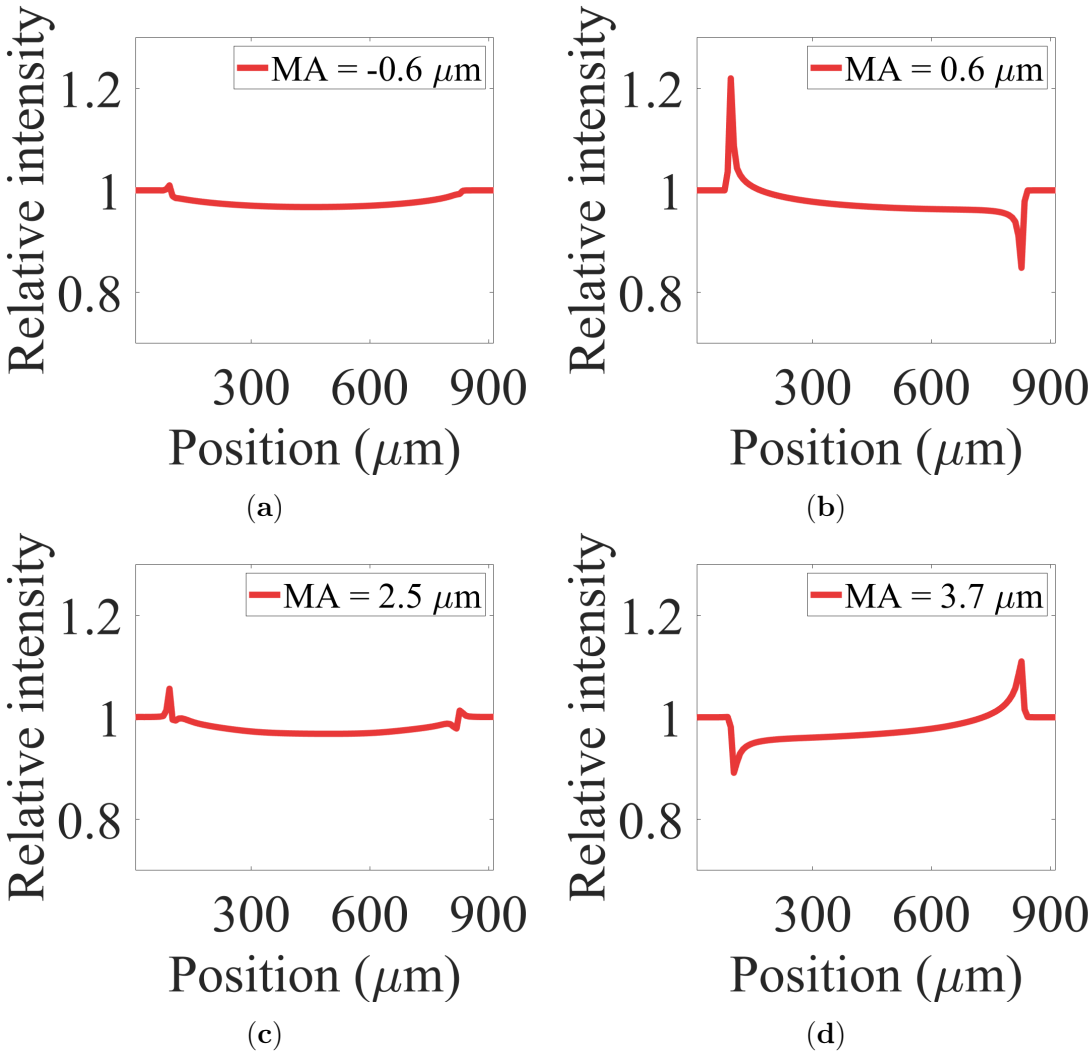


Figure 2.19: (**a**–**d**) Illustration of simulation results of the effect of environmental vibration on the performance of an EI-XPCi system with pixel size equal to 7.8 μm $\times$ 7.8 μm. The behavior of the system dramatically changes even with less than one micrometre shift in the mask misalignment.

This study highlights that, as we move towards higher resolution systems, mechanical vibration can become a significant issue in the system performance, which was not a contributing factor in the performance of lower resolution systems. In general, if proper design practices are followed, environmental vibration can be minimized. However, if one is trying to design a benchtop or mobile XPCi system or, alternately, placing such a system

on an active industrial factory floor, then vibration could become a concern. As a result, higher precision mechanical stages (or optical tables) are required to dampen the environmental vibration. One solution is to use a feedback mechanism to minimize the effect of environmental vibration in post-processing steps. For example, by knowing the intensity transfer function (illumination curve) of the EI-XPCi system and the background signal, any vibration in the background can be translated into a change of intensity, which can be later corrected to lock the masks in position.

2.9 Current XPCi Technologies

2.9.1 Propagation-Based X-ray Phase-Contrast Imaging System

Here, we present a prototype amorphous selenium (a-Se) integration mode X-ray detector, which employs a hybrid a-Se/CMOS detector technology. This high-resolution detector was initially developed in our research group at the University of Waterloo, and is now commercialized by a University of Waterloo spin-off company, KA Imaging Inc. [52,68,76]. The a-Se photoconductor possesses a high intrinsic spatial resolution and is utilized in this X-ray detector in the direct conversion mode. The 7.8 μm pixel pitch prototype X-ray detector used in this work has micron-scale resolution and high detection efficiency for energies >20 keV. We used this detector in a PB-XPCi configuration to demonstrate the potential of this high-resolution X-ray detector. The edge-enhancement effect in PB-XPCi at different geometric magnifications for a Polytetrafluoroethylene (PTFE) rod (with a thickness of 0.7 mm) employing the prototype X-ray detector—1000 $\times$ 1000 pixels with 7.8 μm pixel pitch; a tungsten target Thermo Scientific™ PXS5-927 Microfocus X-ray Source (from Thermo Fisher Scentific Inc., Waltham, MA, USA) working at 60 kV_p, 134 μA, and focal spot size of 9 μm; as well as the source to object distance of z_{so} = 18 cm is demonstrated in Figure 2.20 and Figure 2.21. As we increase the distance between the object and the detector (by keeping the source to object distance constant and equal to z_{so} = 18 cm), the edges of the object—where the refractive index changes abruptly—become more detectable. Figure 2.20a–2.20d illustrate phase-contrast images of the PTFE rod at different geometric magnifications, and Figure 2.21a–2.21d demonstrate cross-sectional view of the relative intensity profile at different object to detector distances, correspondingly. A good agreement between the simulated model and experimental results can be found here.

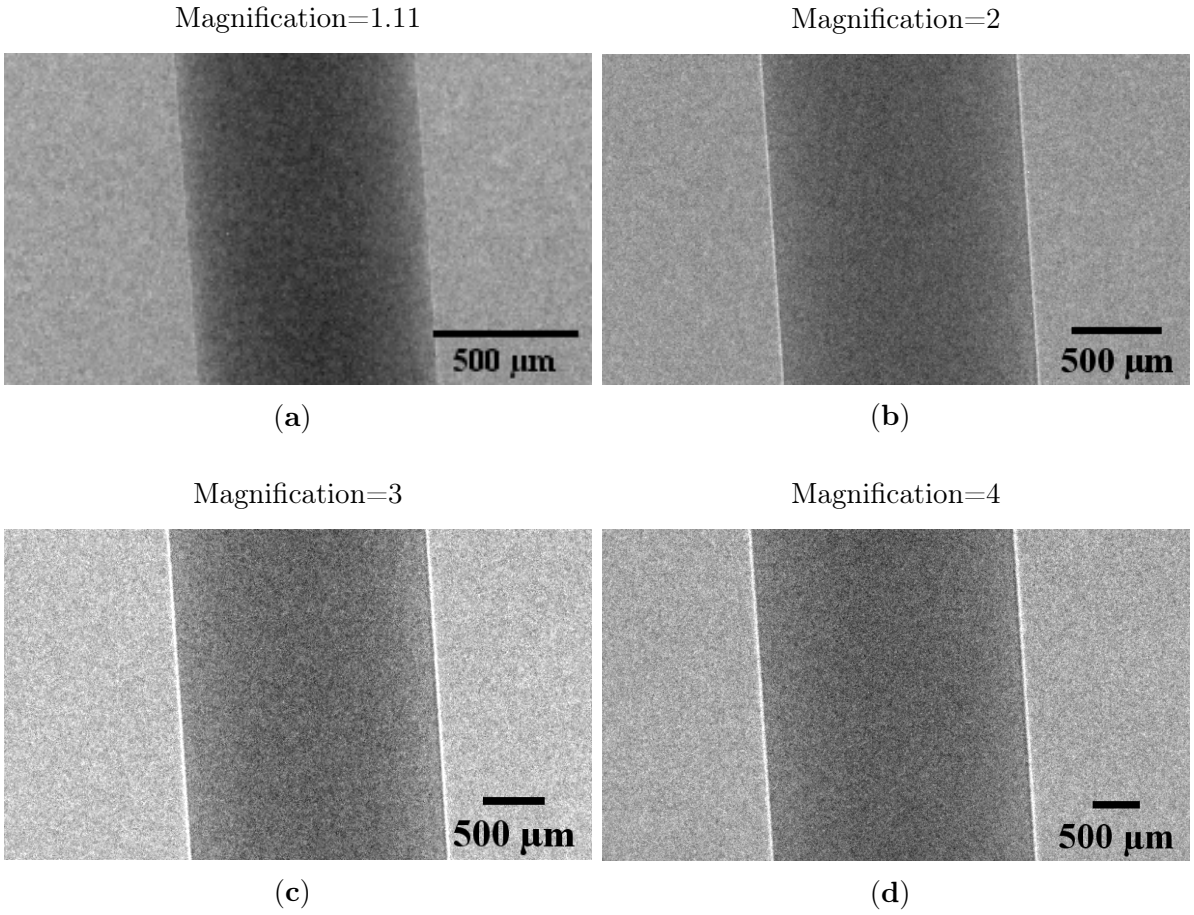


Figure 2.20: Illustration of X-ray projections (phase-contrast images) highlighting the edge-enhancement effect of PB-XPCi for a 0.7 mm PTFE rod at different magnifications of (**a**) 1.11, (**b**) 2, (**c**) 3, and (**d**) 4.

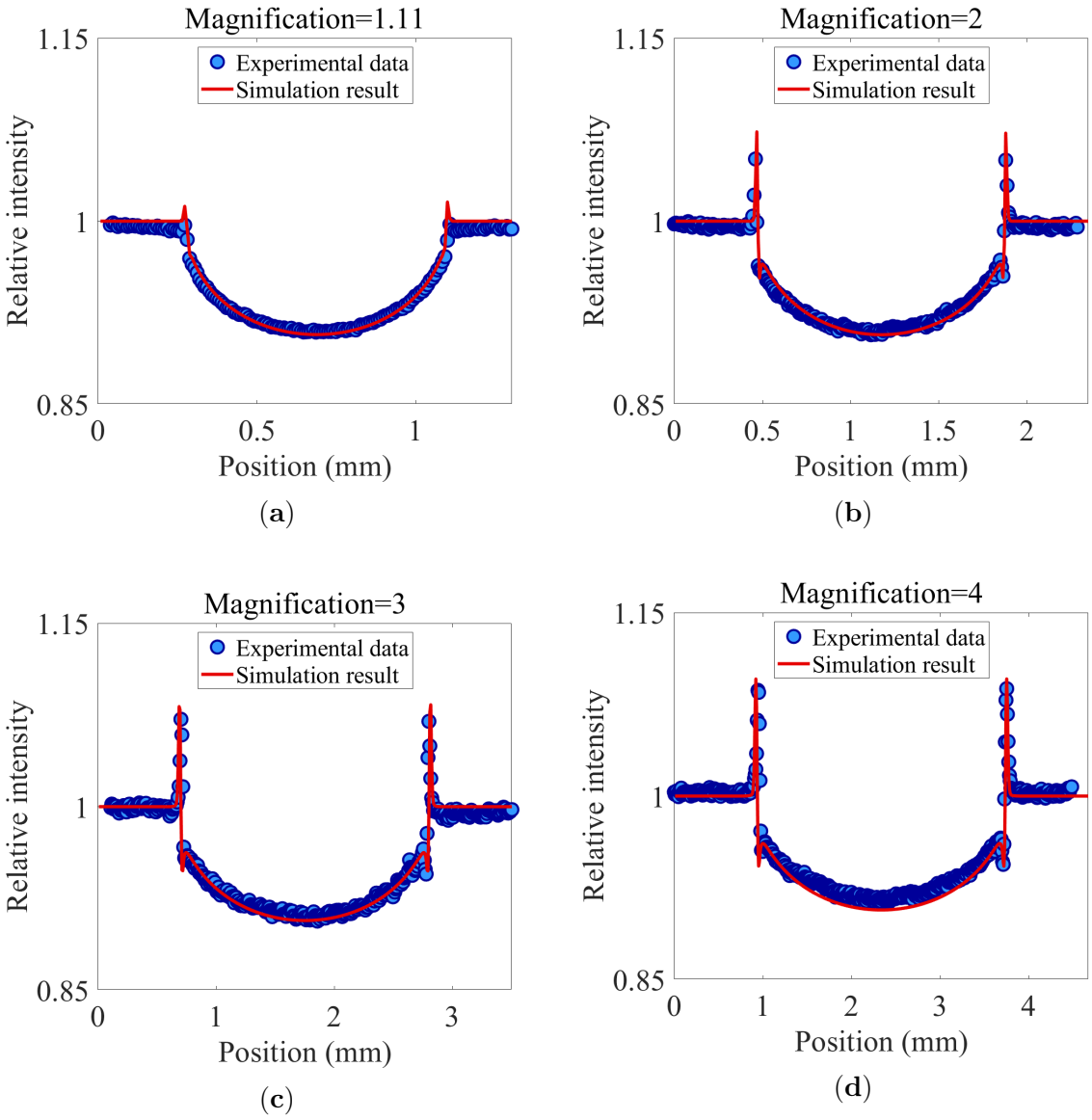


Figure 2.21: Cross-sectional view of the relative intensity profile across the object in Figure 2.20 highlighting the edge-enhancement effect of PB-XPCi for a 0.7 mm PTFE rod at different magnifications of (**a**) 1.11, (**b**) 2, (**c**) 3, and (**d**) 4.

Figure 2.22 displays the imaging setup and configuration used to perform the PB-XPCi. It should be emphasized that using a high-resolution X-ray detector, like the reported prototype detector, not only helps us reveal smaller feature sizes and more information, but makes the final XPCi setup more compact as well. Compactness of an XPCi setup is an advantage when it comes to benchtop and portable imaging systems, such as in intraoperative specimen imaging applications. It should be noted that utilizing such a high-resolution detector to its full potential for higher magnification imaging tasks requires X-ray sources with a finer focal spot, thus the source blurring does not play the limiting factor in the image formation.

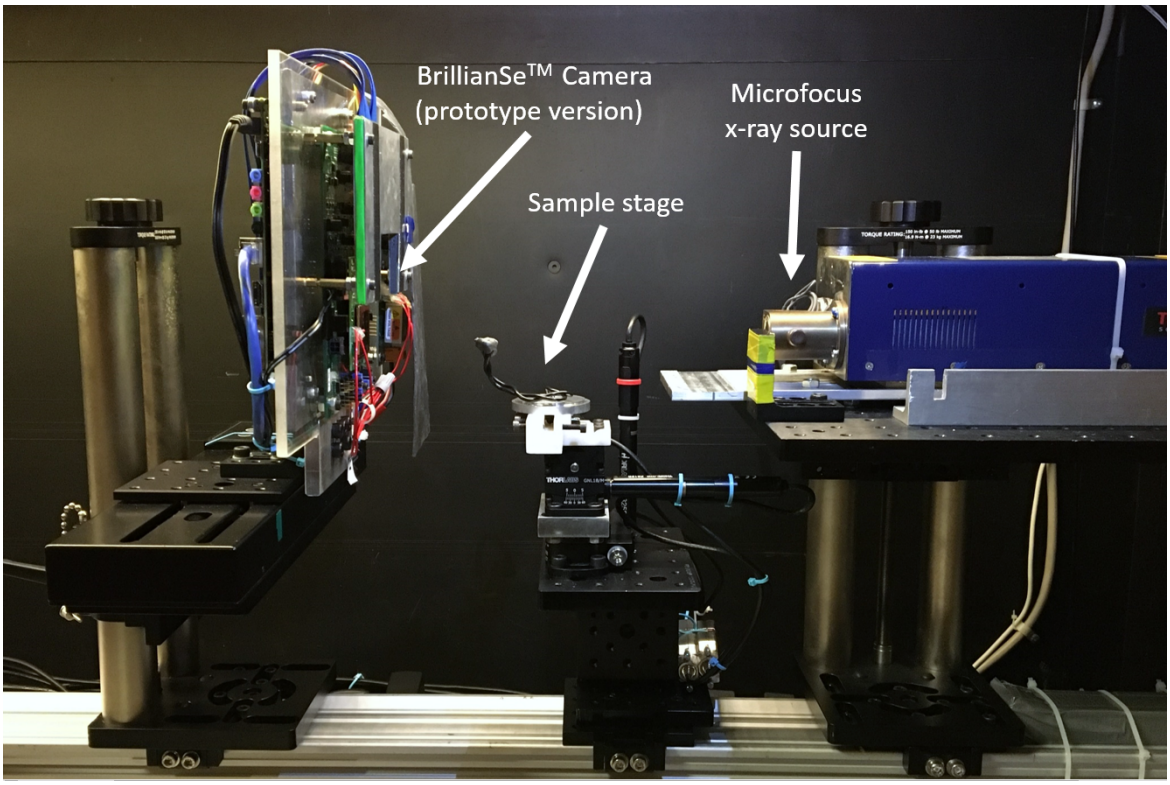


Figure 2.22: The experimental setup used for PB-XPCi imaging with the tungsten target Thermo Scientific™ PXS5-927 Microfocus X-ray Source, sample stage, and a prototype version of the BrillianSe™ X-ray detector.

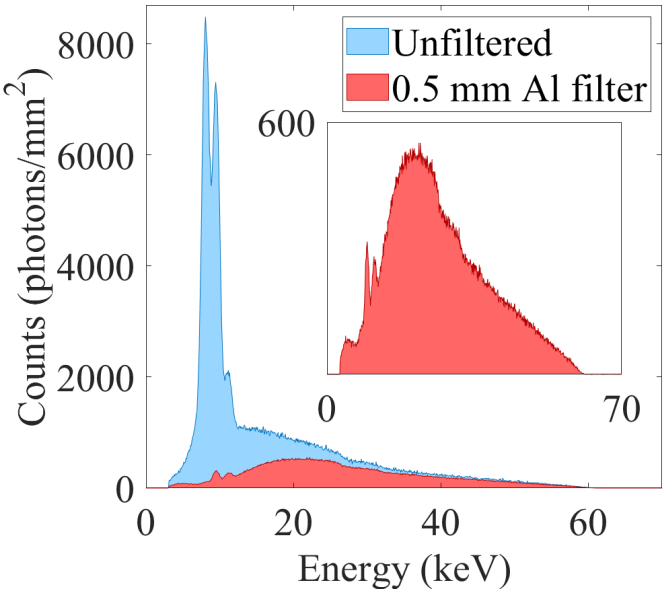
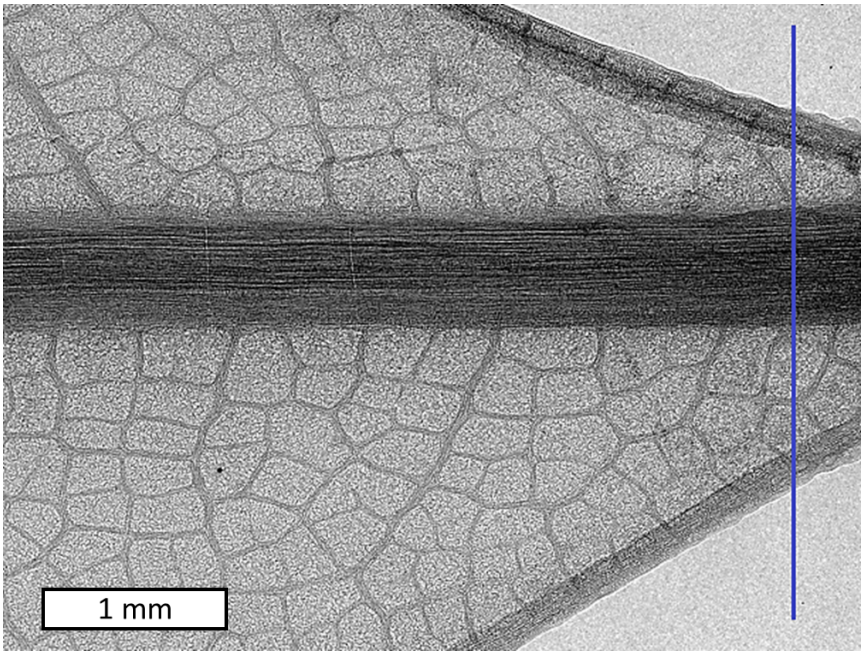
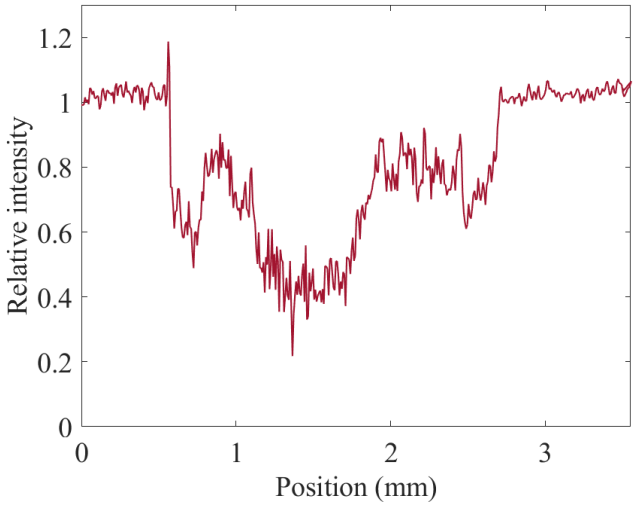


Figure 2.23: Demonstration of the tungsten target Thermo Scientific™ PXS5-927 Microfocus X-ray source spectrum used for imaging—both the unfiltered and 0.5 mm Al filtered spectrum.

The tungsten target X-ray spectrum used for imaging purposes in this work is illustrated in Figure 2.23. The spectrum without any filtration has multiple characteristic lines at around 10 keV, which was filtered using a 0.5 mm aluminum (Al) filter (the inset graph in Figure 2.23 shows the zoomed-in version of the filtered spectrum). Figure 2.24a displays the phase-contrast image of a dried bay leaf imaged at 60 kV_p, $z_{so} = 18$ cm, and $z_{od} = 8$ cm. It is worth mentioning that darker regions in the image displayed in Figure 2.24a correspond to lower X-ray transmission through the object. Figure 2.24a reveals the bay leaf's midrib, margins, veins, and lamina where feature sizes as small as 15–20 μm are clearly visible. Profile of relative intensity along the cross-section (blue line), in Figure 2.24a, is illustrated in Figure 2.24b, which indicates phase-contrast peaks at the boundaries of bay leaf's margins, midrib, and also different parts within the lamina.



(**a**)



(**b**)

Figure 2.24: (**a**) Phase-contrast image of a dried bay leaf using a prototype version of the BrillianSe™ X-ray detector and a microfocus source at 60 kV_p, z_{so} = 18 cm, and z_{od} = 8 cm; (**b**) profile of relative intensity along the vertical cross-section (blue line).

2.9.2 Edge-Illumination X-ray Phase-Contrast Imaging System

Today's existing EI-XPCi systems employ mostly X-ray detectors with pixel sizes in the range of 50 to 100 μm. Table 2.2 is a short list of EI-XPCi systems that are currently being used. Because of the detector pixel sizes used in these setups, they typically require 1.8 m distance from the source to the detector. One of the obstacles in the way of developing compact EI-XPCi systems and upgrading them to smaller pixel size detectors is the fabrication of absorption masks that could match a high-resolution X-ray detector pixel size in a compact setup. Shorter distances and more compact setups impose higher requirements on the absorption masks specifications, although they can alleviate the need for higher X-ray

Table 2.2: List of today's EI-XPCi systems with source, setup size (source to detector), masks, and detector information.

Reference	**X-ray source**, **Energy** or **Potential**	$z_{so} + z_{od}$	**M1 Aperture**, **Period**	**M2 Aperture**, **Period**	**Detector**, **Pixel Pitch**
2017 [77]	Rigaku MM007, 35 kV_p	>160 cm	16 μm, 134 μm	20 μm, 167 μm	Anrad SMAM A-Se, 85 μm
2017 [78]	Rigaku MM007, 40 kV_p	200 cm	12 μm, 48 μm	15 μm, 62 μm	Pixirad, 62 μm
2018 [79]	Hamamatsu L8121-03, 40 keV	184 cm	—	—	Medipix3RX, 55 μm
2019 [80]	Rigaku MultiMax-9, 40 kV_p	300 cm	10 μm, 79 μm	17 μm, 98 μm	PixiRad-2, 62 μm
2020 [81]	Rigaku MM007, 35 kV_p	245 cm	10 μm, 79 μm	17 μm, 98 μm	Hamamatsu C9732DK-11, 100 μm [1]
2022 [82]	Rigaku MM007, 40 kV_p	100 cm	-	20 μm, 98 μm	Hamamatsu C9732DK, 50 μm

[1] Effective pixel size.

source intensities. Some of the main challenges in the fabrication of absorption masks, which are periodic micro-structures containing an X-ray absorber, include:

1. high aspect ratio structures (in the range of 40:1, structural width in the range of a few micrometres and height of more than 100 micrometres) [83, 84].
2. Larger area fabrication (for application such as mammography, e.g., for a field of view of 10×10 cm^2 or 15×15 cm^2) [54–58].
3. Acceptable uniformity across the absorption masks (no distortions and changes in the period and height).
4. Two-dimensional high aspect ratio structures (2D gratings) for sensitivity in the x and y direction.

The problem becomes even more challenging when the energy of the X-ray source increases, where, in order to stop the incident X-ray and to translate the X-ray to smaller beamlets at absorption masks, either the absorption part in the masks should be selected from materials with a higher atomic number (harder materials for the range of X-ray energy of interest), or the thickness of the absorption part should increase.

It should be noted, to address these bottlenecks from the technological perspective, we are both limited to a few number of X-ray stopper materials, the most common X-ray absorber being used in fabrication technology is gold (Au), and the fabrication technology for high-resolution high aspect ratio absorption masks is not yet well developed and available. For instance, in the case of employing a high-resolution detector (7.8 μm pixel pitch) in an EI-XPCi setup, an almost 100 μm thick gold absorber is required to stop 90% of a 40 keV X-ray. Considering a compact system with $z_{so} = 18$ cm and $z_{od} = 8$ cm, a pre-sample mask is required with an aperture size of less than 2 μm and period of less than 7 μm. A similar constraint with slightly bigger aperture size and 7.8 μm period applies for the detector mask. Confounding this situation further, decreasing z_{so} or increasing z_{od} would require the pre-sample mask values to decrease further to match the EI-XPCi system requirement. The above discussion underlines the importance of putting focused effort into improving X-ray absorption mask fabrication technology for high-resolution detectors and high-energy X-ray imaging applications.

Among the different techniques developed for X-ray absorption mask fabrication, there are two well-defined and widely used processes: etching processes—such as deep reactive ion etching (DRIE) on a silicon wafer [85]—and making molds on a conductive substrate, both followed by an electroplating step to create the absorber parts. The former relies on

tools such as atomic layer deposition (ALD) of metals and DRIE process, which impede this fabrication method from scaling up and creating larger X-ray masks. The latter approach of making X-ray masks, however, is based on a mechanically stable mold (the most common one widely used is the negative photoresist SU-8) and a lithography process, either X-ray or UV lithography [43, 86]. Although X-ray lithography is an efficient tool for high aspect ratio structure fabrication [39, 87–89], it is an expensive and hard-to-access method. On the other hand, following conventional UV lithography techniques with SU-8 photoresist typically results in structures with aspect ratios around 5, which are not enough for high-resolution micron-scale pixels and hard X-ray energies (e.g., 40 kV_p). In later chapters, we describe the fabrication of a high-resolution high aspect ratio absorption mask and the implementation of a unique EI-XPCI system that leverages the new X-ray grating and the BrillianSe™ X-ray detector. Employing a micron-scale pixel pitch X-ray detector in a single-mask EI-XPCi setup opens up new opportunities and possibilities to perform imaging tasks with less complexity and at lower dose exposures.

2.10 Conclusion

In this chapter, we investigated PB-XPCi and EI-XPCi techniques in terms of their contrast, edge-enhancement, visibility, and dose efficiency characteristics for a direct conversion detector with micron-scale pixel pitch. We used numerical modelling and a simulation tool to evaluate both techniques and demonstrate the effect of absorption mask thickness and environmental vibration on the performance of the EI-XPCi system. The numerical modelling was verified by employing a direct conversion amorphous selenium (a-Se)/CMOS based micron-scale pixel X-ray detector in the PB-XPCi configuration to highlight the potential of such a detector in revealing small feature size structures. The EI-XPCi configuration demonstrated better performance – compared to PB-XPCi – in simulation results in contrast by about 3×, in edge-enhancement by about 3×, in visibility by about 2.5×, and in dose efficiency by about 4×.

Despite the higher performance of EI-XPCi over PB-XPCi, there remain some experimental challenges associated with using such a high-resolution detector. In the high-resolution EP-XPCi system studied in this chapter, two main challenges are the fabrication of high-resolution high aspect ratio X-ray absorption gratings and the effect of mechanical vibrations on the system performance. Since the latter challenge can be addressed by using higher precision mechanical stages to dampen the mechanical vibrations, we focused our efforts on developing a large-area high-resolution hard X-ray grating technology. The development of such a grating creates new opportunities for translation of EI-XPCi into

clinical imaging applications where contrast, resolution, and dose efficiency are important, such as screening and diagnostic mammography.

This chapter fulfilled the first thesis objective, namely comparing the performance of X-ray phase-contrast propagation and grating-based imaging systems that leverage an in-house developed world first 8 μm pixel size direct conversion X-ray detector.

Chapter 3

Silicon-based X-ray Absorption Grating Fabrication

This chapter covers the fabrication process of an X-ray absorption grating based on silicon wafers. It represents the work done to tackle the second objective of the thesis—to develop a scalable, large-area, fabrication process for a high-resolution, high aspect ratio X-ray grating for large area X-ray imaging applications. Following the requirement of a high-resolution high aspect ratio X-ray absorption grating to realize the high-resolution edge-illumination (EI) X-ray phase-contrast imaging (XPCi) system, two main methods of X-ray grating fabrication are investigated in this thesis: silicon-based etching and UV LIGA. This chapter investigates a silicon-based deep reactive ion etching (DRIE) fabrication process for high-resolution high aspect ratio hard X-ray absorption grating. An additional element in making high aspect ratio X-ray absorption gratings in silicon substrates is the deposition of a conformal seed layer for electroplating to create the absorption regions. Atomic layer deposition (ALD) is a widely reported approach [34, 35, 90–93] to create a conformal seed layer in complex structures (for example, high aspect ratio gratings). However, it is not widely accessible today with most applications being reported in research scenarios [94, 95]. In this research, we explored grating fabrication technologies that are scalable and cost-effective. Here, we examined conventional sputtering physical vapor deposition (PVD) tools for seed layer deposition in high aspect ratio structures.

The primary contributions associated with this chapter include (1) the development of novel bridge-assisted micropillars to achieve mechanically reliable higher aspect ratio gratings, and (2) an examination of seed layers deposited via conventional PVD sputtering for filling in the grating absorber material via electroplating.

3.1 Introduction

In the last decade, the fabrication of gratings–particularly X-ray absorption grating–has significantly benefited from silicon technology. The advances in X-ray grating fabrication have happened thanks to the accessibility and advanced fabrication processes of silicon devices derived from complementary metal-oxide-semiconductor (CMOS) technology. Although large-area fabrication of silicon-based X-ray absorption gratings is still experiencing a significant setback in the path of translating grating-based phase-contrast X-ray imaging systems from their niche applications to the market, there are still some advantages to the silicon-based fabrication processes. For small-size X-ray gratings, nanometer-scale feature size structures, and high-resolution high aspect ratio features, silicon-based fabrication processes provide an excellent framework to meet the requirements. Since the grating quality directly affects the X-ray imaging performance—image quality can be compromised if the fabricated grating is imperfect—it is worth putting effort into enhancing the silicon-based grating fabrication technology.

Fabrication of X-ray absorption gratings – whether via etching or molding – divides into two main parts: creating high aspect ratio features (lamellae or micropillars for 1D or 2D, respectively) and forming the absorption regions in the spaces between high aspect ratio features. Among various methods of fabrication, grating fabrications in silicon wafers are usually performed through wet etching processes [39–41], or anisotropic etching techniques such as metal-assisted chemical etching [31–33] or plasma etching [34–38] methods. Wet etching processes, such as potassium hydroxide (KOH) or tetramethylammonium hydroxide (TMAH) based [96,97], are isotropic etching methods requiring silicon wafers with particular crystalline plane orientation—$\langle 110 \rangle$ or $\langle 111 \rangle$ silicon wafers—for higher vertical etching rates than the horizontal direction. This method works based on defining a pattern as an etching mask in the silicon wafer and processing with a chemical wet process to etch the pattern into the silicon wafer. In spite of the fact that this fabrication process is done in a relatively simple manner–without any sophisticated tools–and provides an acceptable sidewall quality smoothness, there are several disadvantages that make wet etching techniques inefficient. Considering the feature size and horizontal etching rates, disadvantages such as non-uniformity (poor) etching rate across the wafer, limited aspect ratio in etching, limited etching geometries (such as line or crossed lines), and limited periodicity of features, to name but a few, can be mentioned.

Metal-assisted chemical etching (MacEtch or MACE) is a derivative approach of wet etching that can anisotropically etch the substrate and produce high aspect ratio features irrespective of their pattern or substrate crystalline plane orientation [31–33,98–101]. This fabrication method has been applied for micro- and nanofabrication to make devices such

as X-ray zone plates, diffraction gratings, and nanowires. MacEtch operates based on the definition of a patterned noble metal (e.g., gold, platinum, or silver) on a silicon substrate or other semiconductor substrates followed by a wet etching process in a solution composed of an oxidant (e.g., hydrogen peroxide) and an acid (e.g., hydrofluoric acid). The patterned noble metal accelerates the reduction of the oxidant at the interface of metal and silicon, which results in hole carrier generation. The generated hole carriers are then transferred to the valence band of the silicon substrate, where they are consumed and resulting in an ionic material, which is then solubilized via an oxidation mechanism in the acid. As the process continues, the noble metal–catalyst–progressively etches into the silicon substrate leaving behind the unpatterned areas on the silicon. The chemical interaction between the noble metal and the substrate that results in etching the semiconductor, however, is not as straightforward as explained here since a variety of phenomena contribute to the etching process. Despite its extremely high aspect ratio etching capability and excellent sidewall quality, the MacEtch method has not yet been utilized to fabricate large-area X-ray gratings as it suffers from reliability and controllability issues concerning its etching mechanism. The non-uniformity etching characteristic of the MacEtch method has made it unsuitable for large-area high aspect ratio X-ray grating fabrication [99].

Deep reactive ion etching (DRIE) is an alternative method of microfabrication for high aspect ratio structures, particularly for X-ray absorption grating fabrication plasma etching [85, 102]. This method of fabrication falls under plasma dry etching techniques, rather than wet etching processes, with the most widely adopted method of etching being the Bosch etching process. For deep etching applications, the Bosch process employs a passivation layer—through a polymerization step—during each sub-etching step to enhance the etching quality and aspect ratio while maintaining the etching process anisotropic [34–38]. Although the DRIE Bosch process has some limitations and challenges to be applied to large-area X-ray grating fabrication—with micron-scale periods and feature sizes—it still is one of the most advanced and mature microfabrication techniques utilized in the industry for standard wafer-size devices. This chapter aims to investigate the DRIE Bosch process—as the first attempt—for the fabrication of high aspect ratio high-resolution X-ray absorption grating. The chapter continues with an overview of the parameters required to design an X-ray grating and moves to a study on the fabrication steps of silicon wafers. Hard-mask design, deep reactive ion etching parameters, seed layer deposition, and electroplating quality are presented in this chapter as part of the fabrication steps.

3.2 Determining Grating Specifications

X-ray absorption gratings translate an incoming X-ray beam into multiple narrow beamlets through a periodic structure (Figure 3.1). The periodic structure consists of two main parts, the X-ray absorber material and the apertures, with the former being responsible for attenuating the X-ray photons and the latter for letting the photons go through and transmit with minimal attenuation. Gratings are usually fabricated as one-dimensional structures (such as periodic slits or lines) or two-dimensional structures (such as periodic micropillars). Line gratings provide one-directional sensitivity in XPCi, while micropillar-based gratings make multi-directional sensitivity possible. Although several parameters contribute to the design of an absorption grating, detector pixel size, source-to-grating distance, grating-to-detector distance, and the X-ray source energy are among the key factors. As an example, for EI-XPCi, the pre-sample mask (absorption grating) aperture size and period are as:

$$a_g = a_{proj} \times \frac{d_{sg}}{d_{sg} + d_{gd}} \tag{3.1}$$

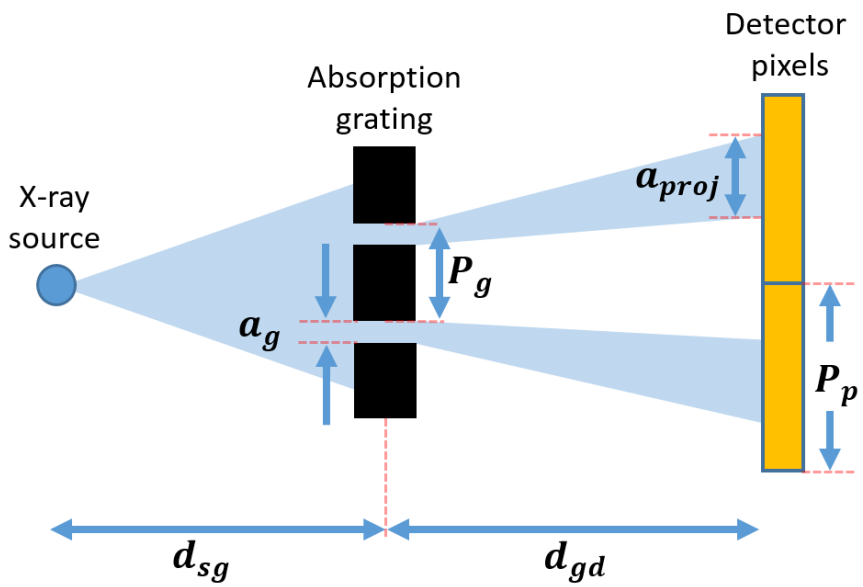


Figure 3.1: Schematic of an X-ray absorption grating specifications in the single-mask EI-XPCi technique.

$$P_g = P_p \times \frac{d_{sg}}{d_{sg} + d_{gd}} \tag{3.2}$$

where the a_g is the aperture size on the grating, the a_{proj} is the projected aperture size on the detector pixel, the d_{sg} is the source-to-grating distance, the d_{gd} is the grating-to-detector distance, the P_g is the grating period, and the P_p is the detector pixel size. The required thickness of an absorber material to attenuate and stop the X-ray photons can be determined according to Beer Lambert's law (as described in 2.12).

Following the detector specifications employed in this research with a pixel size equal to 7.8 μm, and considering d_{sg} and d_{gd} as 18 cm and 8 cm, several aperture sizes and periods were selected to investigate the quality of projected beamlets upon the detector pixels.

3.3 Hard-Mask for DRIE Etching

Selecting a proper hard mask is an inevitable part of performing high aspect ratio Bosch deep reactive ion etching (DRIE) on silicon substrates. The hard mask should be robust

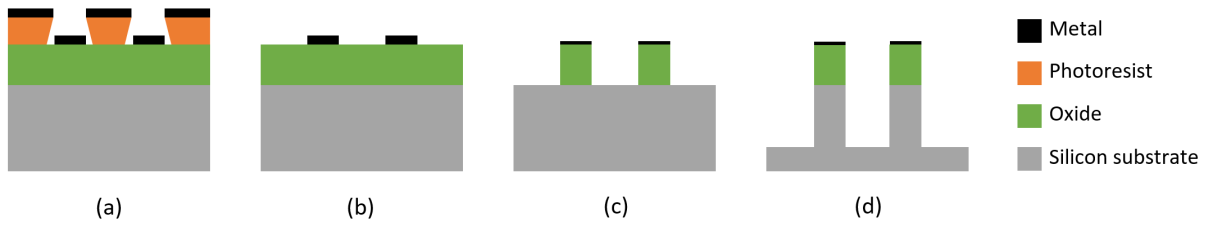


Figure 3.2: A metal/oxide hard mask is defined for Bosch DIRE process by using a negative photoresist in the liftoff process.

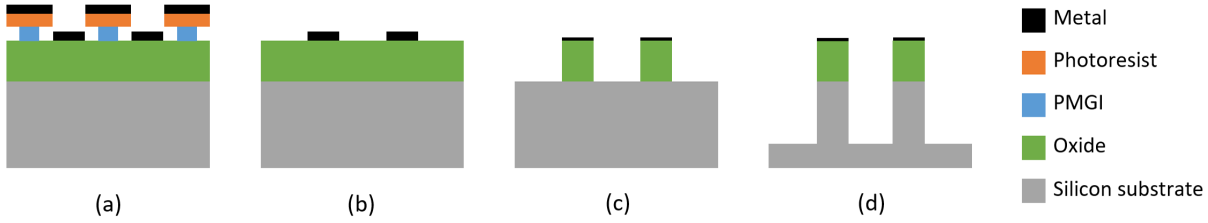


Figure 3.3: A metal/oxide hard mask is defined for Bosch DIRE process by using a positive photoresist in the liftoff process.

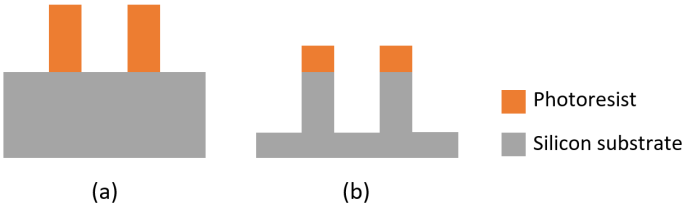


Figure 3.4: Photoresist as the hard mask for Bosch DIRE process.

enough to withstand the dry etching process until the desired depth is etched. Aluminum (Al), aluminum oxide (Al_2O_3), chromium (Cr), chromium oxide (Cr_2O_3), silicon oxide (SiO_2), silicon nitride (Si_3N_4) and photoresists are among hard masks used for DRIE [36, 103–108]. The etching selectivity of the abovementioned materials to silicon and their patterning feasibility are the main factors in determining a suitable hard mask for a high aspect ratio etching process. Liftoff process and patterning of a deposited film, to name but two, are commonly used techniques to define a hard mask on silicon substrates. The quality of the DRIE process using a hard mask based on either of these techniques depends on the minimum feature size of the structures in the design and the thickness of the hard mask itself. As we move toward higher aspect ratio structures, thicker hard masks become necessary. On the other hand, micron-scale feature sizes in a design demand a more precise patterning process for hard masks. That said, we investigated two types of hard mask, a combination of a metal layer with an oxide layer and a thick photoresist layer. For the metal/oxide hard mask, we examined two different oxide layers—silicon oxide (SiO_2) and silicon nitride (Si_3N_4). Figure 3.2 and 3.3 demonstrate the process steps for making a metal/oxide hard mask, and Figure 3.4 is an illustration of a photoresist hard mask, both for the Bosch DRIE process. In Figure 3.2 (a) a negative photoresist is used, which gives undercuts, while in Figure 3.3 (a) or a combination of PMGI and a positive photoresist is used to perform the liftoff process. At the time of this fabrication, we utilized the latter method (process depicted in Figure 3.3) to deposit the metal layer.

3.3.1 Metal/Oxide Hard-Mask

Fabrication began by cleaning 550-μm thick 4-inch <100> n-type silicon wafers through Piranha cleaning process – a 4:1 mixture of %98 sulfuric acid (H_2SO_4) and %30 hydrogen peroxide (H_2O_2). After properly drying the wafers, they were loaded into a PECVD chamber for oxide deposition. Two different oxide layers were deposited and tested, SiO_2, Si_3N_4. We used the WLO1 system in the G2N lab and the ALD/PECVD cluster (OXFORD-cluster) in quantum nano fab (QNF) for oxide deposition, and tested the quality – thickness

and uniformity – of deposition using the Woollam M-2000DI spectroscopic ellipsometer in QNF. Table 3.1 summarizes the conditions considered for depositing SiO_2 and Si_3N_4 as the hard mask. We targeted a thick oxide deposition knowing that the selectivity of SiO_2 to silicon in Bosch DRIE is less than 150:1, and silicon should be etched for more than 200 μm in depth to have an aspect ratio of over 100. Although the selectivity of SiO_2 to silicon is high, it decreases for etching micro-scale feature size patterns. This fact led us to deposit an even thicker oxide layer, around 2 μm thick.

Table 3.1: PECVD deposition process condition for SiO_2 and Si_3N_4 based on two different tools.

Tool (site)	Film type	Gas - Flow (sccm)	Power (W)	Pressure (mTorr)	Temperature (°C)	Time (sec)	Thickness (μm)
WLO1 (G2N)	SiO_2	SiH_4 - 10 N_2O - 100	6	600	300	2000	2.236
WLO1 (G2N)	Si_3N_4	SiH_4 - 5 NH_3 - 100 N_2 - 50	4	600	300	6000	1.2
WLO1 (G2N)	Si_3N_4	SiH_4 - 5 NH_3 - 100 N_2 - 50	4	600	300	1800	0.309
OXFORD-cluster (QNF)	Si_3N_4	SiH_4/N_2 - 400 NH_3 - 22 N_2 - 600	20	650	330	1000	0.435

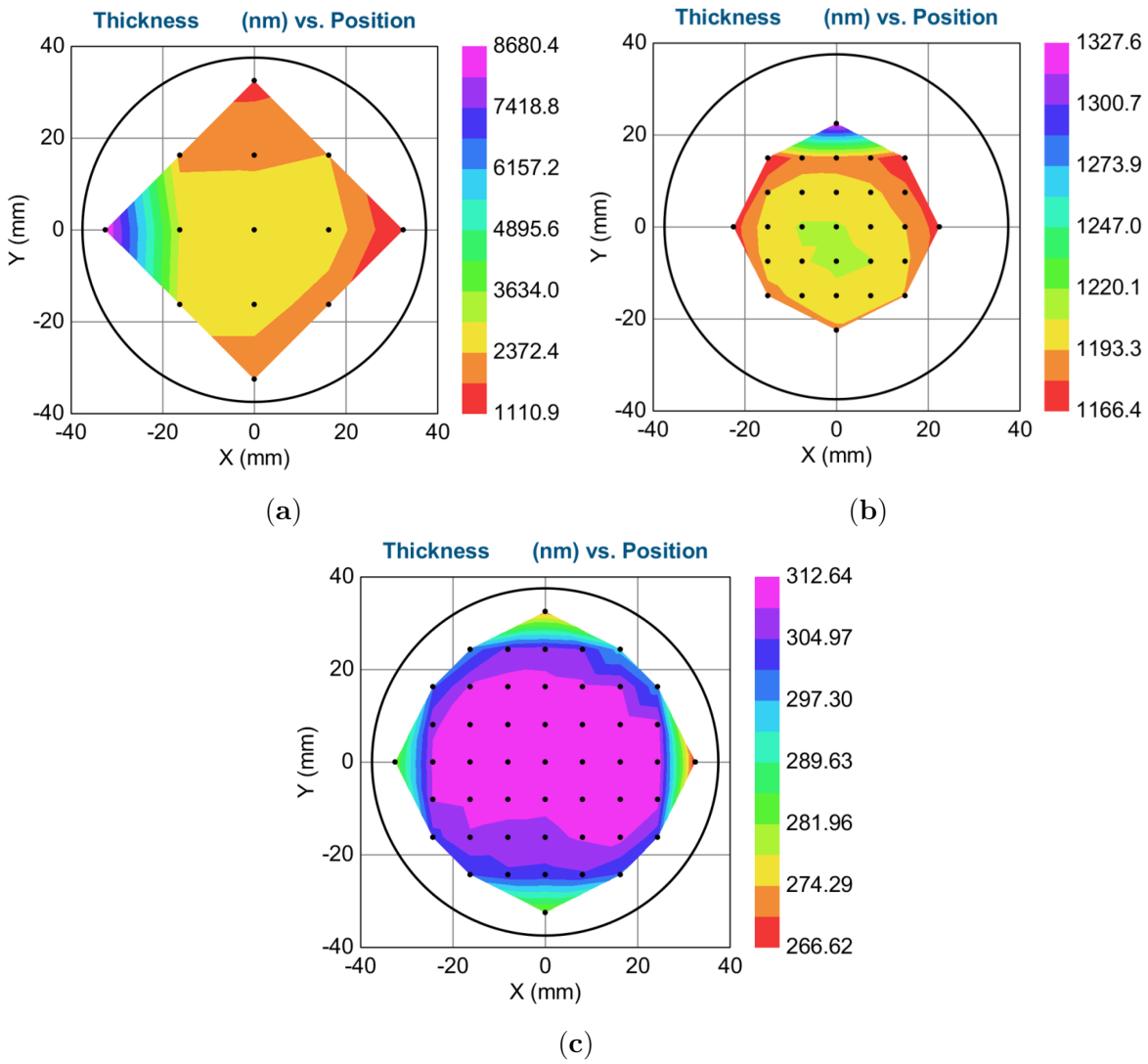
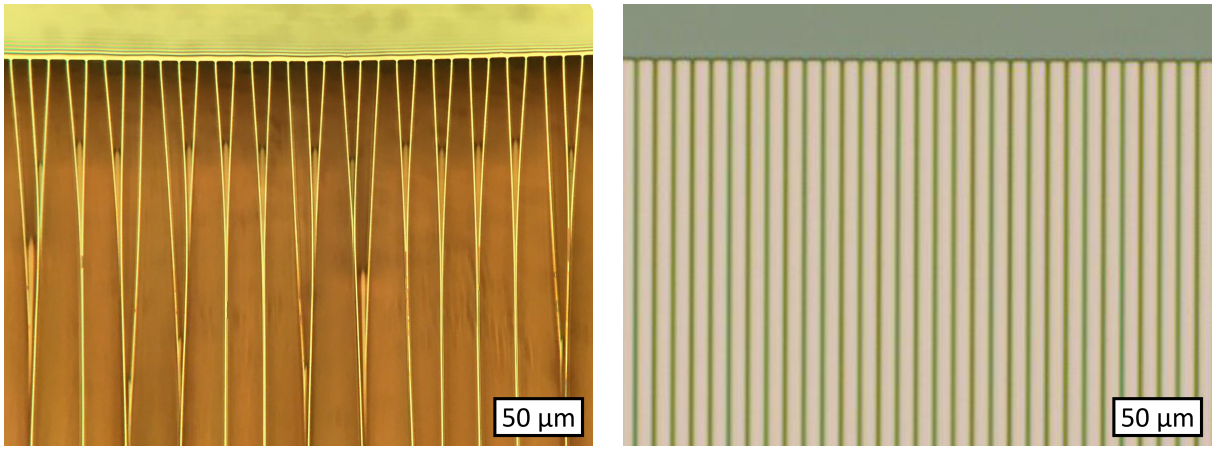


Figure 3.5: Thickness profile map of (**a**) a 2.2 μm thick SiO_2 film, (**b**) a 1.2 μm thick Si_3N_4 film, and (**c**) a 0.3 μm thick Si_3N_4 film, all measured using the Woollam M-2000DI spectroscopic ellipsometer.

Figure 3.5 demonstrates ellipsometry results of the thickness map for a thick SiO_2 film (Figure 3.5a) and a thick Si_3N_4 film (Figure 3.5b), both deposited using the WLO1 system. Analyzing the thickness profiles acquired using the ellipsometry test, it is evident that the profile of oxide films for longer deposition periods (thicker films such as Figure 3.5a) become more nonuniform compared to shorter deposition periods (Figure 3.5c).



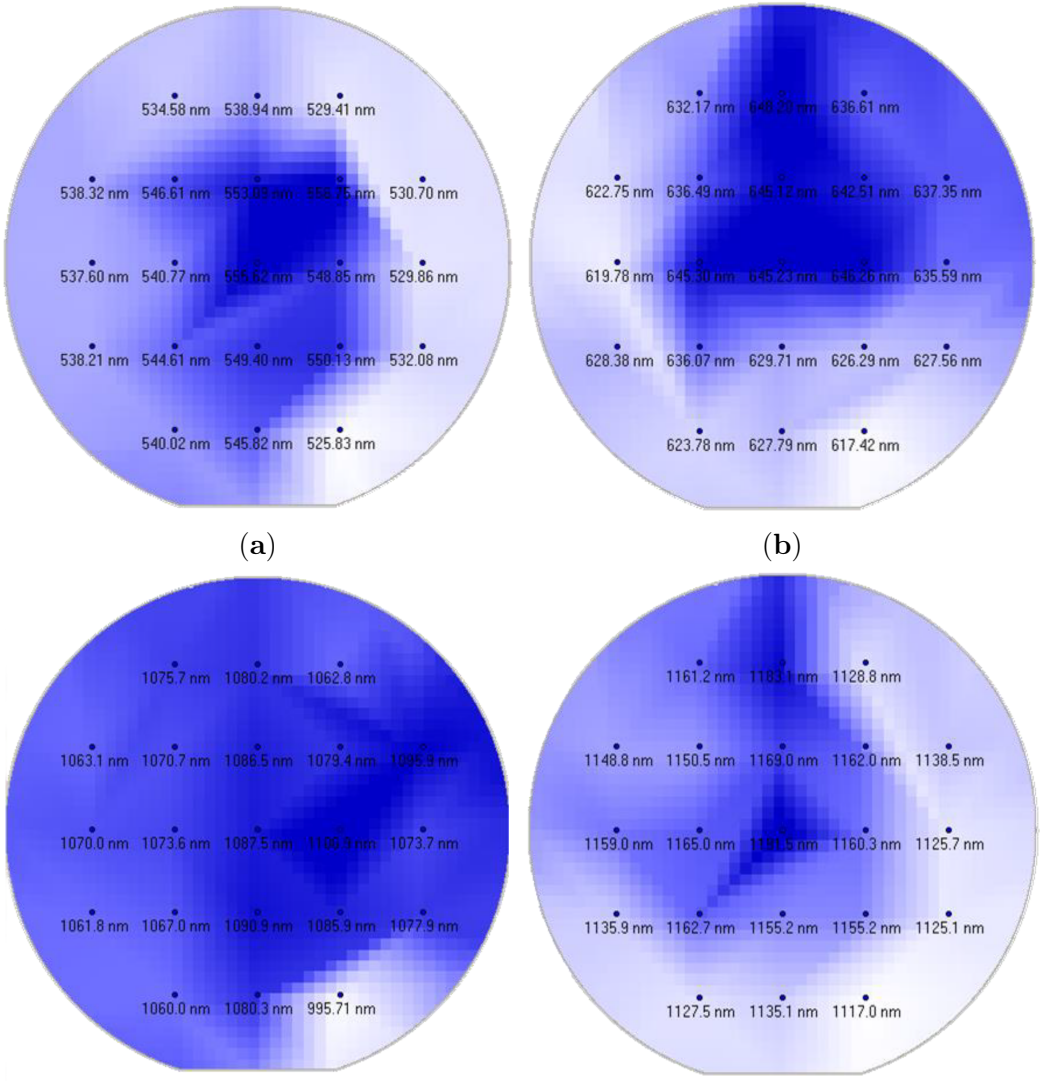
(**a**) (**b**)

Figure 3.6: Optical microscope images of line patterns lithographed on the substrate (**a**) without, and (**b**) with the HMDS application as the adhesion promoter. HMDS increases the bonding strength between the photoresist and the substrate.

After depositing the oxide film on the wafer, a monolayer of hexamethyldisilazane (HMDS) was coated on the oxide film through a vapor treatment using the YES-HMDS oven. HMDS application is beneficial (and recommended) for forming a bond between the oxide film surface and the photoresist, without which the photoresist peels off from the wafer surface during the developing step. Figure 3.6 illustrates two optical microscope images without (3.6a) and with (3.6b) employing HMDS as an adhesion promoter between the photoresist and the surface of the oxide film. As evident in Figure 3.6a, patterned structures not bonded to the substrate collapse, break, or become attached to neighbouring patterns after developing the photoresist. After applying the HMDS and before coating a positive photoresist, PMGI SF7 was coated on the wafer to have an undercut with the positive photoresist for the liftoff process.

A relatively thin photoresist had to be used to transfer micron-scale feature sizes onto the positive photoresist. Shipley S1805 and S1811 were utilized as the positive photoresist throughout this research, and their thickness and uniformity were evaluated using the FILMETRICS F50 tool. Figure 3.7 demonstrates the thickness and uniformity profile for Shipley S1805 and S1811, spin-coated at different speeds. S1805 was selected as the positive photoresist for lithography, considering the micron-scale feature sizes of the design. S1805 was spin-coated at 3000 RPM for 60 seconds, followed by a soft bake at 115°C for 60 seconds. Pattern transfer was conducted through a maskless lithography tool – HEIDELBERG-MLA 150 – using an exposure dose and defocus value of 100 mJ/cm^2 and

-2, respectively. Following the lithography, samples were developed in MIF319 developer for 45 seconds, rinsed with DI water, and dried with N_2. Samples were inspected for the quality and extent of undercut using an optical microscope, where they were developed more until enough undercut was reached.



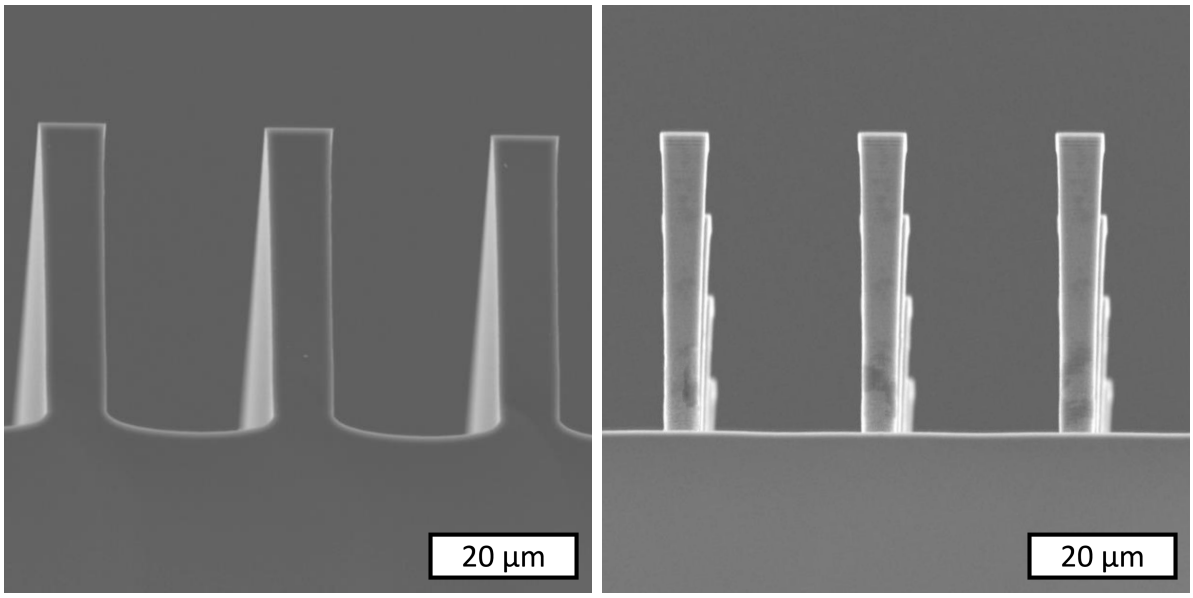
(**a**) (**b**)

(**c**) (**d**)

Figure 3.7: (**a**) S1805 spin coated at 6000 RPM and baked at 115°C ,(**b**) S1805 spin coated at 3000 RPM and baked at 115°C, (**c**) S1811 spin coated at 6000 RPM and baked at 115°C, (**d**) S1811 spin coated at 5000 RPM and baked at 115°C.

A physical vapour deposition (PVD) tool – an e-beam evaporator (Intlvac Inc., CA) – was utilized to deposit an aluminum film onto the patterned wafers. Deposition of aluminum was performed at room temperature and under a vacuum of 2×10^{-6} Torr. After depositing 200 nm aluminum, a liftoff process was conducted by putting the wafers into the PG Remover – warmed up to 75°C – for 10 minutes – until the liftoff process was completed. Wafers were then rinsed with DI water and dried with N_2.

At this point, the thick oxide layer was etched using the OXFORD-metal RIE tool at QNF, using 45 sccm SF_6 gas with 50 W of RF power and 2000 W of ICP power, until the patterned areas on the oxide were completely etched. The combination of the remaining aluminum film and the oxide layer served as the hard mask for the Bosch DRIE process. Etching the silicon was performed through the Bosch DRIE process with 160 sccm of SF_6 gas at 20 W of RF power and 1000 W of ICP power for 7 seconds for etching the silicon, and 160 sccm of C_4F_8 gas at 5 W of RF power and 1000 W of ICP power for 5 seconds for creating a passivation layer over the etched areas. Figure 3.8 and Figure 3.9 illustrate scanning electron microscopy (SEM) images of samples etched for almost 40 μm into the silicon wafer. Lamella and micropillar based structures were fabricated with a minimum feature size of 330 nm and an aspect ratio of over 100.



(**a**) (**b**)

Figure 3.8: (**a**) Lamellae with 8.6 μm width and 32 μm period, and (**b**) micropillars with 4.5 μm width and 27 μm period. All samples were etched for 40 μm into the silicon using a metal/oxide hard mask.

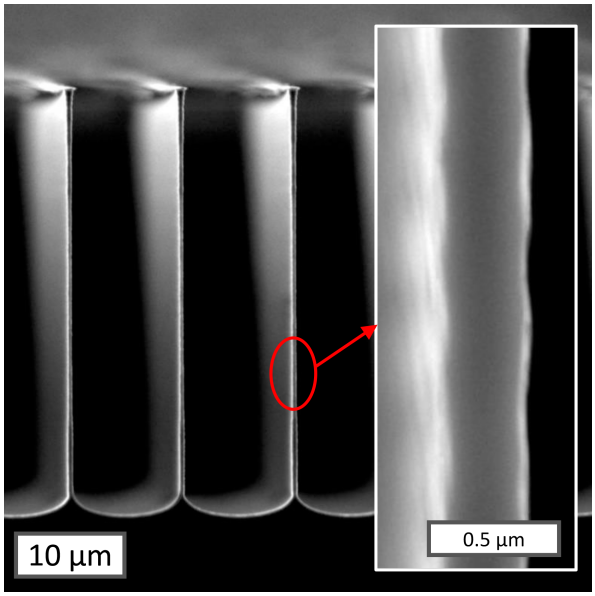


Figure 3.9: Lamellae with 330 nm width and 10.5 μm period. The sample was etched for 40 μm into the silicon using a metal/oxide hard mask.

3.3.2 Photoresist Hard-Mask

Due to frequent equipment failures and problems associated with the OXFORD-metal RIE tool at QNF – at the time of this fabrication – we could not continue employing the metal/oxide hard mask, albeit these combined layers seemed as an efficient dry etching hard mask. That said, we utilized a simple thick photoresist hard mask for the Bosch DRIE process. Employing a thick photoresist – which can be easily applied by a spin coating process – facilitates the grating fabrication, compared to the long process of making a metal/oxide hard mask that requires multiple steps, including PECVD deposition of an oxide layer, photoresist coating, e-beam deposition, liftoff process, and oxide etching. After properly cleaning the silicon wafer – as explained earlier – a double-coated layer of the negative photoresist AZ nLof 2035 – each layer spin coated at 3000 RPM for 60 seconds, followed by a soft bake at 110°C for 60 seconds– was utilized as the hard mask. The AZ nLof 2035 layer was then patterned through the maskless aligner lithography tool with an exposure dose and defocus value of 110 mJ/cm^2 and -1, respectively. The exposed wafer was then baked – post-exposure bake step – at 110°C for 60 seconds, followed by a developing step in MIF319 developer for 45 seconds. After rinsing the wafer and drying it using N_2 gas, the patterned wafer was placed on a hotplate for a hard bake step at

130°C for 10 minutes to further harden the photoresist for the Bosch DRIE process. The hard bake step increases the silicon to photoresist selectivity, which is beneficial for deeper (higher aspect ratio) etching processes. A selectivity of more than 75 was achieved for the hard-baked AZ nLof 2035 photoresist hard mask.

3.4 Bridge-Assisted structures

Long high-aspect ratio features such as silicon lamellae are usually susceptible to mechanical forces (stress or strain) during fabrication. These lamellae can easily distort, break, or collapse due to thermal stress in high temperature process steps, capillary forces during or after wet process steps, or plasma-induced forces during etching processes. Structures fabricated based on resists are even less resilient against the aforementioned forces. Employing auxiliary supporting bridge structures is a common technique to help high aspect ratio features stand alone and withstand various forces applied during and after fabrication [29, 38, 83, 86, 109]. These auxiliary supporting bridge structures can be randomly or non-randomly distributed, which affect the final image quality (visibility) in an XPCi system.

Albeit the fabrication process of high aspect ratio structures for line gratings (lamellae) is well-developed, there are technological challenges in realizing two-dimensional (2D) gratings through the fabrication of fine high aspect ratio micropillars that restrict X-ray imaging systems sensitivity and functionality. The necessary fabrication of high-resolution high aspect ratio – fine-tuned – micropillar-based gratings (for 2D sensitivity in XPCi) has until now been problematic [110, 111]. The main challenge is associated with micropillars mechanical stability throughout the fabrication. Whether resist-based or silicon-based process is used to fabricate high aspect ratio micropillars during developing, cleaning, or electroplating, micropillars that are not stable enough collapse, bend, or deform. Figure 3.10 demonstrate an SEM image of silicon-based micropillars fabricated through the Bosch DRIE process, which are broken and collapsed.

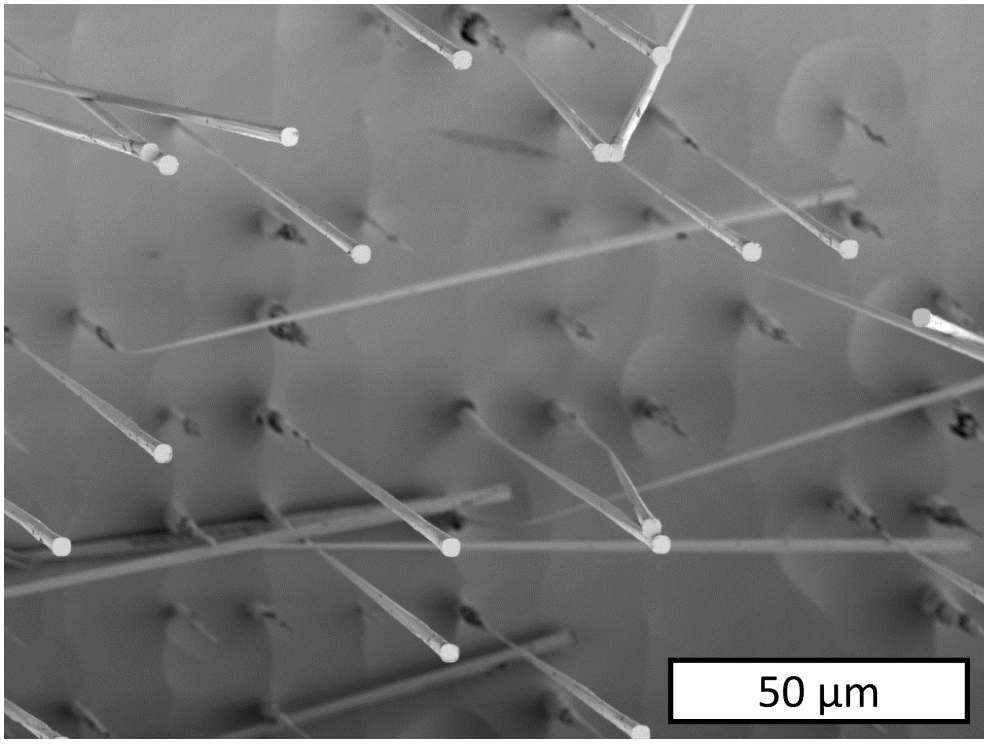


Figure 3.10: SEM image of high aspect ratio micropillars fabricated on a silicon wafer through Bosch DRIE process. Micropillars are broken or collapsed due to plasma-induced forces and partial higher horizontal etching rate at some part of their base.

In this section, we introduce bridge-assisted micropillars to improve micropillars mechanical stability. Adding auxiliary supporting bridge structures helps micropillars stand alone, eliminating the need for a critical point drying step after each wet processing step. To demonstrate a proof-of-concept of bridge-assisted micropillars, we fabricated prototype silicon-based micropillars. The result of this work helps researchers further expand 2D phase-contrast X-ray imaging systems sensitivity.

Before explaining the supporting bridge structure, it is worth mentioning that the silicon wafers etching rate in the Bosch DRIE depends on several parameters, including pattern geometry and density, minimum feature sizes, and duty cycle of patterns, as well as etching parameter [112]. Experimental results in etching different pattern sizes on silicon wafers verified that as patterns become compact, the etching rate drops. Figure 3.11 demonstrates a side view of structures with different periodicity values. Considering the fact that micropillars without supporting bridge structures undergo a slightly higher etch-

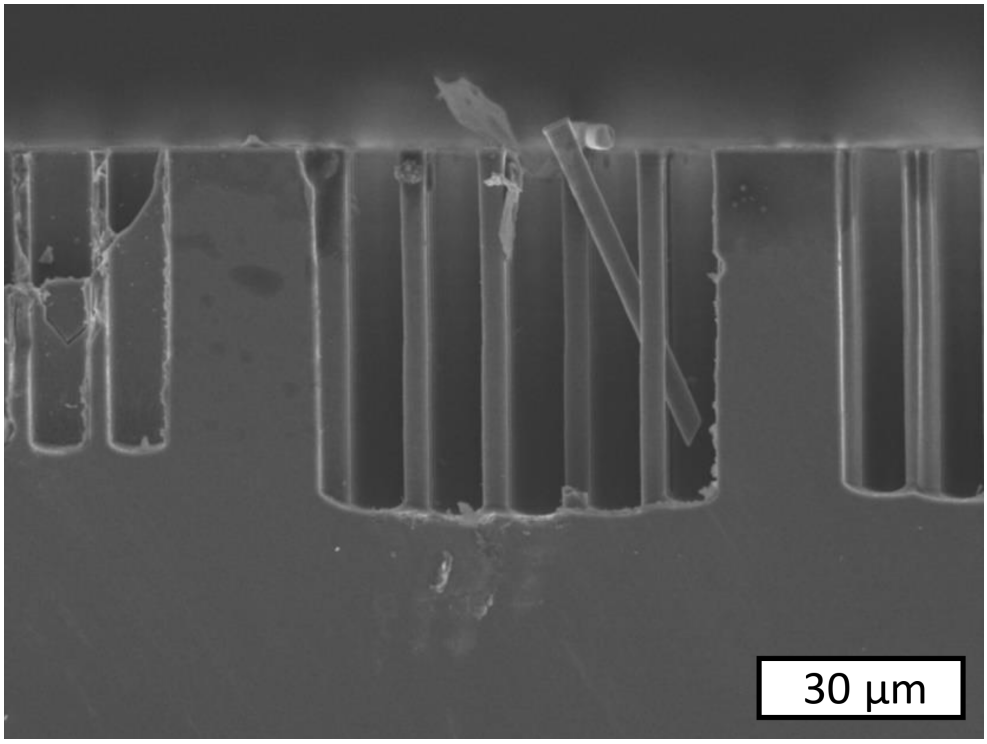
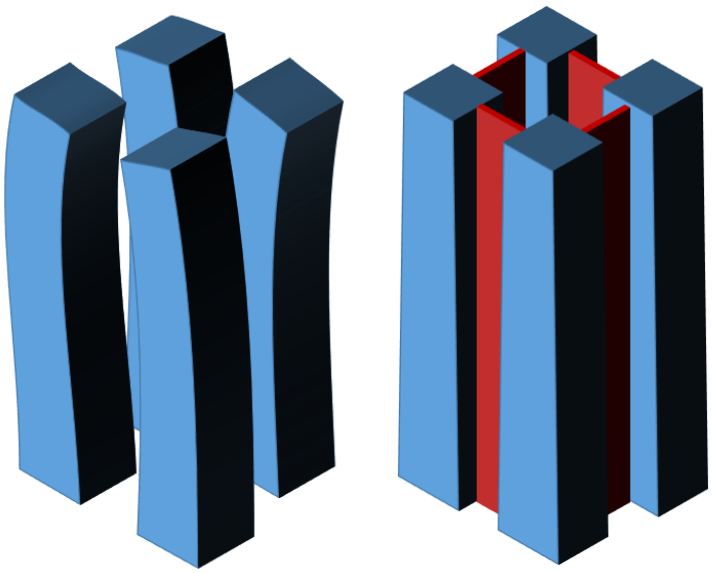


Figure 3.11: SEM image of patterns on a silicon wafer with different periodicity values etched through the Bosch DRIE process.

ing rate at their base and the fact that more dense patterns show a lower etching rate, we designed bridge-assisted micropillars by connecting micropillars using thin bridge structures. These bridges provide a controlled etching rate at the base of micropillars. Because of the controlled etching rate, the base of micropillars does not experience a higher etching rate, which minimizes the possibility of them being broken. Moreover, bridge structures also keep high aspect ratio micropillars connected so they can withstand external forces applied to them. Figure 3.12 illustrates a schematic view of auxiliary supporting bridge structures.



(**a**) (**b**)

Figure 3.12: Schematic illustration of high aspect ratio micropillars (**a**) without and (**b**) with auxiliary supporting bridge structures.

Optimization of the width of these bridge structures was conducted based on the type of hard mask. For the metal/oxide hard mask, bridges had to be designed slightly wider – considering an undercut etch happened during the Bosch DRIE process. Figure 3.13 illustrates the design computer-aided design (cad) along with an SEM image of square-shaped micropillars with 4 μm in width without and with 1 μm, 1.5 μm, and 2 μm thick bridges. The metal/oxide hard mask turned features to appear smaller due to the undercut etching that happened during transferring patterns from the metal mask to the oxide layer. As a result of this pattern shrinkage, micropillars and bridges turned into smaller features than what they were initially designed. The sample was etched for almost 20 μm into the silicon.

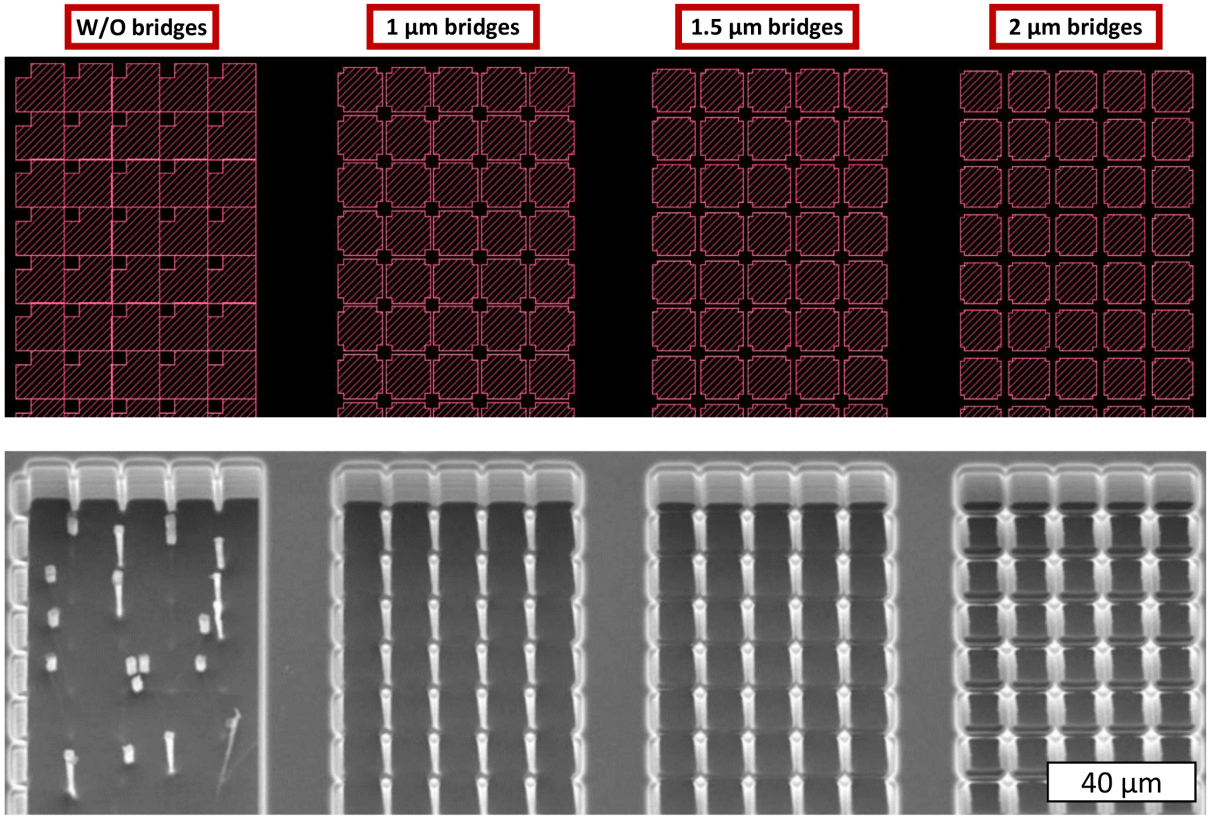


Figure 3.13: Illustration of CAD design of micropillars without and with bridge structures along with the SEM images of the same micropillar designs etched on a silicon wafer.

As evident, micropillars without auxiliary supporting bridge structures become thinned at their base, which causes them to break. Figure 3.14 demonstrates an example of high aspect ratio micropillars without auxiliary supporting bridges which are thinned at their base – but still standing – before the end of etching. However, employing bridge structures helps micropillars to stand alone – even with 1 μm thick bridges. For applications where only free-standing micropillars are required, designing thin bridges helps the formation of micropillars, and the bridges get etched at the end of the etching process – as illustrated in Figure 3.13 for micropillars with 1 μm thick bridge structures.

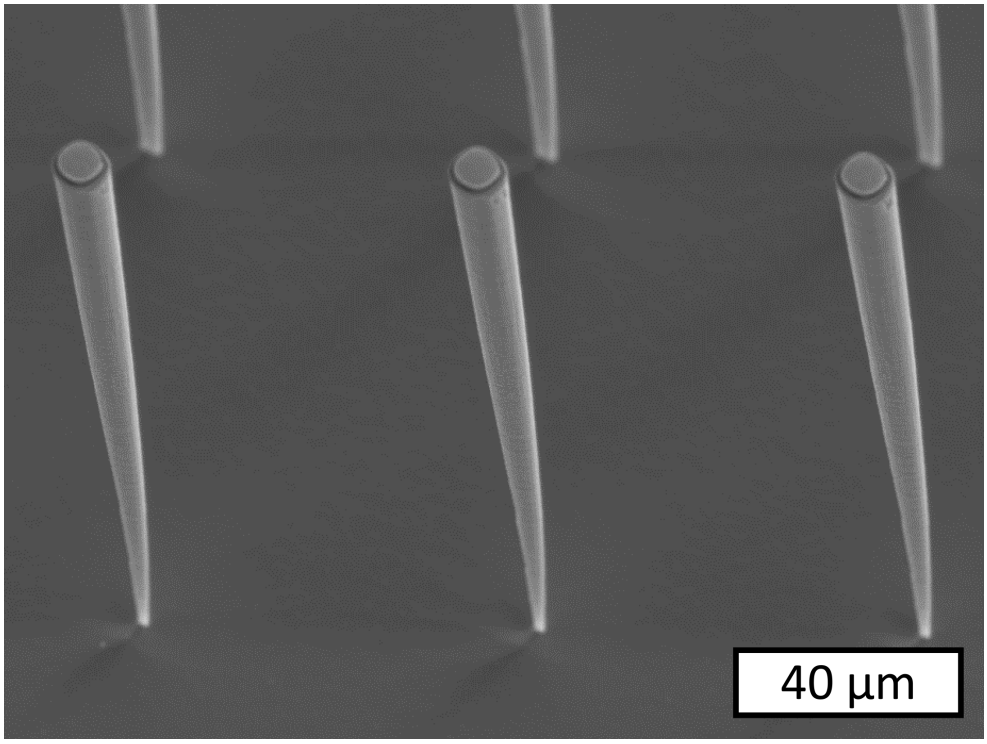


Figure 3.14: Illustration of an SEM image where micropillars became thinned at their base before the end of the Bosch DRIE process.

For the resist-based hard mask, the minimum width of the bridges had to be optimized so that the bridges neither become too thick to interfere with micropillar patterns nor too thin to not appear after lithography. Optimization for the photoresist-based hard mask is illustrated in Figure 3.15. Square-shaped features with 4 μm in width with 1 μm, 1.5 μm, 2 μm, and 2.5 μm thick bridges were patterned on a positive photoresist coated on a silicon substrate. Shipley S1811 – a positive photoresist – was used for the optimization test. Positive photoresists create A-shaped structures after lithography, while negative photoresists form V-shaped structures – depending on the exposure dose and post-exposure bake temperature. Square-shaped micropillar fabricated with 1.5 μm bridge structures – in Figure 3.15 – demonstrates the minimum bridge width required for the Bosch DRIE process. Experimental results for AZ nLof 2035 negative photoresist show a minimum width of 1 μm for bridge structures. Bridges thinner than 1 μm using UV lithography are hard to achieve. On the other hand, thinner bridges for high aspect ratio structures are not practical as they could get etched in the middle of the etching and not last until the end of the process.

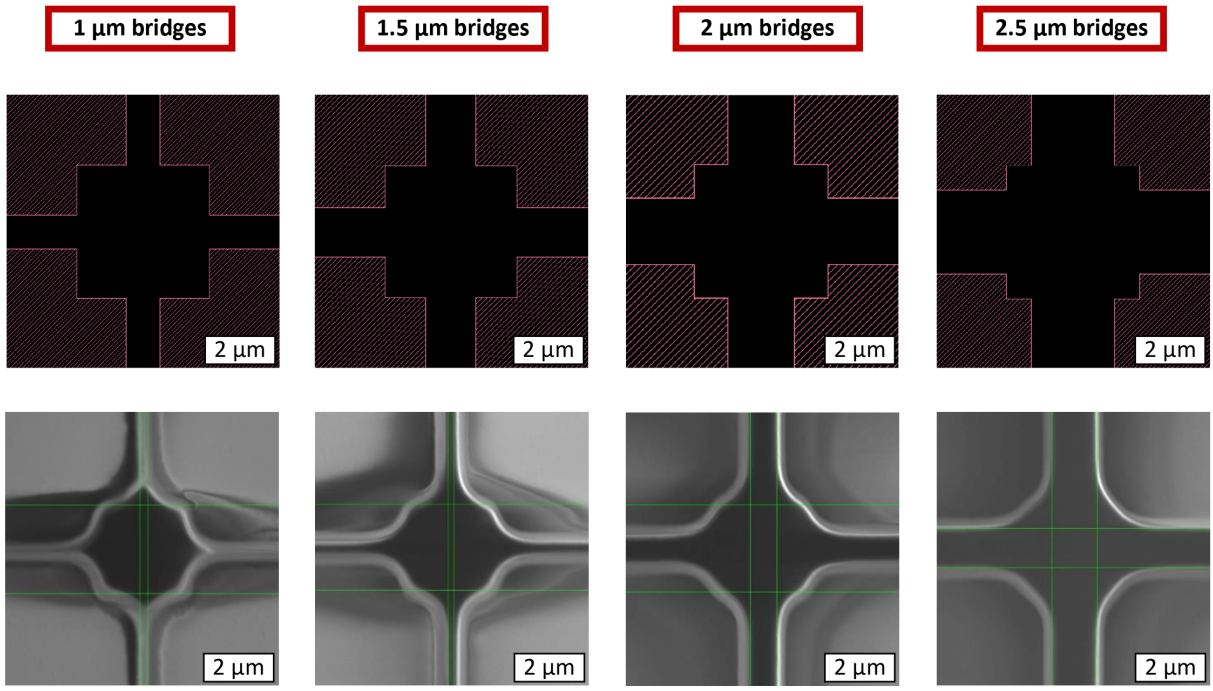
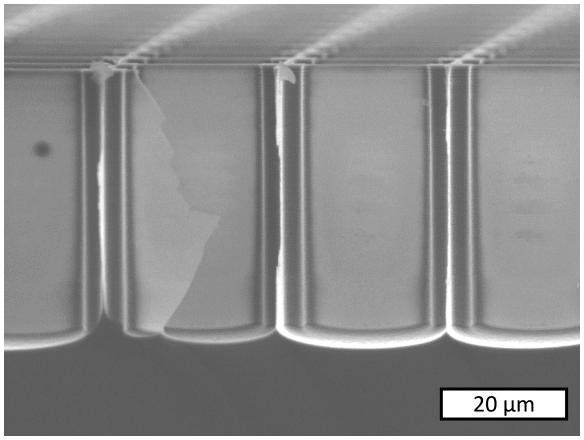
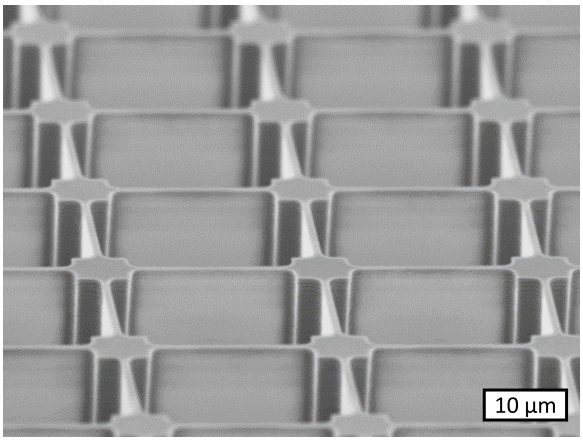


Figure 3.15: Illustration of CAD design of micropillars with 1 μm, 1.5 μm, 2 μm, and 2.5 μm thick bridges along with their SEM images of patterned structures on a silicon wafer coated with photoresist.

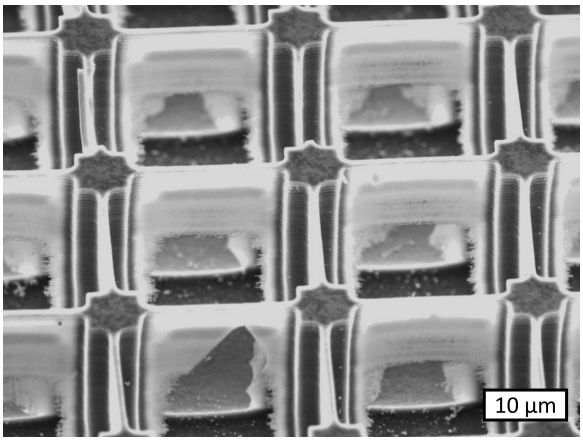
Figure 3.16 illustrates SEM images of bridge-assisted micropillars with almost 1 μm thick bridges. Bosch DRIE process in Figure 3.16a and 3.16b is not complete, and as it is evident bridges are not etched. In Figure 3.16c, however, bridges are about to become etched toward the end of the etching process. It is worth mentioning that to have higher aspect ratio free-standing high-resolution micropillars the supporting bridges should be modified thus that they can withstand longer etching periods.



(**a**)



(**b**)



(**c**)

Figure 3.16: SEM images of micropillars with bridge structures. (**a**) Side view of the sample where bridges still exist in the middle of the etching process, (**b**) top view with an angle of the same sample, and (**c**) top view with an angle of micropillars with bridges about to become etched toward the end of the etching process.

3.5 High Aspect Ratio Silicon-based X-ray Absorption Grating

3.5.1 Etching High Aspect Ratio Structures

The schematic view of the process flow of fabricating a high aspect ratio structure for X-ray absorption grating is illustrated in Figure 3.17. A 550-μm thick 4-inch silicon wafer was first cleaned through RCA-1 and RCA-2 processes (3.17(a)). The silicon wafer was then spin-coated with nLof 2035, a negative photoresist, and the grating pattern was transferred onto the photoresist through a UV lithography step using Karl Suss MA6 Mask Aligner

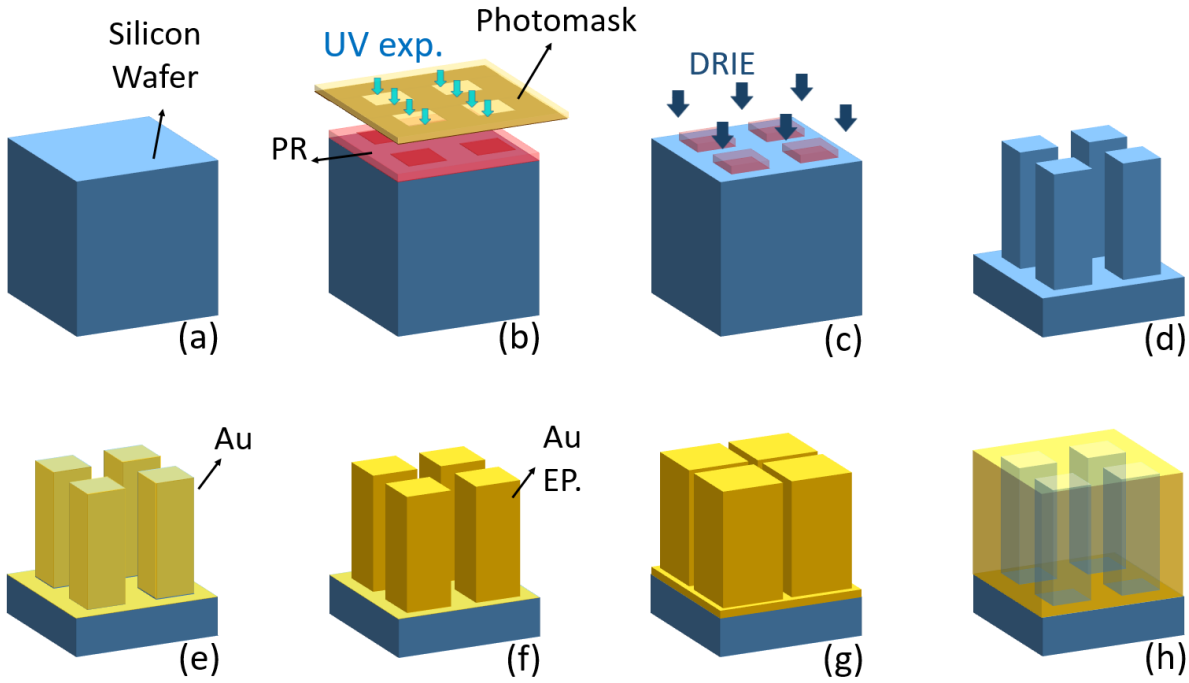
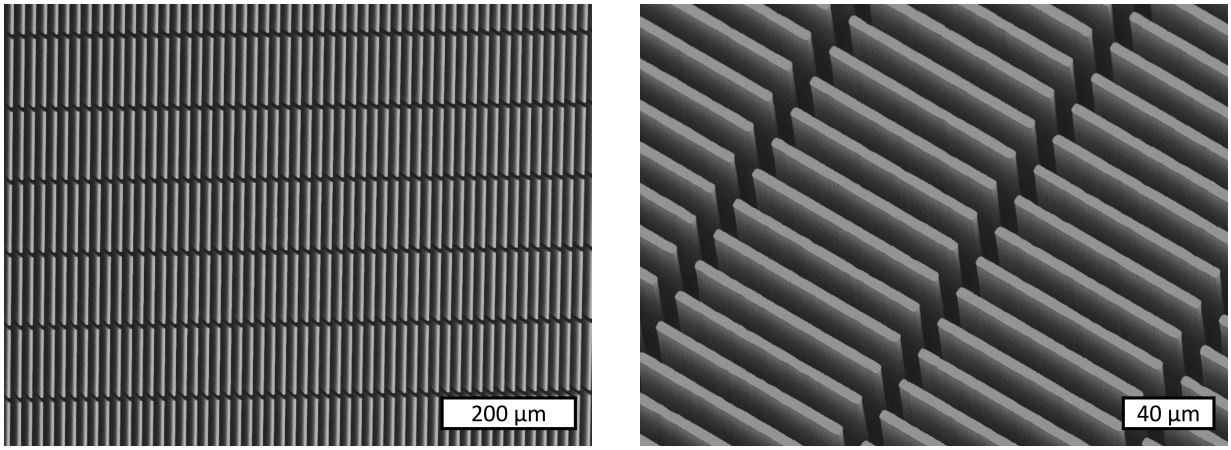


Figure 3.17: Schematic illustration of the process flow for fabricating a high aspect ratio high-resolution X-ray absorption grating on a silicon wafer. (**a**) Obtaining a silicon wafer, (**b**) coating a thick photoresist as the etching hard mask and transferring the pattern onto the photoresist through UV exposure lithography, (**c**) performing Bosch deep reactive ion etching (DRIE), (**d**) stripping the remaining photoresist, (**e**) deposition of a thin layer of gold through atomic layer deposition (ALD), and (**f**) to (**h**) conducting intermittent gold electroplating to form the absorption part of the grating.

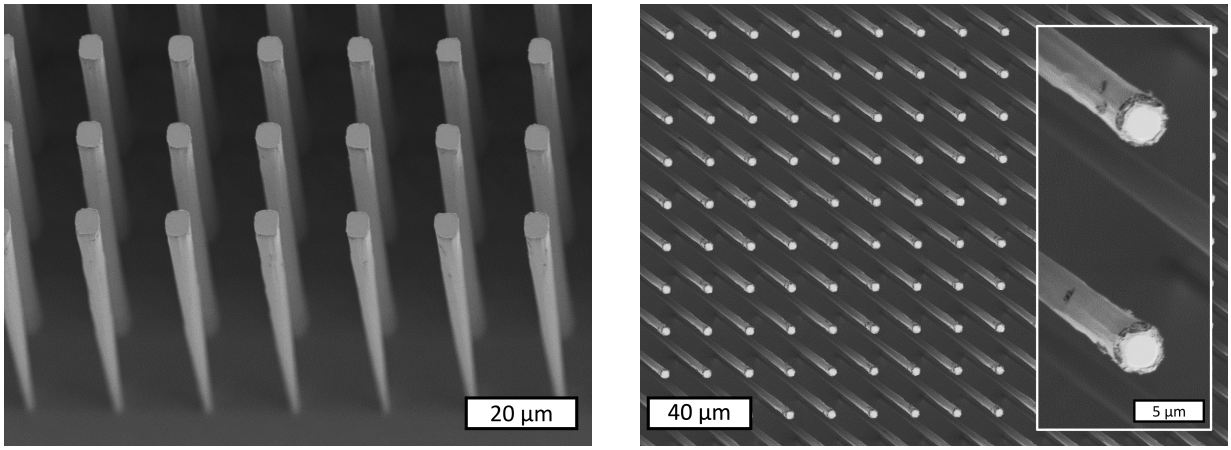
(SUSS MicroTec Group, Garching, Germany) (3.17(b)). For some samples, we also tried a maskless lithography tool – HEIDELBERG-MLA 150 – with an exposure dose and defocus value of 100 mJ/cm^2 and -2, respectively. For both approaches, the patterned photoresist layer, which was designed to serve as a hard mask, was treated with a hard bake step to withstand the subsequent dry etching process. Following the hard bake step, the silicon wafer underwent a Bosch deep reactive ion etching (DRIE) process using C_4F_8 and SF_6 gasses (3.17(c)). The remaining photoresist was stripped from the sample, and the sample was cleaned using DI water and dried using nitrogen (3.17(d)).

Structures with high aspect ratios of more than 50 were fabricated on silicon wafers employing the photoresist-based hard mask and the Bosch DRIE process. Gratings with 4 cm×4 cm active area in two shapes of line features (1D) with width as thin as 4 μm, and micropillars (2D) with diameter as small as 3 μm were fabricated through etching the silicon substrate for almost 150 μm deep. Figure 3.18 and 3.19 present SEM images of fabricated gratings.



(**a**) (**b**)

Figure 3.18: Illustration of SEM images of (**a**) line grating with 5 μm width and 21.6 μm period; (**b**) line grating with 4 μm width and 12.2 μm period.



(**a**) (**b**)

Figure 3.19: Illustration of SEM images of (**a**) micropillar grating with 4 μm in diameter and 12.2 μm period, and (**b**) micropillar grating with 3 μm in diameter and 16.3 μm period.

3.5.2 Seed Layer Deposition for Electroplating

Electroplating is a commonly used technique to form the absorption parts of X-ray gratings. Gold is the widely utilized electroplated metal to absorb X-ray photons as it poses a high atomic number. Moreover, gold electroplating is a well-developed process in MEMS and semiconductor fabrication. Electroplating usually requires a conformal seed layer that should be deposited on the sample prior to starting the electrodeposition (Figure 3.17e). A seed layer is a thin layer of a metal, selected depending on the metal being electroplated, that ensures an electrical connection and acts as the cathode for the electroplating process to allow the growth of the metal being electroplated (Figure 3.17f to 3.17h). For gold electroplating, a thin layer of gold or platinum is normally deposited on the sample. The deposition method for the seed layer varies based on the surface uniformity of the wafer and structures present on the wafer. For uniform samples – that do not have high aspect ratio features – physical vapour deposition (PVD) techniques such as thermal evaporation, e-beam evaporation, or sputtering can be effectively used to form the seed layer. However, for non-uniform surfaces with high aspect ratio structures, the atomic layer deposition (ALD) process—a chemical vapour deposition (CVD) technique—is the most viable technique that can be employed to deposit the seed layer. Although there have been a number of studies on the feasibility of performing electroplating on a conductive substrate without the need for a seed layer, such as highly doped silicon wafers, having a seed layer seems to be a requirement for samples etched through the Bosch DRIE process. The passivation layer left

from the Bosch DRIE process—the polymer formed in the C_4F_8 gas polymerization step—prevents any electrical connection between the silicon substrate and the electroplating anode. Therefore, deposition of the seed layer using the ALD process seems to be an inevitable step in fabricating high aspect ratio X-ray absorption gratings.

Unfortunately, the metal ALD process became inaccessible during the course of this research, which impeded us from depositing a conformal seed layer for conducting the electroplating step and realizing high aspect ratio X-ray absorption gratings. This bottleneck forced us to move to fabrication processes that do not require the metal ALD process. This challenge shifted the fabrication of high aspect ratio structures from etching the silicon wafers to making resist-based molds on conductive films, which will be explained in detail in the following chapters. In spite of the fact that the ALD process was inaccessible, we explored the feasibility of performing gold sputtering on the silicon wafers already etched through the Bosch DRIE process.

3.5.3 Sputtering of Gold

The schematic view of the process flow used to deposit the seed layer onto the high aspect ratio gratings employing a sputtering tool is depicted in Figure 3.20. Figure 3.20a is a schematic diagram of the plasma sputtering using argon (Ar) gas. A sputtering tool (AJA-sputter ATC Orion Series, from AJA International Inc., USA) was employed to deposit the seed layer onto the high aspect ratio structures prior to performing the electroplating step. Sputtering was done following the properties listed in Table 3.2.

Table 3.2: AJA Sputtering properties for chromium (Cr) and gold (Au) film deposition.

Target Matrial	DC Power (W)	Dep. time (sec)	Current (mA)	Base Pres. (Torr)	Dep. Pres. (mTorr)	Temp. (deg. °C)	Ar (sccm)
Cr	200	90	546	2×10^{-7}	3	RT	27
Au	200	600	362	2×10^{-7}	3	RT	27

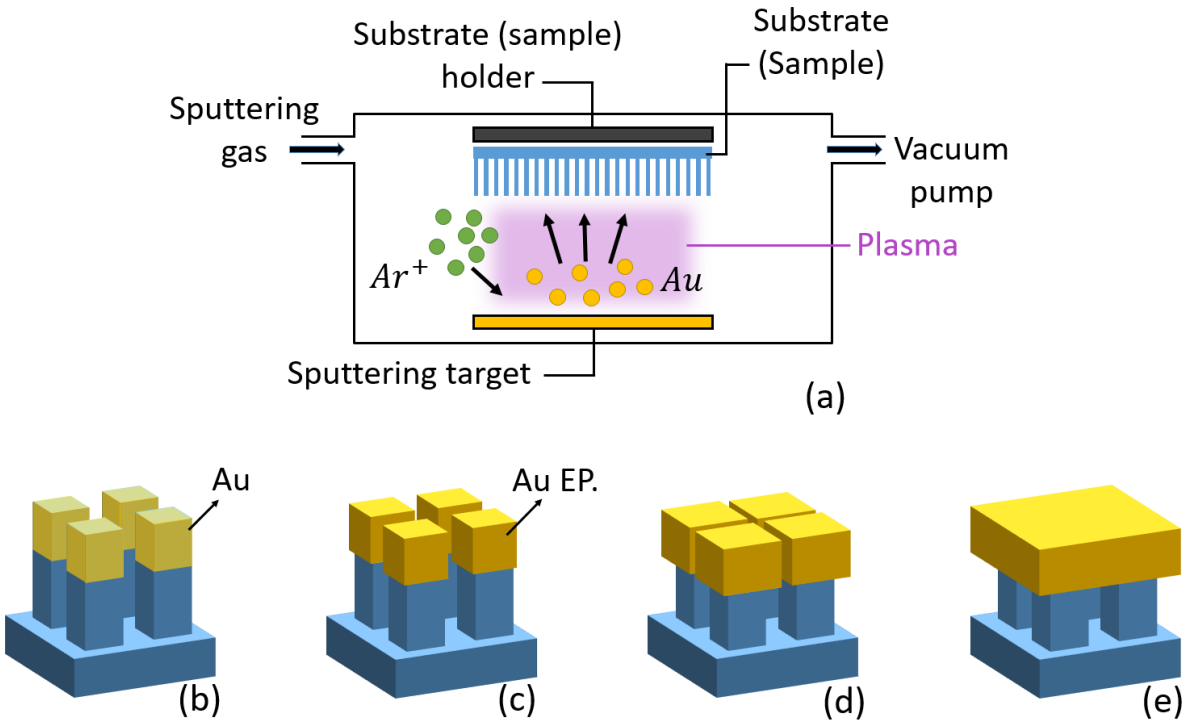


Figure 3.20: Schematic illustration of the process flow for deposition of seed layer onto high aspect ratio gratings using a sputtering tool. (**a**) Depiction of the sputtering process, (**b**) gold particles deposited through sputtering only cover the top part of high aspect ratio structures, and (**c**)-(**e**) conducting intermittent gold electroplating to form the absorption part of the grating.

The seed layer consisted of chromium (Cr) and gold (Au) films, where the chromium film was first sputtered to increase the adhesion of gold to the structures (3.20b). Although we kept the substrate close to the sputtering target, gold particles only reached the top part of the high aspect ratio structures, as presented in 3.20b. The partial deposition of the gold film on the features is because the sputtering step coverage is lower than the ALD process. Figure 3.21 illustrates a schematic view of a high aspect ratio micropillar with five SEM images taken from various locations that are mapped onto the micropillar. SEM images verify the fact that the top part of the micropillar is covered with an acceptable thickness of the seed layer, while the bottom part of the micropillar does not show a considerable thickness of the seed layer – almost zero thickness.

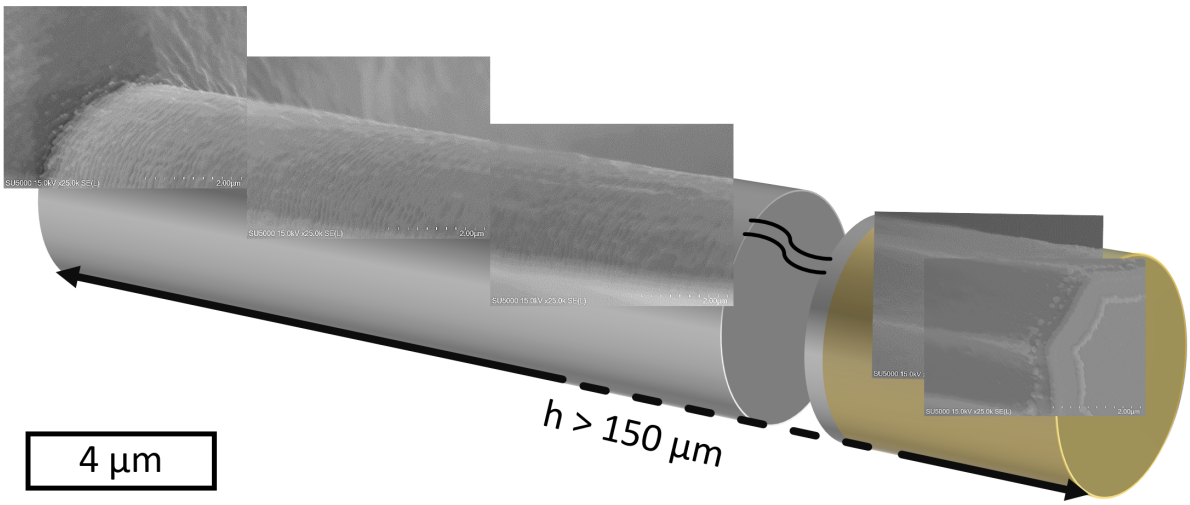


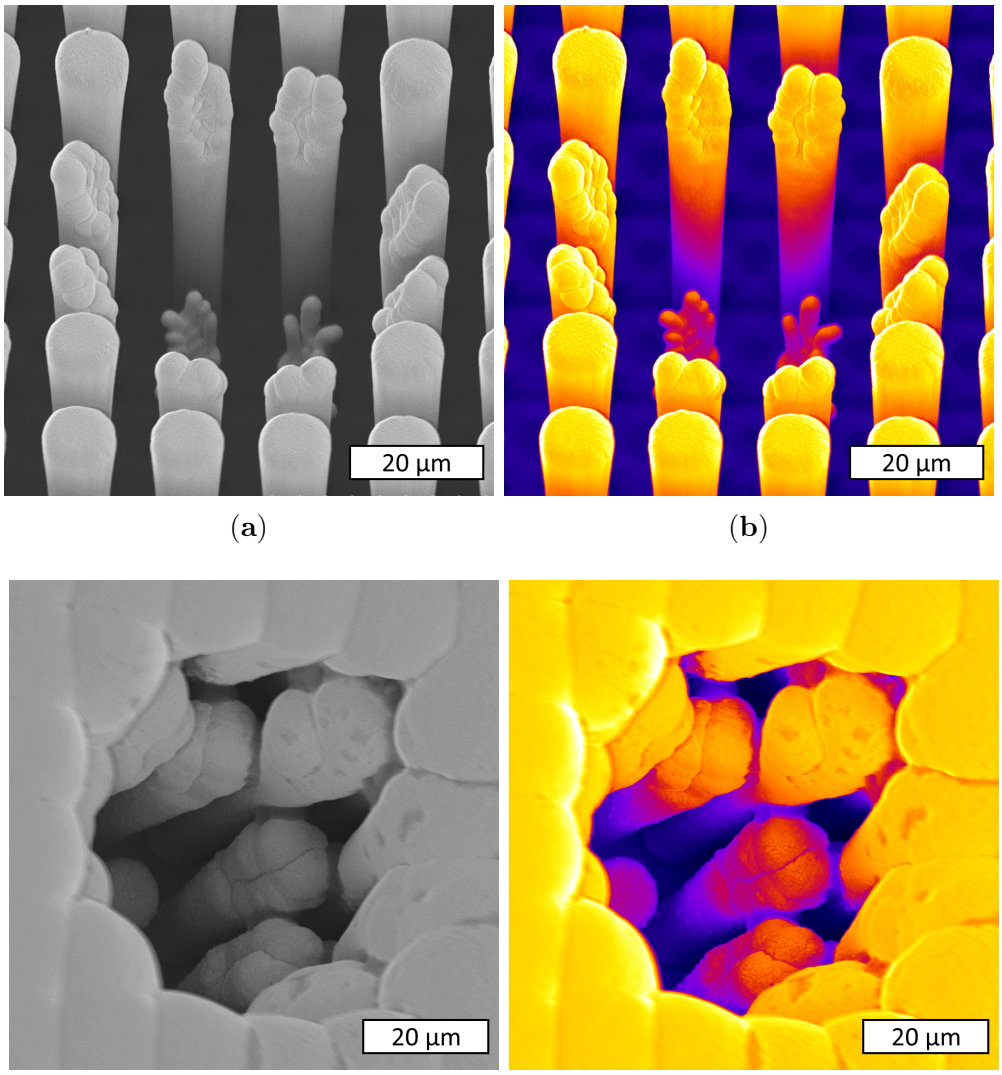
Figure 3.21: Schematic illustration of a high aspect ratio micropillar sputtered with gold. Multiple SEM images at various locations of the micropillar were taken, highlighting the sidewall quality and presence of the sputtered gold film.

3.5.4 Gold Electroplating

Following the non-conformal seed layer deposition onto the high aspect ratio structures using the sputtering tool, gold electroplating was performed using the Elevate Gold 7990 (from Technic Inc., USA). Electroplating was conducted with the solution warmed up to 49°C (121°F) and using a platinized titanium mesh anode kept 10 cm away from the sample. A constant current source was utilized to achieve the optimum current density of 3 mA/cm^2, resulting in a growth rate of around 100 nm/min. Intermittent electroplating was conducted to investigate the quality of electroplating for presentation purposes (schematic view of these steps are illustrated in Figure 3.20(c) to 3.20(e)).

During the intermittent electroplating process, multiple SEM images were taken to investigate the quality of plating and absorption part forming. Figure 3.22 and Figure 3.23 demonstrate high aspect ratio micropillars electroplated with gold at three different stages in gray tone and false color tone:

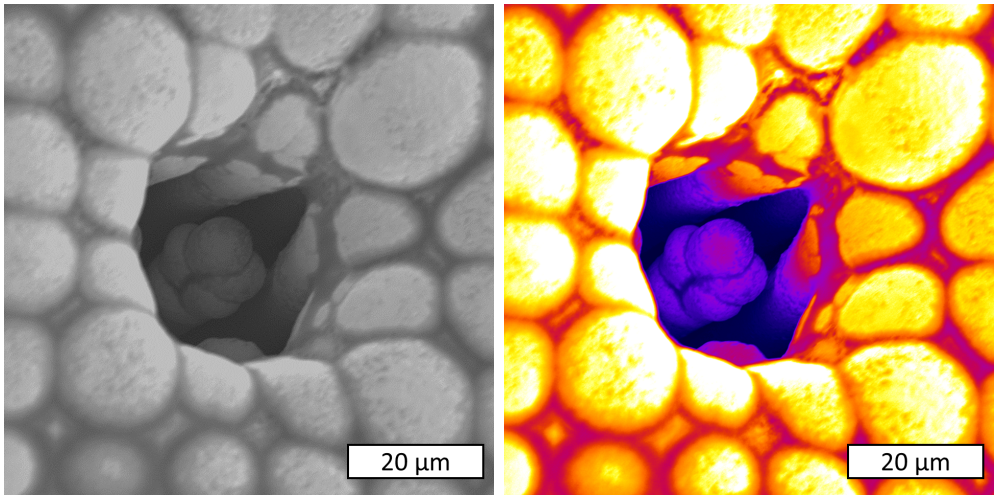
1. At the beginning of the electroplating (Figure 3.22a and 3.22b)
2. When the top parts of micropillars are sufficiently electroplated with gold (Figure 3.22c and 3.22d)
3. After micropillars are overplated (Figure 3.23a and 3.23b)



(**a**) (**b**)

(**c**) (**d**)

Figure 3.22: Illustration of SEM images of the fabricated micropillar-based X-ray absorption grating. (**a** and **b**) At the beginning of the electroplating, and (**c** and **d**) when the top parts of micropillars are sufficiently electroplated with gold.



(**a**) (**b**)

Figure 3.23: (**a** and **b**) Illustration of SEM images of the fabricated micropillar-based X-ray absorption grating with micropillars being overplated.

As evident in Figure 3.22 and Figure 3.23, because the gold seed layer was only on the top parts of micropillars, electroplating began from the same regions. The bottom parts of micropillars were buried under the electroplated parts, which obstructed the gold solution from reaching the bottom parts of micropillars (also illustrated in Figure 3.20e).

3.6 Results and Discussion

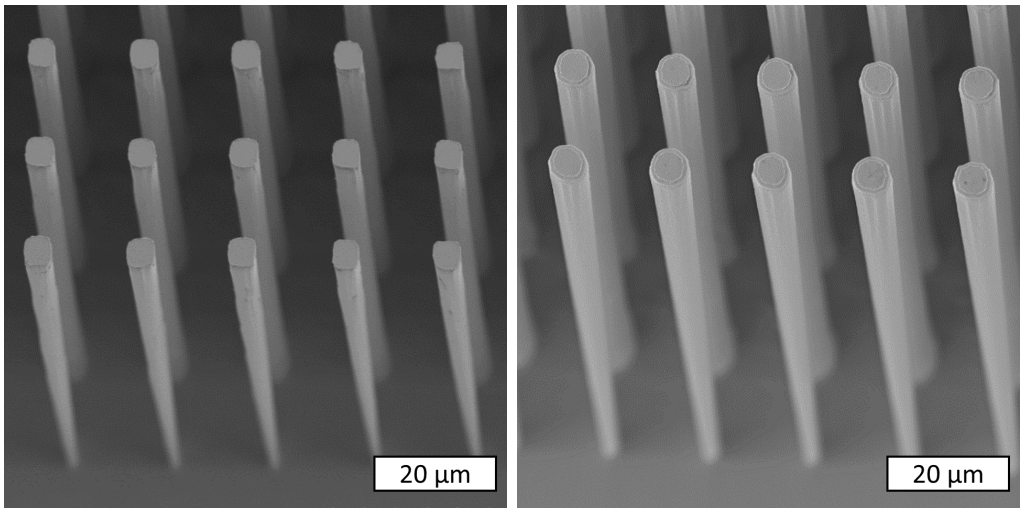
After successfully completing the characterization, we present the results of a prototype grating fabricated in silicon technology.

3.6.1 Fabricated Prototype Gratings

Even with an incomplete absorption region—caused by non-uniform seed layer deposition by gold sputtering—during the gold electroplating, high-resolution line as well as micropillar-based X-ray absorption grating were fabricated on a 4-inch silicon wafer. Four different gratings were designed and fabricated with two main active area sizes of 16 cm^2 (4 cm×4 cm) and 8 cm^2 (4 cm×2 cm). SEM images of patterns etched on the silicon wafer before and after performing gold electroplating are shown in Figure 3.24 and Figure 3.25 for

micropillars, and in Figure 3.26 for lines. Micropillars with a diameter of 4 μm, periodicity of 16.3 μm, and an aspect ratio of more than 40 were fabricated, which is illustrated in Figure 3.24a—the same results for line gratings are demonstrated in Figure 3.26a. During the intermittent gold electroplating to form the absorption part of the grating, multiple SEM images were taken to investigate the quality of electroplating and gratings, which are illustrated in Figure 3.24b and Figure 3.25a to 3.25d—the same results for line gratings are demonstrated in Figure 3.26b to 3.26d.

Although the reported fabrication process failed to completely fill the gaps between micropillars and form the required thickness of the absorption part, it simplified the high-resolution X-ray absorption grating fabrication by eliminating the need for sophisticated synchrotron facilities and atomic layer deposition (ALD) tools. We believe further research into performing sputtering with a tilted sample might improve the seed layer conformal deposition quality, which potentially leads to higher-quality absorption filling through the electroplating process. The Use of UV lithography, a simple photoresist hard mask for DRIE, and a sputtering tool facilitated the fabrication process and made it more affordable. The prototype version of the reported X-ray grating—presented in Figure 3.27—is tested in an XPCi application, the results of which are presented in the next chapters.



(**a**) (**b**)

Figure 3.24: Illustration of SEM images of the fabricated micropillar-based X-ray absorption grating. (**a**) After performing the Bosch DRIE, and (**b**) after conducting a short gold electroplating.

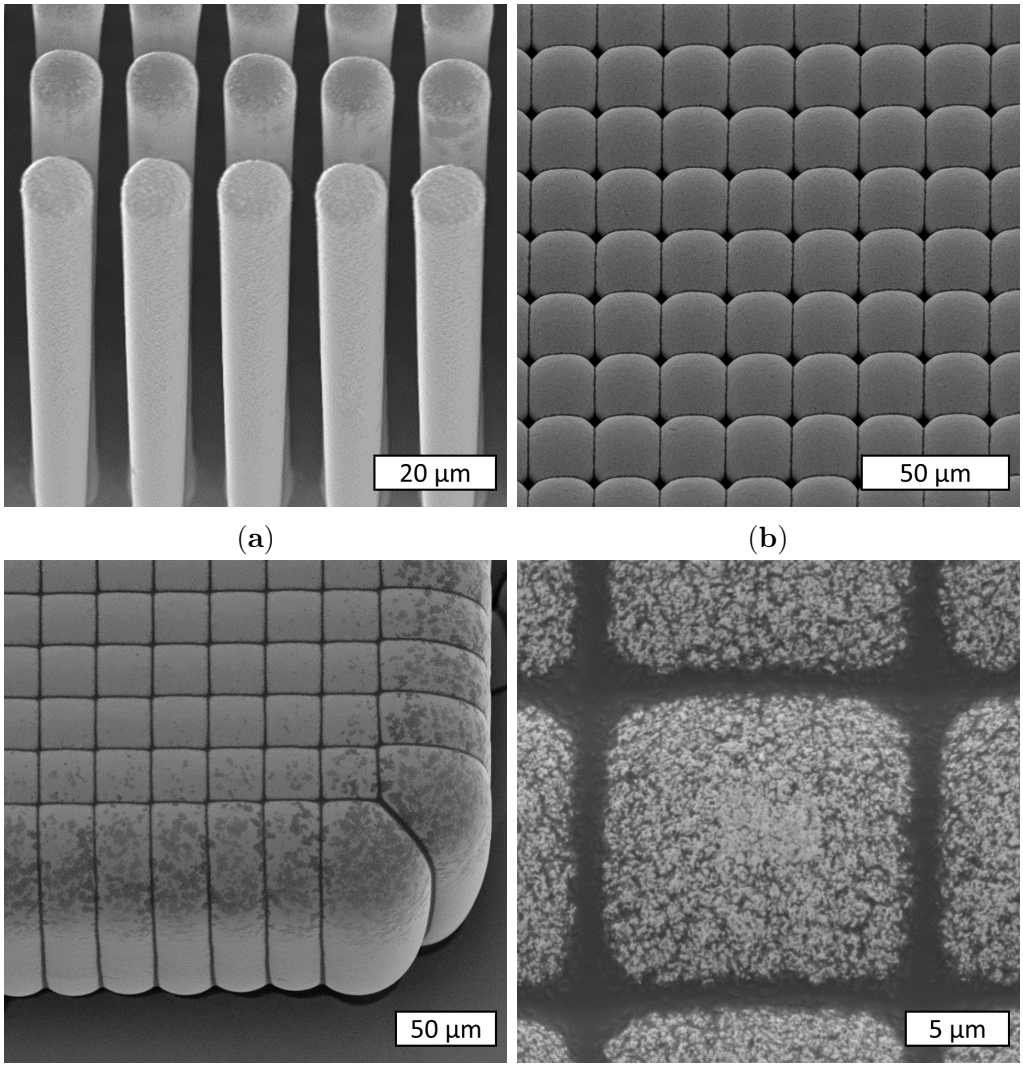


Figure 3.25: Illustration of SEM images of the fabricated micropillar-based X-ray absorption grating. (**a**) After longer gold electroplating, (**b**) when the top part of micropillars is almost overplated with gold, and (**c** and **d**) when micropillars are completely overplated.

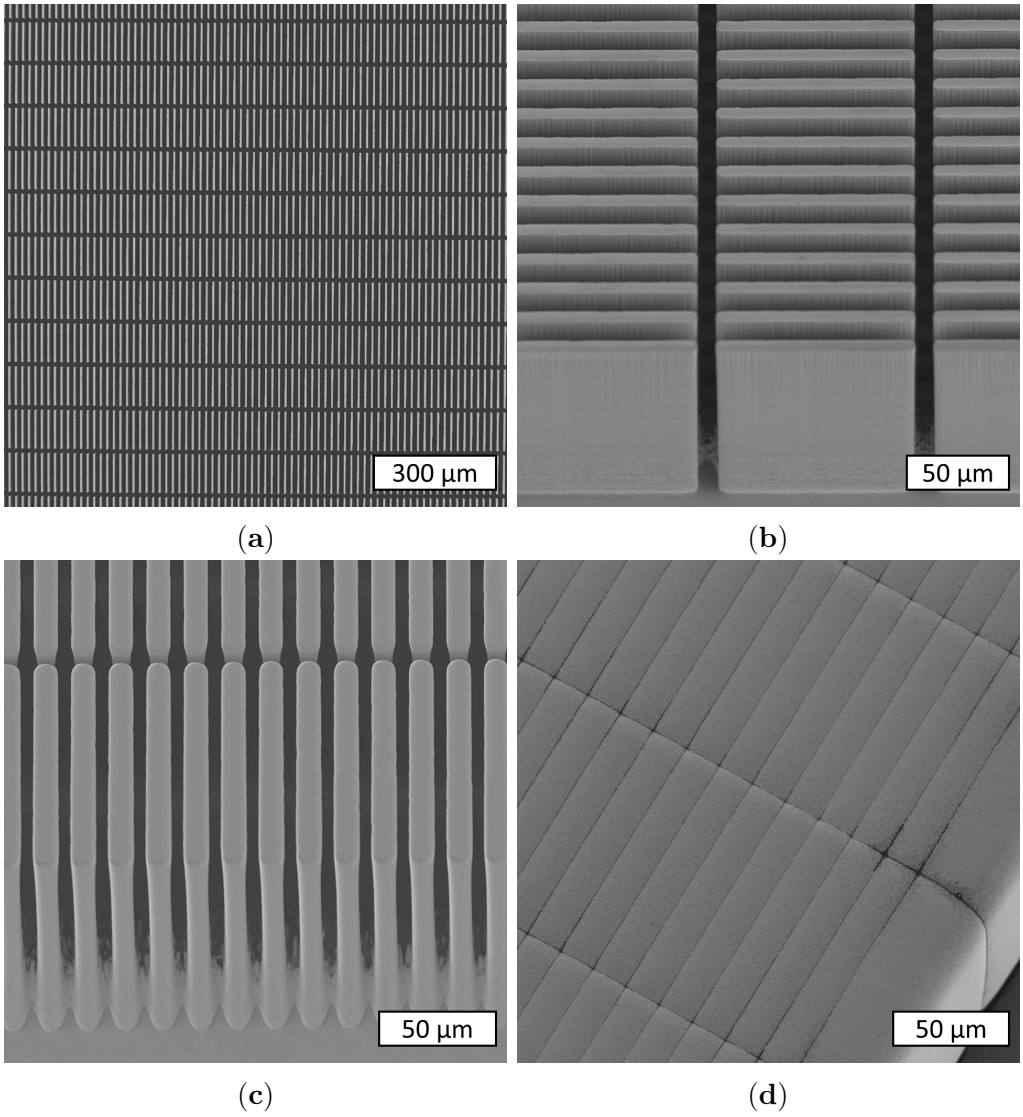


Figure 3.26: Illustration of SEM images of the fabricated line X-ray absorption grating. (**a**) After performing the Bosch DRIE, (**b**) after conducting a short gold electroplating, (**c**) after longer gold electroplating, and (**d**) the top view with the top part of line structures fully electroplated with gold.

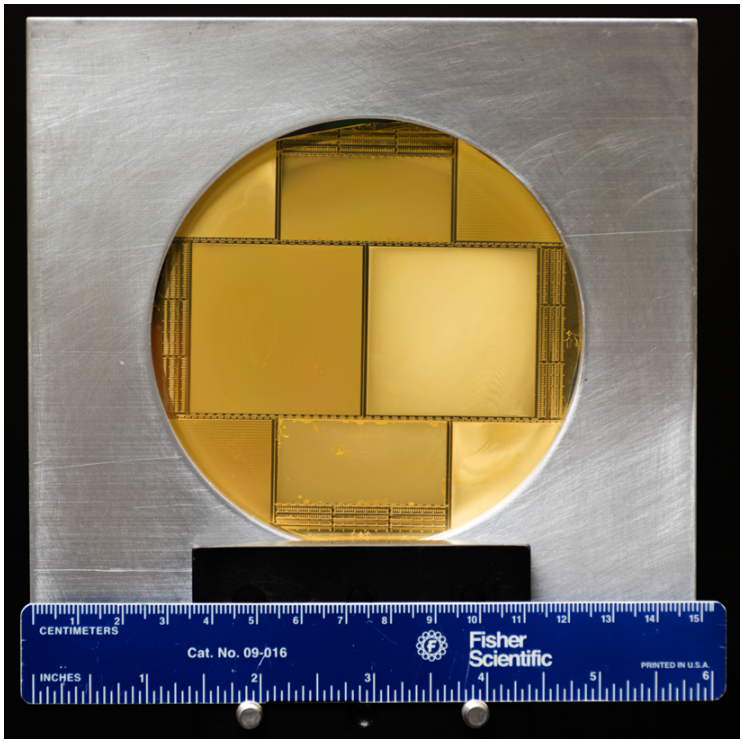


Figure 3.27: Photo of the fabricated silicon-based X-ray absorption gratings mounted on an aluminum holder.

3.6.2 X-ray Projection Image

To measure the X-ray properties of the prototype X-ray absorption granting, X-ray projections of the gratings had to be taken with no object introduced to the system. Figure 3.28 demonstrates the X-ray setup used to take X-ray projections of gratings. We used a 3D X-ray Microscope, inCiTe™ (from KA Imaging, Waterloo, ON, CA), which utilizes a tungsten target Hamamatsu polychromatic microfocus X-ray source L12531 along with a 4K×4K high-resolution X-ray detector with 8 μm pixel size—the BrillianSe™ X-ray detector [52,74]. Imaging was performed with a source-to-grating distance (d_{sg}) of 10 cm and a grating-to-detector distance (d_{gd}) of 35 cm. Figure 3.29 illustrates the X-ray projection of a grating with micropillars with a diameter of 4 μm and periodicity of 16.3 μm, while the polychromatic microfocus X-ray source was working at 60 kV_p and 200 μA.

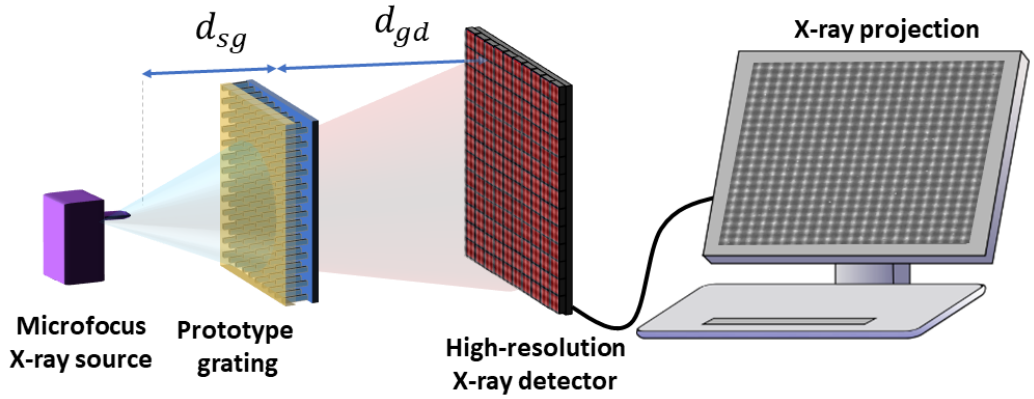


Figure 3.28: Schematic illustration of the X-ray projection setup consisting of a microfocus X-ray source, the prototype silicon-based X-ray absorption grating, a high-resolution X-ray detector, and a post-processing unit to demonstrate the X-ray image.

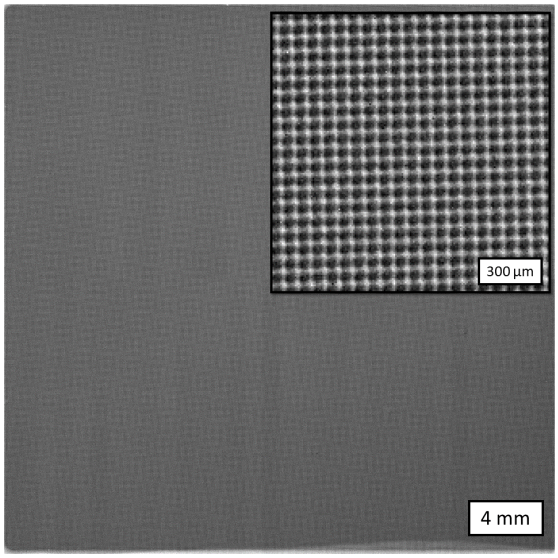


Figure 3.29: Illustration of the X-ray projection of the micropillar-based X-ray grating with a magnified image inset to show the resolution of micropillars' projection on the detector.

A full X-ray transmission of the prototype silicon-based X-ray absorption grating is presented in Figure 3.30. There are some non-uniformities in the fabricated grating, mainly stemming from the electroplating process.

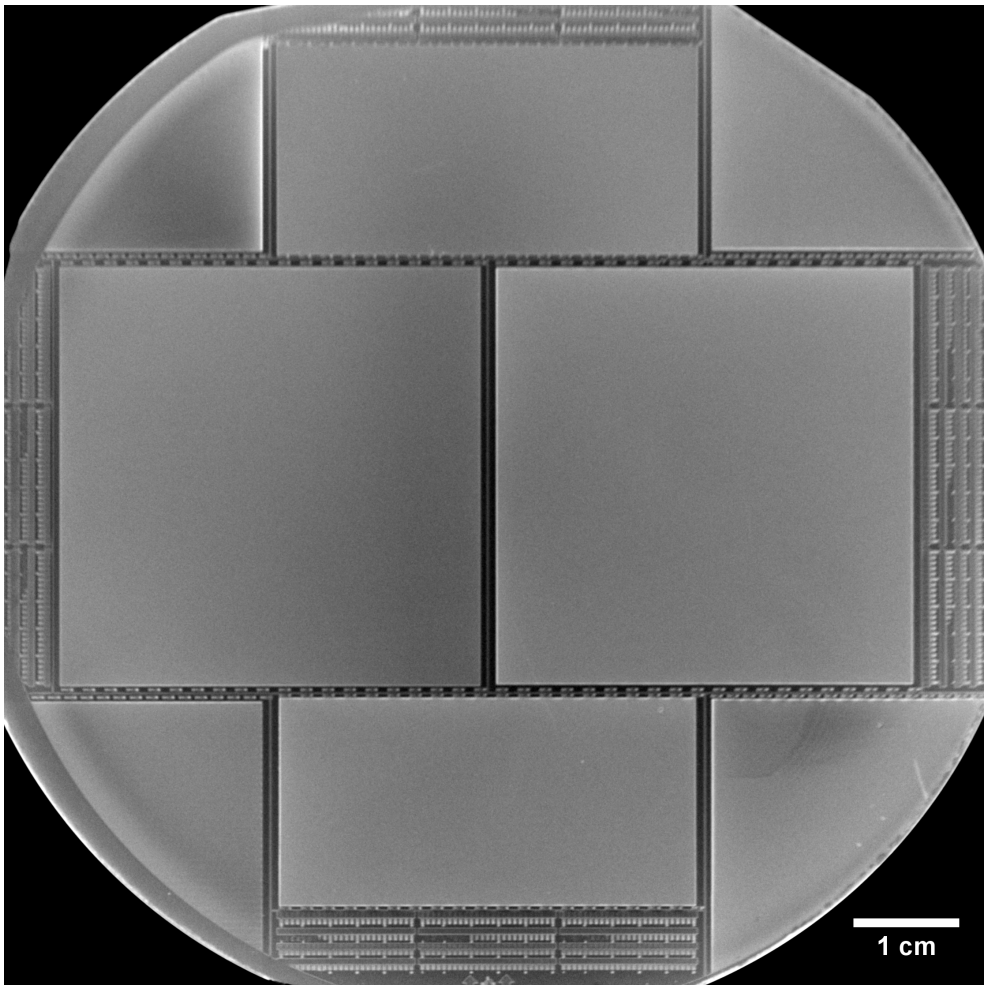
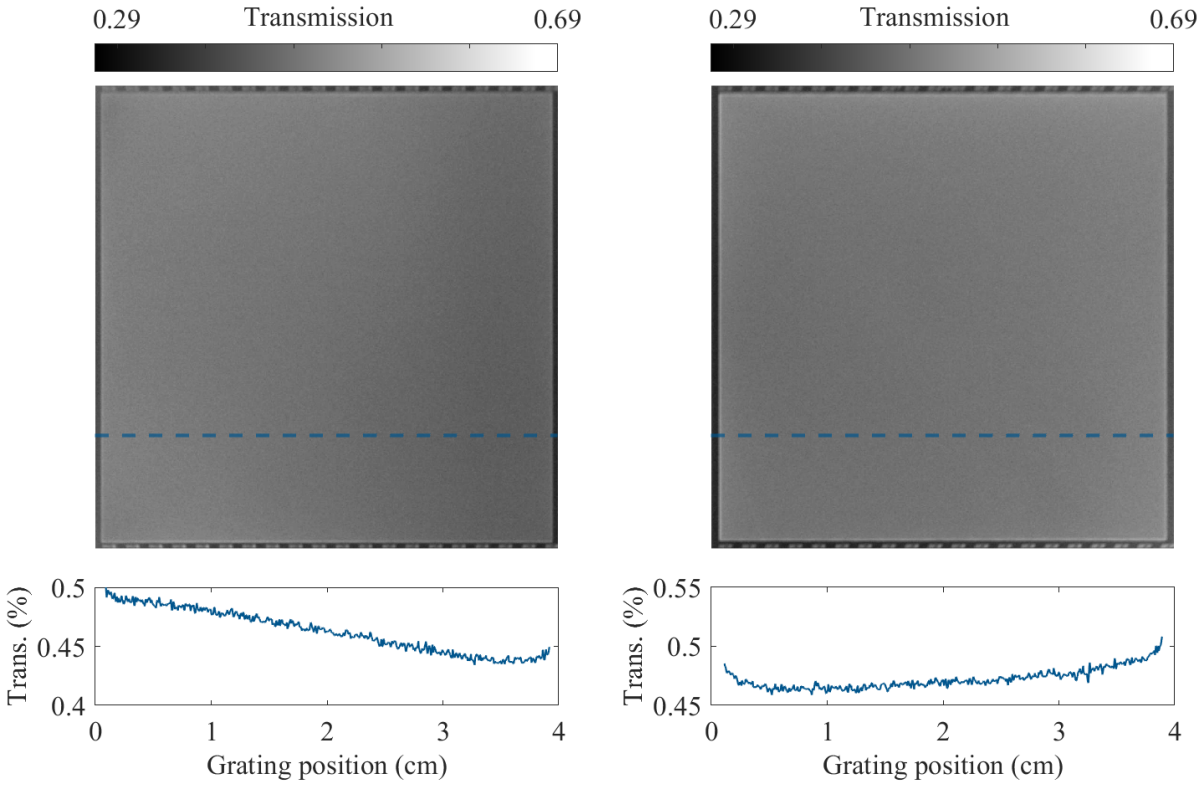


Figure 3.30: A full X-ray transmission image of the fabricated silicon-grating.

Transmission images for the 4 cm×4 cm line grating and the 4 cm×4 cm micropillar grating are illustrated in Figure 3.31. A cross-sectional profile across the dashed blue line in each figure represents the transmission value for the corresponding grating.

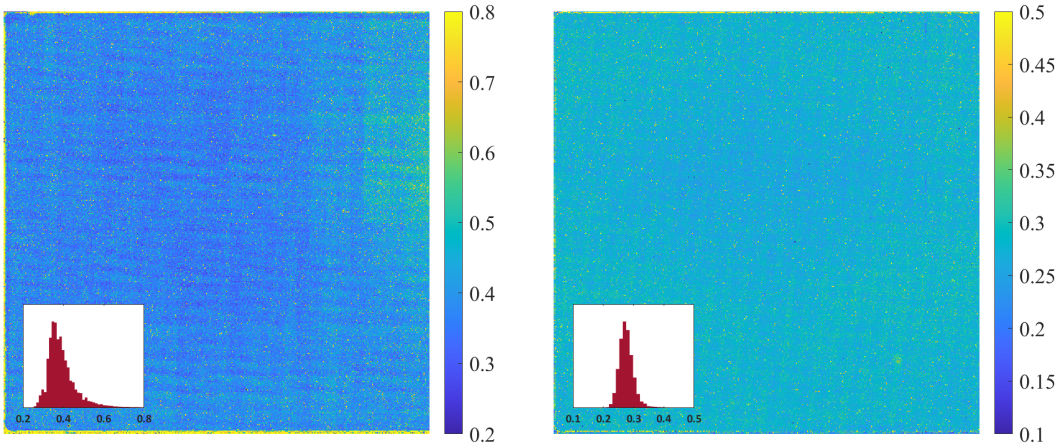


(**a**) (**b**)

Figure 3.31: Transmission map of (**a**) a line and (**b**) a micropillar-based X-ray absorption grating. The transmission value across the blue dashed line is also presented under each transmission map.

3.6.3 Visibility, Transmission, and Absorption Characteristics of the Prototype Gratings

Visibility – an indicator of how sharply the grating-based XPCi system can reveal the details – is one of the merits in quantifying the quality of an X-ray absorption grating. X-ray absorption grating visibility is calculated based on the X-ray projection—with no object defined—following the same equation described in Equation. 2.15. We measured the silicon-based X-ray absorption grating visibility at various X-ray working potentials from 40 kV_p to 90 kV_p—illustrated in Figure 3.32 and Figure 3.33. Moreover, we also measured the transmission and absorption of the prototype grating—demonstrated in Figure 3.34—to investigate the quality of grating in absorbing X-ray photons at various X-ray energies (despite the incomplete electroplating process and absorption region). All the aforementioned parameters were measured for a micropillar-based grating with micropillars with a diameter of 4 μm and periodicity of 16.3 μm, with the same setup and geometrical distances used for the X-ray projection imaging in the previous section. In spite of the incomplete electroplating process for forming the absorption region, the visibility, transmission, and absorption characteristics show promising results for employing this prototype grating in XPCi application—which is presented in the next chapters.



(**a**) (**b**)

Figure 3.32: Illustration of the visibility maps of the fabricated silicon-based micropillar X-ray grating using a polychromatic microfocus X-ray source with the current of 200 μA and working potential of (**a**) 40 kV_p, and (**b**) 50 kV_p; all the insets are visibility histograms with their peaks representing the grating visibility of the X-ray source energy at the source working potential. The 3D X-ray Microscope, inCiTe™ (from KA Imaging, Waterloo, ON, CA) was employed for this measurement.

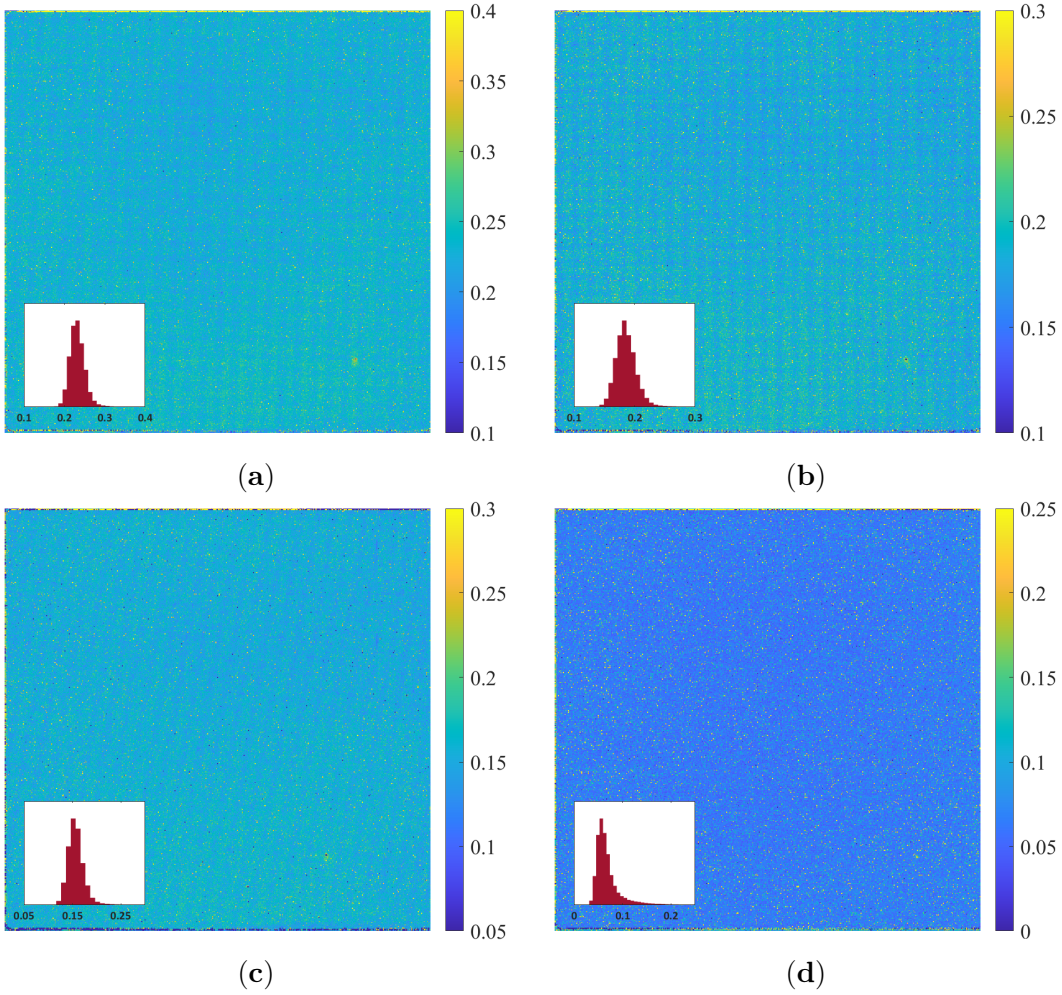
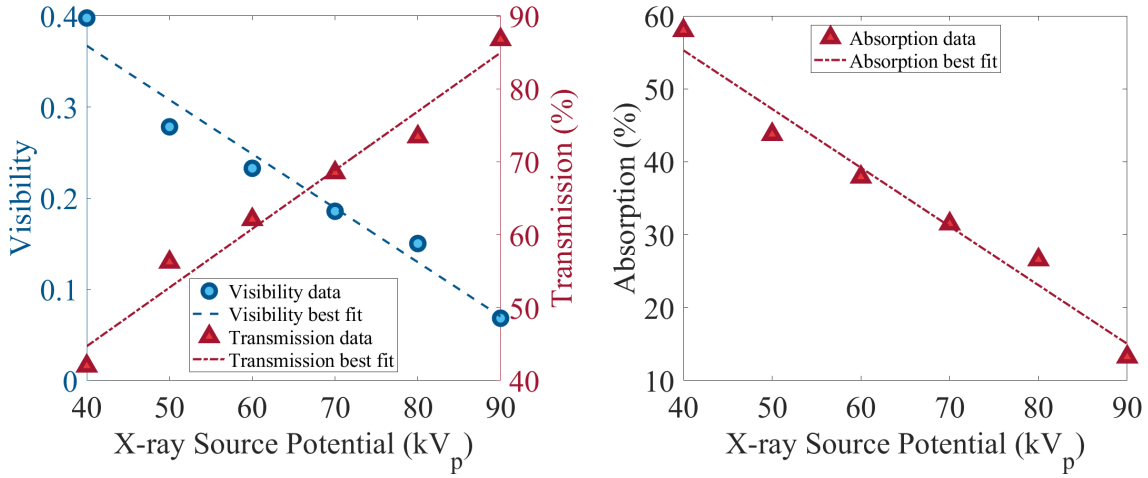


Figure 3.33: Illustration of the visibility maps of the fabricated silicon-based micropillar X-ray grating using a polychromatic microfocus X-ray source with the current of 200 μA and working potential of (**a**) 60 kV_p, (**b**) 70 kV_p, (**c**) 80 kV_p, and (**d**) 90 kV_p; all the insets are visibility histograms with their peaks representing the grating visibility of the X-ray source energy at the source working potential. The 3D X-ray Microscope, inCiTe™ (from KA Imaging, Waterloo, ON, CA) was employed for this measurement.



(**a**) (**b**)

Figure 3.34: Visibility, transmission, and absorption characteristics of the silicon-based micropillar X-ray grating versus various X-ray source potentials.

3.7 Conclusion

In this chapter, we investigated the fabrication of high-resolution higher aspect ratio X-ray bridge-assisted micropillar 2D absorption gratings in silicon technology using the Bosch deep reactive ion etching (DRIE) method. To the best of our knowledge, this is the first report of a bridge-assisted 2D micropillar X-ray grating. Such fine-tuned gratings are valuable for high-resolution, high-energy, and compact grating-based XPCi systems. This chapter also investigated the possibility of utilizing sputtering tools for seed layer deposition—required for electroplating to form the absorption region of gratings—as an alternative to expensive atomic layer deposition (ALD) tools. Although the results of the seed layer deposition via gold sputtering did not show an acceptable conformal coverage on the high aspect ratio feature of silicon wafers, the fabricated prototype gratings are promising for multi-modal information extraction in single-mask XPCi systems. We believe further research in employing sputtering tools with tilted samples might help improve the deposition of the seed layer with a more conformal coverage on silicon-based high-resolution high aspect ratio features for X-ray absorption grating fabrication, which potentially decreases the cost and complexity of grating fabrication.

This chapter partially fulfilled the second objective of the thesis, namely developing a scalable, large-area, fabrication process for a high-resolution, high aspect ratio X-ray grating for large area X-ray imaging applications.

Chapter 4

Self-Aligned Multi-Layer Grating Fabrication

X-ray phase-contrast (XPCi) imaging methods are an emerging medical imaging approach that provides significantly better soft tissue contrast and could function as a viable extension to conventional X-ray, CT, and even some MRI. Absorption gratings play a central role in grating-based XPCi systems especially because they enable the acquisition of three images in a single exposure: transmission, refraction, and dark-field. An impediment to commercial development and adoption of XPCi imaging systems is the lack of large area, high aspect ratio absorption gratings. Grating technology development, primarily due to technological limitations, has lagged system development and today prevents the scaling up of the XPCi system into a footprint and price point acceptable to the medical market.

This chapter tackles the second objective of the thesis, by focusing on advancing and simplifying the fabrication process of scalable high-resolution high aspect ratio X-ray absorption gratings for large area imaging applications through a low-cost high throughput method. In this chapter, we report on a self-aligned multi-layer grating fabrication process that can enable large-area X-ray absorption gratings with micron-scale feature sizes. We leverage large-area fabrication techniques commonly employed by the thin-film transistor (TFT) display industry. Conventional ITO-on-glass substrates are used with a patterned film of Cr/Au/Cr that serves as a self-aligned lithography mask for backside exposure. Commonly available SU-8 photoresist is patterned using the backside exposure mask followed by an electroplating step to fill the gaps in the SU-8 with X-ray attenuating material. Consequently, the electroplated patterned material acts as a self-aligned photomask for subsequent SU-8 layer patterning and so forth. The repeatability of the reported process makes it suitable for achieving higher aspect ratio structures and is advantageous over

previously reported X-ray LIGA approaches.

The contributions reported in this chapter, the scalable and cost-effective approach to building larger area high-resolution high aspect ratio X-ray gratings, can help expedite the commercial development and adoption of previously reported Talbot-Lau, coded-aperture, as well as speckle-tracking XPCi systems for large area clinical and industrial applications. We demonstrate the results of a prototype three-layer X-ray absorption grating with an absorber thickness of around 40 μm, a visibility of 0.28 at 60 kV_p, and a 70 mm $\times$ 70 mm active area that is fabricated on a 4-inch glass substrate, by modifying a commercially available 3D propagation-based XPCi X-ray Microscope.

4.1 Introduction

X-ray phase-contrast is a relatively new X-ray imaging method that provides greatly improved soft-tissue visualization with X-ray, making it a potential extension to conventional X-ray imaging systems as an alternative to expensive and bulky CT and MRI [1, 2]. Applications that are enabled by X-ray phase-contrast imaging (XPCi) span many fields from industry and science to medicine and biology [3, 6, 11, 59]. Among various techniques developed to realize XPCi, Talbot-Lau [16], speckle-tracking [24], and coded-aperture (edge-illumination) [23] all use X-ray absorption gratings. These techniques can provide higher contrast and sensitivity compared to the PB-XPCi technique. Grating-based XPCi techniques can potentially provide three images for each single exposure: transmission (absorption), refraction (phase), and dark-field (small angle scattering) [20, 22]. The single-exposure grating-based XPCi techniques increase the imaging dose efficiency while shortening the imaging time—compared to multi-exposure stepping or scanning methods. The additional images—phase and scattering—help further quantify object characteristics beyond conventional attenuation X-ray imaging. X-ray absorption gratings are typically fabricated using high aspect ratio X-ray absorber structures to transform incoming X-rays into individual beamlets. Any imperfection in the fabrication process directly affects the final image quality, leading to image artifacts, inconsistencies, and/or loss of image quality and detail [29, 30, 74].

Additional challenges for grating fabrication include higher resolution, higher energies, and larger field of view. For example, high resolution X-ray detectors are necessitated by some clinical, material science, and industrial inspection applications [46, 48, 49, 51, 52, 74]. Higher resolution applications require periodic gratings with a high aspect ratio for structures in the micron-scale range to absorb X-ray photons and create fine beamlets. Furthermore, applications requiring higher X-ray energies require even higher aspect ratios

and critically larger field-of-view (FOV) – the FOV in most diagnostic medical and security applications is large, usually exceeding 30 cm × 30 cm [54–58].

Several methods have been explored for high aspect ratio X-ray grating fabrication that can be categorized based on either etching or molding techniques. The former is usually conducted on silicon wafers through anisotropic etching techniques such as metal-assisted chemical etching [31, 33], plasma etching [34, 36, 38], or wet etching [40, 41]. Although silicon-based etching can achieve high aspect ratio structures, fabrication is limited to standard wafer sizes. While tiling and stitching smaller gratings to achieve a larger grating is an option [113,114], it is challenging to overcome tiling gaps for emerging high-resolution applications enabled by new micron-scale pixel pitch X-ray detectors [52, 74].

A widely used method for fabricating high aspect ratio microstructures is the LIGA process – lithographie, galvanoformung, abformung or alternately lithography, electroplating, and molding [42–44]. Lithography methods used in the LIGA process are either based on UV or X-ray. Although the X-ray LIGA process results in high aspect ratio structures [86], the method requires specialized X-ray sources with highly specific beam characteristics. Moreover, fabrication of large-area gratings in X-ray LIGA is challenging due to the limited size of the X-ray beam – typical device area fabricated in X-ray LIGA is less than 4-inch square [115,116]. On the other hand, conventional UV-LIGA [117] is unable to obtain the high aspect ratios of X-ray LIGA because of the drawbacks of UV lithography, i.e., the diffraction of UV light as it travels away from the photomask into the resist.

UV LIGA is a well-established, mature, process where large-area scaling challenges are well-understood and already resolved in the industry, such as fabrication of liquid crystal display (LCD) thin-film transistor (TFT) [118,119]. LCD-TFT technology can be scaled in size – in UV LIGA – as evidenced by large area flat panel television sets. While wafer scale gratings are limited to standard wafer sizes, LCD-TFTs are fabricated on meter-sized glass substrates and are already widely used for large area diagnostic X-ray imaging. UV lithography lamps can uniformly expose areas approaching 1 m×1 m using industry-standard step and repeat processes for large area display manufacturing [120,121]. Moreover, such an approach can also piggyback on ongoing advances in large-area electronics fabrication technology including emerging flexible substrate fabrication processes and improved sensor integration.

LIGA hinges upon creating resist molds – such as with SU-8 – and conducting electroplating to form the absorption part of X-ray absorption gratings. SU-8 is a negative epoxy resist [122] that has been employed to fabricate numerous micro-electromechanical systems (MEMS) such as optical devices, micro-fluidic channels, lab-on-chip devices, and passivation layers [123–126]. Moreover, SU-8 films exceeding 1 mm thickness have been patterned using UV exposures [127–129] in UV LIGA. One of the well-known properties

of SU-8, which makes it a suitable candidate for 3-D processing in MEMS, is its multi-layer coating compatibility [130–133]. SU-8 has been widely used in both X-ray and UV-LIGA techniques for X-ray absorption grating fabrication, but its multi-layer capability has never been reported for grating fabrication.

The dissertation research presented in this chapter explores an alternative to tiling silicon wafers to obtain a large area X-ray grating by leveraging widespread LCD-TFT fabrication technology. The process we report uses both SU-8 and the UV-LIGA process to stack multiple layers of lower aspect ratio grating structures to achieve a high-resolution and potentially a higher aspect ratio structure than reported to date with standard UV-LIGA techniques. UV lithography is widely available and cost-effective, and using the multi-layer approach described in this work to overcome its shortcomings is the primary technique used to achieve large-area, high-resolution gratings.

4.2 Adhesion of SU-8 to Gold Thin Film

SU-8 is valued in MEMS fabrication due to its excellent mechanical and optical properties. For fabricating X-ray absorption grating following the MEMS process, gold is the material most widely used to stop incident X-rays. One of the main bottlenecks in fabricating a quality X-ray absorption grating is the adhesion between SU-8 molds to gold. The poor adhesion of SU-8 to gold and the internal high level of stress of SU-8 during baking steps lead to SU-8 molds delaminating, cracking, or peeling off during developing or electroplating steps [134–136]. This problem becomes even more challenging when a larger SU-8 film is coated for fabricating greater field-of-view gratings. Employing SU-8 on gold-coated substrates requires an adhesion layer—as schematically illustrated in Figure 4.1—to assure the SU-8 mechanical stability during fabrication steps, without which realizing high-quality grating is pretty challenging. In this section, we have qualitatively investigated the adhesion of SU-8 to gold thin film for different adhesion promoters.

4.2.1 Investigating the Adhesion Quality

Fabrication of X-ray absorption gratings can be broken into two main steps: creating free-standing molds, and performing metal electroplating to fill the gaps between the molds. Gold is usually utilized as an X-ray absorber, as it possesses a high atomic number in stopping high-energy X-ray photons and is a well-defined metal widely used in microfabrication processes. Gold electroplating requires a seed layer, which is typically either a thin film of platinum or gold. In either case, SU-8 molds should stand alone on this seed layer

during the fabrication steps. To improve the adhesion quality of SU-8 to gold thin film, we investigated the following three different adhesion promoters:

(i) Hexamethyldisilazane (HMDS).

(ii) OmniCoat.

(iii) 3-(Trimethoxysilyl)propyl methacrylate (MPTS).

We began the fabrication process by dicing a p-type $< 100 >$ silicon wafer into 20 mm×20 mm dies and thoroughly cleaning them through RCA-1 and RCA-2 processes. Chromium (Cr) and gold (Au) thin films were deposited onto the clean silicon samples through a thermal evaporation process using an Intlvac Thermal Evaporator (Intlvac Inc., CA) at room temperature without breaking the vacuum—with the thickness of Cr and Au layers being 5 nm and 100 nm, respectively. The Cr layer ensured the adhesion between Au and the silicon substrate.

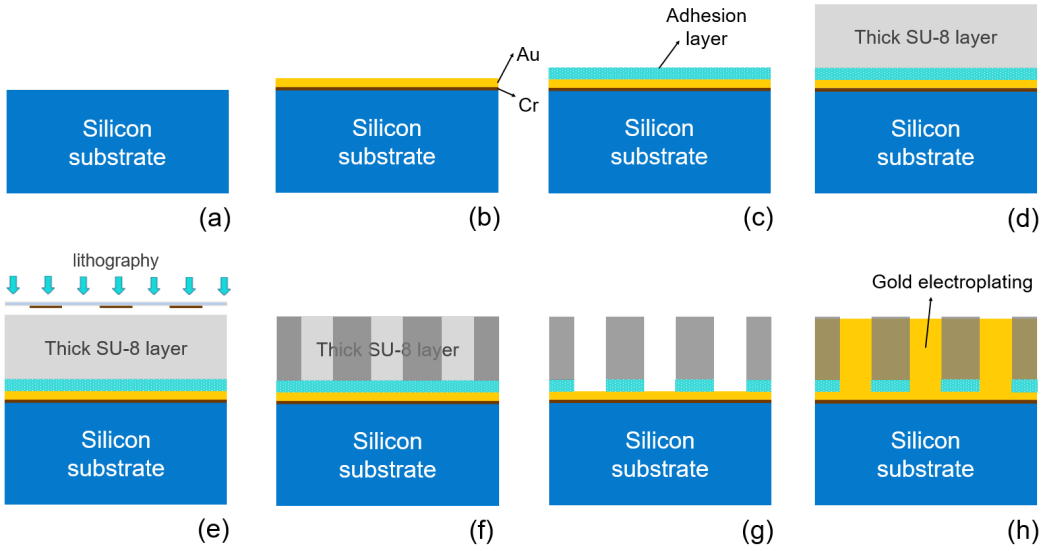


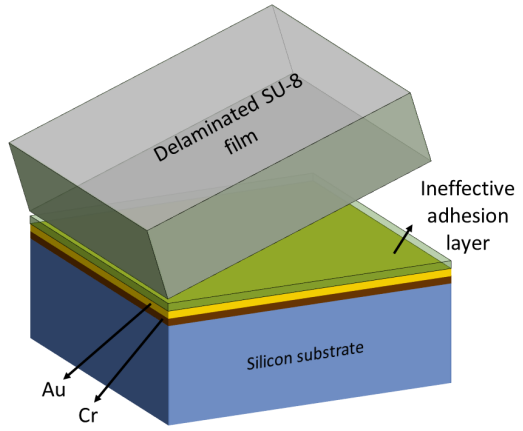
Figure 4.1: A general process flow for fabricating X-ray absorption gratings: (**a**) cleaning the Si wafer, (**b**) deposition of Cr/Au thin films, (**c**) definition of an adhesion layer, (**d**) spin coating the thick SU-8 layer,(**e**) lithography and pattern transfer through a photomask, (**f**) post exposure baking, (**g**) developing uncrosslinked SU-8 regions, and (**h**) Au electroplating to fill the gaps.

Hexamethyldisilazane (HMDS)

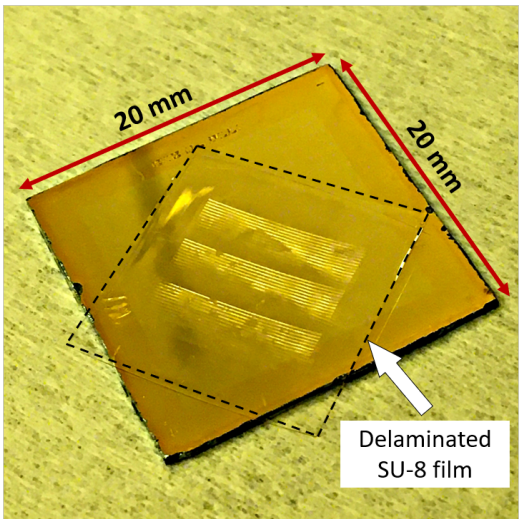
HMDS is one of the adhesion promoters with dissensus on whether it improves the adhesion between SU-8 and noble metals like gold or not. We, however, decided to examine its effectiveness through the spin-coating application of HMDS. Silicon samples were first dehydrated by putting them on a hot plate—(from Torrey Pines Scientific, USA)—set at 150℃ for 15 minutes and then cleaned with N_2. HMDS was then spin coated on the Cr/Au coated silicon samples at 4000 rpm for 30 seconds and was baked at 150℃ for 15 minutes. Following the HMDS application, SU-8 2015 was spin coated onto the samples at 500 rpm for 5 seconds followed by 3500 rpm for 60 seconds and were soft baked at 95℃ for 5 minutes. Lithography was performed using a chromium-patterned glass-based photomask and a Karl Suss MA6 Mask Aligner (SUSS MicroTec Group, Garching, Germany). Post-exposure bake was performed the same as soft bake, for 5 minutes at 95℃, and samples were developed in SU-8 developer—commercially known as 1-Methoxy-2-Propanol Acetate (Kayaku Advanced Materials, USA)— for 3 minutes, until the uncrosslinked features were completely developed. Samples were soaked in isopropyl alcohol (IPA) for 10 seconds, rinsed with DI water, and dried with N_2 gas. Most of the samples treated with HMDS did not last until the end of the developing process, and they completely delaminated during the developing step, as demonstrated in Figure 4.2.

OmniCoat

The commercially available adhesion promoter, OmniCoat, from Kayaku Advanced Materials (Kayaku Advanced Materials, USA) was also tested for its effectiveness in improving the adhesion of SU-8 to the gold thin film. OmniCoat was spin coated on Cr/Au deposited silicon samples—dehydrated following at 150℃ for 15 minutes— at 4000 rpm for 60 seconds and baked at 200℃ for 1 minute. After cooling down to room temperature, samples were spin coated with SU-8 2015 at 500 rpm for 5 seconds and 3500 rpm for 60 seconds, followed by a soft bake at 95℃ for 5 minutes. Grating pattern transfer was conducted through the same photomask and UV lithography technique—using MA6 mask aligner—followed by the post-exposure bake for 5 minutes at 95℃. Samples were developed in the SU-8 developer until the uncrosslinked regions were completely dissolved in the developer—for about 3 minutes. For OmniCoat-treated samples, as same as HMDS-treated ones, most of the SU-8 films delaminated during the developing process, an indication of weak adhesion strength between the SU-8 film and the OmniCoat-treated gold thin film.



(**a**)



(**b**)

Figure 4.2: (**a**) Schematic illustration of a delaminated SU-8 film with an ineffective adhesion layer application. (**b**) SU-8 film delaminated from the HMDS-treated gold-coated silicon substrate.

3-(Trimethoxysilyl)propyl methacrylate (MPTS)

MPTS (from Sigma-Aldrich, USA), as the third adhesion promoter, was investigated in this work to improve the SU-8 to gold thin film adhesion quality. It has been previously

reported that Cr/MPTS combination improves the adhesion of SU-8 to gold thin film [135], however, we began examining its effectiveness by using MPTS in various combinations to reach a strong adhesion quality. MPTS was applied through the liquid treatment [137]—to form a monolayer on the samples—as follows:

(a) Silicon samples—deposited with C/Au—were thoroughly cleaned and dehydrated at 150℃ for 15 minutes.

(b) 1 mL of MPTS was diluted in 200 mL of ethanol, and just before use, 6 mL of acetic acid (1:10 glacial acetic acid:DI water) was added to the solution.

(c) Samples were soaked into the solution, or the solution was poured onto samples and allowed to react for approximately 3 minutes.

(d) Samples were then rinsed with ethanol to remove the residual reagent and allowed to dry thoroughly.

We also tested applying MPTS adhesion promoter via spin coating samples with 8% MPTS diluted in acetone (8:100 MPTS:acetone) at 3000 rpm for 30 seconds and allowing them to dry. Albeit the output of applying diluted MPTS via the spin coating method looked almost the same as liquid treatment, spin coating methods typically result in multilayers of adhesion promoter coating—several nanometers—rather than a monolayer—which the liquid treatments claim to achieve.

Table 4.1 summarizes various adhesion promoters (and their combinations) investigated for the adhesion quality of SU-8 to gold thin film. An adhesive tape test and an acidic electroplating solution were examined to evaluate the adhesion quality and ensure its strength. For the adhesive tape test, both Scotch tape and Kapton tape were utilized, and for electroplating, we used an indium plating solution—with a pH of 1.5—as an acidic environment. Figure 4.3 is an SEM image of a delaminated SU-8 film from the gold thin film, and Figure 4.4 demonstrates the adhesive tape test results when a poor adhesion layer was used.

Table 4.1: List of various adhesion promoters—and their combinations—and the result of adhesion quality during the developing process, through tape test, and under a harsh acidic electroplating process condition.

Adhesion layer	**During developing**	**Tape test**	**Electroplating**
HMDS	Delaminated	-	-
OmniCoat	Delaminated	-	-
MPTS	✓	Delaminated	-
Cr/MPTS	✓	Partially Delaminated	-
Cr/MPTS/SU-8 2000.1	✓	✓	✓

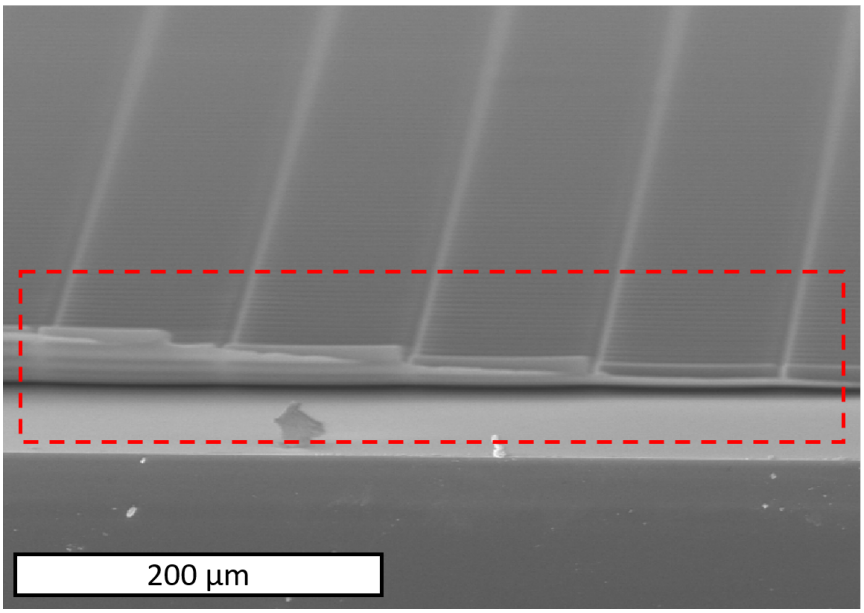


Figure 4.3: Demonstration of an SEM image of a delaminated SU-8 film from a gold substrate – without any adhesion layer.

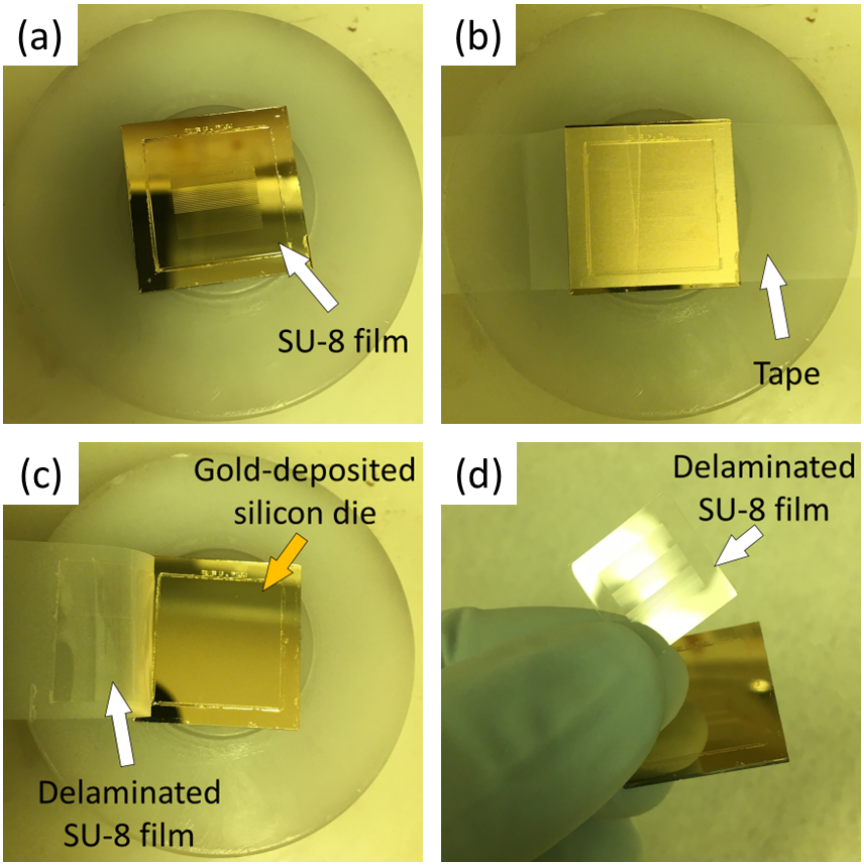


Figure 4.4: Demonstration of adhesive tape test to investigate the quality of adhesion promoter employed between SU-8 film and gold thin film with (**a**) the sample being fixed, (**b**) a strip of adhesive tape applied across the sample onto the SU-8 film, and (**c**) tape peeled off. (**d**) Illustration of SU-8 film delaminated from the substrate during the developing step.

Figure 4.5 is a schematic illustration of a process flow to fabricate an X-ray absorption grating, where the adhesion layer helps keep the thick SU-8 film attached to the substrate. To improve the adhesion quality of SU-8 to the gold thin-film, we utilized a combination of a thin film of chromium atop the gold thin film, a mono-layer of MPTS (from Sigma-Aldrich, USA), and a thin layer of SU-8. The top chromium thin film on the gold also protects the gold film from contaminating the reactive ion etching (RIE) chamber during the etching process – which will be explained later – and keeps the gold film intact for the electroplating step. The mono-layer MPTS on chromium thin film was formed through

the liquid treatment step prior to the definition of a thin layer of SU-8. We made a thin layer of SU-8 by diluting SU-8 2015 with Cyclopentanone (from Sigma-Aldrich, USA) – known as SU-8 thinner – to achieve the desired thin SU-8, which we will call this layer as SU-8 base layer hereafter. A 500 nm thin SU-8 base layer was spin coated followed by a soft bake step at 65℃ for 60 minutes through a ramping up (from room temperature)

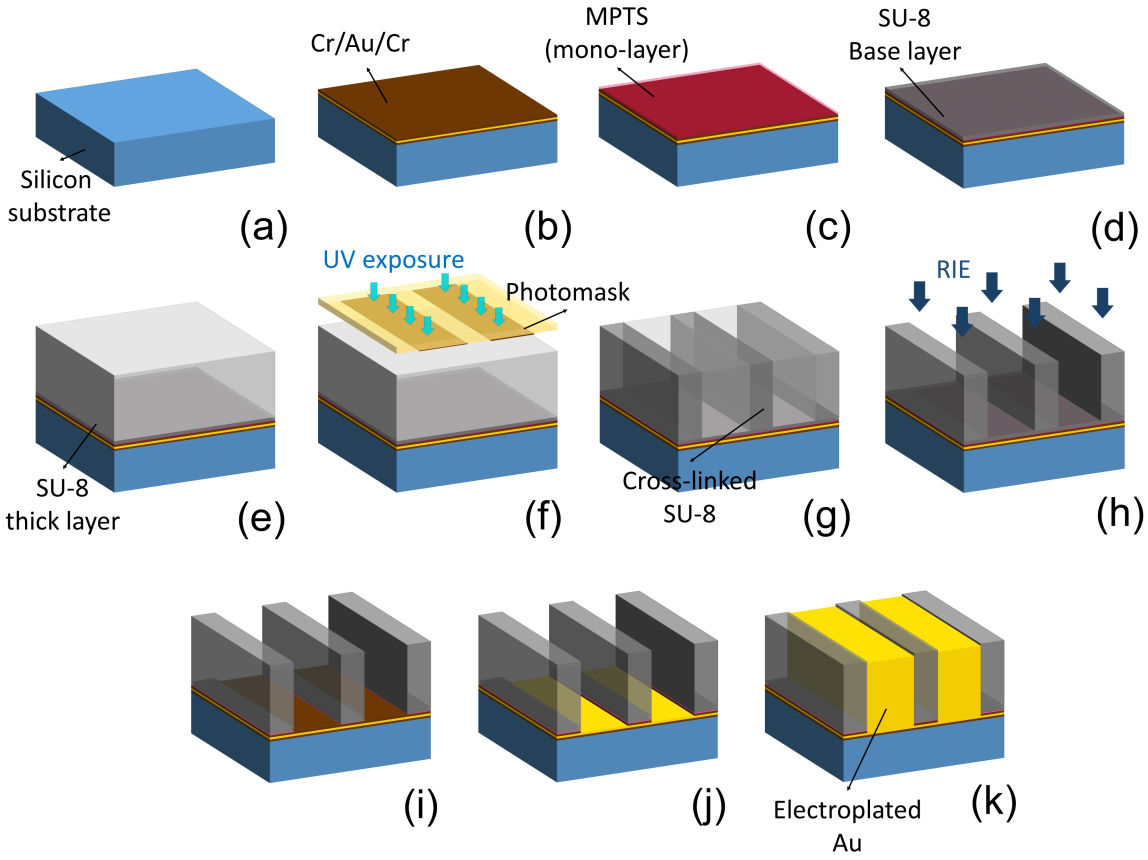


Figure 4.5: The developed process flow for fabricating an X-ray absorption grating with a strong adhesion layer between SU-8 and gold thin film. (**a**) Cleaning the Si wafer, (**b**) thermal deposition of Cr/Au/Cr thin films, (**c**) definition of a mono-layer of MPTS, (**d**) spin coating a thin SU-8 layer,(**e**) spin coating the thick SU-8 layer, (**f**) lithography and pattern transfer through a photomask, (**g**) post-exposure baking, (**h**) developing uncrosslinked SU-8 parts, (**i**) etching the thin SU-8 layer, (**j**) etching top Cr thin film to open Au thin film, and (**k**) Au electroplating to fill the gaps.

and ramping down (to room temperature) process with a rate of 120℃ per hour, all on a hotplate (from Torrey Pines Scientific, USA). Ramping the temperature during the soft bake, post-exposure bake, and hard bake was found to be necessary to minimize the high-stress level associated with the SU-8 polymerization process [128]. This SU-8 base layer was then flood-exposed in i-line, and a post-exposure bake was performed at 65℃ for 60 minutes with the same condition as the soft bake. A hard bake step was carried out for 30 minutes at 170℃—with the same ramping condition as the soft bake—to further improve the mechanical stability of the SU-8 base layer during the next fabrication steps. Our experimental results showed that the combination of a thin film of chromium, a monolayer of MPTS, and a thin layer of hard-baked SU-8 guarantee the adhesion of subsequent thick SU-8 layer, thus it does not delaminate, peel off, or break during the fabrication process. At this point, the SU-8 thick layer is spin coated followed by a soft bake step. After performing lithography and post-exposure bake, the sample is developed to open the uncrosslinked SU-8 regions.

Here it is apparent that the very combination of Cr/MPTS/thin SU-8 adhesion layer considered in the process is now blocking the gold thin film. Before performing metal electroplating and forming the absorption part of the grating, the SU-8 base layer was removed through a reactive ion etching (RIE) process (using Phantom II RIE system, Trion Technology Inc., USA) with a combination of O_2 and CF_4 gases [138] until we reached the top chromium thin film. This chromium thin film, as stated earlier, not only improves the adhesion of the SU-8 structural layer to the gold thin film, but also protects the gold thin film from being attacked by the etching gases and exposed to the RIE chamber—which contaminates the RIE chamber. The chromium thin film was then removed through a short wet etching process at room temperature using a chromium etchant made of ceric ammonium nitrate ($(NH_4)_2[Ce(NO_3)_6]$), acetic acid (CH_3COOH), and deionized (DI) water. The sample was then ready for metal (Au) electroplating to form the absorption parts of the grating.

4.3 Multi-Layer Fabrication of X-ray Absorption Grating

One of the impediments to high aspect ratio X-ray absorption grating fabrication through UV LIGA is the limitations associated with the nature of the UV lithography. SU-8, being an excellent photoresist for the fabrication of high aspect ratio features, can only achieve an aspect ratio of approximately 10 through conventional UV lithography techniques. As articulated in the introduction section of this chapter, to the best of our knowledge, the

multi-layer coating properties of SU-8 have never been investigated—nor reported—for high aspect ratio X-ray absorption grating fabrication. That being said, we developed a fabrication process for X-ray absorption grating employing SU-8 and UV-LIGA process which increases the structure aspect ratio beyond that of conventional methods. By stacking multiple layers of the same grating design, we aimed to achieve a final higher aspect ratio structure that was previously challenging through conventional one-step UV-LIGA techniques. The developed process offers a feasible, repeatable, and relatively simple fabrication based on existing well-established technologies and standard UV lithography tools to realize multi-layer X-ray absorption gratings fabrication.

4.3.1 Fabrication Process Flow

A p-type $< 100 >$ silicon wafer with 500 μm thickness was used as a substrate, which was cleaned through standard RCA-1 and RCA-2 processes. As schematically illustrated in Figure 4.6, the fabrication process began with the definition of a metallic seed layer consisting of chromium (Cr) and gold (Au) layers. The multi-layer Cr/Au/Cr (5nm/100nm/5nm) films were deposited on the substrate through a thermal evaporation process using Intlvac Thermal Evaporator (Intlvac Inc., CA) at room temperature without breaking the vacuum. The bottom chromium layer acts as an adhesion layer between the gold film and the silicon wafer. To improve the adhesion quality of SU-8 to the gold thin film, we utilized the Cr/MPTS/SU-8 base layer combination. The first SU-8 layer (SU-8 2015) was spin coated at 3000 rpm, followed by a soft bake step. After performing UV-lithography through a hard-contact mode and conducting a post-exposure bake, subsequent layers of SU-8 were spin coated, soft baked, aligned with the photomask, and exposed by UV light through a hard-contact mode in the same manner until the desired final thickness of structures was achieved. The uncrosslinked parts of SU-8 resist were then developed in either propylene glycol methyl ether acetate (PGMEA) (from Sigma-Aldrich, USA) or 1-Methoxy-2-Propanol Acetate (supplied by Kayaku Advanced Materials under the name of SU-8 developer, USA), followed by a hard bake step to ensure the mechanical stability of the final structure. Before performing metal electroplating and forming the absorption part of the grating, the SU-8 base layer was removed through an RIE process (Phantom II RIE system, Trion Technology Inc., USA) using a combination of O_2 and CF_4 gases [138] until we reached the top chromium thin film. The chromium thin film was then removed through the short wet etching process using a chromium etchant. The sample was then ready for metal (Au) electroplating to form the absorption parts of the grating.

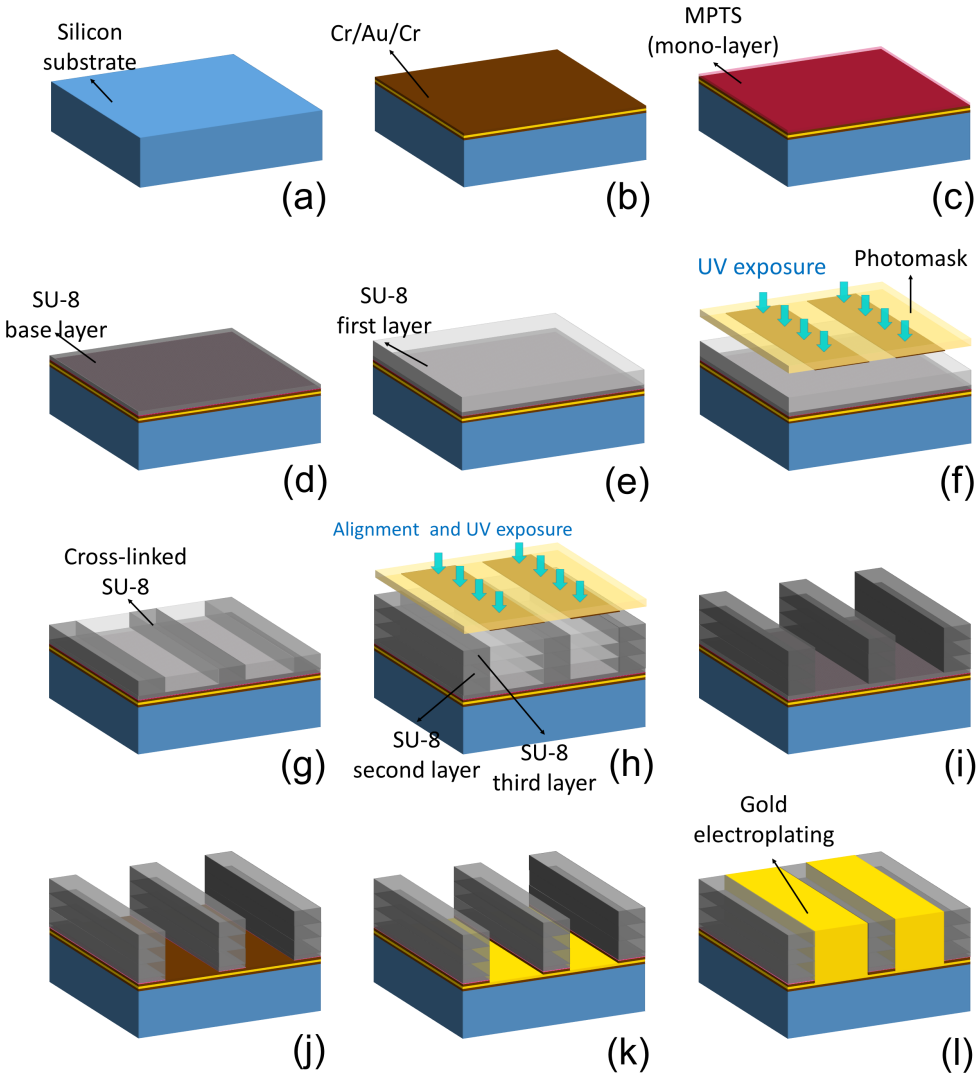
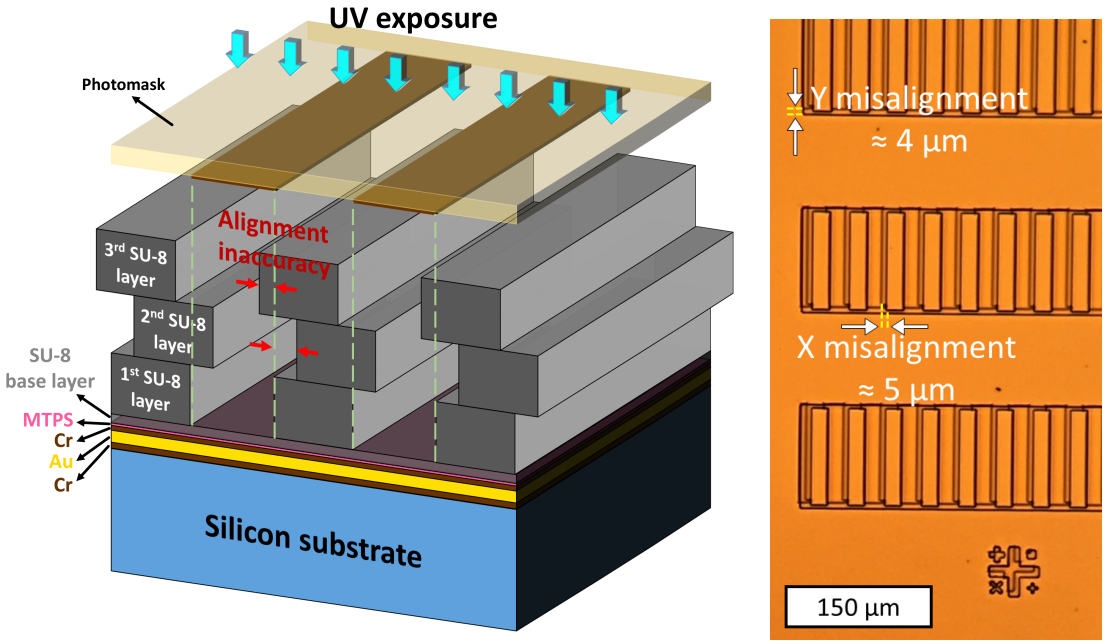


Figure 4.6: Schematic illustration of the process flow for fabricating multi-layer high aspect ratio X-ray absorption gratings. (**a**) Cleaning the Si wafer substrate, (**b**) deposition of Cr/Au/Cr thin films, (**c**) definition of a mono-layer MPTS, (**d**) definition of the SU-8 base layer, (**e**) spin coating the first SU-8 layer, (**f**) lithography and pattern transfer through a photomask, (**g**) post-exposure bake, (**h**) repeating steps (**e**) to (**g**) until the desired thickness is achieved, (**i**) developing uncrosslinked SU-8 regions, (**j**) removing the SU-8 base layer through an RIE process, (**k**) wet etching the top Cr thin film, and (**l**) gold electroplating to fill the gaps and form the absorption region.

4.3.2 Alignment Issue for Micron-Scale Features

The developed fabrication process utilizes a multi-layer design which benefits from breaking a final high aspect ratio structure down into multiple lower aspect ratio ones. As far as we know, achieving a high aspect ratio structure through a multi-layer design had not previously been reported in X-ray grating fabrication. We fabricated various feature sizes of SU-8 structures to investigate the practicality of this method in X-ray absorption fabrication using standard UV-lithography tools—we used Karl Suss MA6 Mask Aligner (SUSS MicroTec Group, Garching, Germany) in this study. Our experimental results demonstrated that alignment accuracy for each SU-8 layer can potentially play a critical role in the final structure integrity, as schematically depicted in Figure 4.7.

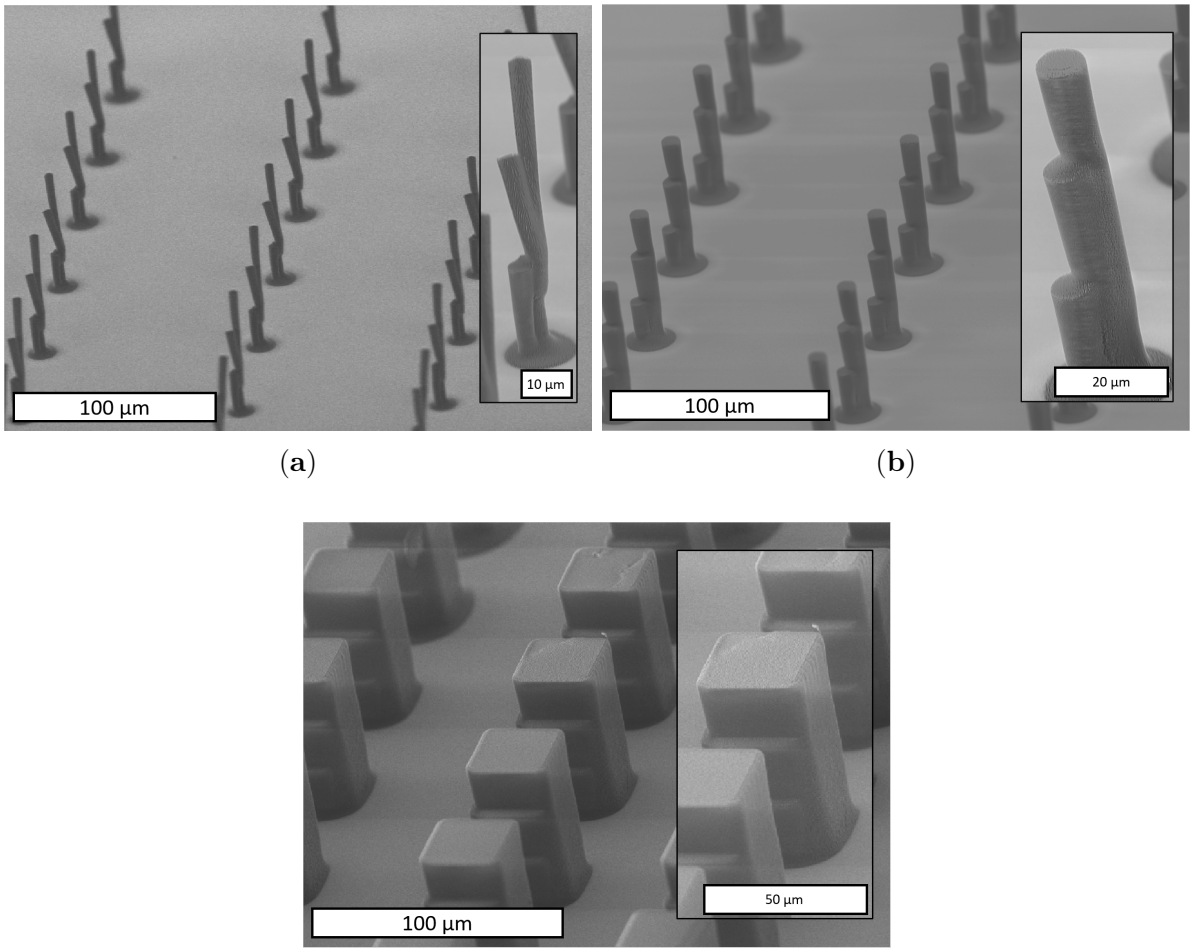
Figure 4.8a to 4.8c demonstrate scanning electron microscopy (SEM) images of a fabricated multi-layer (three-layer) SU-8 structure for three different feature sizes.



(a) (b)

Figure 4.7: (**a**) Schematic illustration of the inaccuracy in aligning multiple layers (three layers) of SU-8 films—during fabrication of each layer—which compromises the high aspect ratio structures integrity. (**b**) An optical microscope image of a misaligned two-layer fabricated SU-8 mold with misalignment for approximately 5 μm in X direction and 4 μm in Y direction.

Although alignment inaccuracy is the bottleneck for fabricating high-resolution structures (Figure 4.8a), a multi-layer design can be effectively employed where alignment inaccuracy is comparably smaller than the minimum feature size of the design (Figure 4.8c). For high-resolution structures, however, this issue led us to develop a novel fabrication process in which the alignment step is eliminated through a self-aligned technique.



(**a**) (**b**)

(**c**)

Figure 4.8: SEM images of alignment accuracy for various feature sizes of SU-8 structures. Alignment inaccuracy compromises the integrity of multi-layer micron-scale feature sizes in (**a**) and (**b**); however, it does not affect the structural integrity of greater feature sizes significantly, as demonstrated in (**c**).

4.3.3 Effect of Exposure Energy and Optimization

We started the UV lithography optimization following the Kayaku Advanced Material SU-8 manual, which recommends to increase the exposure dose for gold-deposited substrates by a factor of 1.5-2×. Unlike what was recommended (1.5-2× of exposure dose), we realized overexposure leads to SU-8 structures being crosslinked together, and underexposure results in SU-8 features delaminating from the substrate. Figure 4.9 illustrates an optical microscope image of an underexposed SU-8 film (4.9(a)), as well as an SEM image of an overexposed SU-8 film ((4.9(c)). Underexposure results in the SU-8 features' base not receiving enough energy to crosslink and adhere to the substrate and, therefore, features delaminate from the substrate during the developing process. On the other hand, overexposure expands the structures feature size, which consequently results in structures being linked together via unwanted crosslinked neighboring regions. The optimal dose exposure was found to be almost 40% less than the recommended exposure dose by Kayakuam, which varies based on the feature size, aspect ratio, and periodicity of structures.

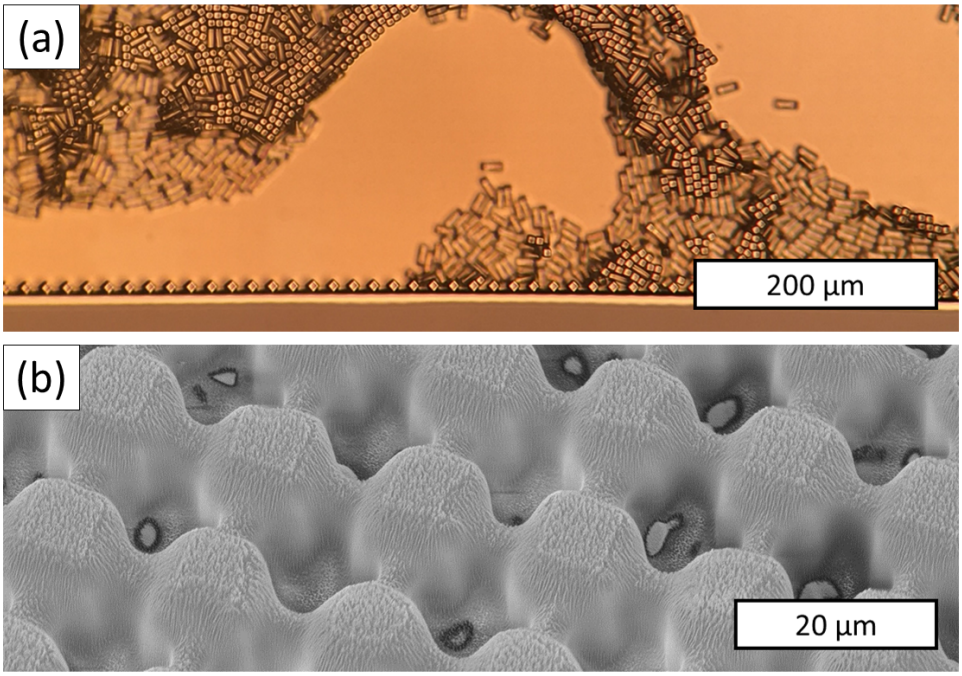


Figure 4.9: (**a**) An optical microscope image of SU-8 based micropillars underexposed in the UV lithography and delaminated during the developing process. (**b**) SEM image of overexposed SU-8 based micropillars.

4.4 Self-Aligned Multi-Layer Fabrication process

Albeit the multi-layer design reported in the previous section is conceptually sound and enables the X-ray grating fabrication to extend structures aspect ratio, alignment inaccuracy impedes us from making high-resolution high aspect ratio micron-scale structures. In this section, we developed a novel fabrication process in UV LIGA for a higher aspect ratio grating by stacking multiple layers of lower aspect ratio grating structures, without encountering the alignment issue. The critical step in achieving alignment accuracy between the multiple grating structure layers is a UV self-alignment step through the backside of the UV transparent substrate [139]. Although self-aligned fabrication processes have been reported for thin film semiconductor devices [140–142], to the best of our knowledge, such a process has never been reported for multi-layer X-ray grating fabrication to date.

4.4.1 Fabrication Process Flow

The process is schematically illustrated in Figure 4.10. First, a Cr/Au/Cr film stack (5 nm/100 nm/ 5nm) was deposited on an ITO-on-glass substrate using a thermal evaporation process with an Intlvac Thermal Evaporator (Intlvac Inc., CA) at room temperature without breaking the vacuum. The Cr/Au/Cr film was patterned on the ITO-on-glass substrate using a selective wet etching process. The chromium thin films were removed through the wet etching process at room temperature using a chromium etchant made of ceric ammonium nitrate ($(NH_4)_2[Ce(NO_3)_6]$), acetic acid (CH_3COOH), and deionized (DI) water. Also, gold wet etching was performed using a commercially available GE-8148 Gold Etchant (from Transene Company Inc., USA). To improve the adhesion quality of SU-8 to the gold thin film, we used a combination of a thin film of chromium (the top Cr film), a mono-layer of 3-(Trimethoxysilyl)propyl methacrylate or MPTS (from Sigma-Aldrich, USA), and a thin layer of SU-8. The mono-layer of MPTS on chromium thin film was formed through a liquid treatment step [137] – using ethanol and acetic acid – prior to the definition of a thin layer of SU-8. We made a thin layer of SU-8 by diluting SU-8 2015 with Cyclopentanone (from Sigma-Aldrich, USA) – known as SU-8 thinner – to achieve a desired thin SU-8 (referred to as the SU-8 base layer hereafter).

A 500 nm thin SU-8 base layer was spin coated followed by a soft baking step at 65℃ for 60 minutes via a ramping up (from room temperature) and ramping down (to room temperature) processes at a rate of 120℃ per hour, all on a hot plate (from Torrey Pines Scientific, USA). This SU-8 base layer was then flood exposed in an i-line (365 nm) using a mask aligner (Karl Suss MA6, Germany), and a post-exposure bake was performed at 65℃ for 60 minutes under the same conditions as the soft bake step. A hard bake step

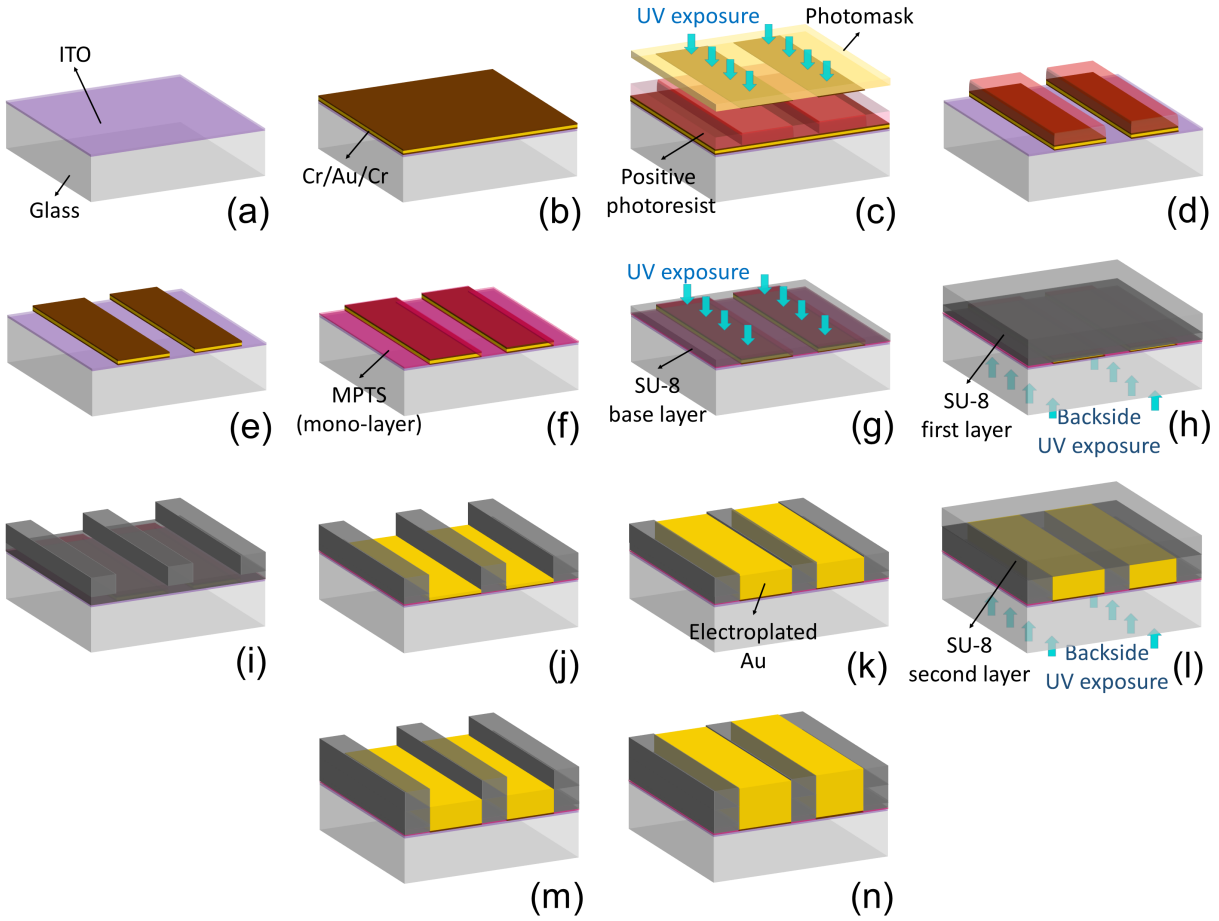


Figure 4.10: Process flow for fabricating multi-layer self-aligned high aspect ratio gratings. This graph illustrates the fabrication steps for two layers, where repeating steps (**l**) to (**n**) results in a multi-layer structure: (**a**) cleaning the ITO-on-glass substrate, (**b**) thermal deposition of Cr/Au/Cr thin films, (**c**) spin coating a positive photoresist and patterning it through a photomask, (**d**) etching uncovered Cr/Au/Cr parts, (**e**) cleaning the sample and removing the photoresist,(**f**) definition of a mono-layer MPTS film, (**g**) definition of the SU-8 base layer and performing a flood exposure from top, (**h**) spin coating the first SU-8 layer and performing a backside exposure, (**i**) developing the uncrosslinked SU-8, (**j**) performing an RIE to remove base SU-8 layer and etching the top Cr film, (**k**) gold electroplating to fill the gaps, (**l**) spin coating the second SU-8 layer and performing a backside exposure, (**m**) developing the uncrosslinked SU-8 parts, (**n**) gold electroplating to fill the gaps and so on.

was performed for 30 minutes at 170°C – with the same ramping condition as the soft bake – to further improve the mechanical stability of the SU-8 base layer.

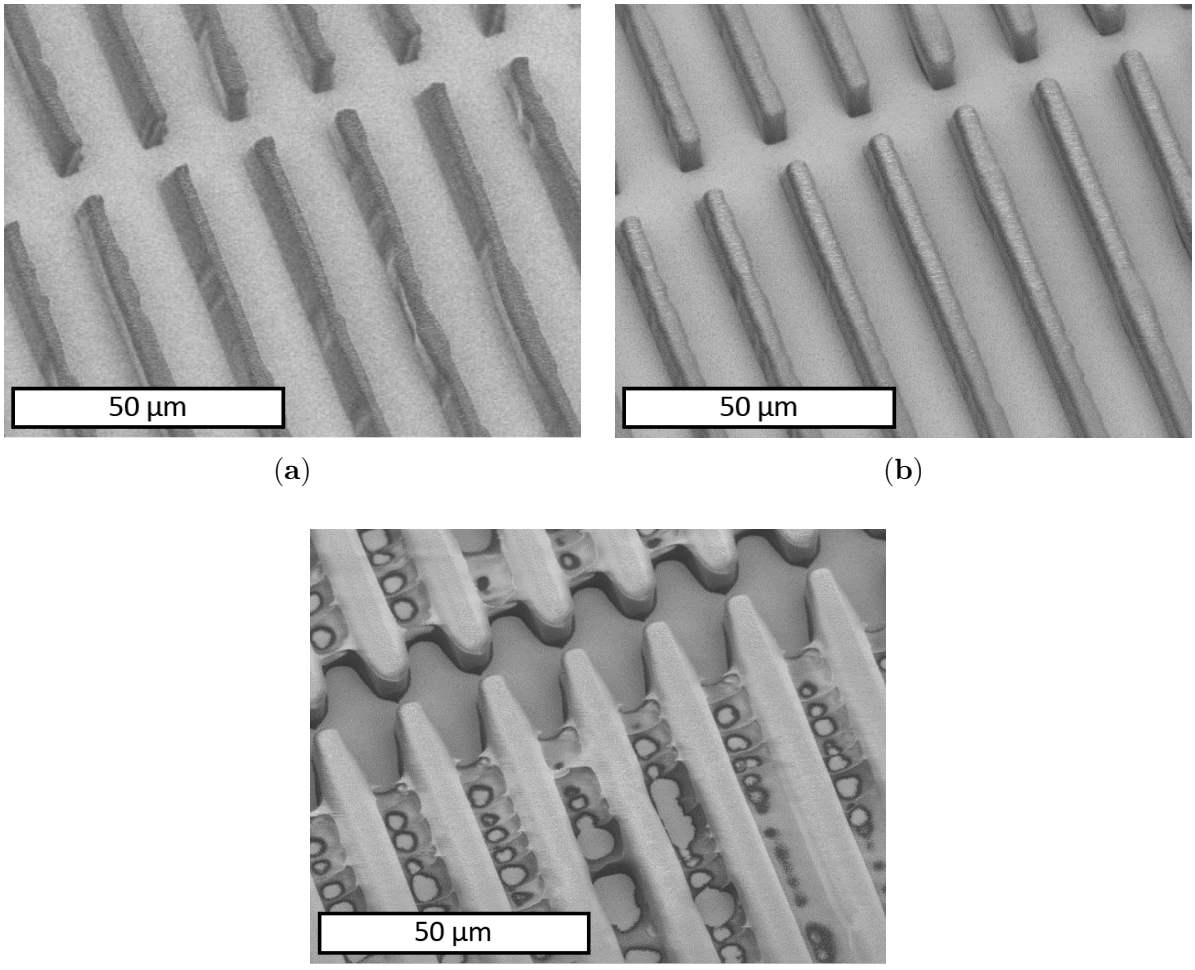
The first SU-8 layer was then exposed to a backside UV flood exposure, with the patterned Cr/Au/Cr layer acting as a photomask underneath the first SU-8 layer. After conducting the post-exposure bake, the un-crosslinked parts of the SU-8 resist were developed in either propylene glycol methyl ether acetate (PGMEA) (Sigma-Aldrich, USA) or 1-Methoxy-2-Propanol Acetate (Kayaku Advanced Materials, USA), followed by a hard bake step to ensure the mechanical stability of the final structure. Before performing metal electroplating and forming the absorption part of the grating, the SU-8 base layer was etched down to the top of the chromium thin film by an RIE dry etching process (Phantom II RIE system, Trion Technology Inc., USA) using a combination of O_2 and CF_4 gases [138]. The chromium thin film was then removed through a wet etching process at room temperature using the chromium etchant.

The sample was electroplated with metal (Au) to form the absorption part of the grating by filling the gaps between the patterned SU-8. The electroplated region thereafter acted as a self-aligned photomask for the next SU-8 layer and so on. Since the grid pattern is transferred via a self-aligned step, any offset between the self-aligned photomask and the next SU-8 layer is minimized. This fabrication process ensures a quality side-wall in SU-8 lithography and could, in principle, be repeated multiple times until the desired thickness of an absorption grating is achieved.

It should be noted that silicon wafers cannot be employed readily as a substrate in the proposed UV-LIGA self-aligned multi-layer fabrication process since a self-aligned design requires UV transparent substrates (e.g. glass). Moreover, the glass substrates require ITO (or another conductive coating) because, depending on the grating design, the patterned Cr/Au/Cr film could result in discrete areas that must be electrically connected for the electroplating process to work correctly. The ITO film (a UV transparent conductive layer) ensures an electrical connection between the discrete areas of the electroplating seed layer even if the Cr/Au/Cr film has electrically disconnected islands.

4.4.2 Effect of Exposure Energy and Optimization

Although the proposed self-aligned backside UV exposure technique benefits from a minimal mask-to-resist gap, the quality of the transferred pattern was found to be energy-dependent [143, 144]. A successful pattern transfer in backside UV exposure lithography was achieved through an optimized UV exposure dose (energy). Experimental results of exposure dose optimization (Figure 4.11) demonstrated that a low exposure dose leads to



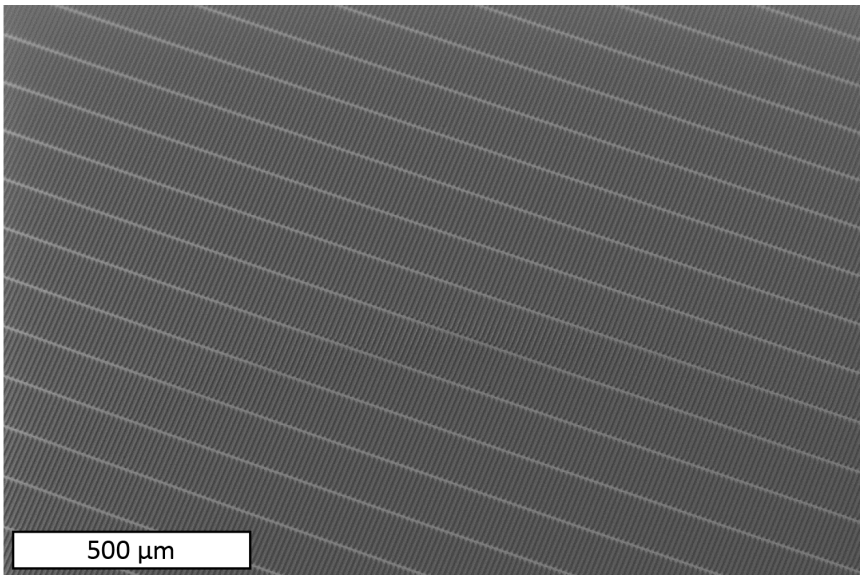
(**a**) (**b**)

(**c**)

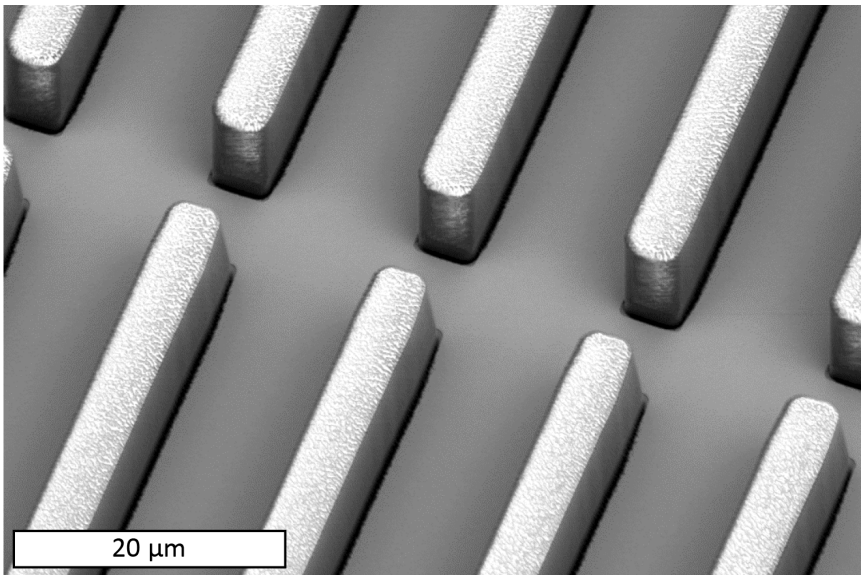
Figure 4.11: SEM images of the effect of exposure dose on the quality of pattern transfer in the self-aligned backside UV lithography. (**a**) Insufficient UV exposure dose results in unstable SU-8 features and incomplete pattern transfer. (**b**) An optimized UV exposure dose transfers the patterns onto the SU-8 layer successfully. (**c**) Higher exposure dose leads to resolution loss in features and SU-8 cross-linking in unwanted areas.

mechanically unstable SU-8 structures, incomplete pattern transfer, and incomplete cross-linking (Figure 4.11a). On the other hand, a high dose exposure results in cross-linking in unexposed areas between structures and loss of resolution (Figure 4.11c). The optimal exposure dose was selected based on the pattern transfer quality, feature sizes, periodicity of features, and SU-8 thickness at the dose that SU-8 features become sufficiently cross-

linked with an acceptable sidewall quality. Figure 4.12 illustrates SEM images of quality backside UV exposure in creating periodic line features over a large area.



(**a**)

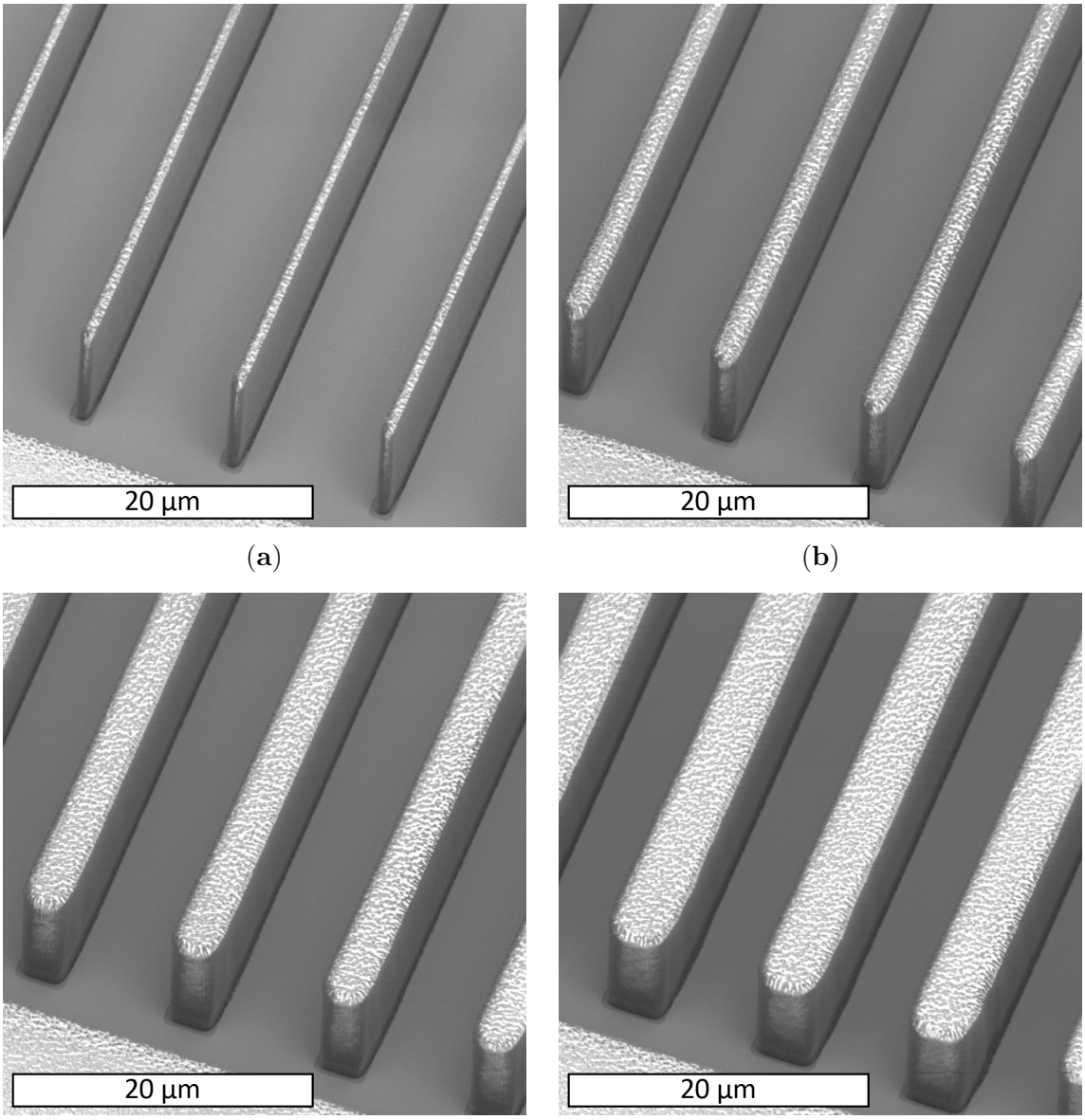


(**b**)

Figure 4.12: SEM images of a quality pattern transfer: (**a**) over a large area, and (**b**) a closer view of the features.

4.4.3 Effect of Feature Size

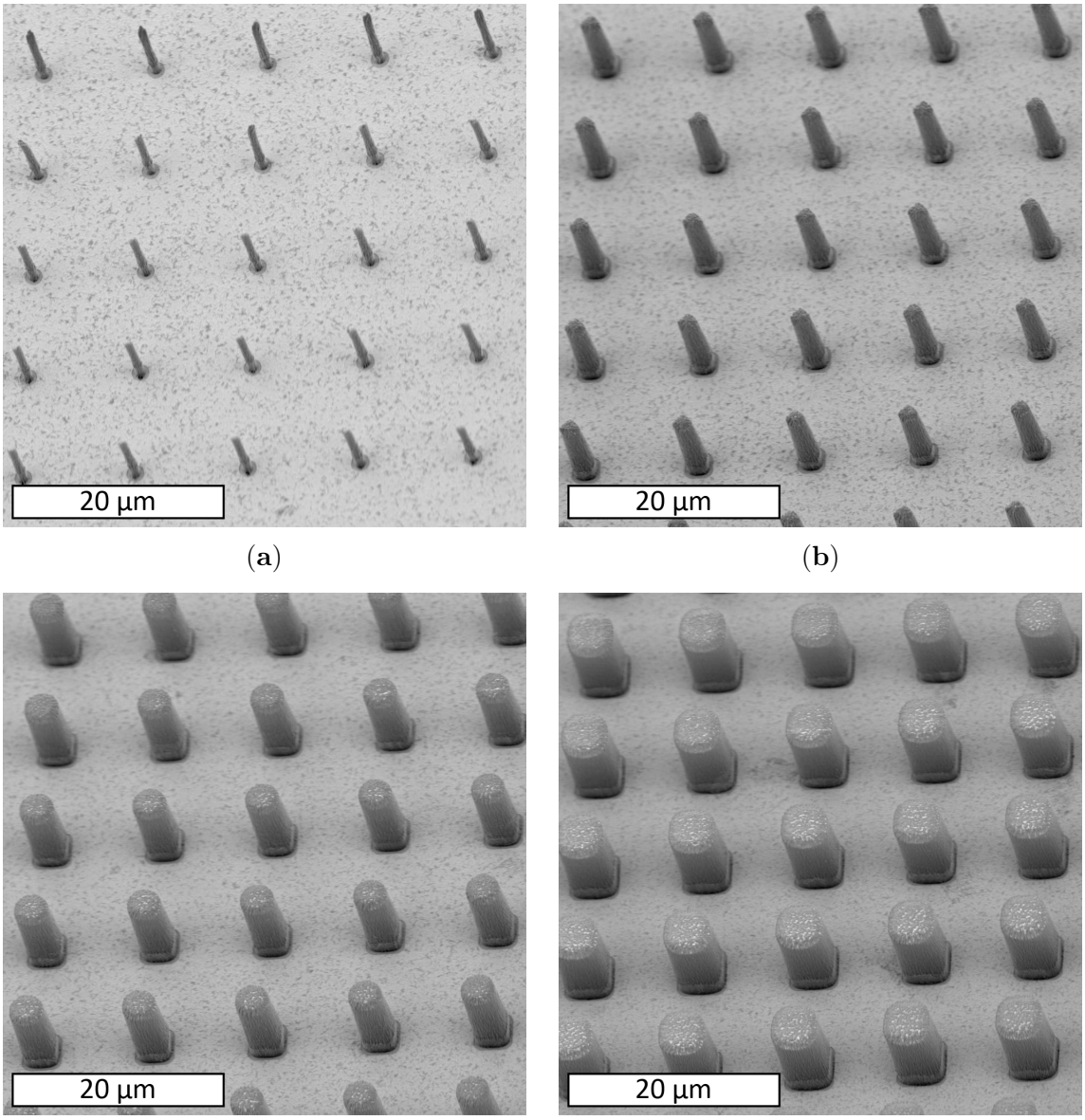
We fabricated various feature sizes of SU-8 structures in the form of periodic lines and micropillars to evaluate the quality of SU-8 structures. The thickness of coated SU-8 was selected to be around 10 μm thus that the aspect ratio of features did not exceed 10, as we had multiple feature sizes (from 1 μm to 5 μm) on the same die. Patterns were created simultaneously through the self-aligned backside UV exposure. We were able to fabricate successfully feature sizes as small as 1 μm thick. Figure 4.13 and 4.14 illustrate features with 1 μm thickness (Figure 4.13a and 4.14a) to 4 μm thickness (Figure 4.13d and 4.14d). The periodicity of all these structures was kept equal to 10.8 μm – to match the grating with the detector pixel size of our X-ray imaging setup. The accomplished results through the self-aligned backside UV exposure were promising, particularly for fabricating micrometre scale gratings for high-resolution systems. As we move toward higher aspect ratio structures – in a single SU-8 layer – the quality of lithography in sub-micron scale feature size structures degrades, a limitation associated with the wavelength of standard UV light sources.



(**a**) (**b**)

(**c**) (**d**)

Figure 4.13: SEM images of pattern transfer of various feature sizes through the self-aligned backside UV lithography. Periodic lines with thicknesses of (**a**) 1 μm, (**b**) 2 μm, (**c**) 3 μm, and (**d**) 4 μm. The thickness of the SU-8 was around 10 μm for all features as there were all fabricated simultaneously on the same die.



(**a**) (**b**)

(**c**) (**d**)

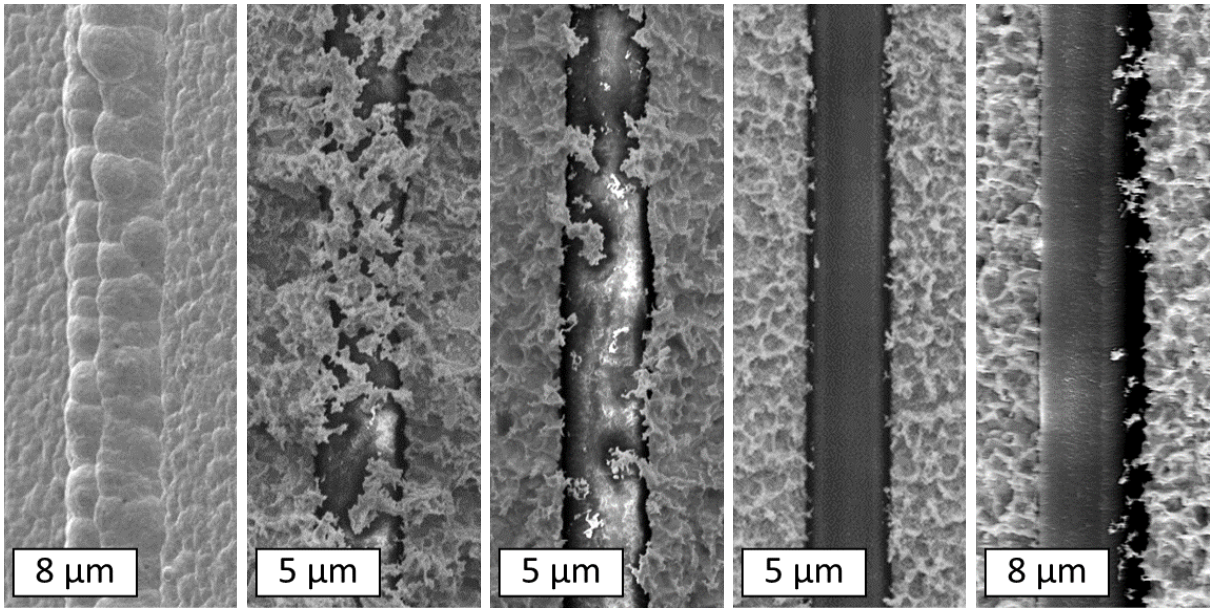
Figure 4.14: SEM images of pattern transfer of various feature sizes through the self-aligned backside UV lithography. Periodic micropillars with diameters of (**a**) 1 μm, (**b**) 2 μm, (**c**) 3 μm, and (**d**) 4 μm. The thickness of the SU-8 was around 10 μm for all features as there were all fabricated simultaneously on the same die.

4.4.4 Electroplating and Optimization

A metal electroplating step was conducted in each step of the self-aligned multi-layer fabrication to form the absorption parts of X-ray gratings. These electroplated parts also served as a lithography mask – in the backside UV exposure technique – for subsequent SU-8 layers. A successful pattern transfer in the self-aligned backside UV exposure was not achievable throughout the process unless quality electroplating was performed. We tested multiple samples by conducting gold (Au) and indium (In) electroplating. Gold is the most commonly utilized metal for X-ray grating fabrication, as it poses a heavy atomic number that can effectively absorb X-ray photons. We employed gold electroplating for our final grating fabrication. However, in addition to gold, we used indium electroplating to investigate the adhesion quality between SU-8 and the substrate in a more acidic solution – since we had access only to gold and indium electroplating setups at the time this research was conducted.

Gold Electroplating

Gold electroplating was conducted using the Elevate Gold 7990 (from Technic Inc., USA), a sodium gold sulfite solution with 8.2 g/L concentration and a slightly acidic pH (6.3). The electroplating solution was warmed up and kept at 49°C (121°F) using a PLC-controlled electric immersion heater, and the solution was filtered and stirred throughout the process to ensure a better electroplating uniformity across the sample. We used a platinized titanium mesh anode with a surface area greater than our samples, which was kept 10 cm away from the sample. Electroplating was performed at 3 mA/cm^2 using a constant current source, resulting in a growth rate of around 100 nm/min. Samples were cleaned and washed using de-ionized (DI) water both before immersion into the electroplating solution and after the electroplating was completed. Samples were dried with nitrogen (N_2) after being rinsed at the end of electroplating. Quality electroplating for successful self-aligned lithography in our design required that samples not be overplated. Overplating results in the UV transparent regions – on the sample – being covered, which eventually changes the shape of the structure in subsequent layers. To avoid such adverse behavior, samples with overplated gold were partially wet etched using GE-8148 Gold Etchant (from Transene Company Inc., USA). We diluted the gold etchant in DI water (1:2 vol/vol) to have better control over the etching rate. Figure 4.15 illustrates SEM images of a SU-8 line buried under overplated gold (Figure 4.15a), which had undergone a partially gold wet etching process (Figure 4.15c) until the excessive gold plated regions were removed, and the SU-8 line was released (Figure 4.15d). Figure 4.15a and 4.15e are SEM images taken at an angle to demonstrate a better view of overplated gold and the etched gold.

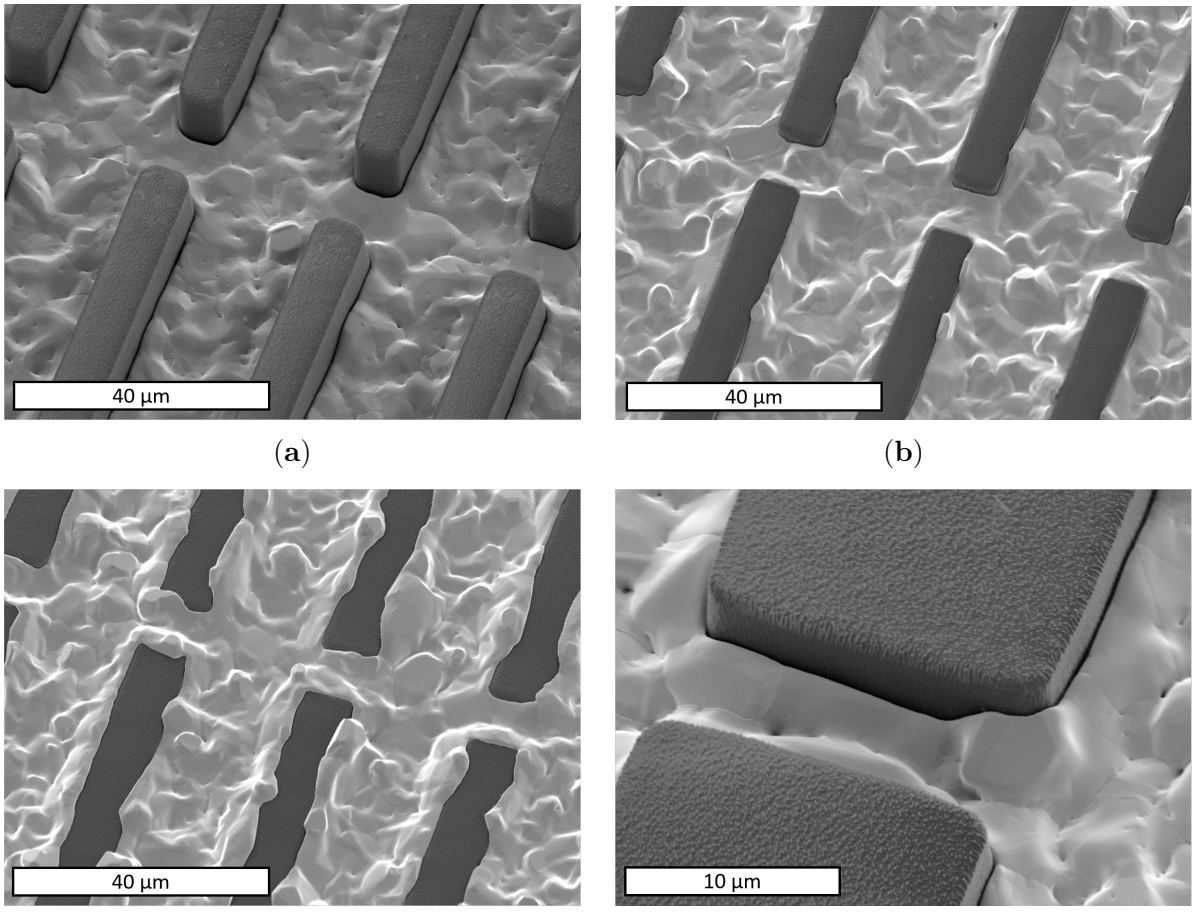


(**a**) (**b**) (**c**) (**d**) (**e**)

Figure 4.15: SEM images of gold electroplating. (**a**) An overplated sample where SU-8 features are buried under excessive gold plating. (**b**) Sample has undergone a short gold wet etching process. (**c**) A longer gold wet etching starts opening the SU-8 features. (**d**) SU-8 features are open and excessive plated gold is completely etched. (**e**) A side view of released Su-8 features.

Indium Electroplating

We used the commercially available In Sulfamate Plating Bath 3N (from Indium Corporation, USA) for indium electroplating. This solution is acidic with a pH of 1.5-2.0. We monitored the pH for each test and adjusted and maintained the pH by titrating a 10% sulfamic acid in DI water (1:9 wt/wt) solution into the indium solution. An indium anode with a surface area greater than the size of samples was placed 6.5 cm away from samples, all in a large beaker, while the solution was being physically stirred using a magnetic stir bar with a speed of 340 RPM. Samples were rinsed with DI water and immersed first in the 10% sulfamic acid to ensure having an acidic base metallization surface and preparing samples for the next step electroplating in indium sulfamate plating bath. Electroplating was then conducted at room temperature utilizing a constant current source with a current density of 16 mA/cm^2, resulting in a growth rate of around 700 nm/min. We rinsed the samples with DI water after the completion of indium plating and dried them with N_2. We



(**a**) (**b**)

(**c**) (**d**)

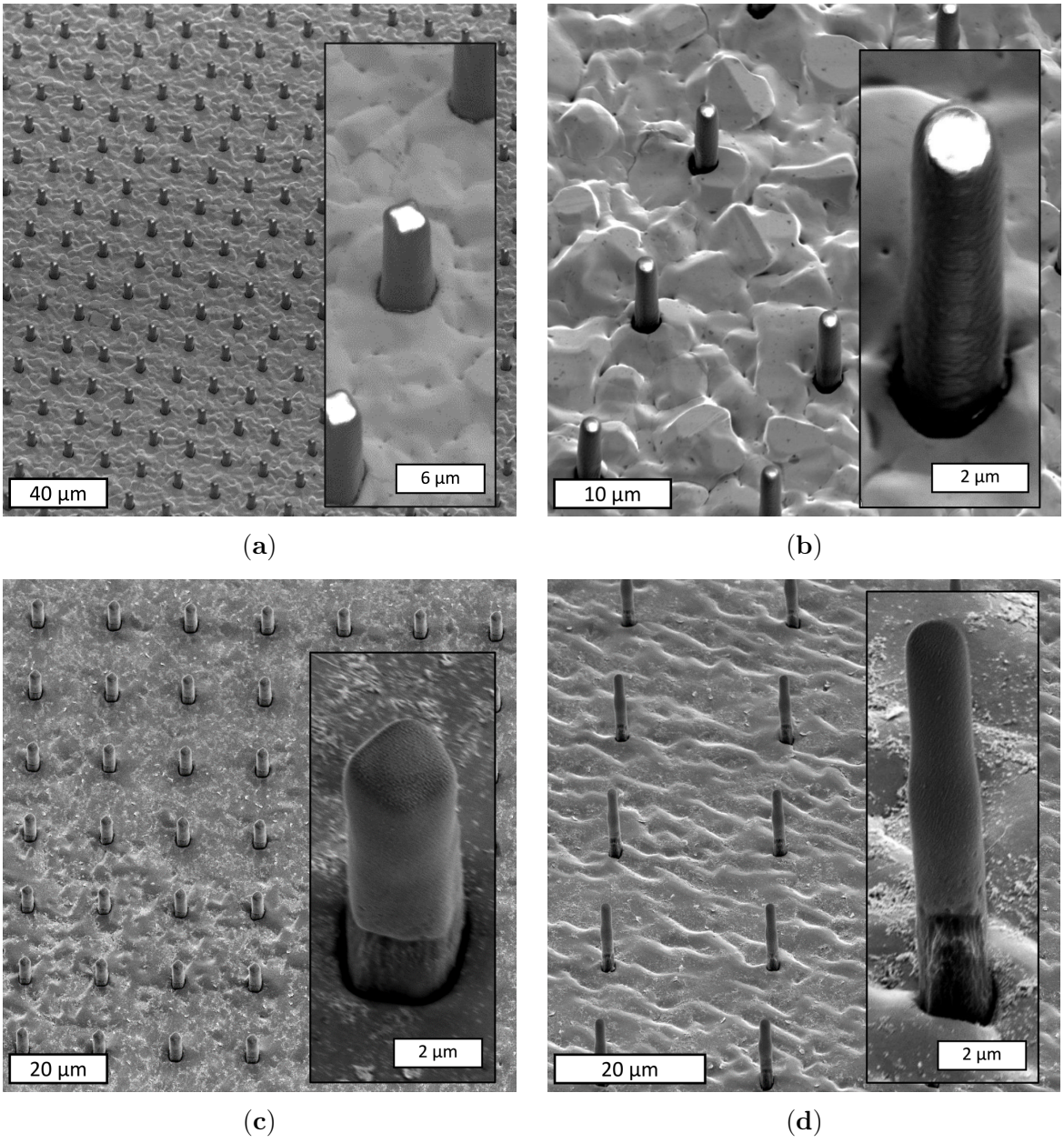
Figure 4.16: SEM images of indium electroplated samples. (**a**) Underplated sample, (**b**) sufficiently plated sample and ready for subsequent SU-8 layer coating, (**c**) overplated sample where features are buried under excessive indium electroplated regions, and (**d**) a closer view of a sufficiently plated sample.

could not perform indium etching – using indium etchant, which is diluted hydrochloric acid solution in DI water – on overplated indium samples due to the presence of ITO on our samples. ITO contains indium which would get etched and results in SU-8 features being peeled off the substrate. Having discussed that, we conducted intermittent indium plating until features were slightly underplated to have better control over pattern transfer in self-align lithography. Figure 4.16 demonstrates SEM images of samples electroplated by – where we performed intermittent electroplating – to observe the plating quality. Fig-

ure 4.16b is an example of sufficiently indium electroplated sample, with a closer view at SU-8 features in Figure 4.16d. An SEM image of an overplated indium sample is also illustrated in Figure 4.16c, where SU-8 is partially covered with overplated indium.

4.4.5 Multi-Layer Backside UV Lithography

After successfully electroplating and forming the absorption parts, samples were rinsed with DI water, dried with N_2, and the subsequent SU-8 layer was coated to make the second layer of structures. The second SU-8 layer thickness, similar to the first SU-8 layer, was selected based on the smallest feature size such that the resulting self-aligned backside UV exposure pattern transfer – with the highest possible aspect ratio and an acceptable sidewall angle – was complete. The self-aligned backside UV exposure was performed considering higher exposure energy to compensate for the energy loss at the first SU-8 layer thus that a successful pattern transfer occurred. After developing samples in SU-8 developer, a hard bake step was also carried out to enhance structures mechanical stability. SEM images of various feature sizes of the second SU-8 layer are illustrated in Figure 4.17. We investigated the quality of the second SU-8 layer backside UV exposure on samples electroplated with indium and gold. In Figure 4.17a and 4.17b micropillars in the first SU-8 layer were sufficiently electroplated using indium plating. In Figure 4.17c and 4.17d, on the other hand, structures in the first SU-8 layer were slightly underplated with gold. We successfully fabricated micropillars with a diameter as small as 1.5 μm with an aspect ratio of 13:1 with two layers of SU-8 (Figure 4.17d).



(**a**) (**b**)

(**c**) (**d**)

Figure 4.17: SEM images of the second SU-8 layer in various feature sizes of micropillar-based gratings. A successful pattern transfer from the first SU-8 layer to the second one is evident in all samples with (**a**) and (**b**) being the micropillars sufficiently electroplated with indium, as well as (**c**) and (**d**) being the micropillars underplated with gold.

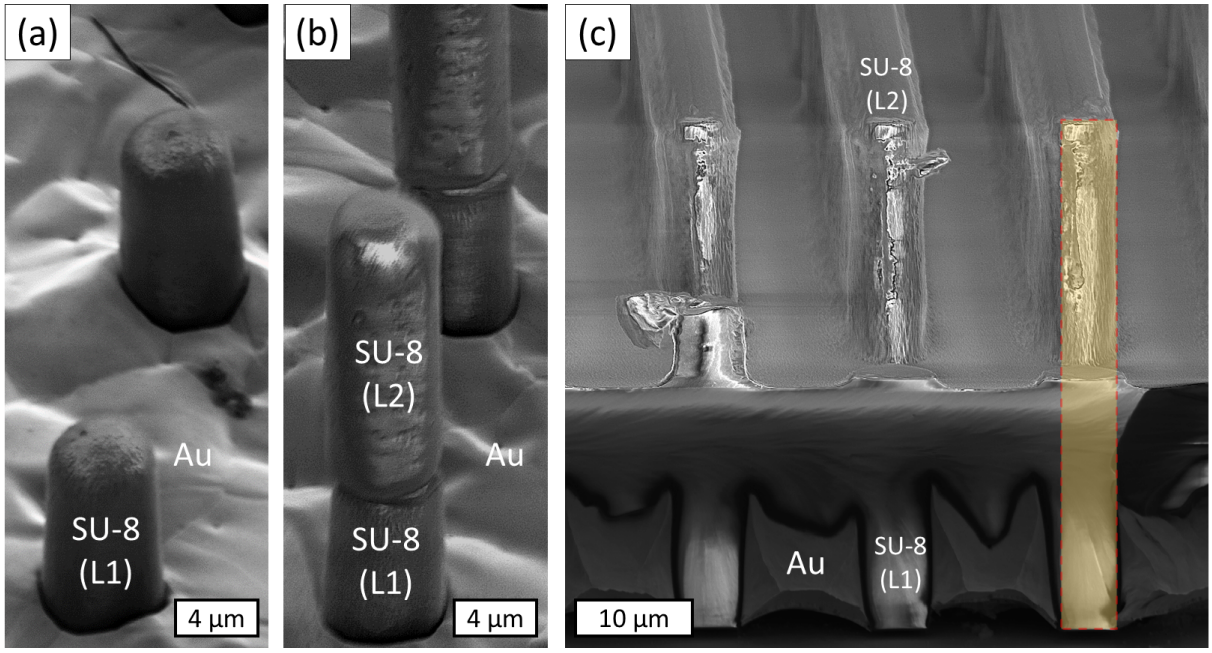
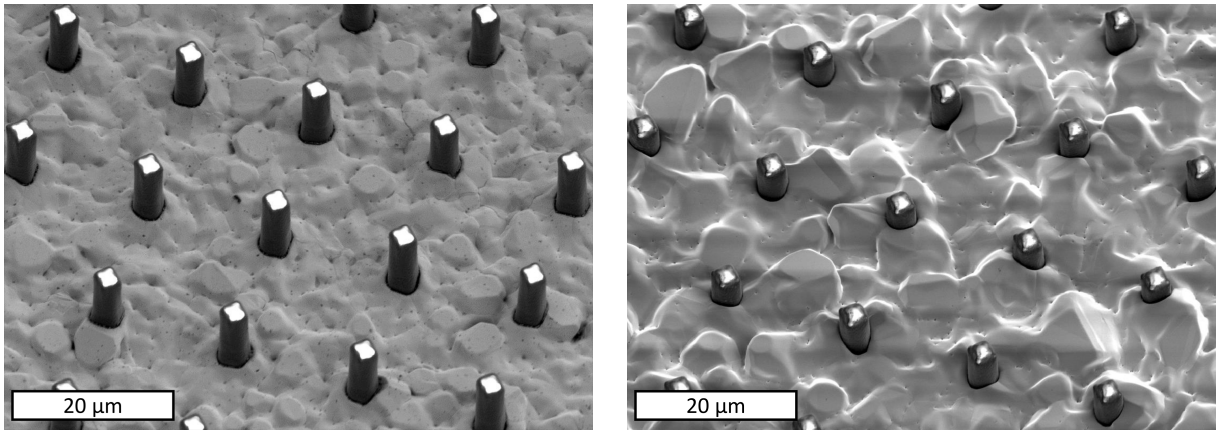


Figure 4.18: SEM images of micropillar and line gratings through the self-aligned multi-layer fabrication process. (**a**) Demonstration of micropillars before the definition of the second SU-8 layer, and (**b**) the same micropillars after the second SU-8 layer is fabricated. (**c**) Illustration of a line grating with two SU-8 layers.

Increasing the number of layers also resulted in structures with a higher aspect ratio, which was fabricated as the prototype version of a wafer-scale X-ray grating. Figure 4.18 also illustrates SEM images of micropillars before (4.18(a)) and after (4.18(b)) creating the second SU-8 layer through the self-aligned backside UV exposure. While micropillars in Figure 4.18(a) were underplated with indium, they resulted in an acceptable pattern transfer from the first SU-8 layer. The same scenario – an underplated first SU-8 layer with indium – was tested on line gratings, where a complete pattern transfer of structures was achieved through the self-aligned backside UV exposure technique. Figure 4.18(c) depicts an SEM image of a line grating with two SU-8 layers (the image was taken before unexposed regions of the second SU-8 layer were developed entirely).



(**a**) (**b**)

Figure 4.19: SEM images of micropillar-based grating with the second layer of SU-8 (**a**) before and (**b**) after being electroplated with indium.

Figure 4.19 illustrates a sample with two SU-8 layers before (4.19a) and after (4.19b) electroplating the second SU-8 layer with indium. The proposed self-aligned multi-layer fabrication process for X-ray grating can be repeated to as many layers as required until a desired thickness of the absorber material is achieved.

4.4.6 Results and Discussion

Toward Large-Area Grating Fabrication: Prototype grating

To demonstrate the self-aligned multi-layer fabrication process, a micropillar-based grating with 4 μm aperture size and 16.2 μm period was fabricated with dimensions of 70 mm×70 mm on a 4-inch square glass substrate of 700 μm thickness. Figure 4.20 demonstrates the 70 mm×70 mm prototype grating mounted on an aluminum holder for easier handling.

The quality of the electroplated layers was examined at each step using a novel, non-destructive large-area alternative to conventional destructive SEM imaging. Here, a 630 nm (red) pointer laser was used to illuminate the grating, and since the grating was on a transparent substrate, we could observe the Fourier transform pattern of the grating on a screen that provided visual feedback on the quality of electroplated structures. For example, if the structures were over-plated, the Fourier transform image on the screen would be deformed. Figure 4.21 illustrates a schematic representation of

the setup used for the quality test of electroplating with a laser source, and Figure 4.22 demonstrates the test setup with two examples of the Fourier transform pattern including one with line and another with micropillar structures. The laser source to the grating distance (z_1) and the grating to the screen (z_2) distance were selected as 10 cm and 35 cm, respectively. These numbers were selected based on the grating feature size, periodicity of features on the grating, as well as the wavelength of the laser source thus that we could distinguish between the Fourier transform patterns of gratings for observation.

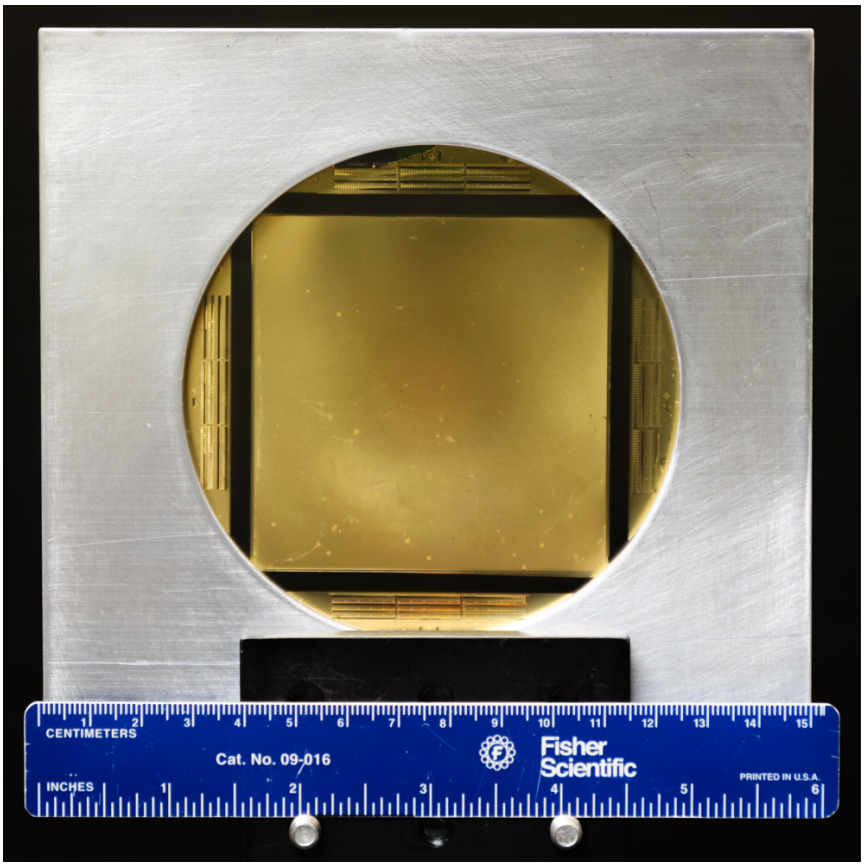


Figure 4.20: Demonstration of a prototype large-area 70 mm×70 mm grating fabricated on a 4-inch glass substrate.

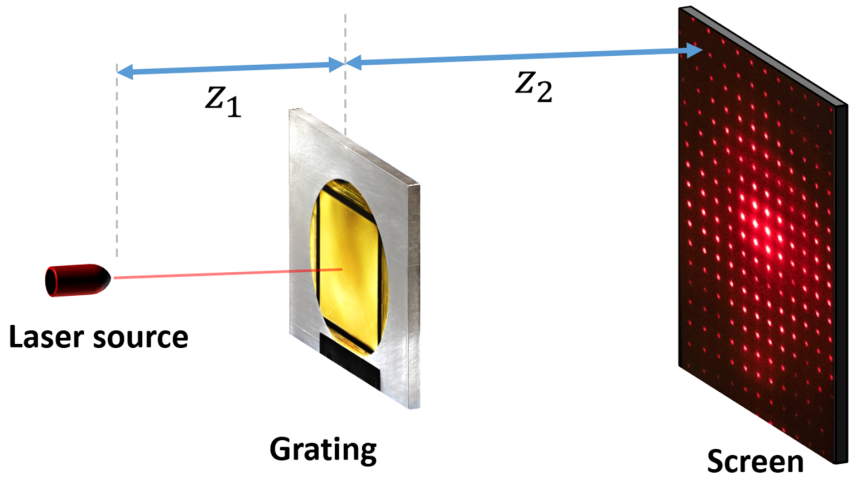


Figure 4.21: Schematic representation of the laser point source setup for testing the electroplating quality.

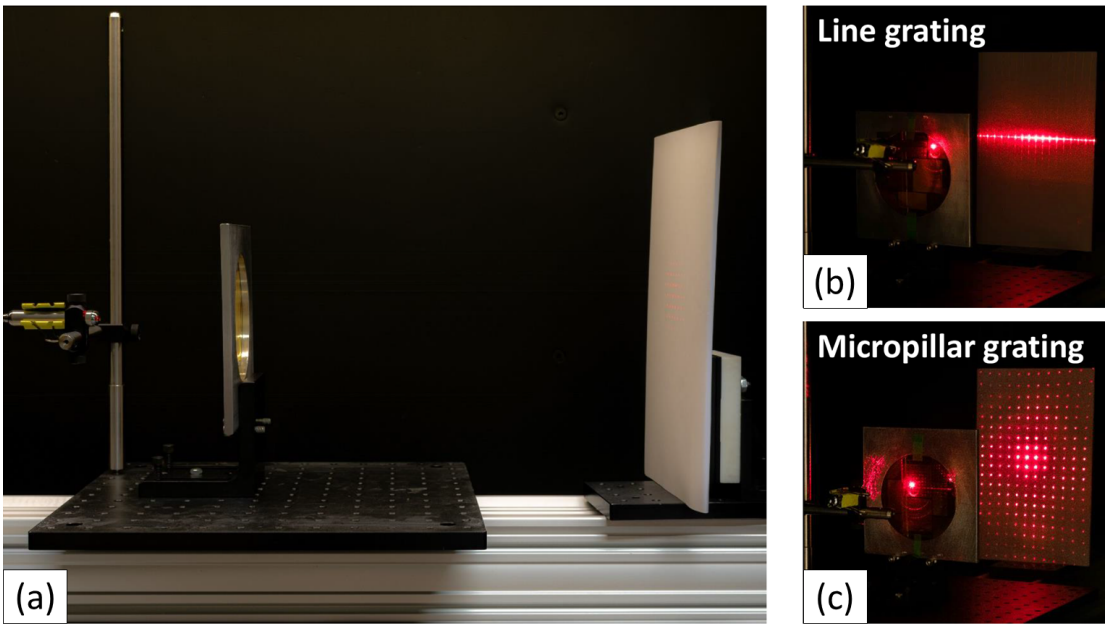


Figure 4.22: (a) Illustration of the test setup, with two Fourier transform images acquired from (b) a line grating and (c) a micropillar grating.

X-ray Projection

While SEM and laser source projection techniques give us a good impression of the quality of fabrication in each step – layer, X-ray projection of fabricated gratings can reveal the ultimate quality of a final device. X-ray projection provides in-depth information about the transmission characteristics of the absorption grating. A final inspection was carried out – employing the setup depicted in Figure 4.23 – by measuring X-ray transmission through the fabricated three-layer micropillar-based grating with 4 μm aperture size and 16.2 μm period size.

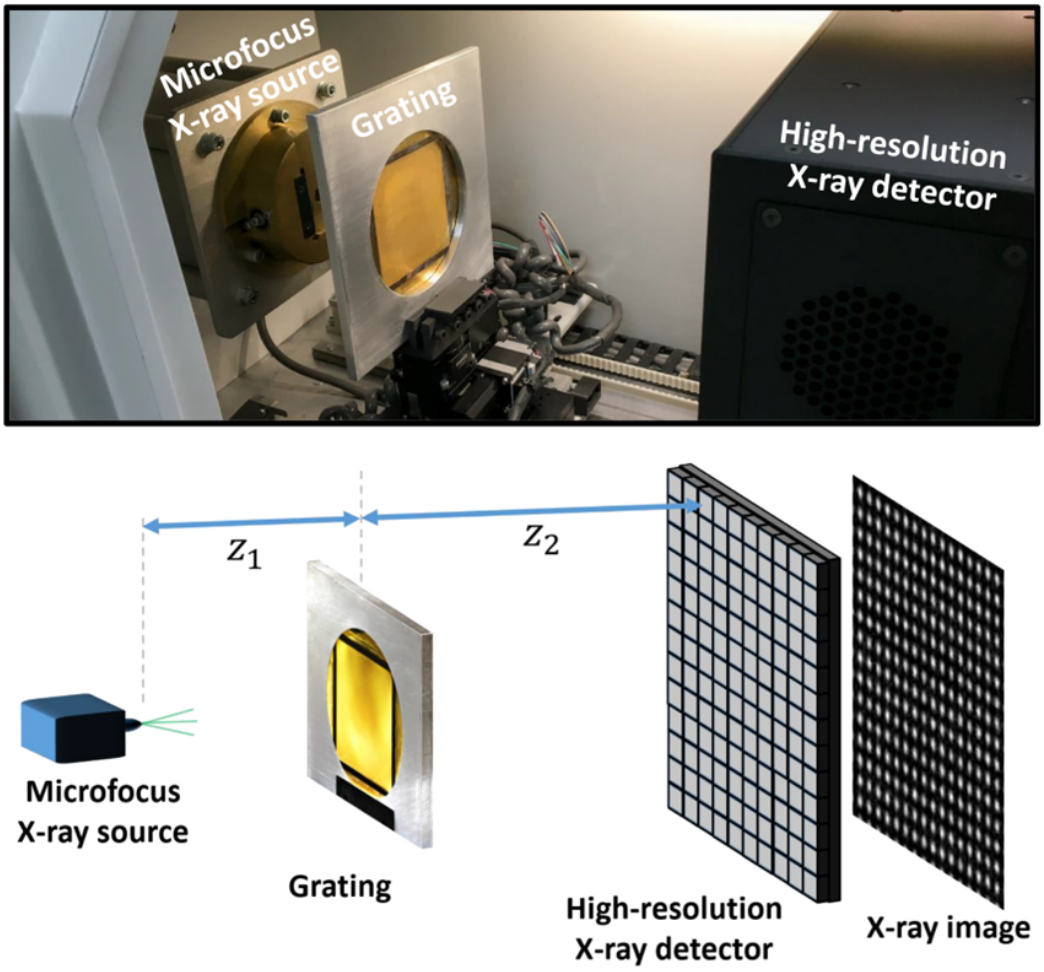
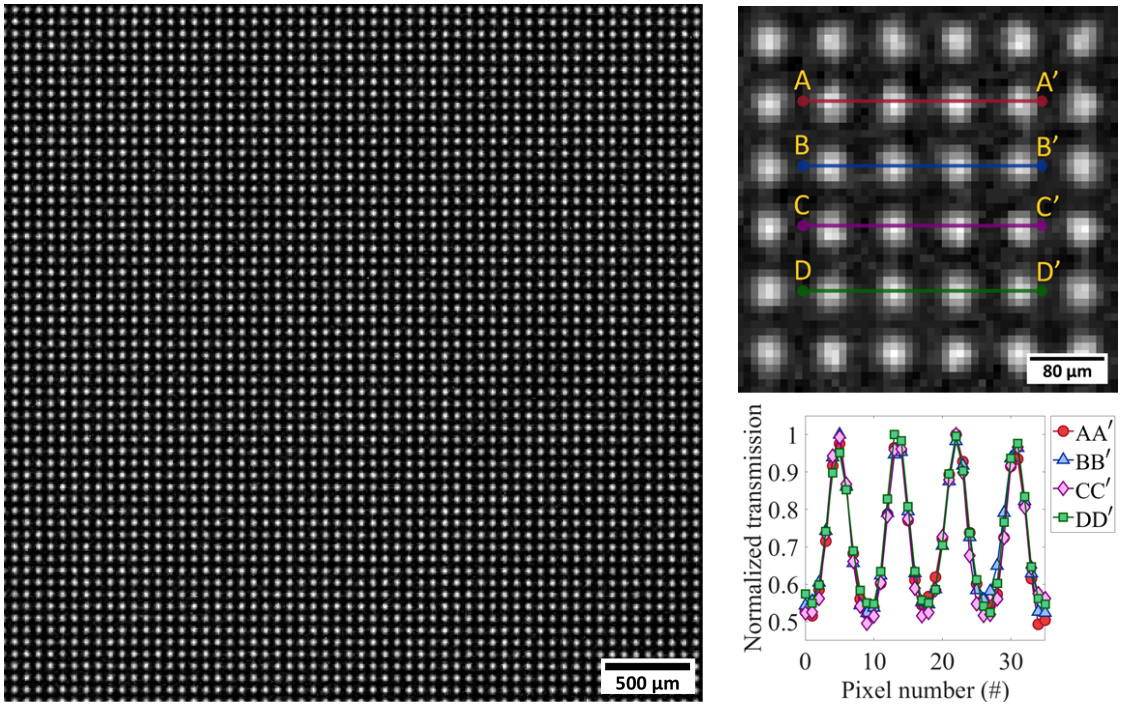


Figure 4.23: Demonstration of the 3D X-ray Microscope – inCiTe™ – and the test setup we used for taking X-ray projection of the prototype version of our grating.

We took an X-ray image of the fabricated grating – as illustrated in Figure 4.24a – with the X-ray source at 60 kV_p and 200 μA (a source focal spot of 5 μm), source to grating distance (z_1) of 10 cm and grating to detector distance (z_2) of 35 cm. These distances were selected to have a magnified image of grids on the detector so that their profile could be resolved. A closer view of the grids profile and cross-sectional graphs of their normalized transmission profiles are shown in Figure 4.24b.



(**a**) (**b**)

Figure 4.24: (**a**) X-ray projection of the micropillar-based X-ray grating with three layers and the X-ray source working at 60 kV_p and 200 μA (focal spot of 12 μm); a magnification of 4.5 was used in this X-ray projection. (**b**) A closer view of grids in the X-ray projection image (top), and the cross-sectional profiles of normalized transmission of grids across four rows of grids (bottom).

Transmission images for a two-layer and a three-layer version of the 70 mm×70 mm prototype grating at 60 kV_p are presented in Figure 4.25a and Figure 4.25b, respectively. A cross-sectional profile across the dashed blue line in each figure represents the transmission value for the corresponding grating.

With regards to common defects observed in the grating, the most prominent one occurs when the grating is over- or under- exposed leading to a change in feature size. Another prominent defect is due to the quality of the electroplating which can also lead to a change in feature size. While the prototype two-layer grating, illustrated in Figure 4.25a, has no easily distinguished blemishes, the prototype three-layer grating in Figure 4.25b exhibits a few visible artifacts. The artifacts are representative of deterministic non-uniformities stemming from the grating fabrication process (primarily, the third electroplating step in the prototype grating of this work) and, being deterministic, are correctable as are presented later in Chapter 5—results of sugar powder sample XPCi.

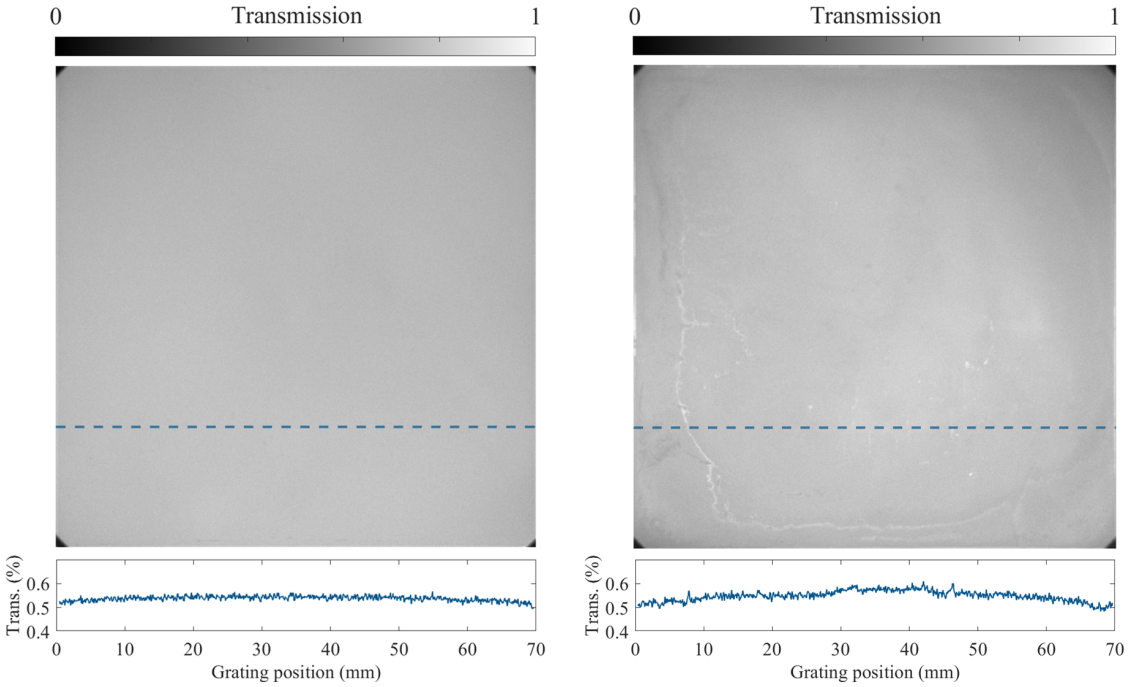
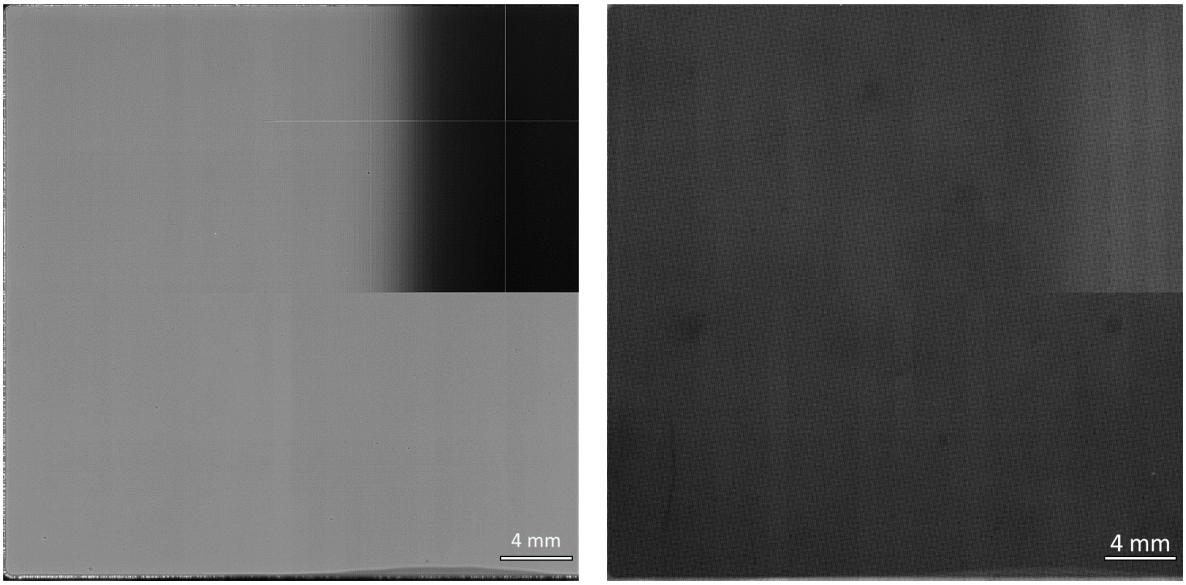


Figure 4.25: Transmission map of (**a**) a two-layer and (**b**) a three-layer 70 mm×70 mm prototype X-ray absorption grating. The three-layer grating exhibits a few visible blemishes stemming from the third layer electroplating.

Visibility, Transmission, and Absorption Characteristics of the Prototype Gratings

Visibility maps of the prototype grating were generated using the prototype 4K×4K high-resolution X-ray detector with the X-ray source working at six different potentials between 40 kV_p to 90 kV_p (with steps of 10 kV_p) all at 200 μA. There are some pixel defects, associated with the prototype X-ray detector (illustrated in Figure 4.26), that are visible even after dark offset and gain corrections. Figure 4.26a shows the gain map of the detector which demonstrates the detector defects and artifacts. Figure 4.26b illustrates the transmission image for part of the prototype X-ray grating fabricated in this work. Whereas some detector artifacts are corrected after gain (and offset) correction, the detector defective areas and pixel clusters remain in the X-ray projection. The visibility maps—at various X-ray source potentials—of the same part of the prototype grating employed for XPCi in this work are illustrated in Figure 4.27 and 4.28. The visibility map at each energy was calculated considering the maximum and minimum values of individual micropillar X-ray projections in the corresponding transmission image.



(**a**) (**b**)

Figure 4.26: (**a**) Gain map of the prototype 4K×4K high-resolution X-ray detector, showing detector defects and artifacts; the top right quarter of the detector is defective. (**b**) Transmission image for part of the prototype fabricated grating at 60 kV_p.

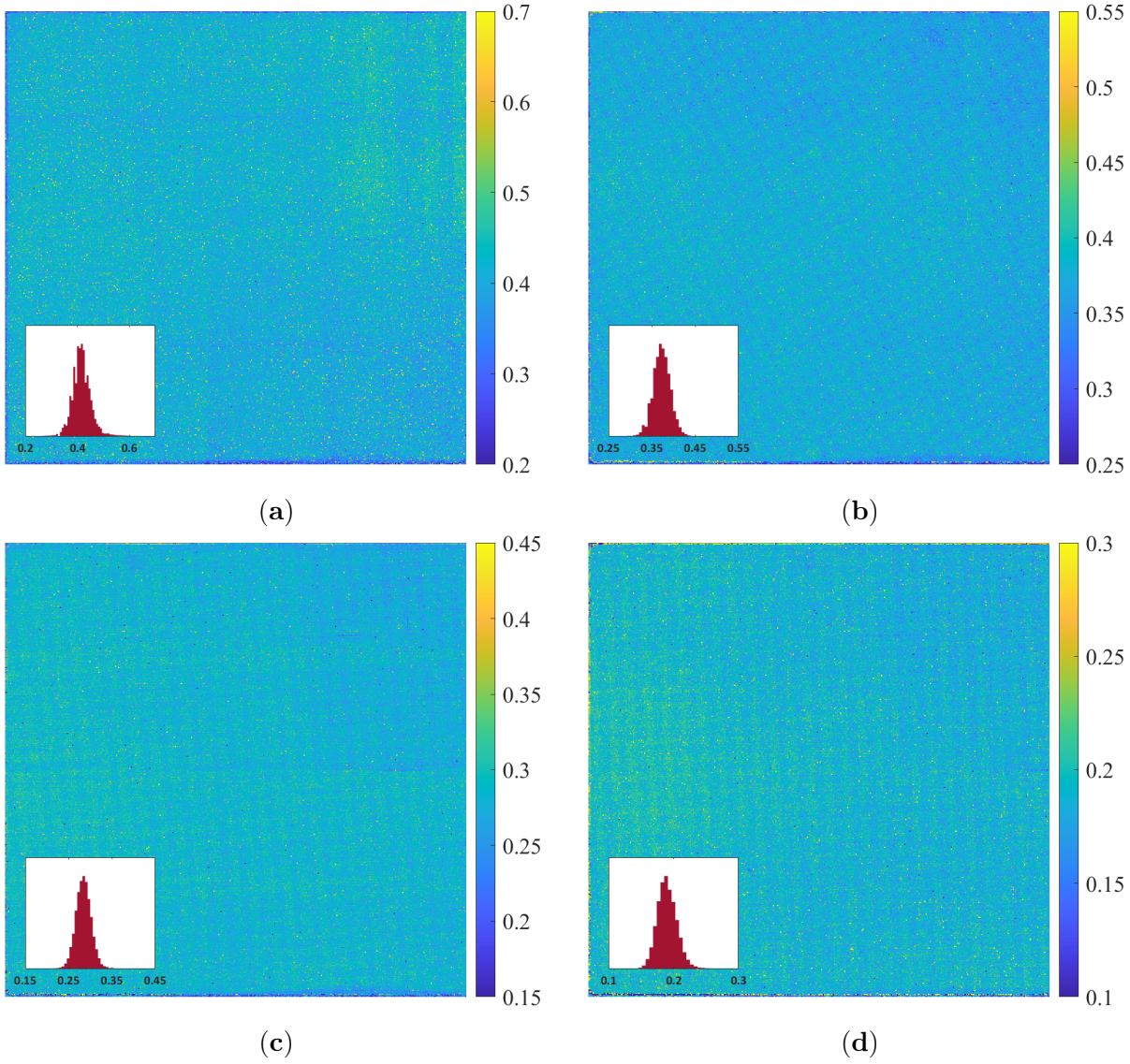
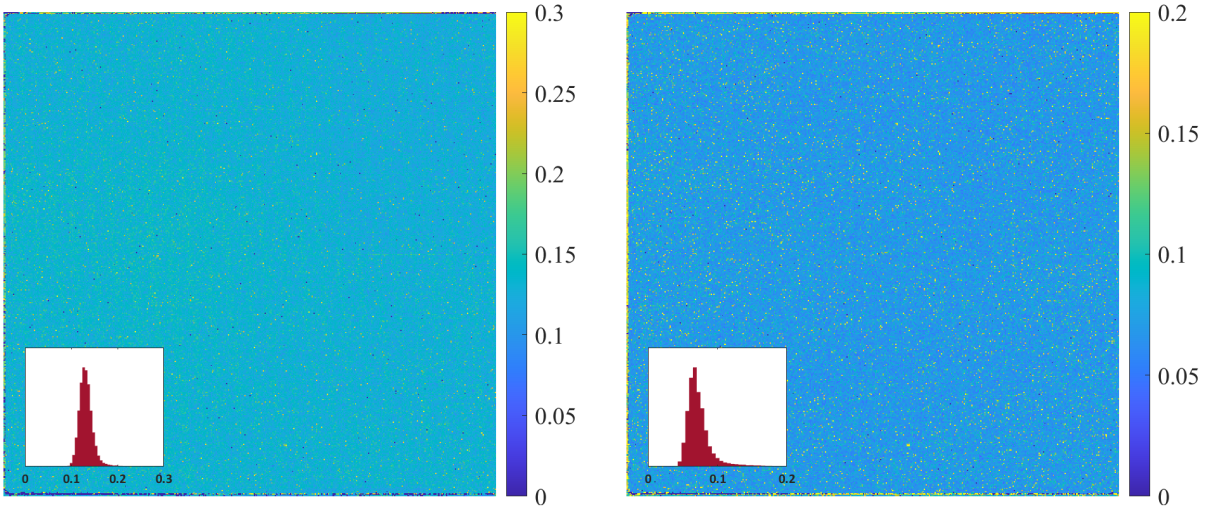


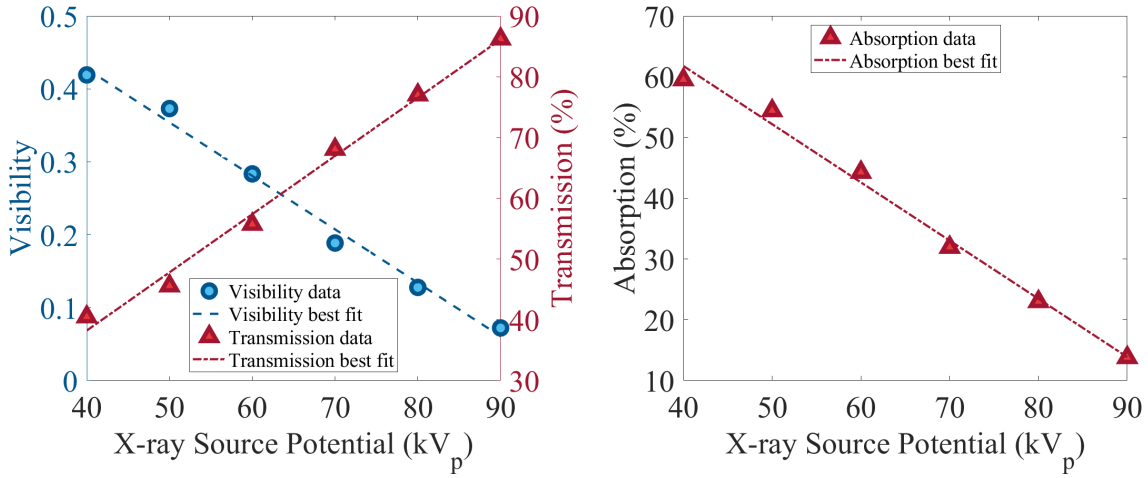
Figure 4.27: Illustration of the visibility maps of the fabricated silicon-based micropillar X-ray grating using a polychromatic microfocus X-ray source with the current of 200 μA and working potential of (**a**) 40 kV_p, (**b**) 50 kV_p, (**c**) 60 kV_p, and (**d**) 70 kV_p; all the insets are visibility histograms with their peaks representing the grating visibility at the corresponding X-ray source potential. The 3D X-ray Microscope, inCiTe™ (from KA Imaging, Waterloo, ON, CA) was employed for this measurement.



(**a**) (**b**)

Figure 4.28: Illustration of the visibility maps of the fabricated silicon-based micropillar X-ray grating using a polychromatic microfocus X-ray source with the current of 200 μA and working potential of (**a**) 80 kV_p and (**b**) 90 kV_p; all the insets are visibility histograms with their peaks representing the grating visibility at the corresponding X-ray source potential. The 3D X-ray Microscope, inCiTe™ (from KA Imaging, Waterloo, ON, CA) was employed for this measurement.

Moreover, transmission and absorption characteristics of the fabricated grating were investigated at various X-ray energies shown in Figure 4.29. Although the results in Figure 4.29 are sufficient for XPCi, higher visibility, if desired, could be achieved by increasing the number of layers in the multi-layer grating fabrication process to create a higher contrast between the absorbed and transmitted X-ray patterns on the X-ray projection.



(**a**) (**b**)

Figure 4.29: Visibility, transmission, and absorption characteristics of the silicon-based micropillar X-ray grating versus various X-ray source potentials.

4.5 Conclusion

In this chapter, we presented a scalable fabrication process for the fabrication of large-area, high-resolution X-ray absorption gratings—undertaken in a university lab with no specialized equipment. The reported method relies on a self-aligned multi-layer technique based on a conventional UV-LIGA lithography process to fabricate high aspect ratio micron-scale structures. Furthermore, the process does not require any specialized processing steps or equipment such as access to synchrotron facilities for X-ray LIGA, deep reactive ion etching (DRIE), or even atomic layer deposition (ALD) commonly seen in silicon-based fabrication processes.

By stacking multiple layers of the same grating design (multi-layer structures) through a backside self-aligned UV flood exposure technique, larger area X-ray gratings can be realized in an established and mature large-area thin film electronics processing facility. Table. 4.2 demonstrates a summary of the limitations and potentials of various X-ray absorption grating fabrication process methods. Even with our first prototype, we achieved a total absorption grating thickness of 40 μm for SU-8 micropillars of 4 μm in diameter and 16.2 μm period (with three layers), with an average visibility of 0.28 at 60 kV_p. We also demonstrated aspect ratios of up to 13:1 with 1.5 μm diameter SU-8 micropillars (with two layers), all following an unoptimized process using SU-8 2015 which provided only a thickness of 12-14 μm for each layer. If we consider phase contrast mammography

Fab. Process / Parameter	Silicon-based	X-ray LIGA	UV LIGA	Multi-layer UV LIGA
Conventional lithography equipment	Yes	No	Yes	Yes
Typical area	<4" square [36]	< 4" square (limited by X-ray beam size and uniformity [115, 116])	>12" square (large area glass substrates compatible [120, 121])	>12" square (large area glass substrates compatible)
Typical aspect ratio for grating with fine features	60:1 [36, 145]	50:1 [35, 86]	5:1 (with conventional techniques)	13:1 (first demonstration with unoptimized process)

Table 4.2: A summary of limitations and potentials of various X-ray grating fabrication process methods.

application, where a polychromatic beam of 30 kV_p (i.e., X-ray energies of around 22 keV) is typical, then a 40 μm thick gold grating that stops almost 90% of incident 22 keV X-ray photons is potentially sufficient. This implies the prototype grating fabricated in this work has an X-ray attenuation profile that is suitable for 30 kVp X-ray mammography, a prominent X-ray phase contrast medical imaging application.

X-ray absorption gratings are fundamental components in all grating-based XPCi systems, as they directly determine all salient image characteristics. This chapter has addressed a key technological bottleneck in the commercial deployment of grating-based XPCi systems and paves the way for both clinical and non-clinical applications of XPCi where better visibility, higher X-ray energies, larger field-of-view, higher spatial resolution, and/or compact imaging are desirable.

This chapter partially fulfilled the second objective of the thesis, namely developing a scalable, large-area, fabrication process for a high-resolution, high aspect ratio X-ray grating for large area X-ray imaging applications.

Chapter 5

Application of High-Resolution X-ray Phase-Contrast Imaging

This chapter explores the third objective of the thesis to examine and improve upon X-ray phase-contrast imaging (XPCi) system performance, particularly, single-mask XPCi configuration. The work presented expands on the use of high-resolution X-ray detectors with high-resolution gratings to create compact dose-efficient XPCi setups. Specific contributions also include a faster multi-modal information retrieval technique. Known high-resolution X-ray imaging applications using propagation-based, single-mask edge-illumination (coded-aperture), and speckle-tracking XPCi methods are examined for use with the high-resolution X-ray detector and high-resolution X-ray absorption gratings fabricated in this work as reported in previous chapters.

This chapter presents a blend of qualitative and preliminary quantitative results from an unoptimized in-house designed system. The contributions presented establish a baseline for further comprehensive quantitative studies on high-resolution compact dose-efficient multi-modal X-ray phase-contrast imaging (XPCi) systems for in vivo, micro-CT, and living sample (dose-sensitive) imaging tasks in medical, industrial, and scientific applications.

5.1 Introduction

X-ray imaging in general is a workhorse of medical imaging, and recently, high-resolution X-ray imaging is also being used in key applications such as the detection of carcinomas, micro-calcification, small fractures, and early stages of cancerous tumors. In addition, high-

resolution X-ray imaging is critical for material characterization, material differentiation, and minute crack detection in industrial imaging [2, 9, 59].

High-resolution X-ray imaging can be performed through attenuation-contrast or phase-contrast techniques [1, 2, 9, 59, 74]. The latter—which was explained in Chapter 2—is an emerging technique with higher sensitivity and contrast, especially for attenuation X-ray transparent materials.

X-ray detectors, an essential component for X-ray imaging, are classified into two main categories: indirect and direct conversion. Indirect conversion detectors suffer from low spatial resolution due to blur in the scintillator or, alternately, poor detection efficiency if the scintillator is made thin to overcome blurring. In contrast, direct conversion high-resolution X-ray detectors like amorphous selenium (a-Se) integrated with complementary-metal-oxide-semiconductor (CMOS) technology—introduced in Chapter 2—can achieve much higher spatial resolutions [52, 74]. In this chapter, we utilized an early 4K×4K prototype of a novel high-resolution a-Se CMOS hybrid direct conversion X-ray detector that was designed and developed—in our group—at the University of Waterloo [70]. We used the above-mentioned detector to investigate XPCi systems using propagation-based (PB-XPCi) and edge-illumination (EI-XPCi) methods.

PB-XPCi is investigated using a microfocus X-ray source to emphasize the high resolution performance of the micron-scale pixel pitch X-ray detector. The PB-XPCi method, using such a high-resolution X-ray detector, does not require any sophisticated optical apparatus to reveal micron-scale feature sizes of objects and, in fact, can easily highlight the boundaries of internal structures of objects where the refractive index changes abruptly—through a phenomenon called edge-enhancement. Qualitative analysis of this method is beneficial in applications where the detection of boundaries is of high importance, such as tomosynthesis in dental imaging or crack detection in non-destructive testing (NDT) in the industry. Quantitative analysis based on the PB-XPCi method, however, is not as straightforward as other methods—such as grating-based; if anything, PB-XPCi information retrieval can be performed based on multiple X-ray projections—at different X-ray energies or distances—which comes at the cost of lower dose-efficiency, less precision, or loss of information. This method provides merely one additional information—phase—which is computationally intensive to be retrieved from a single X-ray projection when the object of interest is composed of more than two different materials. Overall, PB-XPCi, with its simple setup, becomes impractical in quantitative analysis.

On the other hand, grating-based XPCi systems offer higher sensitivity and contrast compared to other methods—such as propagation-based. They also offer multi-modal information—absorption, phase, and dark-field—through a single X-ray projection. In the three images acquired through grating-base XPCi methods, absorption indicates the

attenuation properties of an object; phase reveals the X-ray refraction at the boundaries where the refractive index changes; however, dark-field deals with sub-resolution scale feature sizes in a sample. The dark-field image is important as it highlights inhomogeneities in the refractive index of a sample at resolutions higher than the system's, thereby allowing structures significantly smaller than the system resolution to be studied [22, 146]. The dark-field image helps differentiate materials with dissimilar internal structures at the microscopic level that share similar absorption and phase characteristics [18, 20, 22, 147].

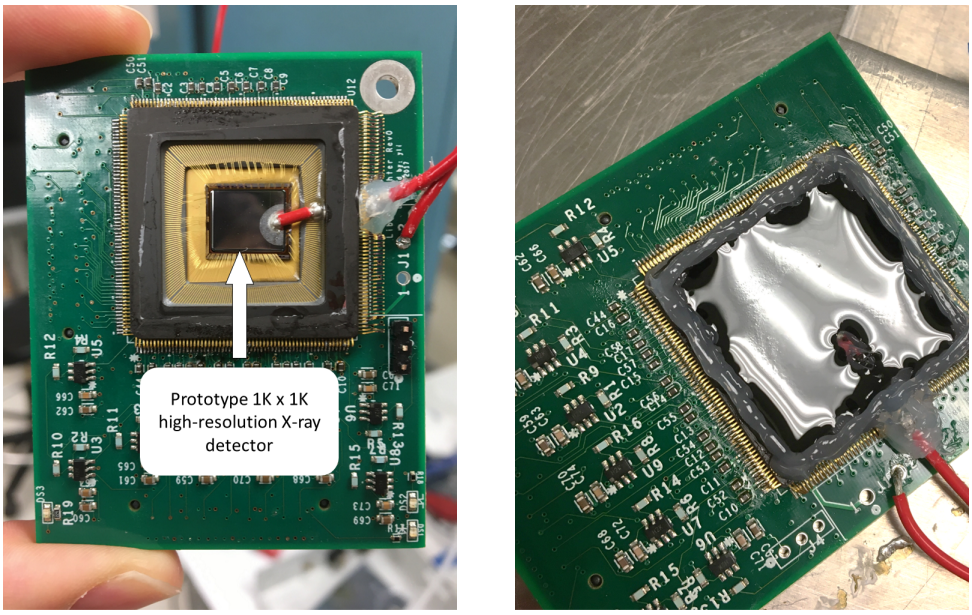
As explained in previous chapters, X-ray absorption gratings are central to grating-based XPCi methods. In particular, employing high-resolution X-ray gratings is integral to high-resolution imaging systems. High-resolution X-ray absorption gratings become exceptionally fundamental to compact systems due to stringent requirements on the resolution of systems. High-resolution grating-based XPCi systems, with the three distinct images they provide, can potentially facilitate the quantification and detection of cancerous tumors, microcalcifications in mammography, and pulmonary emphysema (a chronic obstructive pulmonary disease) in medical diagnosis. These systems also enhance material characterization, detection of hazardous substances, and quality control in industry and security applications [148].

Among various methods of grating-based XPCi, we have focused on EI-XPCi—edge illumination or as it is known alternatively, coded-aperture. The EI-XPCi, operates based on two X-ray absorption gratings—as previously explained in Chapter 2. Despite its superiority over other grating-based XPCi, double-mask EI-XPCi is susceptible to environmental vibration in high-resolution systems [74]. Single-mask EI-XPCi modality is an alternative to double-mask EI-XPCi, which only employs the pre-sample (object) absorption grating. Single-mask EI-XPCi releases the alignment condition and increases the system tolerance to environmental vibration. Moreover, it eases the system operation and complexity by removing the detector mask and, consequently, the alignment step. The other advantage of single-mask EI-XPCi is its higher dose efficiency, thanks to the second mask removal. We, therefore, focused on the single-mask EI-XPCi by employing our high-resolution micron-scale pixel pitch X-ray detector alongside the X-ray absorption gratings fabricated in Chapter 3 and Chapter 4. Both line (1D) and micropillar (2D) gratings are utilized in a single-mask EI-XPCi system to extract absorption, phase, and scattering information, all via a single exposure and in a compact benchtop setup.

5.2 Propagation-Based X-ray Phase-Contrast Imaging

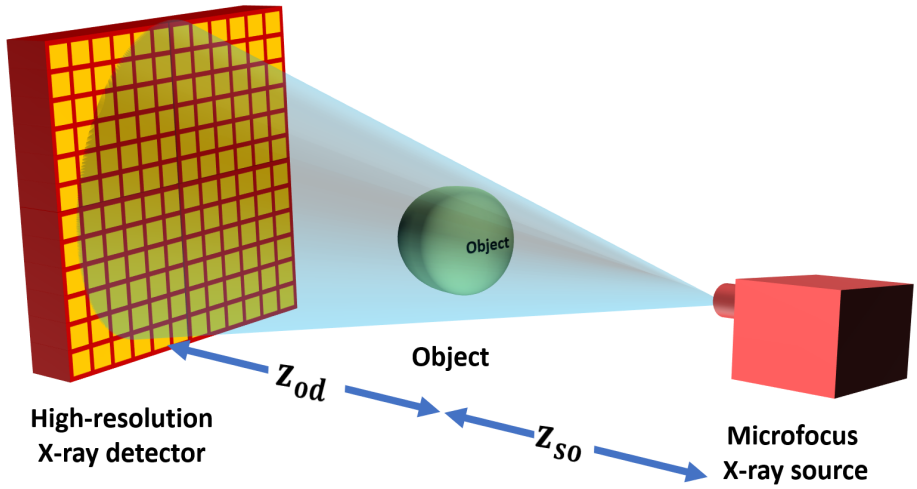
We used two different PB-XPCi systems in this work: a prototype version and a commercial setup. The prototype PB-XPCi system was set up in a two meters long X-ray cabinet—shielded with millimeter-thick lead (pb)—using a Thermo Scientific™ PXS5-927 microfocus polychromatic X-ray source with a prototype 1K×1K pixels and 7.8 μm pixel size and pitch. For some applications, a collimator was also utilized in front of the X-ray source—to limit the X-ray field-of-view—to only expose the object of interest to X-ray exposure. The X-ray source, object stage, and detector stage were all mounted on an optical rail for higher movement precision and alignment.

Figure 5.1 depicts the prototype version of the 4K×4K resolution X-ray detector, and Figure 5.2 demonstrates a schematic illustration of the PB-XPCi system (in 5.2a) as well as the prototype version of PB-XPCi setup in the X-ray cabinet with the 1K×1K prototype X-ray detector installed on the motherboard (in 5.2b).

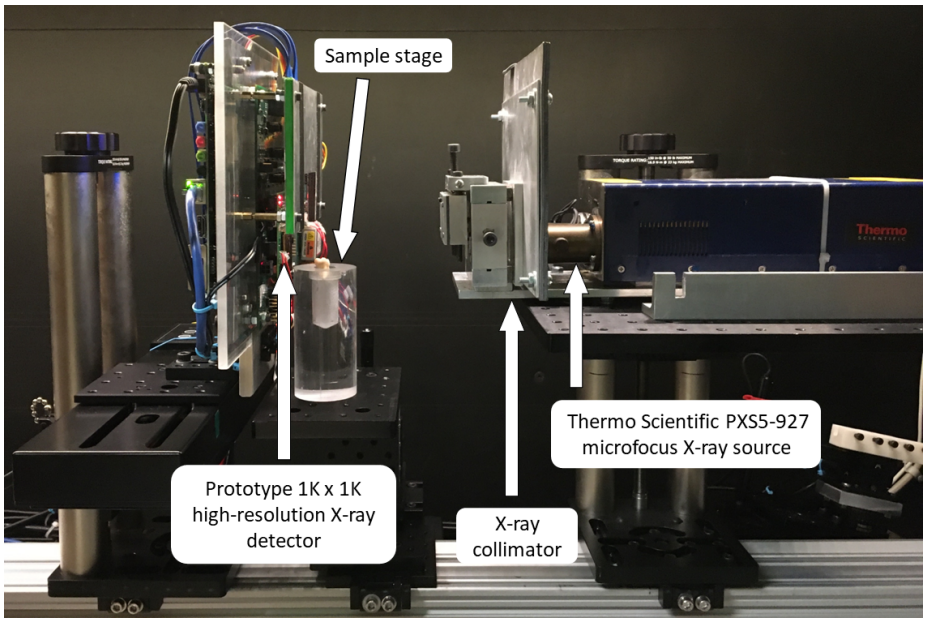


(**a**) (**b**)

Figure 5.1: Demonstration of a prototype 1K×1K resolution X-ray detector soldered on its daughterboard, (**a**) before, and (**b**) after encapsulation.



(**a**)



(**b**)

Figure 5.2: Demonstration of the PB-XPCi: (**a**) Schematic illustration of the system, and (**b**) the prototype version of the system setup mounted on an optical rail in the X-ray cabinet.

The commercial version of the PB-XPCi system under the name inCiTe™ (KA Imaging Inc., Waterloo, CA)—a 3D X-ray Microscope—employs the BrillianSe™ X-ray detector (KA Imaging Inc., Waterloo, CA)—a 4K×4K high-resolution X-ray detector with pixel size and pitch of 8 μm—alongside a tungsten target Hamamatsu L12531 microfocus polychromatic X-ray source (Hamamatsu Photonics, Shizuoka, JP).

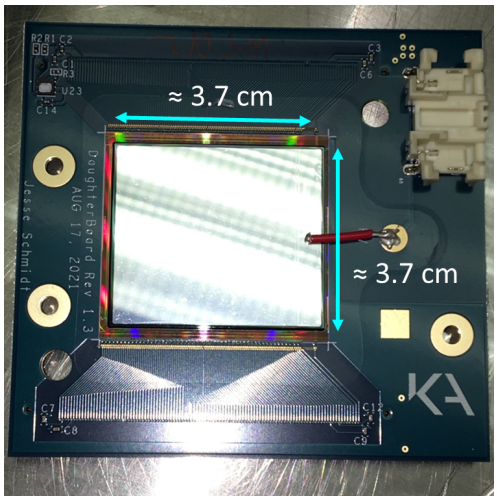


Figure 5.3: Demonstration of the prototype 4K×4K resolution X-ray detector soldered on its daughterboard.

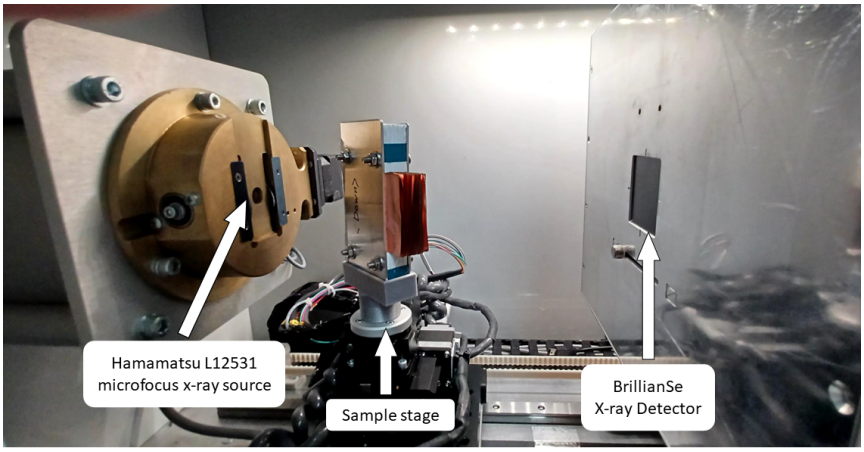
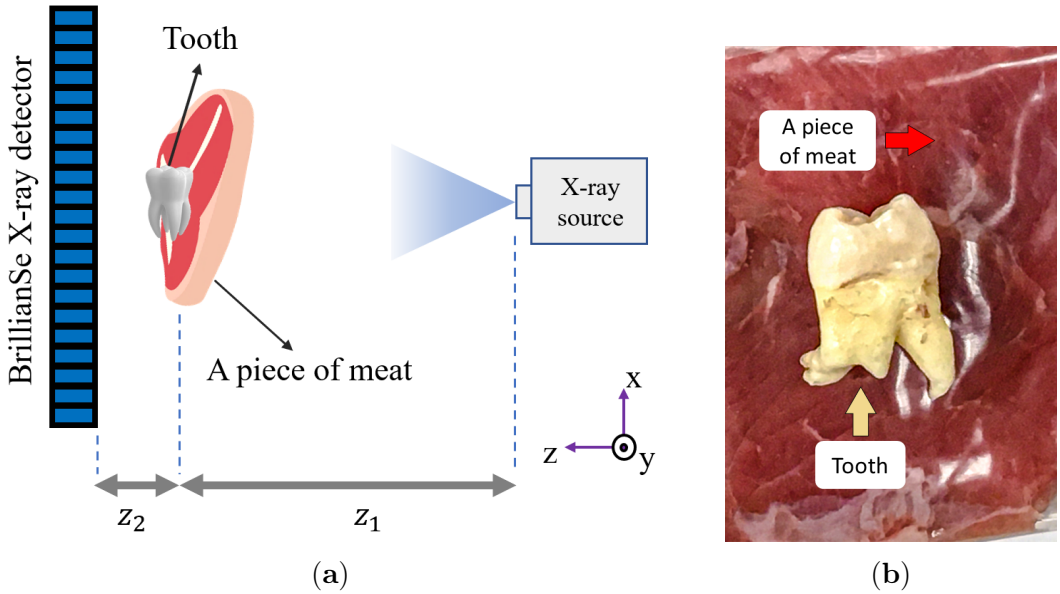


Figure 5.4: Illustration of the inCiTe™—a 3D X-ray Microscope—used for PB-XPCi in this work.

5.2.1 Intraoral Tomosynthesis

Intraoral tomosynthesis (IOT), or 2D X-ray tomography, is seeing increasing use in dental imaging [149]. Typically, the object-to-detector distance is limited (to around 4 cm), thus making phase contrast X-ray techniques unsuitable. Other techniques, such as the use of carbon nanotube X-ray sources for stationary intraoral tomosynthesis (s-IOT) have been reported to improve the imaging performance [150]. However, image quality ultimately depends on the performance of the X-ray detector. Small-feature sized cracks, root fractures, root canal obturations, tooth caries (which is the most common disorder), periodontal disease, dental implants, restorative dental materials, as well as endodontic surgery all demand high-resolution imaging [149]. Here, we investigated the potential of using the prototype 4K×4K resolution X-ray detector in conjunction with the microfocus X-ray source to achieve a higher contrast dental imaging system.

A schematic of the system used for dental imaging and an actual extracted human tooth as the sample are illustrated in Figure 5.5. To include the gum as the soft tissue, a piece of meat was placed between the tooth and detector with the piece of meat fully covering the tooth (Figure 5.5b).

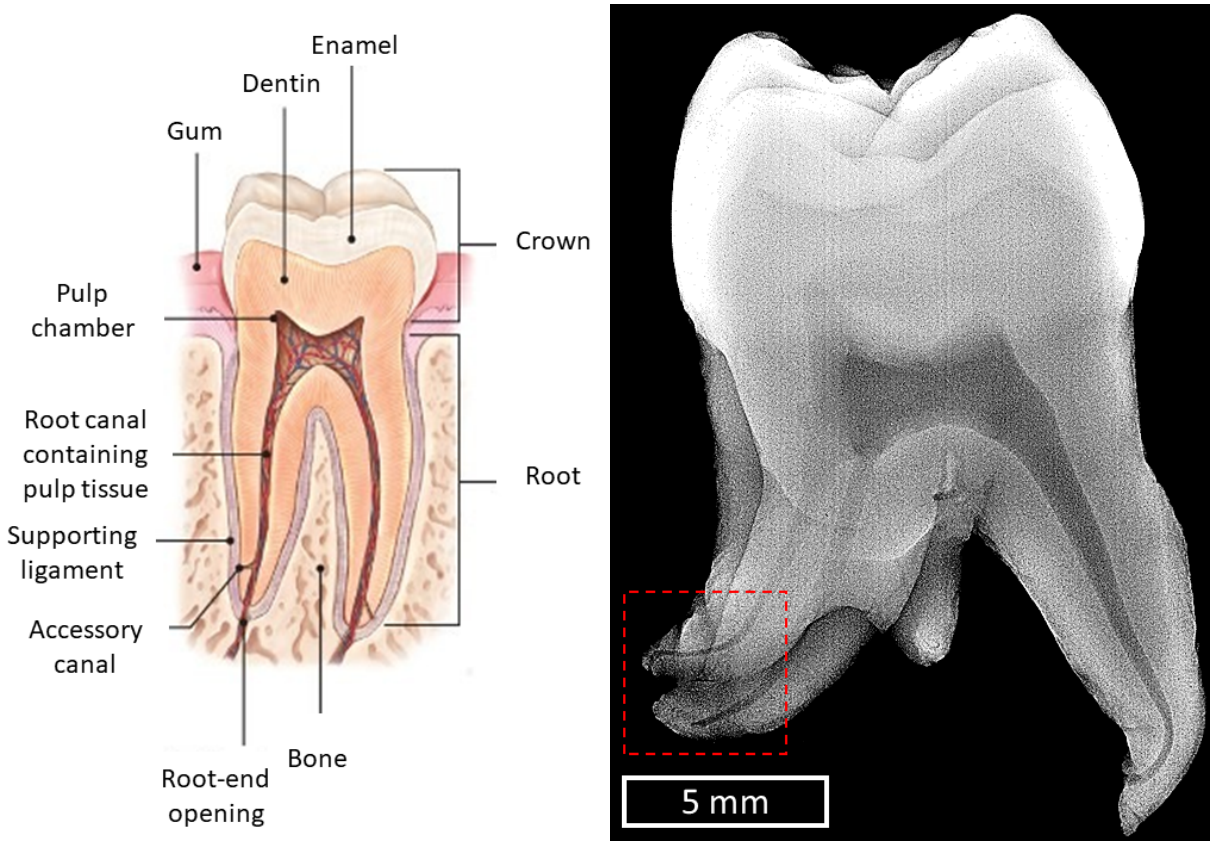


(a) (b)

Figure 5.5: (**a**) Illustration of the X-ray system model used for IOT. (**b**) The extracted tooth is covered with a piece of meat to resemble the real scenario in IOT.

We performed X-ray imaging at integration times of 800 ms, where a total number of 25 frames were captured and averaged to produce the final image. Figure 5.6 depicts the X-ray projection taken using the Hamamatsu microfocus X-ray source L12531—working at 60 kV_p and 199 μA—and the prototype 4K×4K high-resolution X-ray detector, where z_1 and z_2 are equal to 23 cm and 3 cm, respectively. It is important to highlight the realistic 3 cm distance between the tooth and detector.

Based on the images obtained, dentin, pulp chamber, and even root canals—as shown in Figure 5.6a [151]—can be seen in the X-ray projection in Figure 5.6b. We believe some of the improved imaging to be a result of propagation-based phase-contrast X-ray effects that the high-resolution detector employed in this experiment has enabled. To highlight



(**a**) (**b**)

Figure 5.6: (**a**) Schematic illustration of a tooth [151] and (**b**) the X-ray projection of the tooth covered with a piece of meat, imaged at 60 kV_p and 199 μA.



Figure 5.7: The zoomed-in view of the red dashed line region of Figure 5.6b clearly shows the root canals completely.

the efficacy of the proposed dental imaging system with the high-resolution detector, a zoomed-in view of the dashed line area (in Figure 5.6b), representing the root canal, is demonstrated in Figure 5.7. It is also worth noting that imaging was performed at a much lower current compared to conventional X-ray dental imaging. Increasing the current of the X-ray tube will only further improve the signal-to-noise ratio, and consequently the image quality.

5.2.2 Mammography

Breast cancer, which is the most common cancer and also constitutes almost 25% of all cancers in the world, plays the leading role in women's cancer mortality. Periodic mammographic screening has been shown to be an effective measure that can substantially improve the breast cancer survival rate. We aimed to investigate the feasibility and potential of employing the prototype 4K×4K resolution X-ray detector in the PB-XPCi system for mammography application. We used a tissue equivalent mammography phantom from CIRS company (model 011A) in the PB-XPCi system using the Hamamatsu L12531 microfocus X-ray source working at 60 kV_p and 200 μA, z_{so}=18 cm, and z_{od}=8 cm. As can be seen in the Figure 5.8 small-sized (as small as 250 μm) Calcium Carbonate ($CaCO_3$) grains, which represents microcalcification, can be picked up using the prototype 4K×4K high-resolution X-ray detector in a compact PB-XPCi setup. Albeit for mammographic screening larger X-ray detectors are required, this experiment reveals the potential of using such a high-resolution X-ray detector for mammography applications.

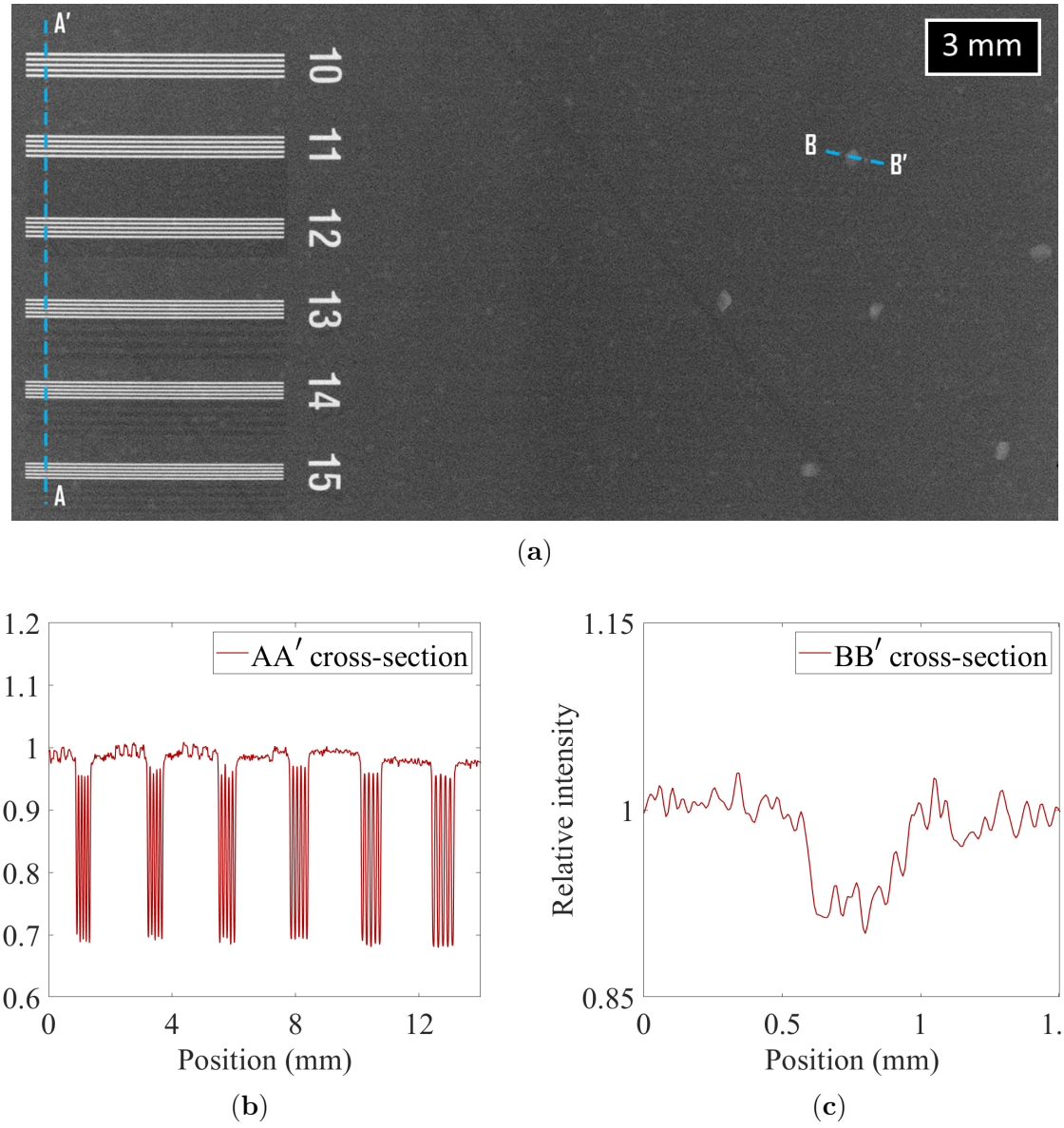


Figure 5.8: (**a**) Phase-contrast X-ray image of a tissue equivalent mammography phantom using the prototype 4K×4K resolution X-ray detector and a microfocus X-ray source at 60 kV_p, z_{so}=18 cm, and z_{od}=8 cm; (**b**) and (**c**) illustration of profiles of relative intensity along the vertical cross-section lines of AA′ and BB′, respectively. Microcalcifications as small as 250 μm are visible using the high-resolution detector and the phase contrast X-ray imaging setup.

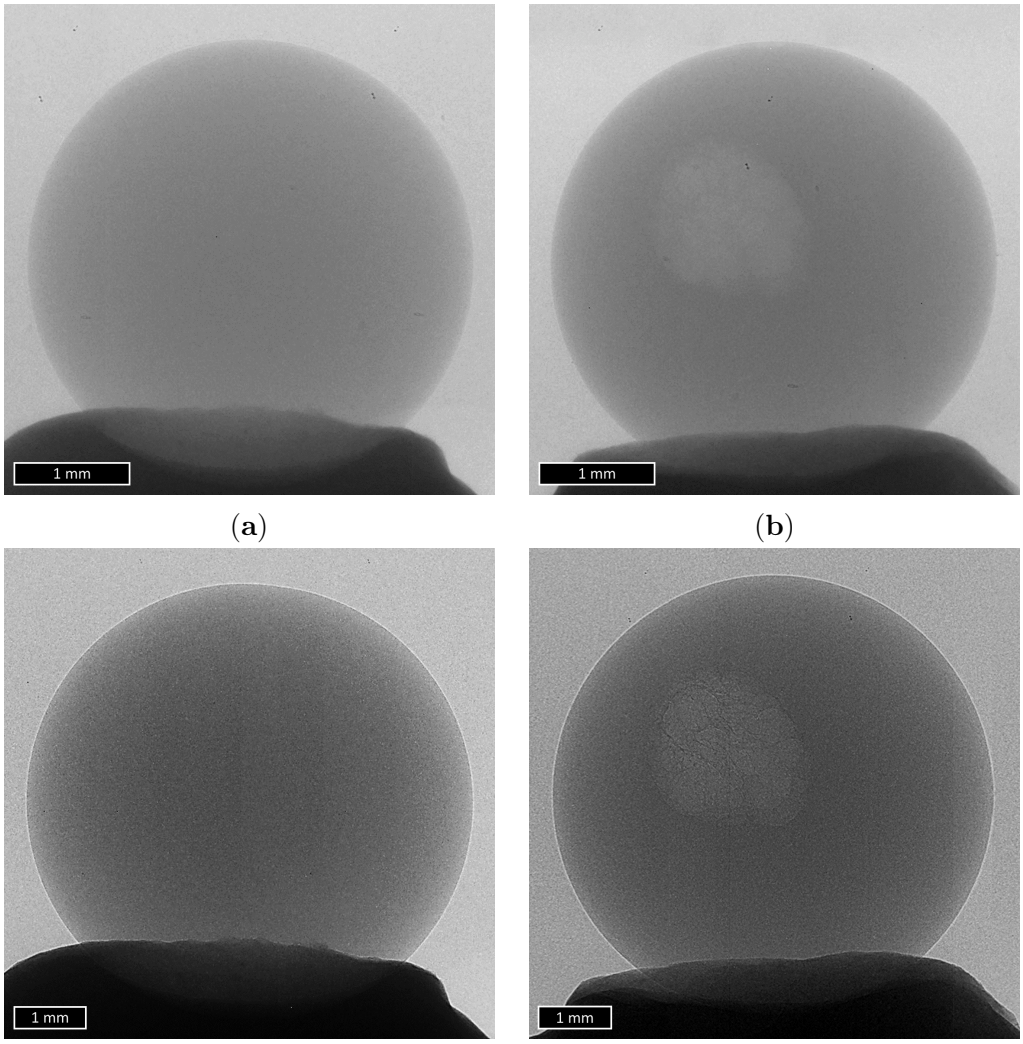
5.2.3 Microscopy

High-resolution PB-XPCi can also be utilized in microscopy to perform non-destructive testing tasks and quality control in the industry, as well as to study internal structures of biological samples in scientific applications. The high-resolution PB-XPCi method in microscopy helps visualize fine features by highlighting internal structures boundary through the edge-enhancement phenomenon in a compact setup, thanks to micro-scale pixel size X-ray detectors, such as the prototype 4K×4K high-resolution X-ray detector. The salient images produced by this method benefit from higher contrast for low and high atomic number materials, which provide considerable additional data, complementary to conventional absorption images, about the internal structures of an object of interest. Moreover, high-resolution PB-XPCi in material science, in particular, facilities the detection of low-density materials intrinsically unseen by conventional X-ray imaging—as they do not attenuate X-rays sufficiently—to analyze and characterize them in applications including but not limited to crack detection, void detection, and multiphase material studies.

Void Detection

We used the high-resolution PB-XPCi system to image plastic beads, inspecting their internal structure to visualize and locate possible defects and voids that might have occurred during the manufacturing process. Acrylic plastic beads (from McMaster-Carr, Illinois, US) with a diameter of 3.96 mm (i.e., 5/32") were imaged at two different sample-to-detector distances: 1 cm (the practical lower limit of the system) and 9 cm. The former was used as an example to demonstrate the attenuation image, while the latter represents the phase-contrast image. For both cases, the source-to-sample distance was set to 18 cm to ensure that the transverse spatial coherence is sufficient for the phase-contrast effect—considering the 9 μm focal spot size of the X-ray source. Imaging was performed using the Thermo Scientific™ PXS5-927 microfocus X-ray source working at 40 kV_p and 180 μA—with a focal spot size of 9 μm—and the prototype 1K×1K high-resolution X-ray detector.

Figure 5.9 demonstrates the attenuation and phase-contrast images of two acrylic plastic beads—with and without a defect—corresponding to the sample-to-detector distance of 1 cm and 9 cm, respectively. Edge-enhancement effect in Figure 5.9c and 5.9d highlights the boundaries as well as the void defect inside of the plastic bead more clearly. There are still some edge-enhancement effects in attenuation images in Figure 5.9a and 5.9b, thanks to the high-resolution X-ray detector used in work even at the finite 1 cm sample-to-detector distance.



(**a**) (**b**)

(**c**) (**d**)

Figure 5.9: Demonstration of attenuation images of acrylic plastic beads (**a**) without, and (**b**) with a void defect—although attenuation images include some edge enhancements thanks to the high-resolution X-ray detector used in this work. Illustration of X-ray phase-contrast images of the same beads (**c**) without, and (**d**) with the void defect. Images were taken using the Thermo Scientific™ PXS5-927 microfocus X-ray source working at 40 kV_p and 180 μA—9 μm focal spot size; with the source-to-sample distance of 18 cm; as well as the sample-to-detector distance of 1 cm and 9 cm for transmission and phase-contrast images, respectively.

PB-XPCi phase-retrieval of the acrylic plastic bead—single-material sample—is performed utilizing *ANKAphase* software [152], which works based on Paganin's retrieval method [153]. The software is written mainly to retrieve phase from single-material objects imaged with monochromatic X-ray sources—synchrotron facilities. However, the authors claimed some tolerance from the original conditions set for the software—such as polychromatic X-ray sources—are still acceptable. We tested the software to retrieve the thickness of an acrylic plastic bead (presented in Figure 5.10) with the imaging setup of 40 kV_p and 180 μA—9 μm focal spot size—polychromatic X-ray source, the source-to-sample distance of 18 cm, and the sample-to-detector distance of 8 cm.

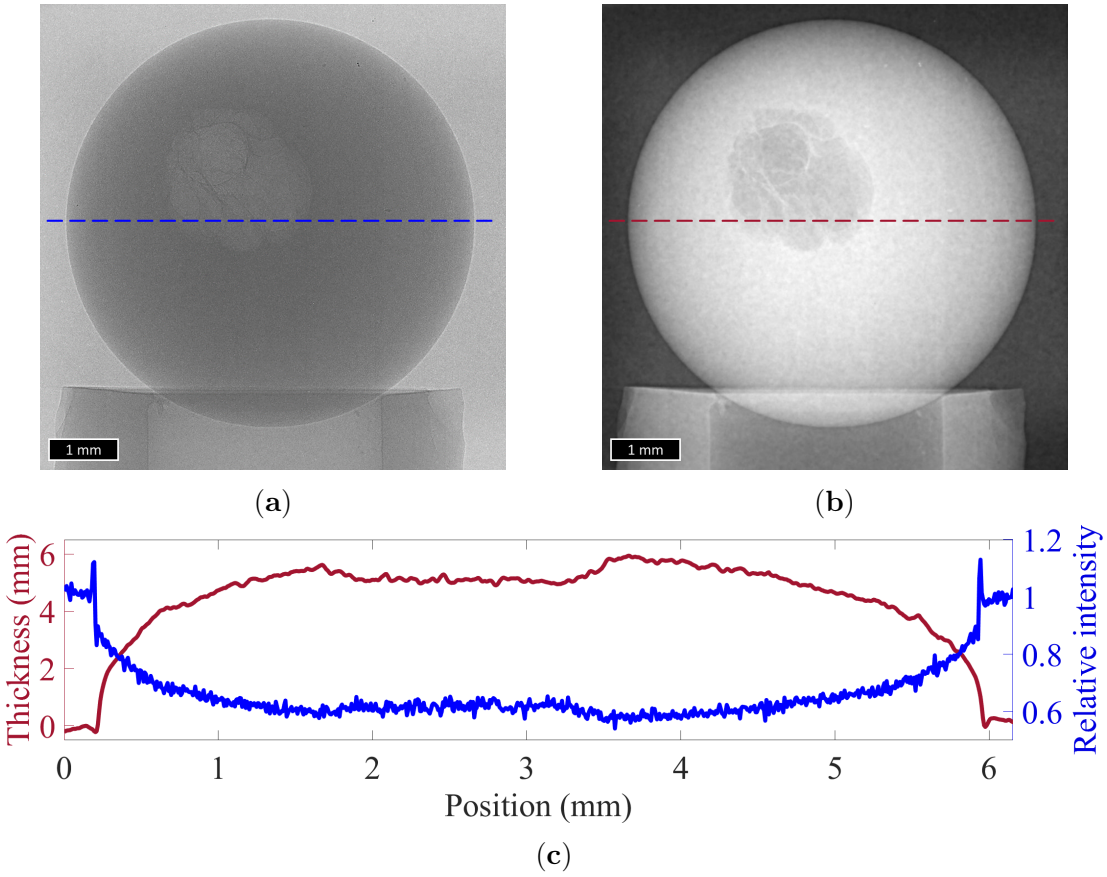
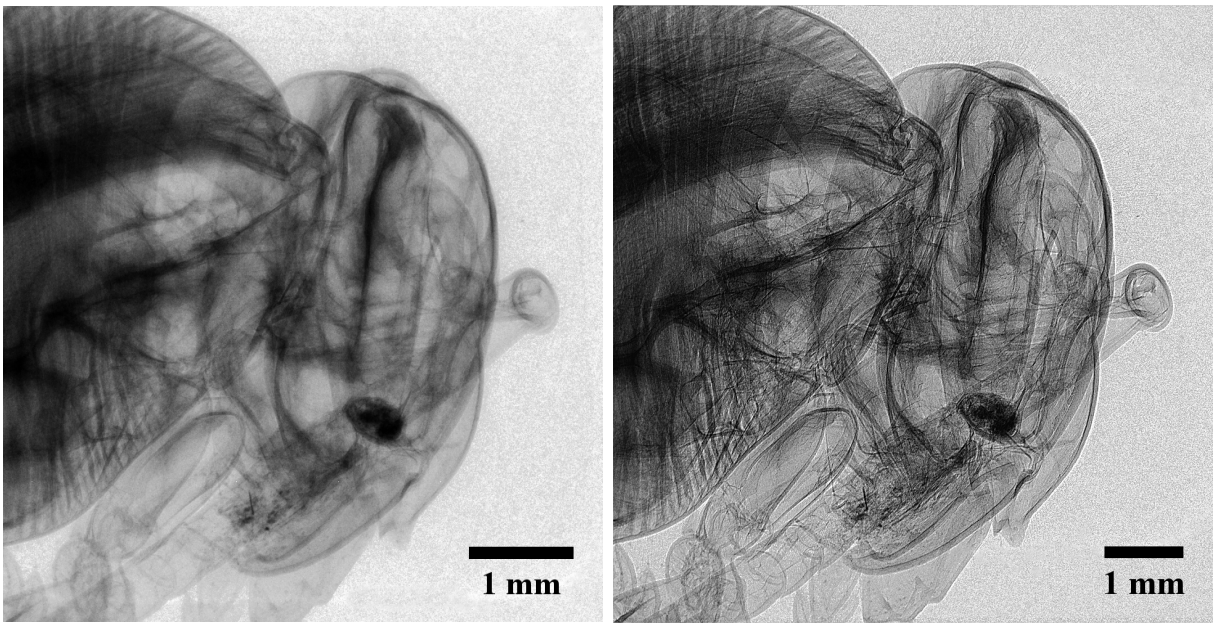


Figure 5.10: (**a**) Phase-contrast image and (**b**) thickness map image—retrieved using *ANKAphase* software—of an acrylic plastic bead, imaged at 40 kV_p and 180 μA with the source-to-sample distance of 18 cm and the sample-to-detector distance 8 cm. (**c**) A cross-sectional profile of the object thickness (red solid line) and the edge-enhancement (blue solid line) across the corresponding dashed lines.

Biological Samples

A bee head is imaged through the prototype PB-XPCi setup in two different scenarios: first when the object is close to the detector (z_{od} = 1 cm), which corresponds to the attenuation image (Figure 5.11a), and then when the detector is put further away from the object (z_{od} = 8 cm) (Figure 5.11b), which leads to a phase-contrast image. There is a small difference in resolution, roughly 7.8 μm for the attenuation image and 5.5 μm for the phase-contrast image—due to the magnification in the latter image. However, the slightly better resolution is insufficient to explain the significantly improved contrast in the phase-contrast image, which is due to phase contrast refraction effects—mainly edge-enhancement. The clear edge-enhancement around the boundaries of the bee organs observable in the phase-contrast image is thanks to the phase effect and the high-resolution detector employed, all in a compact system.

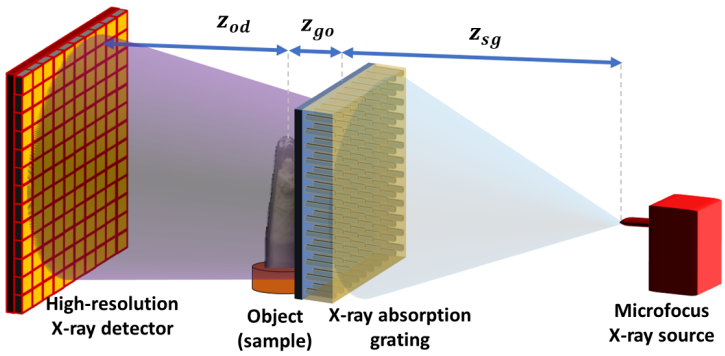


(**a**) (**b**)

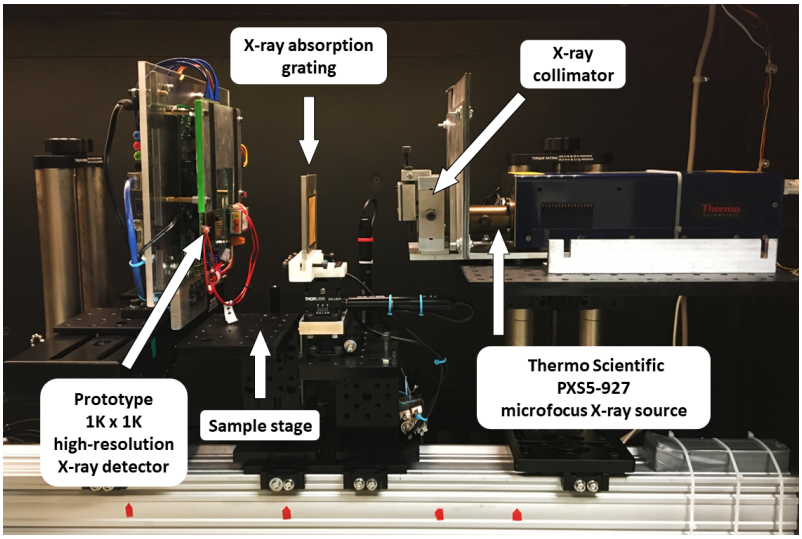
Figure 5.11: Illustration of (**a**) X-ray attenuation image of a bee head imaged at 60 kV_p, z_{so} = 18 cm, and z_{od} = 1 cm; and (**b**) X-ray phase-contrast image of the same bee head imaged at 60 kV_p and 120 μA, z_{so} = 18 cm, and z_{od} = 8 cm, using the prototype version of the 1K×1K high-resolution X-ray detector and the Thermo Scientific™ PXS5-927 microfocus X-ray source.

5.3 Edge-Illumination X-ray Phase-Contrast Imaging

For EI-XPCi, we used the same imaging systems presented in Section 5.2 with a slight modification—adding a separate stage to install the X-ray absorption grating. Figure 5.12 shows a schematic illustration the EI-XPCi system (in 5.12a) and the prototype EI-XPCi system (in 5.12b) including the Thermo Scientific™ PXS5-927 microfocus X-ray source, an



(a)



(b)

Figure 5.12: Illustration of the EI-XPCi: (**a**) Schematic view of the system, and (**b**) the prototype version of the system setup mounted on an optical rail in the X-ray cabinet; where the z_{sg} is the source-to-grating distance, the z_{go} is the grating-to-object distance, and the z_{od} is the object-to-detector distance.

X-ray collimator, an X-ray absorption grating (between the source and sample) a sample stage (between grating and detector), and the prototype 1K×1K high-resolution X-ray detector, all installed on an optical table inside the X-ray cabinet.

For the purpose of this study and to benefit from a larger detector size for EI-XPCi, we utilized the inCiTe™ system—that employs the BrillianSe™ X-ray detector. We modified the system by including a 3D-printed grating holder jig to the micro-CT stage and extending an elevated stage (sample stage) to place the object of interest in front of the X-ray grating—between the grating and detector. The modified inCiTe™ system for conducting EI-XPCi is illustrated in Figure 5.13.

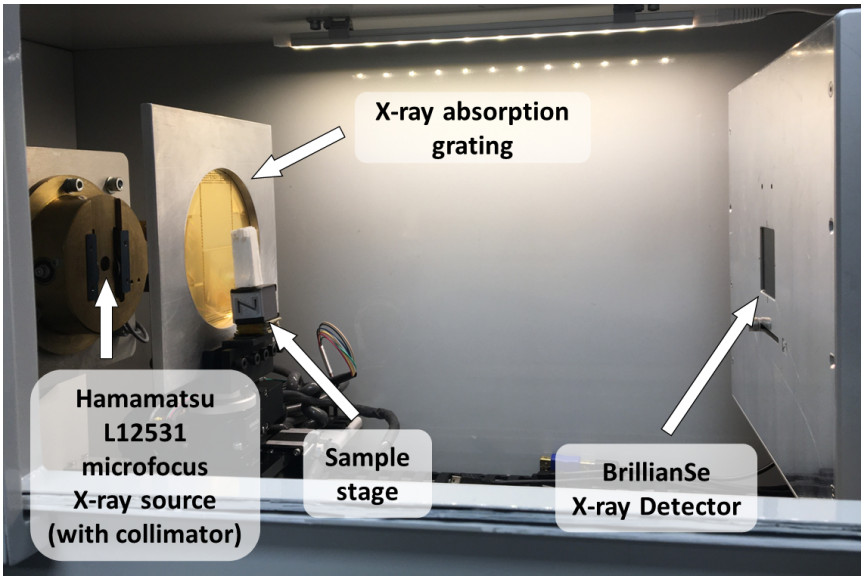


Figure 5.13: Illustration of the inCiTe™ system–that employs the BrillianSe™ X-ray detector–modified to include the X-ray absorption grating and perform EI-XPCi in this work.

5.3.1 Line Grating

A line grating was used to perform single-mask EI-XPCi, with the grating made of 90 μm thick SU-8 molds on a 500 μm-thick graphite substrate with 10 μm-wide lines (apertures) and periodicity of 79 μm. 800 μm-long SU-8 mold lines were separated with 30 μm-long bridges, as illustrated in Figure 5.14. The SU-8 mold was electroplated with gold to a thickness of approximately 80 μm, with the final grating active size being 48 mm × 48 mm.

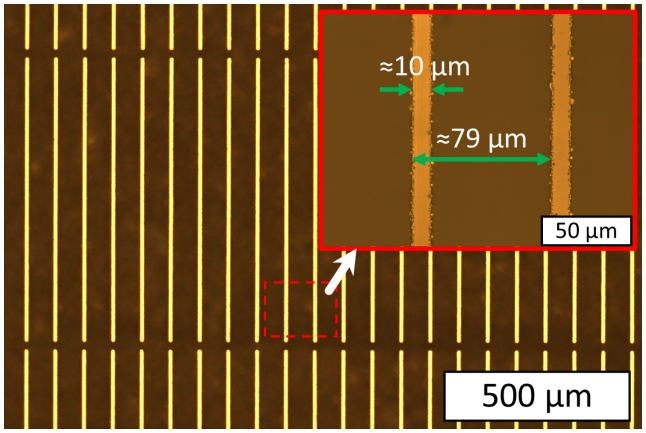


Figure 5.14: Demonstration of a line X-ray absorption grating with 10 μm-wide apertures and 79 μm period. Vertical line apertures—SU-8 molds—are separated by 30 μm bridges.

The fabricated grating was installed on an aluminum holder for handling purposes (Figure 5.12b).

Illumination Curve

Information retrieval in the EI-XPCi depends on a parameter called the illumination curve (IC)—which is simply the intensity profile of beamlets on the detector. The IC plays a central role in EI-XPCi performance, especially in quantifying the imaging information acquired. Not having sufficient information on IC results in partially missing quantitative information about the sample of interest. Obtaining the IC requires multiple, typically at least three, exposures per projection thus that the beam intensity profile can be extracted [77, 154]. In computed tomography, where a large number of projections (e.g. 1000) at different angles are captured, obtaining the IC can lead to at least three times the number of exposures to the sample, increasing radiation exposure, and lengthening imaging times. Moreover, sample motion during the three exposures can negatively impact the IC, which consequently decreases the imaging performance due to blurring.

Despite the potential advantages of EI techniques over other XPCi methods, EI's practicality is limited in imaging dose-sensitive and living samples. Here, we demonstrate how employing a very high-resolution direct conversion X-ray detector can potentially help obtain a more accurate beamlet shape through only a single exposure in a compact imaging system geometry, consequently leading to the mitigation of motion artifacts and an increase in dose efficiency.

We first simulated a single-mask EI-XPCi system (Figure 5.15) in MATLAB® through the model explained in Chapter 2. The intensity profile of the beamlets is measured by reading the corresponding pixel values, which is described in Equation (5.1). This beamlet shape is related to absorption, phase, and scattering information where it can be expressed through (5.2):

$$I_{SM-EI}(x) = S_r\left(\frac{x}{M-1}\right) * T_M\left(\frac{x}{M}\right) * PSF_d(x) \tag{5.1}$$

$$I(x) = I_0\ T(x - z_2\Delta\theta_R)\ *\ s(x) \tag{5.2}$$

where $S_r(x)$ is the source spatial intensity distribution, $T_M(x)$ is the transmission function of the pre-sample mask; $PSF_d(x)$ is the detector point spread function; $M = (z_1 + z_2)/z_1$ is the magnification—with z_1 and z_2 being the distance between source to object and object to detector); I and I_0 are the intensity profile distribution of beamlets with and without the sample, respectively; T is the transmitted portion of the beamlet passed through the

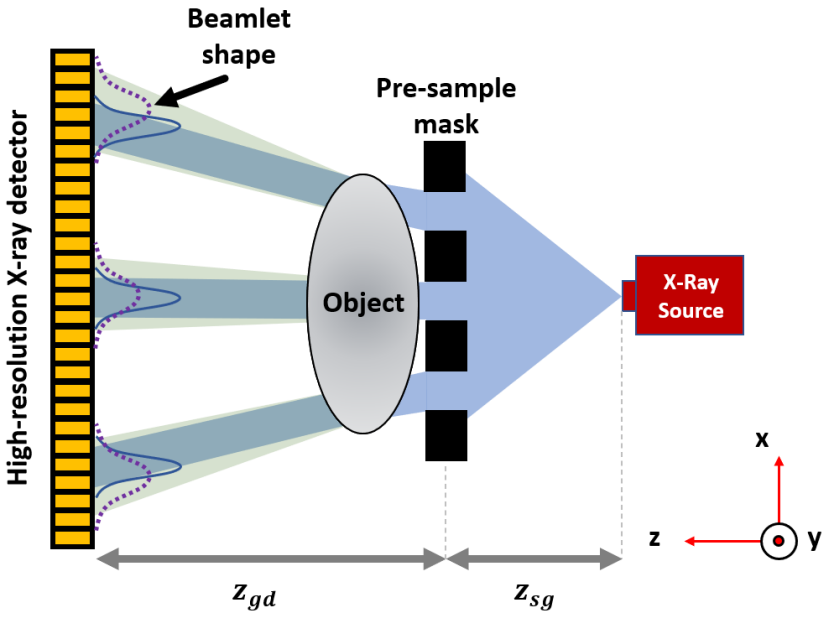


Figure 5.15: Illustration of the single-mask EI-XPCi system model used for simulation. The Gaussian profiles on the detector are the intensity profile distribution of beamlets before (solid blue line) and after (dashed purple line) definition of the object.

sample; $\Delta\theta_R$ is the refraction angle of the beamlet; and $s(x)$ is the scattering introduced by the sample.

We used the prototype version of EI-XPCi system with the Thermo Scientific™ PXS5-927 microfocus X-ray source working at 60 kV_p, 134 μA, 9 μm spot size, 8 W; a pre-sample absorption mask with 10 μm opening and 79 μm period; and the prototype 1K×1K high-resolution X-ray detector—with 7.8 μm pixel size and pitch. The z_{sg} and z_{gd} were 18 cm and 8 cm, respectively.

The simulation result of the intensity profile distribution of beamlets, without any sample defined to the system, is illustrated in Figure 5.16; the beamlets' profile, the horizontal Gaussian patterns, that are detected by groups of pixels through only a single exposure are clearly noticeable. Figure 5.17 depicts the relative intensity profile registered at the detector—in the experimental setup. The good agreement between the simulation result and experimental data (Figure 5.18) confirms the fact that an EI-XPCi system employing an ultra high-resolution X-ray detector, such as the prototype 4K×4K X-ray detector in this work, provides an accurate intensity profile distribution of beamlets through a single exposure. The small difference between experimental and simulation intensity signal levels at the far left and right plateaus is caused by the X-ray transmission – almost 20% – through the absorption regions of the grating, which is considered zero in the simulation. The final EI setup is also a compact system—with less than 30 cm source-to-detector distance—thanks to the micron-scale pixel size X-ray detector.

In a regular EI-XPCi system with large pixel size detectors, each beamlet impinges upon one individual pixel, where to extract the IC profile one must scan the pre-sample mask meticulously for N steps equally distanced by a fraction of the pre-sample mask pitch—in one period—and sample the signal intensity with respect to the position of the

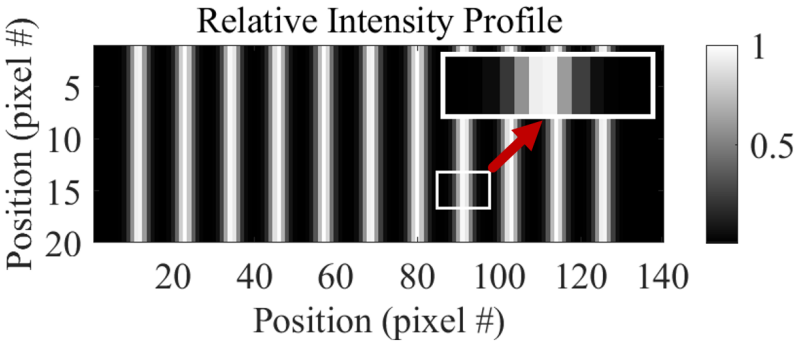


Figure 5.16: Simulation result of relative intensity profile clearly highlights the beamlet's profile (the Gaussian pattern) detected by groups of pixels.

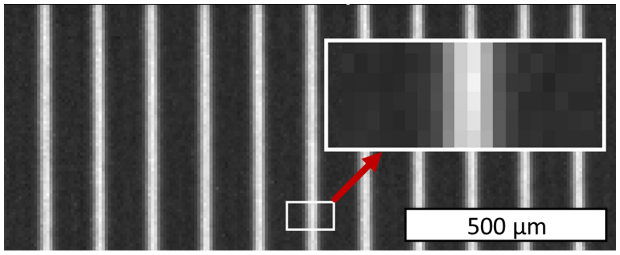


Figure 5.17: Experimental data of relative intensity profile registered at the detector shows the beamlets' profile (the Gaussian pattern) obtained from groups of pixels.

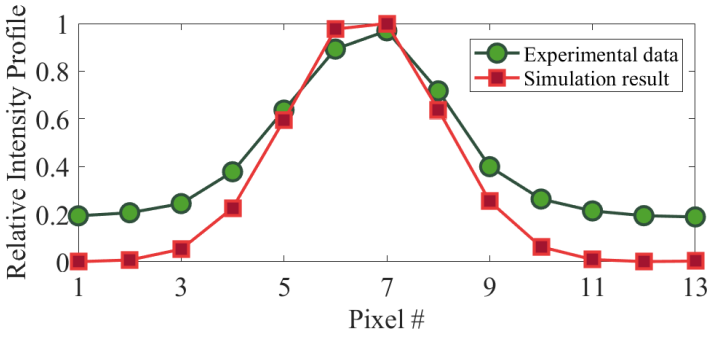


Figure 5.18: The agreement between beamlet shape from experimental data and simulation result. The higher value of lower left and right tails of experimental data is related to pre-sample mask imperfection and detector PSF.

beamlet thus a profile of the IC can be obtained. On the contrary, thanks to the ultra-high-resolution micron-scale pixel size X-ray detector, each beamlet in a single-mask EI-XPCi system can be sampled by multiple pixels—per beamlet—simultaneously. Although the high-resolution X-ray detector does not increase the imaging resolution in the single exposure technique, the well-known dithering technique can still be employed to increase the resolution of imaging. In the dithering technique, and considering the 1D (line) pre-sample grating, multiple frames are collected while the sample is moved over M sub-pixel distance steps [23, 155, 156]. The final image—a combination of all frames—possesses a resolution M times of what the detector provides. It is worth mentioning that dithering comes at the cost of increasing the dose exposure on the sample and lengthening the imaging time.

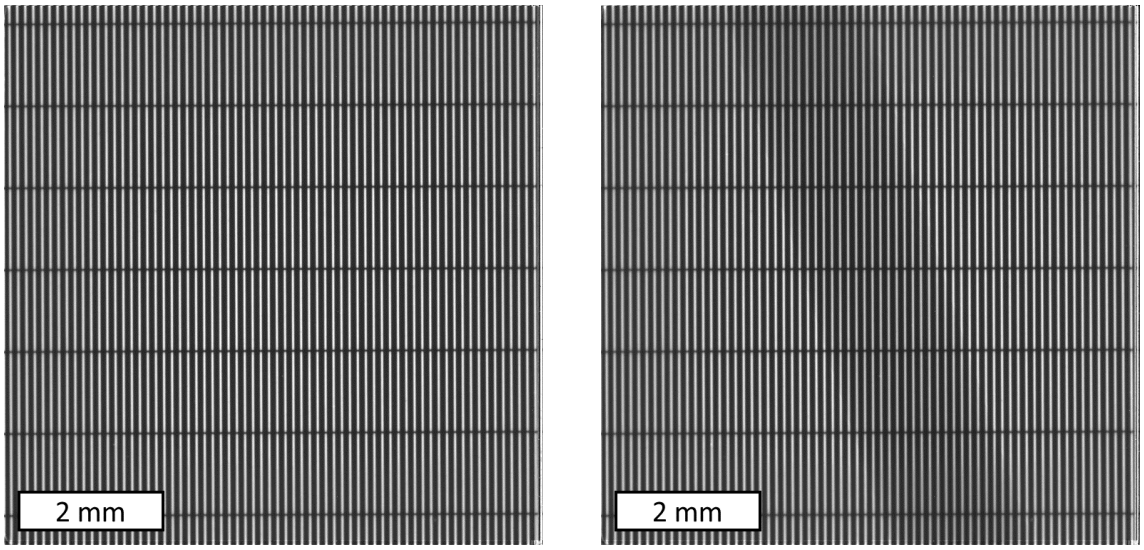
The IC, as pointed out earlier, is required for proper retrieval of the significant data necessary to obtain the three established images of absorption, phase, and scattering about an object from the X-ray projection(s). Knowing the IC profile enabled us to perform

quantitative imaging through the single-mask EI-XPCi method by employing the high-resolution X-ray detector.

Given the fact that absorption, phase, and scattering information are extracted from the obtained IC profiles, line gratings only provide one-directional sensitivity in the direction perpendicular to the mask septa. That said, details with phase shift and scattering information parallel to the mask septa become invisible in the final image.

Preliminary Qualitative Results

We first conducted imaging with the prototype EI-XPCi system, using prototype 1K×1K high-resolution X-ray detector. A polytetrafluoroethylene (PTFE) rod was imaged using the Thermo Scientific™ PXS5-927 microfocus X-ray source working at 40 kV_p and 180 μA, with the detector integrating for 1500 msec and capturing 50 frames. The source-to-grating, grating-to-sample, and sample-to-detector distances were 18 cm, 1 cm, and 7 cm, respectively. To analyze the IC profiles of the sample image and extract the three images—absorption, phase, and scattering—a reference image, in addition to the sample image, had to be taken in the absence of the sample (depicted in Figure 5.19). Information retrieval was initially performed using an algorithm by which individual IC profiles—corresponding



(**a**) (**b**)

Figure 5.19: Illustration of the (**a**) reference and (**b**) sample images of the PTFE rod imaged at 40 kV_p and 180 μm using the prototype 1K×1K high-resolution X-ray detector.

to the dataset of a group of pixels representing the IC profile—were first detected and fitted with a normal distribution. The amplitude, the center of gravity, and the full width at half maximum (e.g., FWHM, or alternatively standard deviation) values of the fitted curves represent the input data for calculating the absorption, phase-shift, and scattering, respectively—illustrated qualitatively in Figure 5.20.

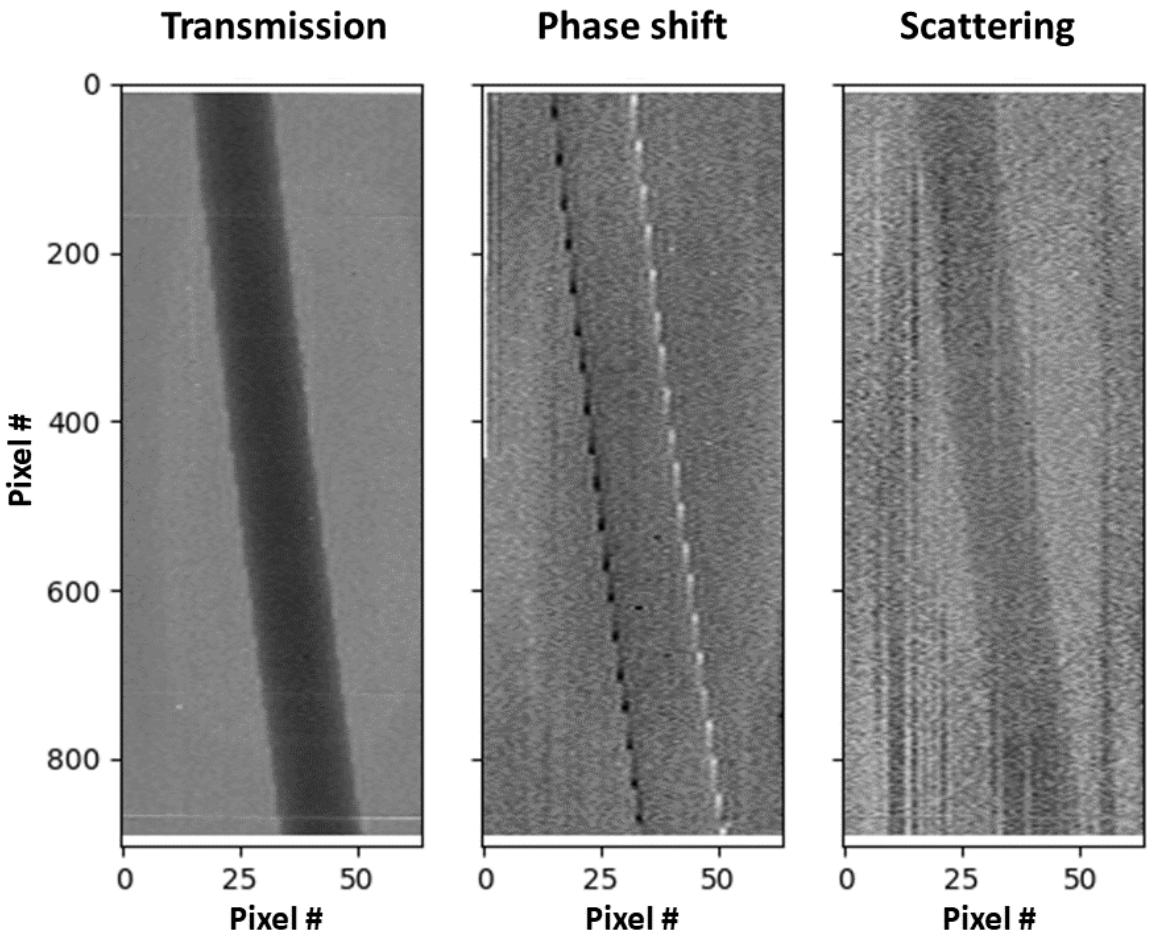


Figure 5.20: Preliminary qualitative results of (**a**) transmission, (**b**) phase shift, and (**c**) scattering of a PTFE rod imaged at 40 kV_p and 180 μA with source-to-grating, grating-to-sample, and sample-to-detector distances of 18 cm, 1 cm, and 7 cm, respectively.

Quantitative Results

After successfully retrieving information in the line grating EI-XPCi system—using the prototype setup—we proceeded to the modified inCiTe™ EI-XPCi system with the larger detector – illustrated in Figure 5.13. In collaboration with University College London—Professor Alessandro Olivo's group—we ran two different information retrieval algorithms to extract absorption, phase shift, and scattering information: Gaussian fitting and moment analysis [157].

- **Gaussian fitting**: An analogous approach to what was used for fitting IC profiles – in the qualitative analysis – has been employed for Gaussian fitting here. The algorithm was implemented in Matlab which takes a reference image (e.g., with the object absent) and a sample image (e.g., with the object present) as the inputs, and runs based on detecting periodic datasets—the IC profiles—and fitting them to Gaussian distributions with regard to Equation 5.3:

$$f(x) = \boldsymbol{a}\, exp\big(-\frac{(x-\boldsymbol{b})^2}{2\boldsymbol{c}^2}\big) \tag{5.3}$$

  with the $\boldsymbol{a}$, $\boldsymbol{b}$, and $\boldsymbol{c}$ denoting the height of the peak, the position of the peak, and the standard deviation of the Gaussian distribution, respectively. By comparing the aforementioned values for both images, the perturbation of the Gaussian profiles in the sample image provides the transmission, phase-shift, and scattering information of the object of interest. Although the Gaussian perturbation method results in accurate outputs, it is computationally tedious and requires graphics processing units (GPU) to expedite the processing time. This time-consuming process could cause challenges in CT tasks with a larger number of projections (e.g., 1000 projections at different angles).

- **Moment analysis**: Assuming a sample causes a scattering with scatter angle of α—as illustrated in Figure 5.21—with a propagation distance $z \gg x$, and considering $s(\alpha)$ and $f(\alpha)$ the IC profiles for with and without the sample present, the distortion occurred in the sample IC can be modelled by:

$$s(\alpha) = f(\alpha) \circledast g(\alpha) \tag{5.4}$$

  with $g(\alpha)$ denoting the scattering distribution and $\circledast$ representing the convolution operator. Thus, $g(\alpha)$ can be retrieved from experimental data and by deconvolving $s(\alpha)$ with $f(\alpha)$. By calculating the moments of M_0, M_1, and M_2 denoting, absorption,

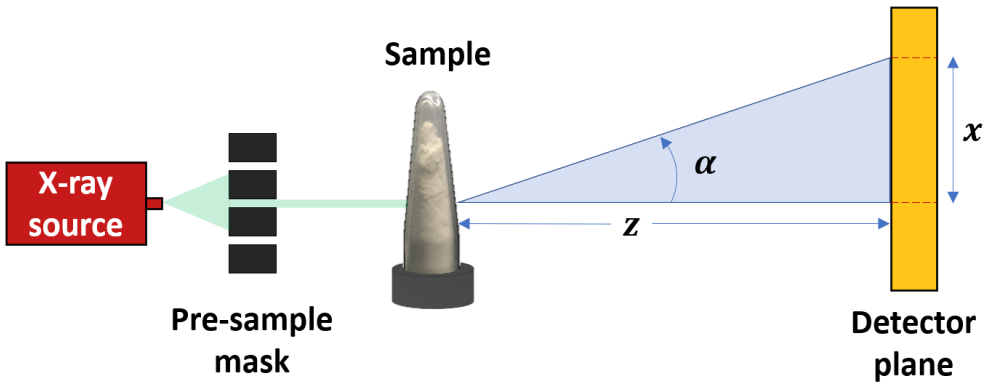
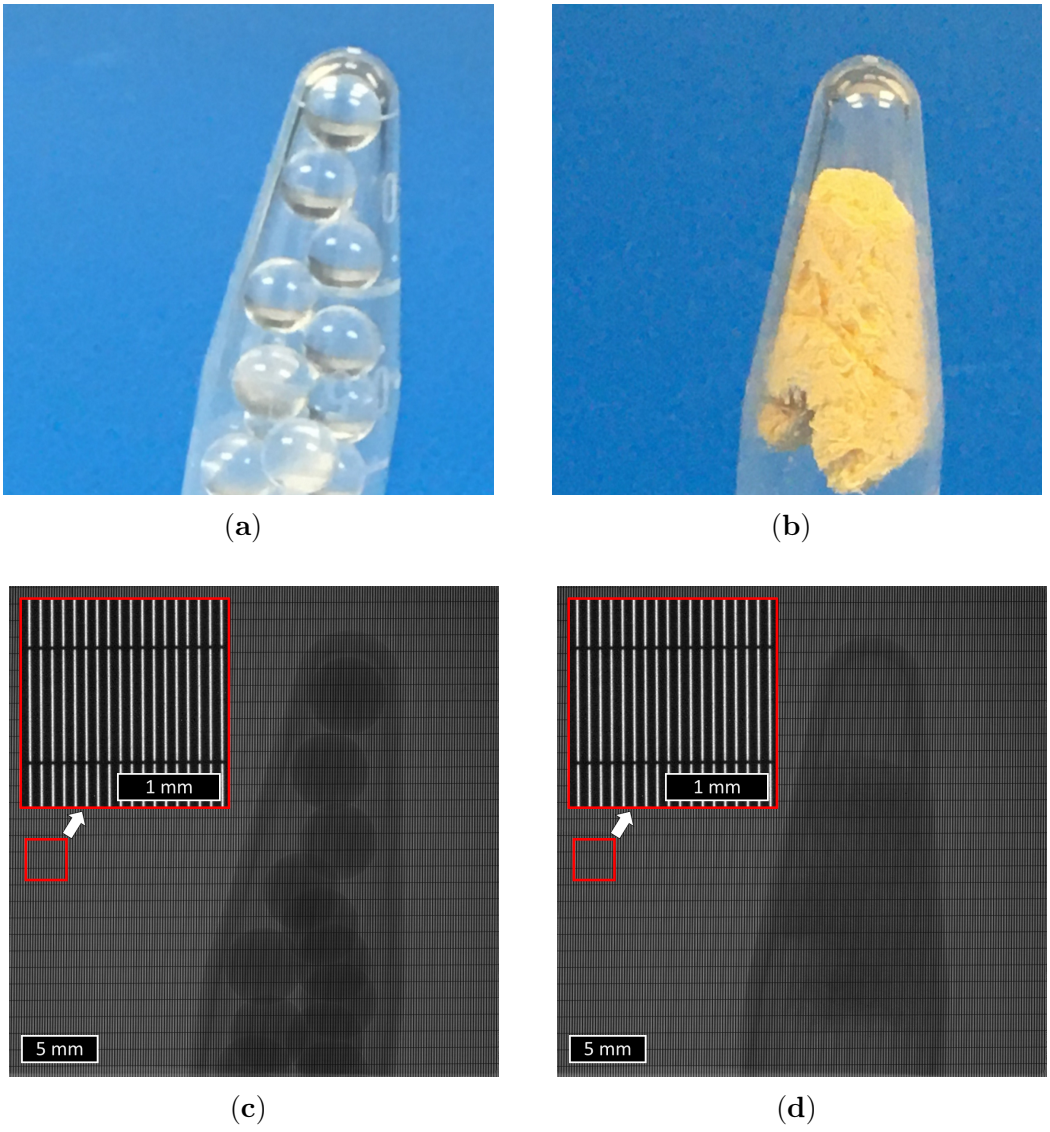


Figure 5.21: Representation of the EI-XPCi system highlighting the sensitivity to X-ray scattering by α angle for one beamlet.

phase, and scattering, respectively, one can retrieve the three established contrast images [21, 157, 158].

We examined two different objects, acrylic beads and a piece of a dry solder sponge. The former object was used to highlight the refraction of beamlets. Acrylic beads, given their semi-homogeneous internal structure, would not scatter X-rays strongly—a weak scattering image; however, the boundaries of acrylic beads refract X-rays resulting in a moderately strong phase image. Contrarily, the latter object—dry sponge—with its inhomogeneous (i.e., porous) internal structure would scatter X-rays leading to a stronger scattering image. The dry sponge phase image demonstrates a relatively weak signal, which can be explained by its fibrous skeleton not refracting X-rays greatly.

Objects were imaged with a source-to-grating distance of 32 cm, grating-to-object distance of 1 cm, and object-to-grating distance of 12 cm. The Hamamatsu L12531 microfocus X-ray source was working at 40 kV_p and 200 μA. Figure 5.22 shows the optical images of the objects alongside their X-ray projections.



(**a**) (**b**)

(**c**) (**d**)

Figure 5.22: Illustration of the optical image of (**a**) acrylic beads, and (**b**) dry sponge. The X-ray projections using the line grating in the EI-XPCi system are illustrated in (**c**) and (**d**) for acrylic beads and dry sponge, respectively. The source-to-grating, grating-to-object, and object-to-grating distances were 32 cm, 1 cm, and 12 cm, respectively. The line grating had 10 μm-wide apertures and 79 μm period. The Hamamatsu L12531 microfocus X-ray source was working at 40 kV_p and 200 μA, and we used the prototype 4K×4K high-resolution 8 μm pixel size X-ray detector.

The transmission, phase, and scattering images of the acrylic beads sample for the Gaussian fitting method are presented in Figure 5.23a-5.23c. The same information datasets retrieved from the acrylic beads sample using the moment analysis method are illustrated in Figure 5.23d-5.23f. As evident in Figure 5.23, both information retrieval methods produce almost similar transmission and phase images. However, the scattering image in the moment analysis represents a stronger signal level for the acrylic beads sample. Whereas the moment analysis scattering image has nearly captured all the beads and the container, the

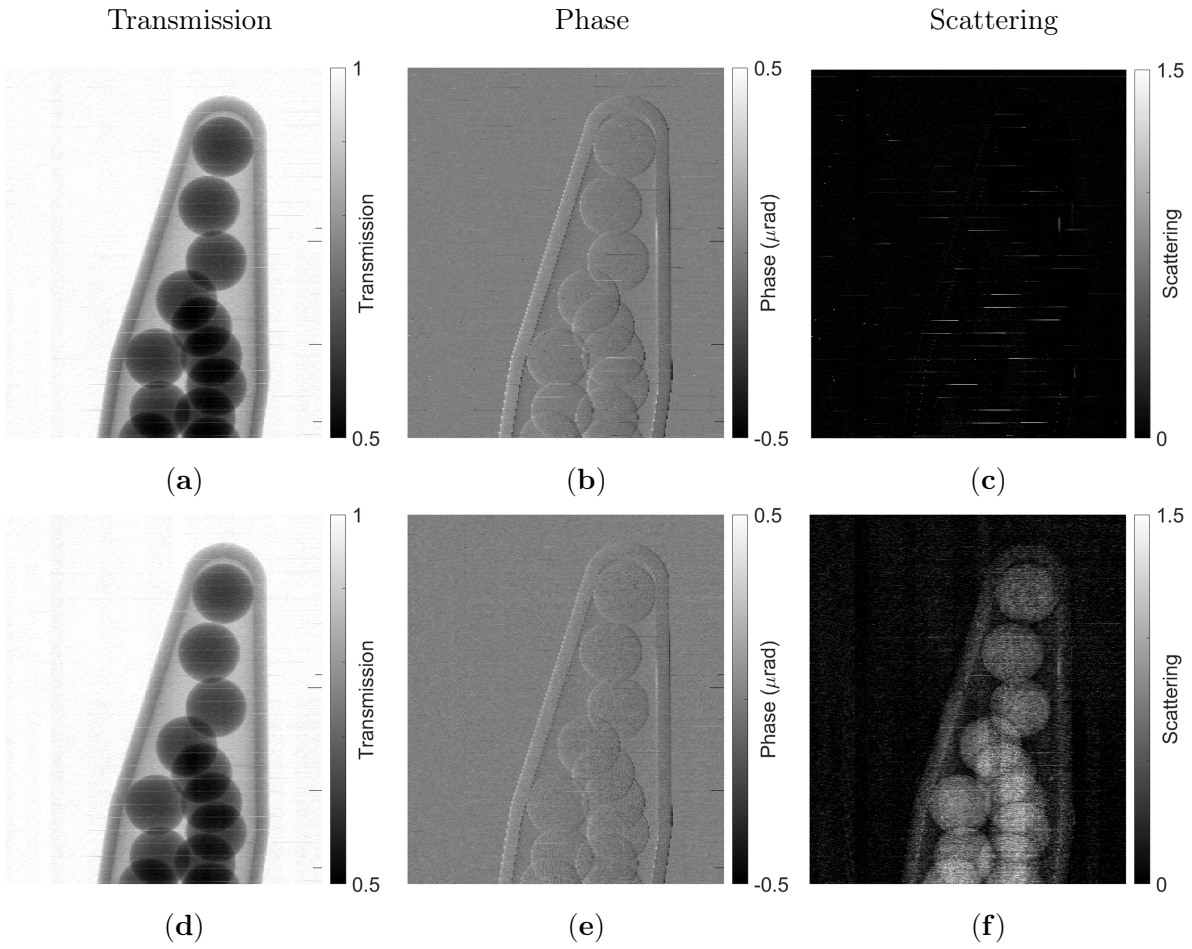


Figure 5.23: Illustration of (**a**) transmission, (**b**) phase, and (**c**) scattering images of the acrylic beads sample retrieved through the Gaussian fitting method; (**d**), (**e**), and (**f**) also represent the transmission, phase, and scattering images, respectively, of the same sample using the moment analysis method.

scattering image produced by the Gaussian fitting method has detected some boundaries of the object—mostly the outer part of the container. In contrast to the Gaussian fitting method, the moment analysis considers individual data points rather than the beamlet shape, which explains its higher sensitivity.

The transmission, phase, and scattering images of the dry sponge sample employing the Gaussian fitting method are illustrated in Figure 5.24a-5.24c. The same three distinct images retrieved from the dry sponge sample utilizing the moment analysis method are

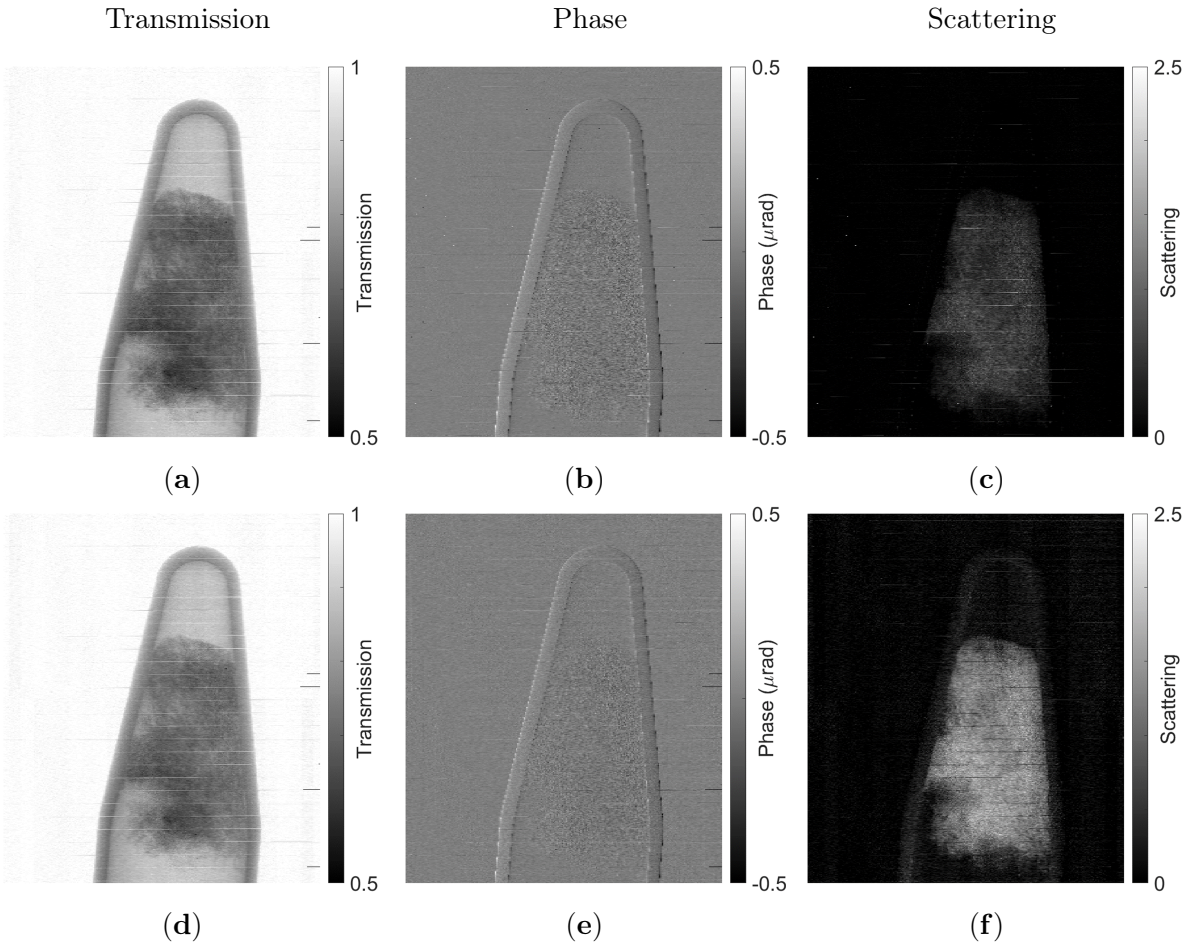


Figure 5.24: Illustration of (**a**) transmission, (**b**) phase, and (**c**) scattering images of the dry sponge sample retrieved through the Gaussian fitting method; (**d**), (**e**), and (**f**) also represent the transmission, phase, and scattering images, respectively, of the same sample using the moment analysis method.

also illustrated in Figure 5.24d-5.24f.

An analogous explanation can still be applied to the three images retrieved from the dry sponge sample. Transmission and phase images in the Gaussian fitting and moment analysis methods look alike. The phase image of the dry sponge—given its fibrous skeleton—represents a porous pattern with a moderate signal intensity, which is an indication of relatively weak X-ray refraction. On the other hand, the sponge's porosity—an inhomogeneous internal structure— creates a relatively strong scattering signal, which is observable in both Figure 5.24c and Figure 5.24f. The moment analysis, as elaborated earlier, demonstrates a stronger signal intensity than the Gaussian fitting method. We believe—for scattering information—the Gaussian fitting method produces the correct quantitative output rather than the moment analysis. However, the computation time is the advantage of using the moment analysis method over the Gaussian fitting. While the Gaussian fitting information retrieval could take tens of minutes—10 to 20 minutes depending on the algorithm, computation tool, and the image size—to process one X-ray projection, the moment analysis computation time is well below one minute for the same sample. Fourier transform application in the moment analysis shortens the computation time, which makes it advantageous and practical for CT applications.

Direction-Dependence Sensitivity

As mentioned earlier, EI-XPCi systems employing line gratings are only sensitive to objects oriented parallel to the grating septa. The object direction dependency on the grating orientation results in features perpendicular to the grating septa becoming invisible in the X-ray phase-contrast image—as depicted in Figure 5.25. This also has been experiment-

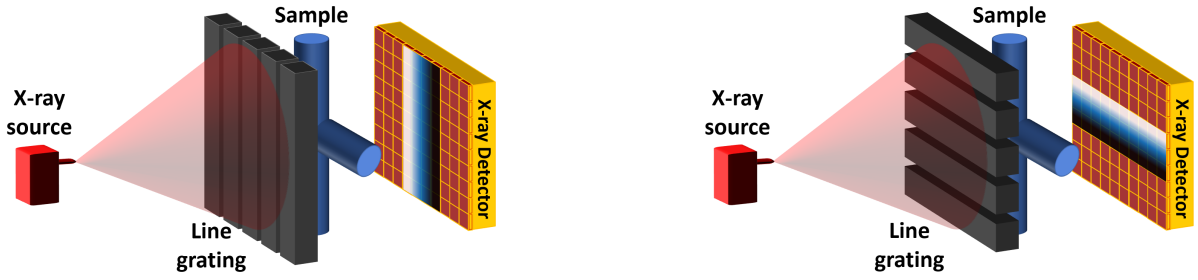
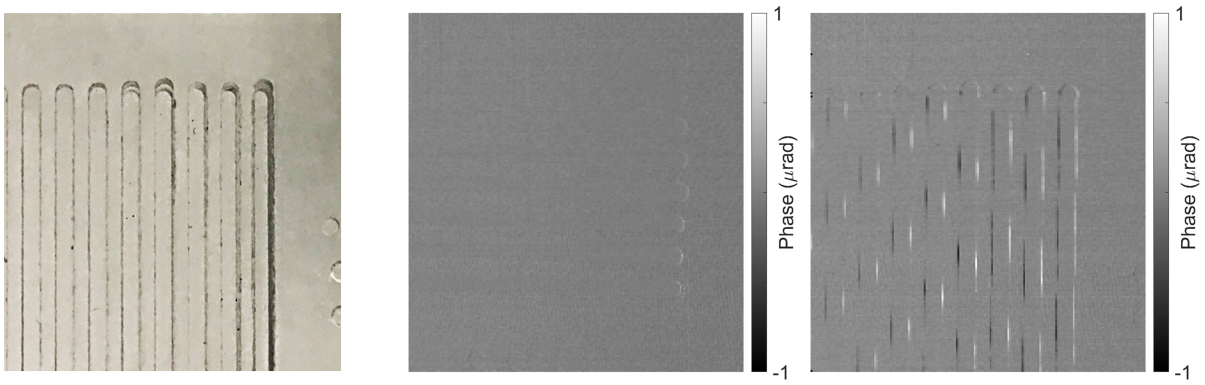


Figure 5.25: Illustration of the line grating direction dependency in imaging multi-direction oriented objects. Features perpendicular to grating septa—i.e., horizontal cylinder in (**a**) and vertical cylinder in (**b**)—become invisible in the X-ray phase-contrast image.



(**a**) (**b**) (**c**)

Figure 5.26: (**a**) Photo of the acrylic phantom with line grooves. (**b**) Illustration of the phase image of the acrylic phantom using the setup depicted in Figure 5.25a with the phantom oriented with line grooves almost perpendicular to grating septa. (**c**) Illustration of the phase image of the same phantom using the setup depicted in Figure 5.25a with the phantom oriented with line grooves almost parallel to the grating septa; the edges of line grooves appear in the phase images.

ally examined using an acrylic phantom (in-house fabricated) with multiple parallel line grooves—with 0.7 mm wide grooves and different depths from 1 mm to 3.5 mm. We conducted EI-XPCi employing the line grating in two setups with line grooves in the phantom parallel and perpendicular to the grating septa. Figure 5.26 shows the phantom and phase images at both imaging setups. The edges of the line grooves are almost invisible in the phase image—Figure 5.26b—when they are perpendicular to the grating septa. However, orienting them in the direction parallel to the grating septa increases the diffraction sensitivity of the system to the grooves, resulting in a phase image revealing the edge of the grooves—Figure 5.26c.

One solution to administer X-ray phase-contrast images with multi-directional sensitivity is to integrate – combine – multiple X-ray phase-contrast images taken at different angles to compensate for the phase information direction dependency of the object. Higher dose exposure to the object, alignment issues, and imaging time, to name a few, are pitfalls one would encounter in resolving the direction-dependency sensitivity problem with line gratings. The practical solution to overcome this impediment would be employing 2D gratings. 2D grating-based EI-XPCi systems resolve the object direction dependency on the grating by providing multi-directional sensitivity to X-rays.

5.3.2 2D Grating

Application of 2D X-ray absorption gratings in the EI-XPCi system—as stated earlier—delivers the three established X-ray image contrasts (i.e., transmission, phase, and scattering) with multi-directional sensitivity. Employing 2D gratings is the ultimate and sound solution to overcoming the object direction dependency sensitivity to phase properties of X-rays. Unlike line gratings, there is no perpendicularity correlation between the object features and the grating. Here we utilized 2D X-ray absorption gratings fabricated in Chapter 3 and Chapter 4 to realize a multi-directional sensitive EI-XPCi system. The single-mask EI-XPCi method employing the micron-scale pixel pitch X-ray detector and fabricated prototype 2D high-resolution gratings demonstrated a significantly improved performance in obtaining the three X-ray contrast modalities. Thanks to the fabricated high-resolution 2D gratings, the final system enabled multi-directional sensitivity to features in an object regardless of their orientation to the grating. Analogously, ICs profiles of the new EI-XPCi system must be obtained, albeit in two dimensions rather than one.

Illumination Curve

Despite the similar role IC profiles in 1D (i.e., line) and 2D grating-based EI-XPCi systems information retrieval play, the acquisition of IC profiles in 2D Ei-XPCi systems is different. Utilizing high-resolution micron-scale X-ray detectors in single-mask EI-XPCi systems is not just complementary but seems to be essential in obtaining 2D IC profiles. Figure 5.27 is a schematic demonstration of a system with an X-ray source, a single X-ray

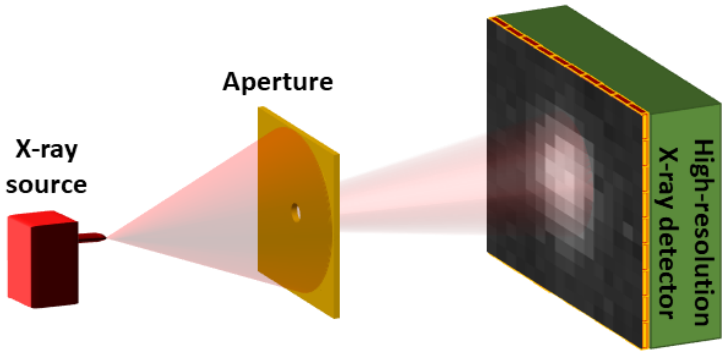


Figure 5.27: Schematic illustration of a system with an X-ray source, a single X-ray aperture, and a high-resolution X-ray detector to register the X-ray beamlet. The detector pixel size is smaller than the beamlet size.

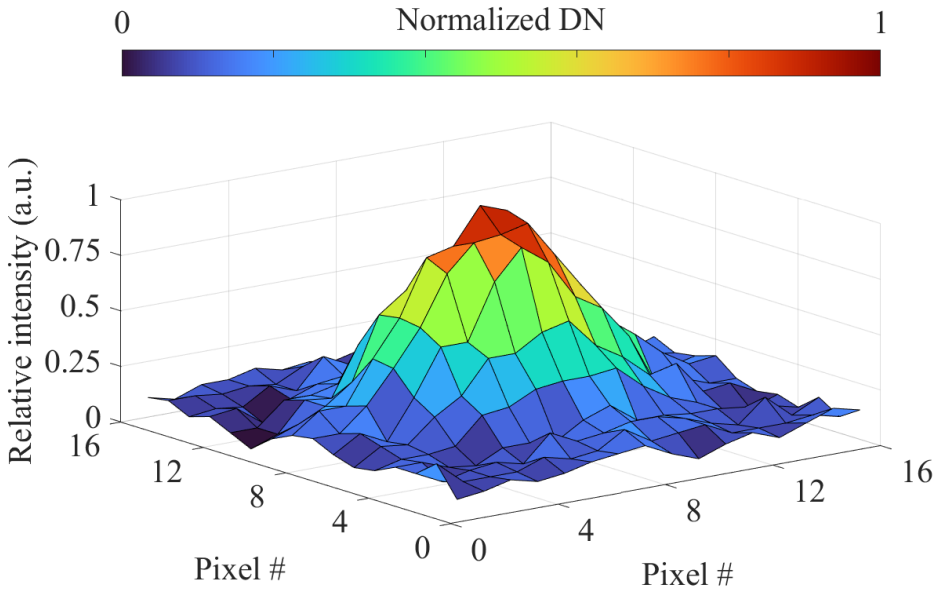


Figure 5.28: Demonstration of the two-dimensional Gaussian distribution—IC profile—of a single pencil-shape beamlet.

aperture, and a high-resolution detector. The X-ray beamlet—translated by the X-ray aperture—produces a signal intensity downstream of the aperture, which is then registered by the detector. If the high-resolution X-ray detector possesses a pixel size smaller than the beamlet, the registered image presents an observable intensity of a two-dimensional Gaussian distribution. Figure 5.28 shows the 3D distribution of the 2D Gaussian profile for a window of 16 × 16 pixels. Assuming the high-resolution X-ray detector sampled sufficient data points, the IC profile can be simply obtained by applying the Gaussian fitting method:

$$f(x,y) = \boldsymbol{a}\ exp\left(-\left(\frac{(x-\boldsymbol{X}_0)^2}{2{\sigma_X}^2}+\frac{(y-\boldsymbol{Y}_0)^2}{2{\sigma_Y}^2}\right)\right) \tag{5.5}$$

with the $\boldsymbol{a}$ denoting the height of the peak, $(\boldsymbol{X}_0, \boldsymbol{Y}_0)$ denoting the location – position – of the center of gravity, and (σ_X,σ_Y) denoting the standard deviation of the Gaussian distribution, respectively.

Figure 5.29 schematically illustrates a single-mask EI-XPCi system with a focus on pencil-shape beamlets created by a 2D X-ray absorption grating. Upon impinging on the detector, these beamlets create an intensity map of IC profiles that attribute Gaussian

parameters to the three established contrast modalities. Figure 5.30 depicts the 3D distribution of a 3 × 3 pencil-shape beamlets' intensity profile detected by the prototype 4K×4K high-resolution X-ray detector.

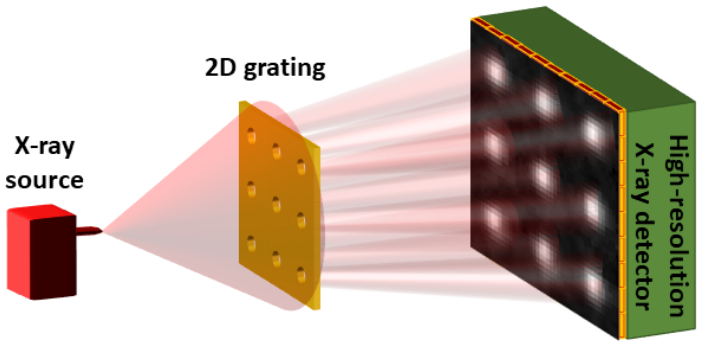


Figure 5.29: Schematic illustration of a single-mask EI-XPCi system with a 2D grating, representing the pencil-shape beamlets. The detector pixel size is smaller than the beamlets', enabling the high-resolution X-ray detector to register IC profiles with groups of pixels.

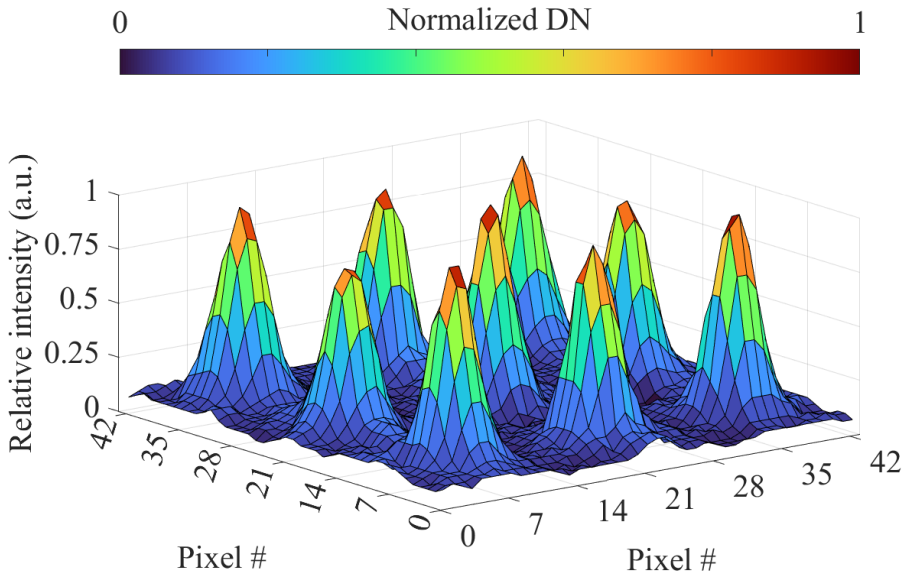


Figure 5.30: Demonstration of the two-dimensional Gaussian distribution—IC profile—of a 3 × 3 pencil-shape beamlets' intensity profile detected by the prototype 4K×4K high-resolution X-ray detector.

Quantitative Results

Obtaining IC profiles from the pencil-shape beamlets provides input data to perform quantitative EI-XPCi and retrieve the three established contrast modalities. For the sake of quantitative imaging, IC profiles with and without an object present should be obtained—namely the reference image and sample image. Five parameters—$\boldsymbol{a}$, $\boldsymbol{X}_0$, $\boldsymbol{Y}_0$, σ_X, and σ_Y—of the IC profiles can be extracted following the Gaussian fitting method for individual two-dimensional distributions detected by the detector in the 2D EI-XPCi system. Information retrieval based on the Gaussian fitting method was performed using a Python code (Appendix B). Comparing the retrieved parameters—for the reference image and sample image—results in transmission, phase shift, and scattering images.

We utilized the prototype 4K×4K high-resolution X-ray detector alongside the Hamamatsu L12531 microfocus polychromatic X-ray source in the modified inCiTe™ system for single-mask EI-XPCi as schematically illustrated in Figure 5.31. The X-ray source was working at 60 kV_p and 200 μA and imaging was performed for a centrifuge tube filled with sugar powder, as shown in Figure 5.32a. We conducted imaging employing the 2D X-ray absorption grating fabricated in Chapter 4 with the source-to-grating, grating-to-object, and object-to-detector distances of 10 cm, 1 cm, and 35 cm, respectively. The three established contrast modalities for the sugar powder sample are illustrated in Figure 5.32 represented on a false color tone.

The fabricated micropillar grating enabled the acquisition of the three established con-

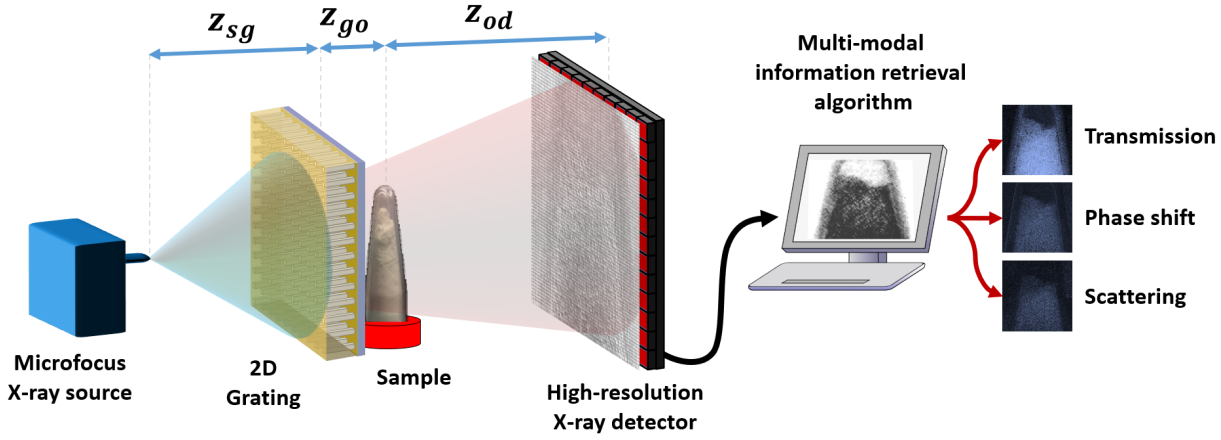
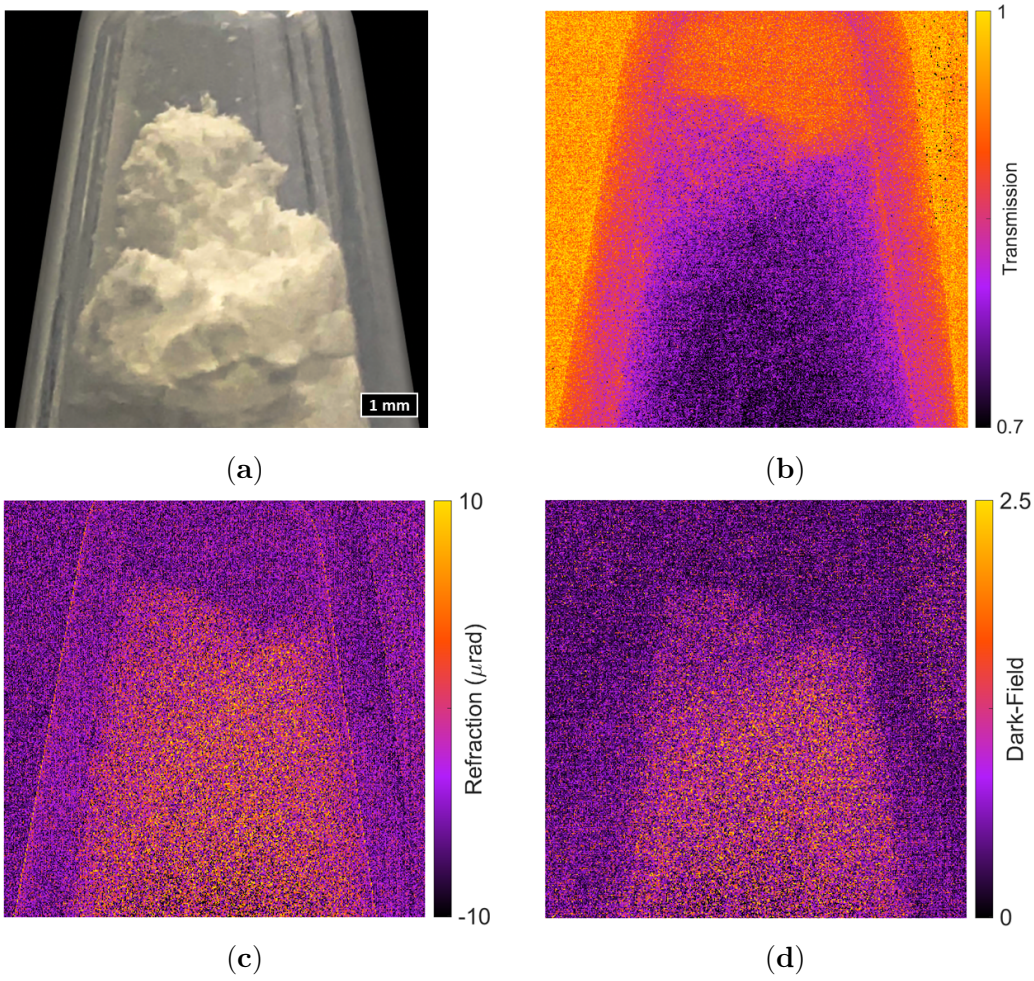


Figure 5.31: Schematic illustration of the X-ray setup used to perform XPCi using a single X-ray absorption grating.

trast modalities in a single X-ray exposure with multi-directional sensitivity. The reported result in Figure 5.32 is especially significant in light of the ultra-compact geometry of the EI-XPCi system due in large part to the 8 μm pixel pitch prototype 4K×4K X-ray detector and the 2D X-ray absorption grating fabricated in Chapter 4. The reported result, due to a single exposure scan, also demonstrates promise for the reduction of dose to the



(**a**) (**b**) (**c**) (**d**)

Figure 5.32: (**a**) A centrifuge tube filled with sugar powder as the sample of interest, although the sugar powders are not in the same position as when the EI-XPCi was taken. (**b**) Transmission, (**c**) refraction, and (**d**) scattering images retrieved from a single-exposure X-ray phase-contrast image taken at 60 kV_p of the sample. X-ray phase-contrast images are represented based on a false color tone for better representation.

sample, which could be potentially beneficial for biological samples and in vivo imaging applications. Further system-level optimizations for dose could further result in lowering of the sample radiation.

5.4 Speckle-tracking X-ray Phase-Contrast Imaging

Speckle-tracking XPCi studies the distortions induced by an object (i.e., sample) to a reference interference pattern—used as a wavefront marker—to retrieve X-ray phase-contrast information, in particular the small angle scattering signal. The reference interference pattern is generated by an X-ray diffuser—placed between the X-ray source and the detector—which can be either a random or a non-random interference pattern. A piece of sandpaper (e.g., silicon carbide sandpaper) creates a random interference pattern, while a 2D X-ray absorption grating with a periodic structure leads to a non-random – rather structured – interference pattern. Introducing the sample to the system—placed between the diffuser and the detector—distorts the reference interference pattern and creates a new pattern called the sample interference pattern. Upon detection of both interference patterns—reference and sample—within the near-field regime, the observable distortions in the sample inter-

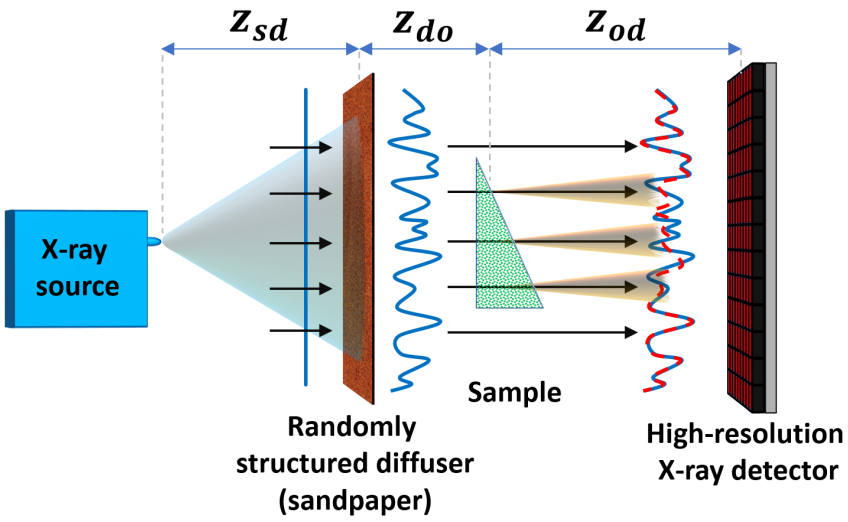


Figure 5.33: Schematic illustration of the speckle-tracking XPCi system with a reference interference pattern (blue solid line) and a sample interference pattern (red dashed line). The random interference pattern created by a sandpaper diffuser distorts after passing through an inhomogeneous sample—due to scattering effects.

ference pattern represent the sample scattering properties [28, 147, 159–163]. Figure 5.33 illustrates a schematic of the speckle-tracking XPCi system model.

Although speckle-tracking XPCi systems that utilize randomly structured diffusers – such as sandpapers – seem to operate in a simple manner, to date, and to the best of our knowledge, they do not result in high-quality images. That said, speckle-tracking XPCi systems with randomly structured diffusers are still in the research phase, pushing the technology limits to achieve higher image qualities and reach a higher system performance. On the other hand, speckle-tracking XPCi systems employing high-resolution X-ray absorption gratings with periodic structures – 2D gratings – offer higher-quality phase-contrast images.

In collaboration with the University of Pennsylvania (Professor Peter B. Noël's group), we investigated a speckle-tracking method to retrieve the three established XPCi images generated with our setup. The system model is analogous to the single-mask EI-XPCi one, as illustrated in Figure 5.34. Originally implemented for randomly structured diffusers (i.e., sandpaper), a speckle displacement tracking information retrieval algorithm was employed in our single-mask XPCi system. Speckle displacement tracking was performed with a full-resolution end-to-end convolutional neural network (CNN) [164] consisting of four

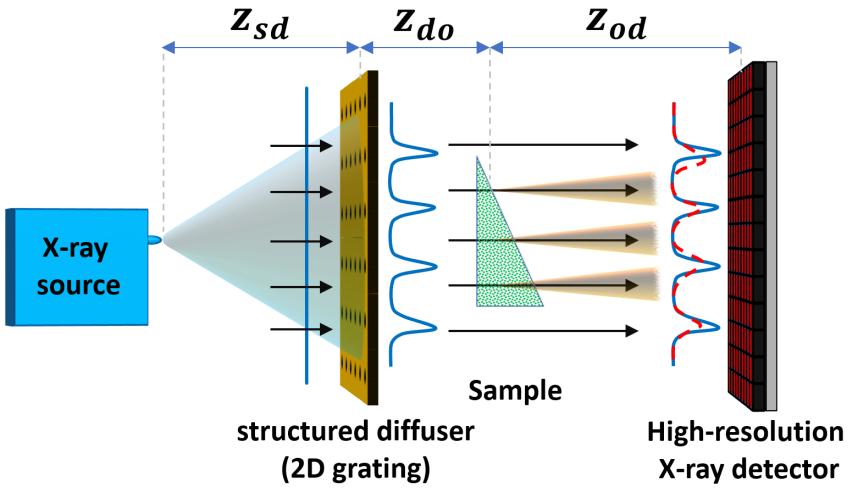


Figure 5.34: Schematic illustration of the speckle-tracking XPCi system with a reference interference pattern (blue solid line) and a sample interference pattern (red dashed line). The structured interference pattern created by a 2D grating distorts after passing through an inhomogeneous sample—due to scattering effects.

down-sampling and four up-sampling steps, a method that offered some improved accuracy and spatial resolution when compared to conventional window-based methods. Transmission [160] and dark-field [28] images were subsequently retrieved based on conventional definitions. Phase information, however, was not accessible as the speckle displacement tracking method was still under development.

5.4.1 Silicon-based 2D Grating

Silicon-based X-ray absorption gratings fabricated in this research and reported in Chapter 3 were used in the single-mask speckle-tracking XPCi system. We employed the silicon micropillar 2D grating with a diameter of 4 μm and periodicity of 16.3 μm as the structured diffuser in the modified inCiTe™ system for single-mask speckle-tracking XPCi. Imaging was performed with the source-to-diffuser (z_{sd}), diffuser-to-object (z_{do}), and object-to-detector (z_{od}) distances of 10 cm, 2 cm, and 35 cm, respectively. The Hamamatsu L12531 microfocus polychromatic X-ray source was working at 60 kV_p and 200 μA, resulting in a focal spot of 12 μm.

We studied various samples with different characteristics to investigate the phase-contrast properties of the retrieved images. Samples (illustrated in Figure 5.35) were as follows:

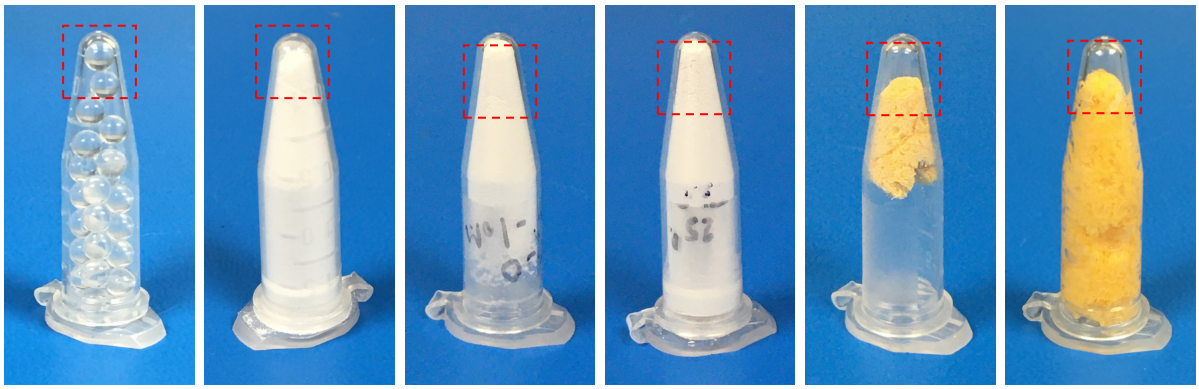
- Acrylic beads
- Sugar powder
- Titanium oxide powder with 10 μm×100 nm size particles
- Titanium oxide powder with 25 nm size particles
- Dry solder sponge
- Wet solder sponge

Samples were all kept inside 1.5 mL centrifuge tube containers. Transmission and dark-field images retrieved from these samples are presented in Figure 5.36 to Figure 5.39. Images are all presented based on a false color tone for better representation.

The acrylic beads sample was chosen to investigate the sensitivity and quality of the speckle displacement tracking information retrieval algorithm in retrieving the dark-field

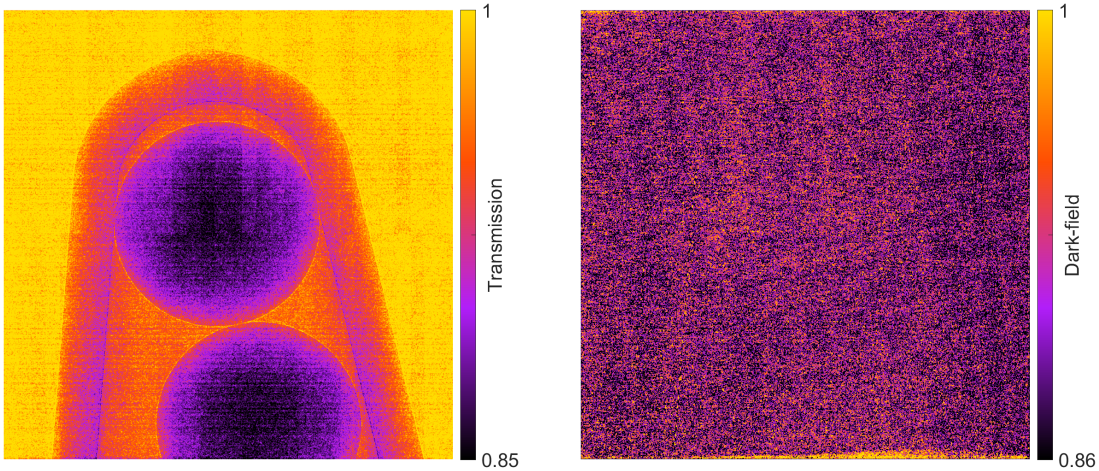
image. Acrylic beads, as previously presented in Figure 5.23c, do not create a strong scattering, which results in a weak dark-field signal (illustrated in Figure 5.36b). On the other hand, an inhomogeneous sample, such as the sugar powder, clearly demonstrated a dark-field signal that is an indication of the sub-resolution size of sugar particles (Figure 5.37b).

The intensity of the dark-field signal is related and proportional to the sample's internal feature particle size. The titanium oxide powder samples were selected to justify the correlation between the dark-field signal intensity and sample particle size. The dark-field image provided additional information that helped differentiate the difference between the fine titanium oxide powder (i.e., 25 nm size particles illustrated in Figure 5.38d) and the coarse titanium oxide powder (i.e., 10 μm$\times$100 nm size particles illustrated in Figure 5.38b). As evident in the images, the finer particle size sample indicates a higher dark-field signal. Water weakens the X-ray scattering, which results in the loss of most of the dark-field signal; this is indicated by comparing dry and wet sponge samples, with the dry sponge sample presenting a higher dark-field signal level (Figure 5.39d) compared to the wet sponge sample (Figure 5.39b).



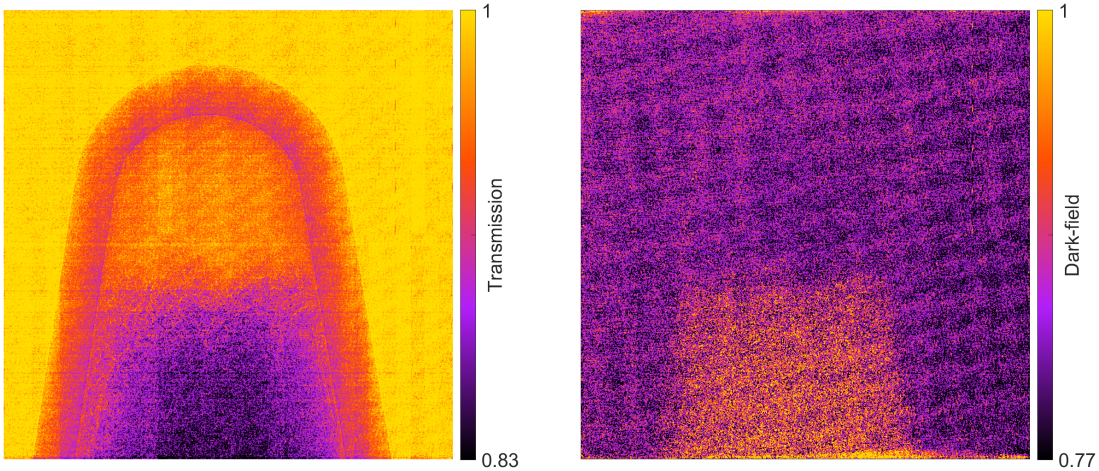
(**a**) (**b**) (**c**) (**d**) (**e**) (**f**)

Figure 5.35: Image of object used for speckle-tracking XPCi: (**a**) acrylic beads, (**b**) sugar powder, (**c**) titanium oxide powder with 10 μm$\times$100 nm size particles, (**d**) titanium oxide powder with 25 nm size particles, (**e**) dry solder sponge, and (**f**) wet solder sponge. The red dashed squares represent the region of interest (ROI) in X-ray phase-contrast images.



(**a**) (**b**)

Figure 5.36: Illustration of (**a**) transmission and (**b**) dark-field images of the acrylic beads, imaged in the speckle-tracking XPCi system using the silicon micropillar 2D grating. The dark-field image does not reveal the semi-homogeneous acrylic beads and the centrifuge tube container.



(**a**) (**b**)

Figure 5.37: Illustration of (**a**) transmission and (**b**) dark-field images of the sugar powder sample, imaged in the speckle-tracking XPCi system using the silicon micropillar 2D grating. The dark-field image reveals the inhomogeneous sugar powder with particle sizes well below the system resolution (i.e., defined by the grating aperture size).

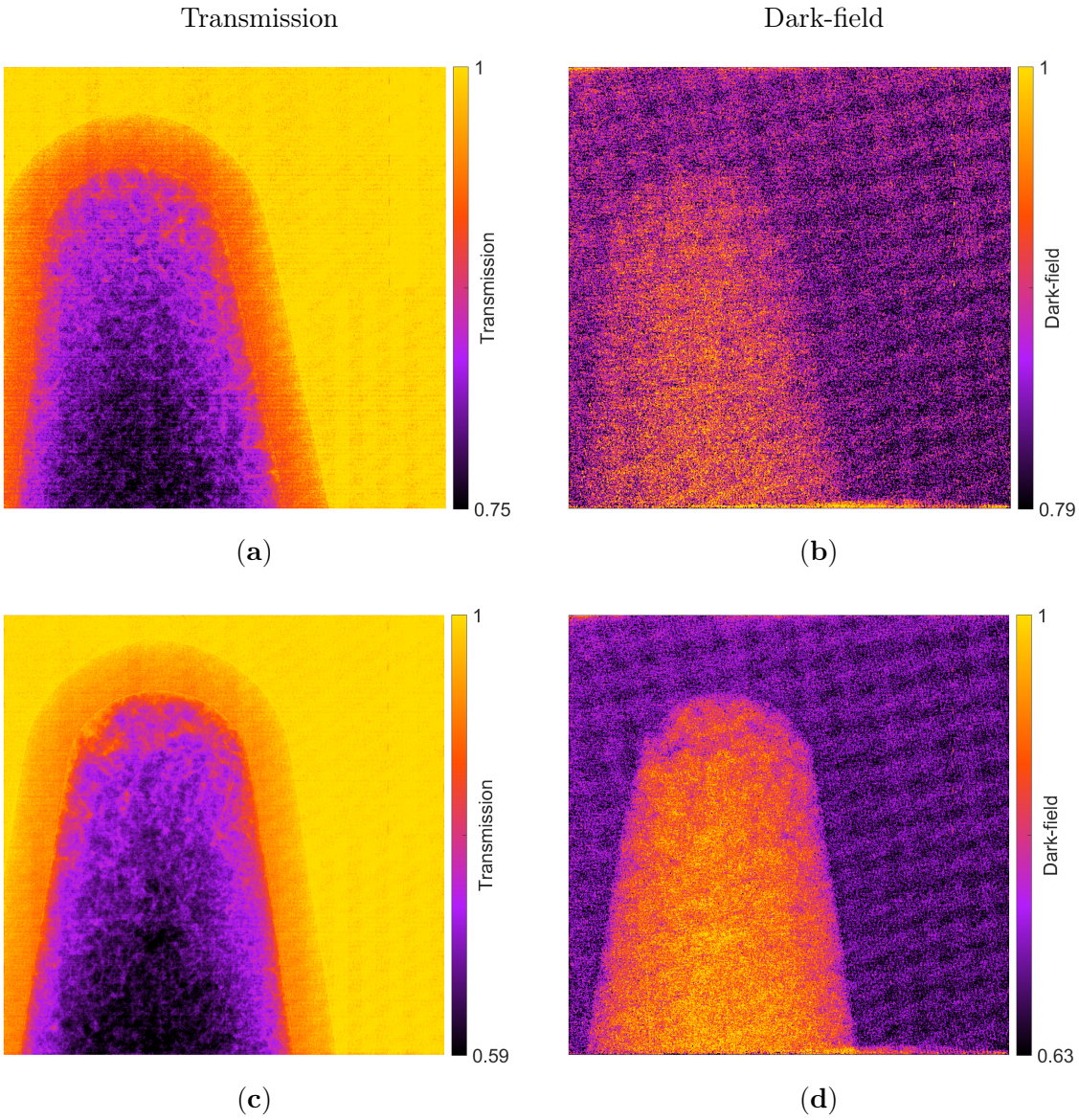


Figure 5.38: Illustration of (**a**) transmission and (**b**) dark-field images of the titanium oxide powder sample with 10 μm×100 nm size particles, and (**c**) transmission and (**d**) dark-field images of the titanium oxide powder sample with 25 nm size particles; both samples were imaged in the speckle-tracking XPCi system using the silicon micropillar 2D grating. The finer particle size sample indicates a higher dark-field signal.

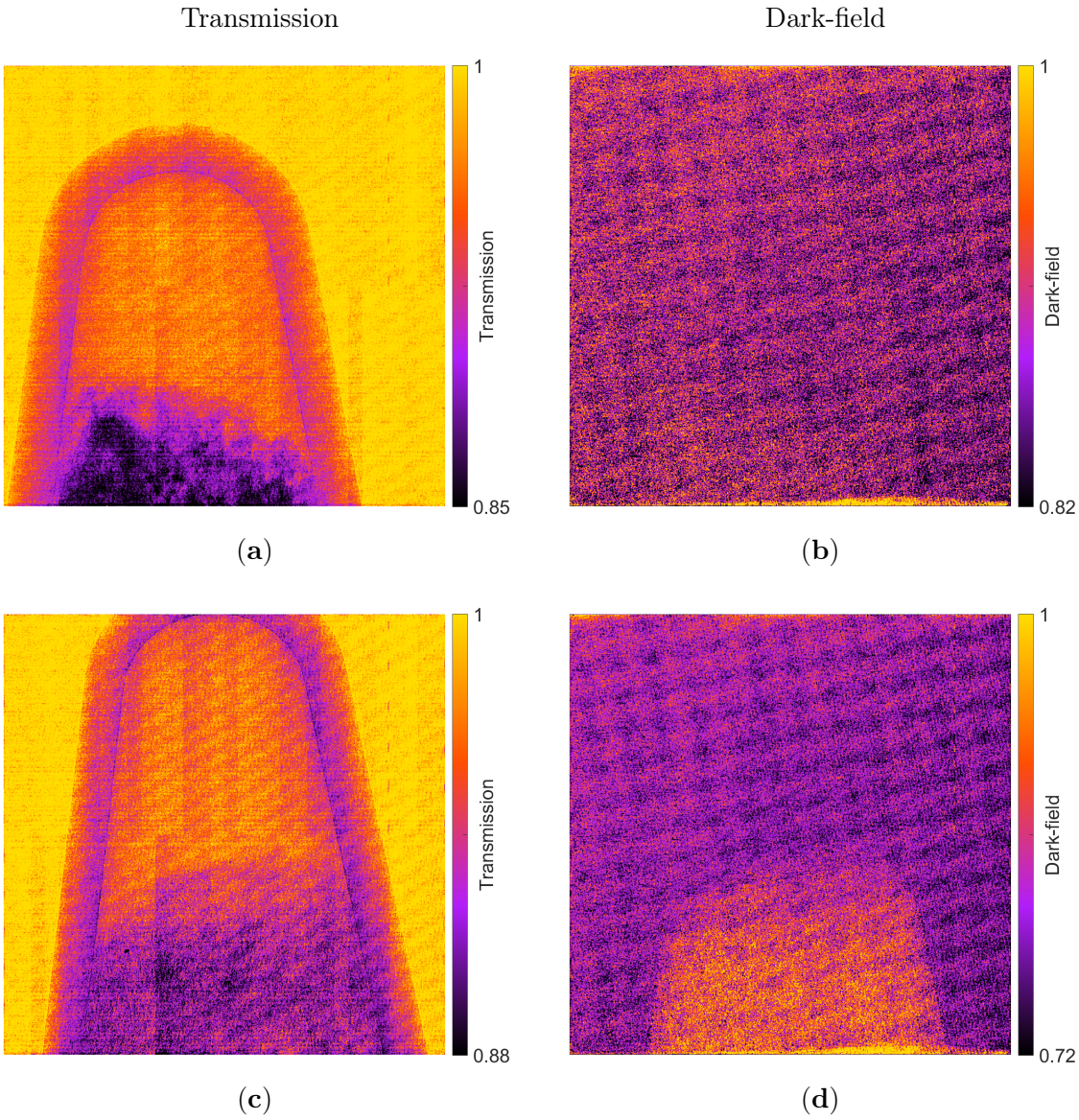
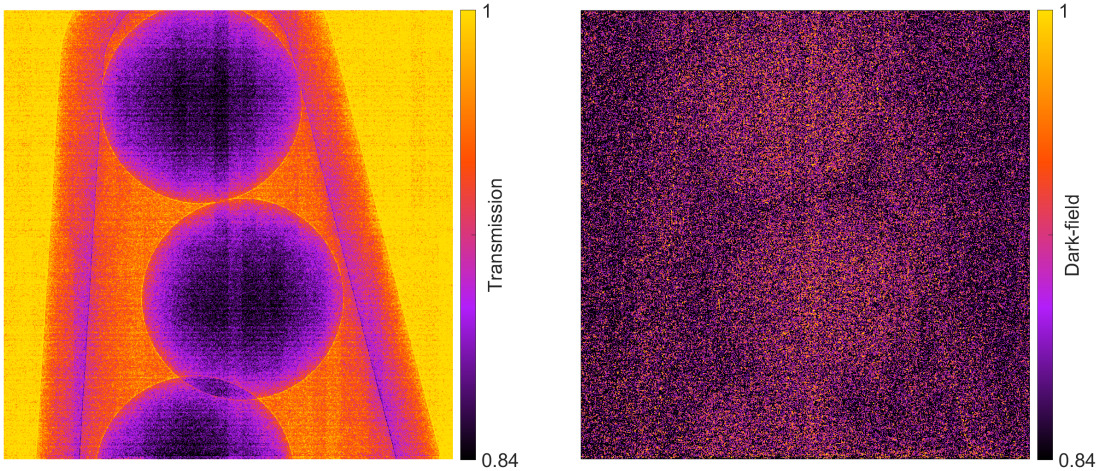


Figure 5.39: Illustration of (**a**) transmission and (**b**) dark-field images of the wet sponge sample, and (**c**) transmission and (**d**) dark-field images of the dry sponge sample; both samples were imaged in the speckle-tracking XPCi system using the silicon micropillar 2D grating. Water weakens the dark-field signal as evident in the wet sponge dark-field image.

5.4.2 Self-Aligned Multi-Layer SU-8 2D Grating

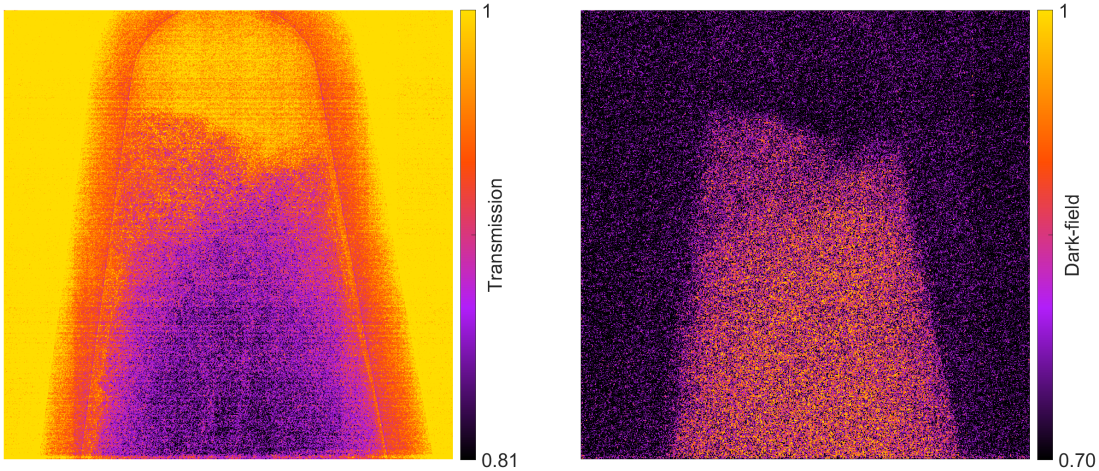
The prototype three-layer 2D X-ray absorption grating fabricated in this research and reported in Chapter 4 was employed as the structured diffuser in the modified inCiTe™ system for the single-mask speckle-tracking XPCi. Imaging was performed with the source-to-diffuser (z_{sd}), diffuser-to-object (z_{do}), and object-to-detector (z_{od}) distances of 10 cm, 2 cm, and 35 cm, respectively. The Hamamatsu L12531 microfocus polychromatic X-ray source was working at 60 kV_p and 200 μA, resulting in a focal spot of 12 μm. We studied the same samples, introduced in Figure 5.35. Transmission and dark-field images retrieved from these samples are presented in Figure 5.40 to Figure 5.43. Images are all presented based on a false color tone for better representation.

Employing the prototype three-layer SU-8 2D grating, with its higher quality structures compared to the silicon grating, helped reveal even the weak scattering signal of semi-homogeneous samples such as acrylic beads, presented in Figure 5.40b. The wet sponge sample also demonstrated a weak dark-field signal (shown in Figure 5.43b). The dark-field images for other samples also indicated slightly higher scattering signals, due in large part to the higher quality prototype SU-8 three-layer 2D grating. We believe increasing the number of layers in the multi-layer SU-8 grating would result in a thicker absorption region, consequently, higher contrast and visibility in the micropillars' projections.



(**a**) (**b**)

Figure 5.40: Illustration of (**a**) transmission and (**b**) dark-field images of the acrylic beads, imaged in the speckle-tracking XPCi system using the prototype three-layer SU-8 2D grating. The dark-field image reveals the weak scattering signal from the acrylic beads in the centrifuge tube container.



(**a**) (**b**)

Figure 5.41: Illustration of (**a**) transmission and (**b**) dark-field images of the sugar powder sample, imaged in the speckle-tracking XPCi system using the prototype three-layer SU-8 2D grating. The dark-field image reveals the inhomogeneous sugar powder with particle sizes well below the system resolution (i.e., defined by the grating aperture size).

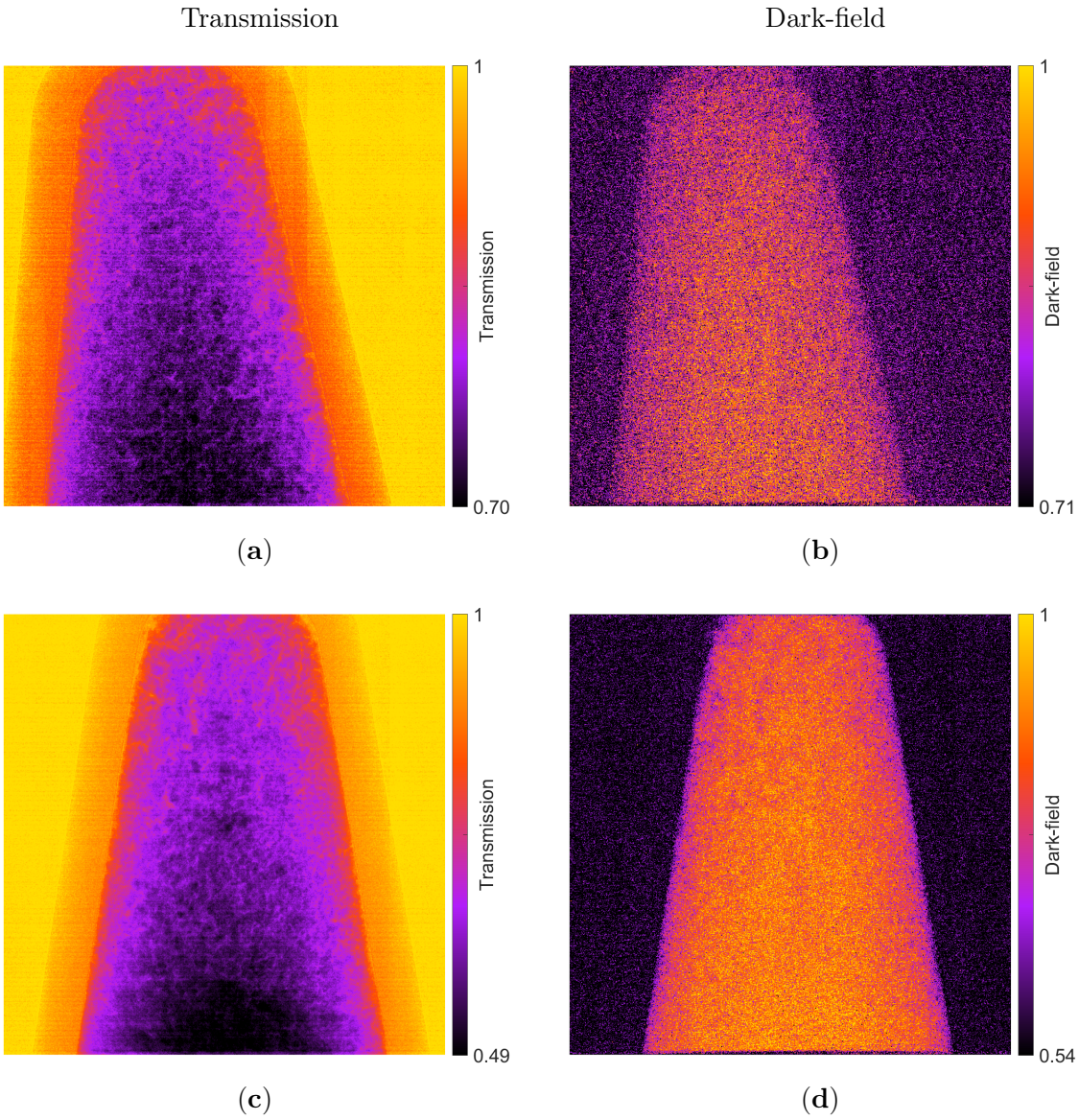


Figure 5.42: Illustration of (**a**) transmission and (**b**) dark-field images of the titanium oxide powder sample with 10 μm×100 nm size particles, and (**c**) transmission and (**d**) dark-field images of the titanium oxide powder sample with 25 nm size particles; both samples were imaged in the speckle-tracking XPCi system using the prototype three-layer SU-8 2D grating. The finer particle size sample indicates a higher dark-field signal.

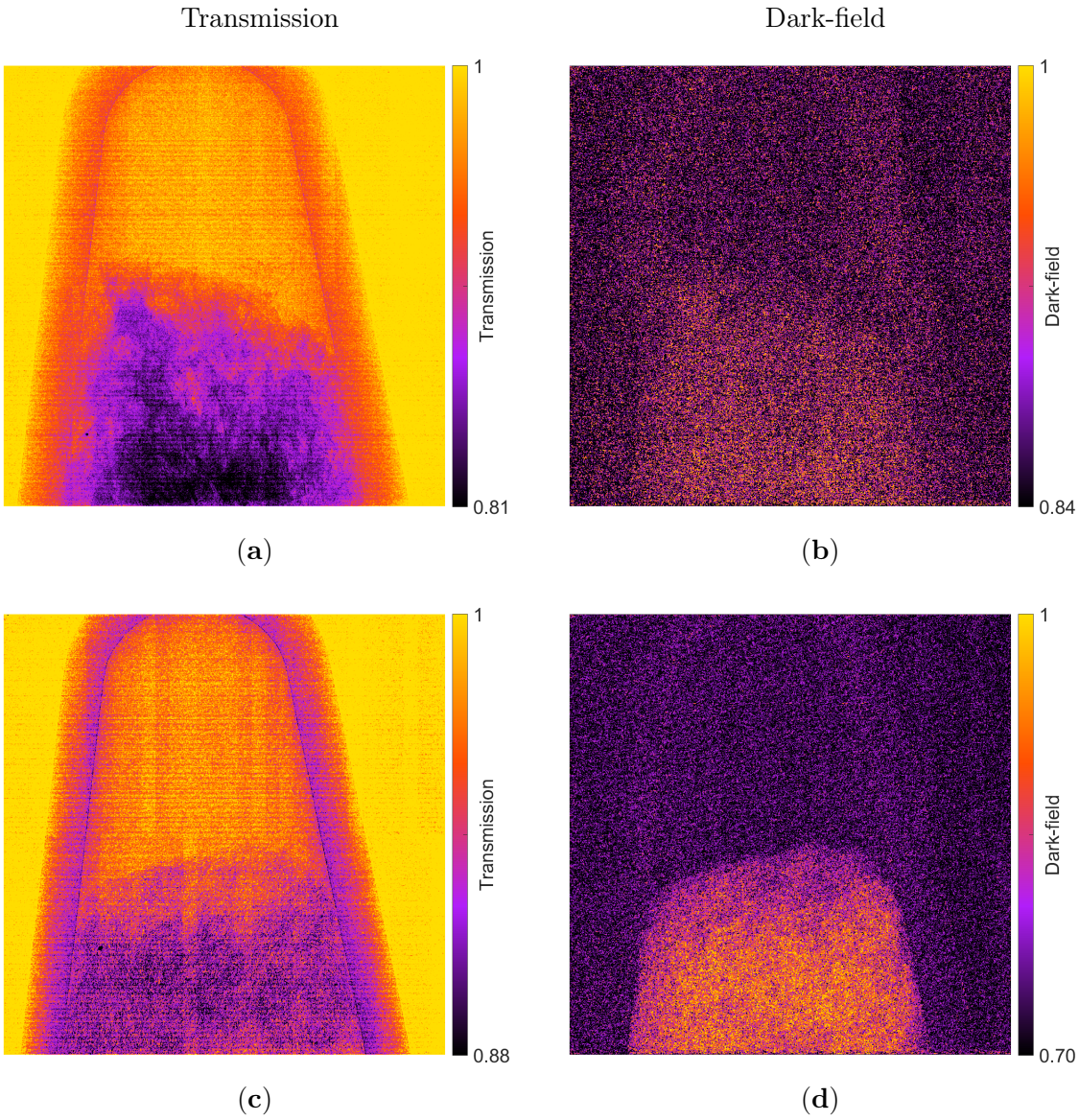


Figure 5.43: Illustration of (**a**) transmission and (**b**) dark-field images of the wet sponge sample, and (**c**) transmission and (**d**) dark-field images of the dry sponge sample; both samples were imaged in the speckle-tracking XPCi system the prototype three-layer SU-8 2D grating. Water weakens the dark-field signal, as evident in the wet sponge dark-field image.

5.5 Conclusion

In this chapter, we explored some use cases of high-resolution XPCi, with a focus on PB and EI-XPCi methods. We reviewed the applications of high-resolution X-ray detectors in general and, in particular, an in-house prototype micron-scale pixel size direct conversion X-ray detector in both PB and EI-XPCi. Although PB-XPCi systems provide a high-resolution imaging capability without any additional optical apparatus, computational demands and approximation requirements make their use impractical for achieving accurate quantitative phase information for multi-material objects in a single X-ray exposure. Moreover, the PB-XPCi systems do not offer the objects' X-ray scattering information (that already exists in the X-ray phase information), a limitation associated with the physics of PB-XPCi. However, employing the prototype 4K×4K high-resolution X-ray detector increased the system resolution and also made the final system more compact by decreasing the source-to-detector distance. The prominent X-ray edge-enhanced images taken with the micron-scale pixel size detector employed in this work provided the foundation for higher-quality EI-XPCi systems.

In the second part of this chapter, we focused on the EI-XPCi system, particularly the single-mask configuration systems. A prototype 4K×4K high-resolution micron-scale pixel size X-ray detector was utilized with a line grating for multi-modal information retrieval. The IC profiles were successfully obtained in a single X-ray exposure, and two different algorithms (i.e., Gaussian fitting and moment analysis) were implemented to retrieve transmission, phase, and scattering images from the line grating EI-XPCi systems. The object orientation dependence sensitivity in line grating EI-XPCi systems leads to the loss of information in one direction. While this information loss could be resolved by taking two exposures if the X-ray grating (or the object) orientation is altered in each exposure, not all applications (e.g., medical imaging) can afford the higher dose exposure to patients. Moreover, the object's displacement between multiple exposures results in image artifacts that are not acceptable in some applications, particularly diagnostic imaging.

An alternative to the multi-exposure technique to resolve the object direction dependence sensitivity is to utilize 2D X-ray absorption gratings. The high-resolution 2D gratings fabricated in Chapter 3 and Chapter 4 facilitated the data acquisition in a single X-ray exposure by eliminating the object orientation dependence sensitivity in the system. The combination of the high-resolution direct conversion X-ray detector with the high-resolution 2D X-ray absorption gratings in this work expanded the practicality of the single-mask XPCi systems by shortening the imaging time (around 2× because of a single exposure) and improving the patient dose efficiency (around 2×, again due to a single exposure). We also investigated two different information retrieval algorithms (i.e. the

Gaussian fitting and speckle-tracking) in 2D grating single-mask EI-XPCi systems. The speckle-tracking algorithm was used to retrieve transmission and dark-field images by employing the high-resolution grating fabricated in this work as a structured diffuser. The retrieval of the phase image in the speckle tracking method is still under development. The multi-modal information offered by the single-mask single-exposure 2D XPCi method in a compact system defines new opportunities for higher quality, higher dose efficiency, and more accurate imaging tasks in all fields of applications. 2D single-mask EI-XPCi can pave the way for physicians to diagnose, for instance, early stages of chest or breast cancerous tumors.

This chapter fulfilled the third objective of the thesis, namely investigating XPCi system performance, particularly single-mask edge-illumination X-ray phase-contrast imaging systems, by providing early (unoptimized) results based on the in-house developed detector and the in-house developed high-resolution grating.

Chapter 6

Conclusions and Contributions

6.1 Conclusions

X-ray absorption gratings are fundamental components in all grating-based X-ray phase-contrast imaging (XPCi) systems, as they directly determine all salient image characteristics. Grating-based XPCi systems offer numerous advantages over conventional attenuation-contrast X-ray imaging systems, the most prominent being the additional two images of refraction (phase-shift) and dark-field (scattering). The three established contrast images—transmission, phase-shift, and scattering—provide essential complementary information about an object which enables quantitative studies. In this thesis, we have invented a scalable fabrication process for making high-resolution (and potentially higher aspect ratio) X-ray absorption gratings and developed a high-resolution single-mask edge-illumination (EI) XPCi system.

We successfully implemented a simulation model to study the high-resolution propagation-based (PB) and EI-XPCi systems in Chapter 2, where we investigated the effect of employing high-resolution direct conversion micron-scale X-ray detectors on the quality of X-ray phase-contrast images. We confirmed that the EI-XPCi configuration, compared to PB-XPCi, exhibits higher performance in simulation studies: in contrast by about 3×, in edge-enhancement by about 3×, in visibility by about 2.5×, and in dose efficiency by about 5×. Despite the higher performance of EI-XPCi over PB-XPCi, we found the fabrication of high-resolution X-ray absorption gratings was the main impediment to the realization of high-resolution EI-XPCi systems.

Following the high-resolution EI-XPCi system requirement, we reported on a novel technique, bridge-assisted micropillars, in silicon technology to improve the mechanical stabil-

ity and etching performance of 2D micropillars in X-ray grating fabrication in Chapter 3. Moreover, we investigated sputtering tools as an alternative to atomic layer deposition (ALD) tools to deposit the seed layer—for electroplating—on structures etched in silicon wafers. We found that while gold sputtering did not result in a conformal seed layer deposition over the entire high aspect ratio silicon structures, it resulted in an X-ray absorption grating for some hard X-ray XPCi applications—such as the speckle-tracking method.

In Chapter 4, to address the high-resolution X-ray absorption grating fabrication, we invented a novel fabrication method, a self-aligned multi-layer technique. By stacking multiple layers of the same grating design (multi-layer structures) through a backside self-aligned UV flood exposure technique, larger-area X-ray gratings were successfully realized in an established and mature large-area UV-LIGA process. We demonstrated the process by building an SU-8 micropillar-shaped (2D) three-layer X-ray absorption grating with 4 μm aperture size and 16.2 μm period (thickness of around 40 μm), with an average visibility of 0.28 (i.e., 28%) at 60 kV_p. The reported grating indicated sufficient thickness to absorb 30 kV_p X-rays that could potentially be employed for XPCi in mammography applications. We successfully addressed a key technological bottleneck in the commercial deployment of grating-based X-ray phase-contrast imaging systems in Chapter 4 that paves the way for both clinical and non-clinical applications of XPCi where better visibility, higher X-ray energies, larger field-of-view, higher spatial resolution, and compact imaging are desirable.

Application of high-resolution XPCi systems, in PB and EI-XPCi configurations, was also studied in Chapter 5. We introduced intraoral tomosynthesis as a potential application for the in-house developed world's first 8 μm pixel size direct conversion X-ray detector. In this chapter, we successfully developed a single-mask EI-XPCi employing the in-house high-resolution X-ray detector alongside the high-resolution X-ray absorption gratings fabricated in this work. The compact single-mask high-resolution EI-XPCi system developed in this thesis significantly improved the imaging performance. The improvement resulted in a reduction in imaging time—and consequently, dose exposure—thanks to the single exposure XPCi realization, and restored the three established contrast information of the object by eliminating the object orientation dependency thanks to the fabricated high-resolution X-ray grating. We also explored various algorithms in retrieving the three established contrast modalities, namely transmission, phase-shift, and dark-field images, and successfully presented early (unoptimized) results in retrieving all the abovementioned information.

6.2 Contributions

The original contributions of this work to the development of high-resolution X-ray phase-contrast imaging systems at both the device and system levels are summarized as follows:

- Evaluation of the PB and EI-XPCi systems employing high-resolution micron-scale pixel size direct conversion X-ray detectors.
- Finding impediments on the path of utilizing micron-scale pixel size X-ray detectors in EI-XPCi systems.
- Investigation of silicon-based high aspect ratio high-resolution X-ray absorption grating fabrication via deep reactive ion etching (DRIE) and using sputtering tools as an alternative to ALD for electroplating seed layer deposition.
- Invention of auxiliary supporting bridge structures to improve the mechanical stability of micropillars etched in silicon wafers for 2D (silicon micropillar-based) absorption grating fabrication.
- Fabrication of a working high-resolution high aspect ratio X-ray absorption grating in silicon wafers.
- Improving the adhesion quality of SU-8 films to gold thin film for X-ray grating fabrication in UV-LIGA process.
- Invention of multi-layer X-ray grating implementation to address technological limitations associated with fabrication of high aspect ratio X-ray grating fabrication in conventional UV-LIGA process.
- Invention of self-aligned multi-layer implementation enabling scalable high-resolution high aspect ratio X-ray absorption grating fabrication in conventional UV-LIGA process.
- The first successful self-aligned multi-layer SU-8 based 2D X-ray absorption grating with 70 cm$\times$70 cm active area, with sufficient transmission for mammography screening application.
- Introduction of intraoral tomosynthesis employing the in-house developed world's first 8 μm pixel pitch direct conversion X-ray detector.

- Development of a compact single-mask XPCi system employing the in-house high-resolution X-ray detector alongside the in-house developed high-resolution X-ray absorption grating in EI and speckle-tracking configurations.
- Demonstration of transmission, phase-shift, and dark-field image retrieval in a single X-ray exposure single-mask XPCi system using the in-house high-resolution X-ray detector and in-house fabricated high-resolution X-ray absorption grating.
- Demonstration of multi-directional (2D) high-resolution EI-XPCi employing the in-house high-resolution X-ray detector and in-house fabricated high-resolution X-ray absorption grating.

Patents

- Karim Sallaudin Karim, and **Abdollah Pil-Ali**. "Multi-layer high-aspect ratio X-ray grating and method of manufacture." U.S. Patent Application, filed August 17, 2022. (*US Provisional Application No. 63/233,880 filed August 17, 2021*)

Journal Publications

- **Abdollah Pil-Ali**, Sahar Adnani, Christopher C. Scott, and Karim S. Karim. "Direct Conversion X-ray Detector with Micron-Scale Pixel Pitch for Edge-Illumination and Propagation-Based X-ray Phase-Contrast Imaging." Sensors 22, no. 15 (2022): 5890.
- **Abdollah Pil-Ali**, Sahar Adnani, and Karim S. Karim. "Self-Aligned Multi-Layer X-ray Absorption Grating using Large-Area Fabrication Methods for X-ray Phase-Contrast Imaging." Scientific Reports 13 (2023): 2508.

Conference Publications

- **Abdollah Pil-Ali**, Serena Qinyun Z. Shi, Sahar Adnani, Peter B. Noël, and Karim S. Karim. "Multimodal Single-Shot X-ray Phase-Contrast Imaging using a High-Resolution Micropillar-based Grating." Accepted for oral presentation in Medical Imaging 2023: Physics of Medical Imaging. SPIE, 2023.

- **Abdollah Pil-Ali**, Sahar Adnani, Pranav Gavirneni, Seokjee Shin, Bahareh Sadeghimakki, Mahla Poudineh, William Wong, and Karim Sallaudin Karim. "Self-aligned fabrication of high-aspect ratio high-resolution X-ray gratings." In Medical Imaging 2022: Physics of Medical Imaging, vol. 12031, pp. 903-907. SPIE, 2022.

- **Abdollah Pil-Ali**, Mohammad Soltani, Sahar Adnani, Bo Cui, and Karim Salaudin Karim. "A novel multi-layer grating structure for X-ray phase-contrast imaging." In Medical Imaging 2022: Physics of Medical Imaging, vol. 12031, pp. 898-902. SPIE, 2022.

- **Abdollah Pil-Ali**, Mohammad Soltani, Sahar Adnani, Muhammed Kayaharman, Mahla Poudineh, Bo Cui, and Karim Salaudin Karim. "Improving adhesion quality of SU-8 to gold thin film for absorption grating fabrication in X-ray phase-contrast imaging." In Medical Imaging 2022: Physics of Medical Imaging, vol. 12031, pp. 913-918. SPIE, 2022.

- **Abdollah Pil-Ali**, Sahar Adnani, Celal Con, Zain H. Warsi, and Karim S. Karim. "Bridge-Assisted Micropillar Structure for High-Aspect Ratio X-ray Grating Fabrication." In 2021 IEEE Nuclear Science Symposium and Medical Imaging Conference (NSS/MIC), pp. 1-3. IEEE, 2021.

- **Abdollah Pil-Ali**, Sahar Adnani, Christopher C. Scott, and Karim S. Karim. "A 7.8-μm Pixel Pitch Direct Conversion X-ray Detector for High-Resolution Intraoral Tomosynthesis Application." In 2021 IEEE Nuclear Science Symposium and Medical Imaging Conference (NSS/MIC), pp. 1-3. IEEE, 2021.

- **Abdollah Pil-Ali**, Sahar Adnani, Christopher C. Scott, Alessandro Olivo, and Karim S. Karim. "Single-Exposure, Single-Mask, Edge-Illumination X-ray Phase-Contrast Imaging Using a 7.8-μm Pixel Pitch Direct Conversion X-ray Detector." In 2021 IEEE Nuclear Science Symposium and Medical Imaging Conference (NSS/MIC), pp. 1-3. IEEE, 2021.

- **Abdollah Pil-Ali**, Sahar Adnani, Christopher C. Scott, and Karim S. Karim. "Challenges of employing a high-resolution X-ray detector in a coded-aperture X-ray phase-contrast imaging system." In Medical Imaging 2021: Physics of Medical Imaging, vol. 11595, pp. 1225-1232. SPIE, 2021.

- **Abdollah Pil-Ali**, Sahar Adnani, Christopher C. Scott, and Karim S. Karim. "Evaluation of edge-illumination and propagation-based X-ray phase contrast imaging methods for high resolution imaging application." In Medical Imaging 2021: Physics of Medical Imaging, vol. 11595, pp. 441-452. SPIE, 2021.

- Rhiannon L. Lohr, Chris C. Scott, **Abdollah Pil-Ali**, and Karim S. Karim. "A comparison of phase retrieval methods for propagation-based contrast X-ray imaging with polychromatic sources." In Medical Imaging 2020: Physics of Medical Imaging, vol. 11312, pp. 1242-1249. SPIE, 2020.

Poster Presentations

- **Abdollah Pil-Ali**, and Karim S. Karim. "Illumination Curve Extraction of a Coded-Aperture Phase-Contrast X-Ray Imaging System Using a High-Resolution X-ray Detector." In 2020 IEEE Student Poster Competition. IEEE, 2020. (*Won the 3rd place award*)

Other Publications

- Sahar Adnani, **Abdollah Pil-Ali**, Celal Con, and Karim S. Karim. "Investigation of position linearity in position-sensitive microstrip amorphous selenium-based detector." In Medical Imaging 2022: Physics of Medical Imaging, vol. 12031, pp. 125-129. SPIE, 2022.

- Sahar Adnani, **Abdollah Pil-Ali**, Celal Con, and Karim S. Karim. "A Position-Sensitive Microstrip Detector using Amorphous Selenium Photoconductor." In 2021 IEEE Nuclear Science Symposium and Medical Imaging Conference (NSS/MIC), pp. 1-3. IEEE, 2021.

- Sahar Adnani, **Abdollah Pil-Ali**, Christopher C. Scott, and Karim S. Karim. "Monte Carlo simulation of an amorphous selenium-based multi-layer photon-counting detector for SPECT applications." In Medical Imaging 2021: Physics of Medical Imaging, vol. 11595, pp. 306-312. SPIE, 2021.

- **Abdollah Pil-Ali**, Razieh Khalili, S. Mohammad Reza Safaee, and Mohammad Azim Karami. "A Radiation-Hardened Wide Spectral Response 4T CMOS Image Sensor Pixel Employing a Through-Silicon Via based Photodetector." In 2021 IEEE International IOT, Electronics and Mechatronics Conference (IEMTRONICS), pp. 1-6. IEEE, 2021.

- Razieh Khalili, **Abdollah Pil-Ali**, Sahar Adnani, and Mohammad Azim Karami. "Employing Total Ionizing Dose Effect in PN-Junction Photodetectors Implemented in Standard CMOS Technology for Dosimetry Application." In 2021 IEEE Nuclear Science Symposium and Medical Imaging Conference (NSS/MIC), pp. 1-3. IEEE, 2021.

- Kiarash Hassas Irani, **Abdollah Pil-Ali**, and Mohammad Azim Karami. "A new guard ring for radiation induced noise reduction in photodiodes implemented in 0.18 μm CMOS technology." Optical and Quantum Electronics 49, no. 9 (2017): 1-10.

6.3 Future Works

Larger-area XPCi systems are of high interest in medical and industrial imaging applications. Further optimization on the reported novel self-aligned multi-layer X-ray absorption grating process to translate its fabrication from the university lab to industrial facilities can be conducted, mainly for larger area X-ray phase-contrast imaging applications. The translation phase has already begun by establishing the required infrastructures, particularly an electroplating station compatible with large-area substrates.

Information retrieval for 2D single-mask EI-XPCi systems to extract prominent images of transmission, phase-shift, and dark-field via a single X-ray exposure is still a work in progress. Implementation of a computationally efficient, fast, and accurate information retrieval algorithm can potentially extend the practicality of high-resolution 2D single-mask EI-XPCi systems and facilitate their use in computed tomography (CT) applications, where thousands of projections are captured to reconstruct a 3D map of an object of interest. To that extent, CT opens up the opportunity to quantitatively analyze objects with various material compositions, which is the next phase of this research.

References

[1] S. Wilkins, T. E. Gureyev, D. Gao, A. Pogany, and A. Stevenson, "Phase-contrast imaging using polychromatic hard x-rays," *Nature*, vol. 384, no. 6607, pp. 335–338, 1996.

[2] M. Endrizzi, "X-ray phase-contrast imaging," *Nuclear Instruments and Methods in Physics Research Section A: Accelerators, Spectrometers, Detectors and Associated Equipment*, vol. 878, pp. 88–98, 2018. Radiation Imaging Techniques and Applications.

[3] S. C. Mayo, A. W. Stevenson, and S. W. Wilkins, "In-line phase-contrast x-ray imaging and tomography for materials science," *Materials*, vol. 5, no. 5, pp. 937–965, 2012.

[4] Z. Wang, E. Herremans, S. Janssen, D. Cantre, P. Verboven, and B. Nicolaï, "Visualizing 3d food microstructure using tomographic methods: Advantages and disadvantages," *Annual review of food science and technology*, vol. 9, pp. 323–343, 2018.

[5] A. W. Stevenson, T. E. Gureyev, D. Paganin, S. Wilkins, T. Weitkamp, A. Snigirev, C. Rau, I. Snigireva, H. Youn, I. Dolbnya, *et al.*, "Phase-contrast x-ray imaging with synchrotron radiation for materials science applications," *Nuclear Instruments and Methods in Physics Research Section B: Beam Interactions with Materials and Atoms*, vol. 199, pp. 427–435, 2003.

[6] P. Coan, A. Bravin, and G. Tromba, "Phase-contrast x-ray imaging of the breast: recent developments towards clinics," *Journal of Physics D: Applied Physics*, vol. 46, no. 49, p. 494007, 2013.

[7] S.-A. Zhou and A. Brahme, "Development of phase-contrast x-ray imaging techniques and potential medical applications," *Physica Medica*, vol. 24, no. 3, pp. 129–148, 2008.

[8] P. Suortti and W. Thomlinson, "Medical applications of synchrotron radiation," *Physics in Medicine & Biology*, vol. 48, no. 13, p. R1, 2003.

[9] S. T. Taba, T. E. Gureyev, M. Alakhras, S. Lewis, D. Lockie, and P. C. Brennan, "X-ray phase-contrast technology in breast imaging: principles, options, and clinical application," *American Journal of Roentgenology*, vol. 211, no. 1, pp. 133–145, 2018.

[10] T. Baum, E. Eggl, A. Malecki, F. Schaff, G. Potdevin, O. Gordijenko, E. G. Garcia, R. Burgkart, E. J. Rummeny, P. B. Noël, *et al.*, "X-ray dark-field vector radiography—a novel technique for osteoporosis imaging," *Journal of computer assisted tomography*, vol. 39, no. 2, pp. 286–289, 2015.

[11] K. Willer, A. A. Fingerle, W. Noichl, F. De Marco, M. Frank, T. Urban, R. Schick, A. Gustschin, B. Gleich, J. Herzen, *et al.*, "X-ray dark-field chest imaging for detection and quantification of emphysema in patients with chronic obstructive pulmonary disease: a diagnostic accuracy study," *The Lancet Digital Health*, vol. 3, no. 11, pp. e733–e744, 2021.

[12] E. Dreier, A. Bergamaschi, G. K. Kallon, R. Brönnimann, U. L. Olsen, A. Olivo, and M. Endrizzi, "Tracking based, high-resolution single-shot multimodal x-ray imaging in the laboratory enabled by the sub-pixel resolution capabilities of the mönch detector," *Applied Physics Letters*, vol. 117, no. 26, p. 264101, 2020.

[13] E. E. Bennett, R. Kopace, A. F. Stein, and H. Wen, "A grating-based single-shot x-ray phase contrast and diffraction method for in vivo imaging," *Medical physics*, vol. 37, no. 11, pp. 6047–6054, 2010.

[14] H. H. Wen, E. E. Bennett, R. Kopace, A. F. Stein, and V. Pai, "Single-shot x-ray differential phase-contrast and diffraction imaging using two-dimensional transmission gratings," *Optics letters*, vol. 35, no. 12, pp. 1932–1934, 2010.

[15] M. Das and Z. Liang, "Spectral x-ray phase contrast imaging for single-shot retrieval of absorption, phase, and differential-phase imagery," *Optics letters*, vol. 39, no. 21, pp. 6343–6346, 2014.

[16] F. Pfeiffer, T. Weitkamp, O. Bunk, and C. David, "Phase retrieval and differential phase-contrast imaging with low-brilliance x-ray sources," *Nature physics*, vol. 2, no. 4, pp. 258–261, 2006.

[17] T. Weitkamp, A. Diaz, C. David, F. Pfeiffer, M. Stampanoni, P. Cloetens, and E. Ziegler, "X-ray phase imaging with a grating interferometer," *Optics express*, vol. 13, no. 16, pp. 6296–6304, 2005.

[18] F. Pfeiffer, M. Bech, O. Bunk, P. Kraft, E. F. Eikenberry, C. Brönnimann, C. Grünzweig, and C. David, "Hard-x-ray dark-field imaging using a grating interferometer," *Nature materials*, vol. 7, no. 2, pp. 134–137, 2008.

[19] A. Olivo and R. Speller, "A coded-aperture technique allowing x-ray phase contrast imaging with conventional sources," *Applied Physics Letters*, vol. 91, no. 7, p. 074106, 2007.

[20] M. Endrizzi, P. C. Diemoz, T. P. Millard, J. Louise Jones, R. D. Speller, I. K. Robinson, and A. Olivo, "Hard x-ray dark-field imaging with incoherent sample illumination," *Applied Physics Letters*, vol. 104, no. 2, p. 024106, 2014.

[21] P. Modregger, T. P. Cremona, C. Benarafa, J. C. Schittny, A. Olivo, and M. Endrizzi, "Small angle x-ray scattering with edge-illumination," *Scientific reports*, vol. 6, no. 1, pp. 1–8, 2016.

[22] F. A. Vittoria, M. Endrizzi, P. C. Diemoz, A. Zamir, U. H. Wagner, C. Rau, I. K. Robinson, and A. Olivo, "X–ray absorption, phase and dark–field tomography through a beam tracking approach," *Scientific reports*, vol. 5, no. 1, pp. 1–5, 2015.

[23] A. Olivo, "Edge-illumination x-ray phase-contrast imaging," *Journal of Physics: Condensed Matter*, vol. 33, no. 36, p. 363002, 2021.

[24] H. Wang, Y. Kashyap, and K. Sawhney, "From synchrotron radiation to lab source: advanced speckle-based x-ray imaging using abrasive paper," *Scientific reports*, vol. 6, no. 1, pp. 1–9, 2016.

[25] K. S. Morgan, D. M. Paganin, and K. K. Siu, "X-ray phase imaging with a paper analyzer," *Applied Physics Letters*, vol. 100, no. 12, p. 124102, 2012.

[26] S. Berujon, H. Wang, and K. Sawhney, "X-ray multimodal imaging using a random-phase object," *Physical Review A*, vol. 86, no. 6, p. 063813, 2012.

[27] T. Zhou, I. Zanette, M.-C. Zdora, U. Lundström, D. H. Larsson, H. M. Hertz, F. Pfeiffer, and A. Burvall, "Speckle-based x-ray phase-contrast imaging with a laboratory source and the scanning technique," *Optics letters*, vol. 40, no. 12, pp. 2822–2825, 2015.

[28] S. Meyer, S. Z. Shi, N. Shapira, A. D. Maidment, and P. B. Noël, "Quantitative analysis of speckle-based x-ray dark-field imaging using numerical wave-optics simulations," *Scientific Reports*, vol. 11, no. 1, pp. 1–9, 2021.

[29] N. Gustschin, A. Gustschin, P. Meyer, M. Viermetz, P. Riederer, J. Herzen, J. Mohr, and F. Pfeiffer, "Quality and parameter control of x-ray absorption gratings by angular x-ray transmission," *Optics Express*, vol. 27, no. 11, pp. 15943–15955, 2019.

[30] F. Koch, T. Schröter, D. Kunka, P. Meyer, J. Meiser, A. Faisal, M. Khalil, L. Birnbacher, M. Viermetz, M. Walter, *et al.*, "Note: Gratings on low absorbing substrates for x-ray phase contrast imaging," *Review of Scientific Instruments*, vol. 86, no. 12, p. 126114, 2015.

[31] L. Romano, M. Kagias, J. Vila-Comamala, K. Jefimovs, L.-T. Tseng, V. A. Guzenko, and M. Stampanoni, "Metal assisted chemical etching of silicon in the gas phase: A nanofabrication platform for x-ray optics," *Nanoscale Horizons*, vol. 5, no. 5, pp. 869–879, 2020.

[32] L. Romano, J. Vila-Comamala, K. Jefimovs, and M. Stampanoni, "High-aspect-ratio grating microfabrication by platinum-assisted chemical etching and gold electroplating," *Advanced Engineering Materials*, vol. 22, no. 10, p. 2000258, 2020.

[33] C. Chang and A. Sakdinawat, "Ultra-high aspect ratio high-resolution nanofabrication for hard x-ray diffractive optics," *Nature communications*, vol. 5, no. 1, pp. 1–7, 2014.

[34] J. Vila-Comamala, L. Romano, V. Guzenko, M. Kagias, M. Stampanoni, and K. Jefimovs, "Towards sub-micrometer high aspect ratio x-ray gratings by atomic layer deposition of iridium," *Microelectronic Engineering*, vol. 192, pp. 19–24, 2018.

[35] A. E. Hollowell, C. L. Arrington, P. Finnegan, K. Musick, P. Resnick, S. Volk, and A. L. Dagel, "Double sided grating fabrication for high energy x-ray phase contrast imaging," *Materials Science in Semiconductor Processing*, vol. 92, pp. 86–90, 2019.

[36] Z. Shi, K. Jefimovs, L. Romano, and M. Stampanoni, "Towards the fabrication of high-aspect-ratio silicon gratings by deep reactive ion etching," *Micromachines*, vol. 11, no. 9, p. 864, 2020.

[37] K. Jefimovs, L. Romano, J. Vila-Comamala, M. Kagias, Z. Wang, L. Wang, C. Dais, H. Solak, and M. Stampanoni, "High-aspect ratio silicon structures by displacement talbot lithography and bosch etching," in *Advances in Patterning Materials and Processes XXXIV*, vol. 10146, pp. 140–146, SPIE, 2017.

[38] S. Pinzek, A. Gustschin, N. Gustschin, M. Viermetz, and F. Pfeiffer, "Fabrication of x-ray absorption gratings by centrifugal deposition of bimodal tungsten particles in high aspect ratio silicon templates," *Scientific Reports*, vol. 12, no. 1, pp. 1–11, 2022.

[39] C. David, J. Bruder, T. Rohbeck, C. Grünzweig, C. Kottler, A. Diaz, O. Bunk, and F. Pfeiffer, "Fabrication of diffraction gratings for hard x-ray phase contrast imaging," *Microelectronic Engineering*, vol. 84, no. 5-8, pp. 1172–1177, 2007.

[40] P. S. Finnegan, A. E. Hollowell, C. L. Arrington, and A. L. Dagel, "High aspect ratio anisotropic silicon etching for x-ray phase contrast imaging grating fabrication," *Materials Science in Semiconductor Processing*, vol. 92, pp. 80–85, 2019.

[41] H. Ekinci, R. K. Dey, and B. Cui, "Two-step potassium hydroxide etching to enhance aspect ratio in trench fabrication," *Journal of Vacuum Science & Technology B, Nanotechnology and Microelectronics: Materials, Processing, Measurement, and Phenomena*, vol. 37, no. 6, p. 062001, 2019.

[42] W. Bacher, W. Menz, and J. Mohr, "The liga technique and its potential for microsystems-a survey," *IEEE transactions on industrial electronics*, vol. 42, no. 5, pp. 431–441, 1995.

[43] D. Noda, M. Tanaka, K. Shimada, W. Yashiro, A. Momose, and T. Hattori, "Fabrication of large area diffraction grating using liga process," *Microsystem technologies*, vol. 14, no. 9-11, pp. 1311–1315, 2008.

[44] V. Saile, U. Wallrabe, O. Tabata, and J. G. Korvink, *LIGA and its Applications*, vol. 7. Wiley Online Library, 2009.

[45] A. Koch, C. Raven, P. Spanne, and A. Snigirev, "X-ray imaging with submicrometer resolution employing transparent luminescent screens," *JOSA A*, vol. 15, no. 7, pp. 1940–1951, 1998.

[46] T. Martin and A. Koch, "Recent developments in x-ray imaging with micrometer spatial resolution," *Journal of synchrotron radiation*, vol. 13, no. 2, pp. 180–194, 2006.

[47] M. Bech, O. Bunk, C. David, P. Kraft, C. Brönnimann, E. Eikenberry, and F. Pfeiffer, "X-ray imaging with the pilatus 100k detector," *Applied Radiation and Isotopes*, vol. 66, no. 4, pp. 474–478, 2008.

[48] S. Kasap, J. B. Frey, G. Belev, O. Tousignant, H. Mani, L. Laperriere, A. Reznik, and J. A. Rowlands, "Amorphous selenium and its alloys from early xeroradiography to high resolution x-ray image detectors and ultrasensitive imaging tubes," *Physica status solidi (b)*, vol. 246, no. 8, pp. 1794–1805, 2009.

[49] P. Bidola, K. Morgan, M. Willner, A. Fehringer, S. Allner, F. Prade, F. Pfeiffer, and K. Achterhold, "Application of sensitive, high-resolution imaging at a commercial lab-based x-ray micro-ct system using propagation-based phase retrieval," *Journal of Microscopy*, vol. 266, no. 2, pp. 211–220, 2017.

[50] H. Cochard, S. Delzon, and E. Badel, "X-ray microtomography (micro-ct): a reference technology for high-resolution quantification of xylem embolism in trees," *Plant, Cell & Environment*, vol. 38, no. 1, pp. 201–206, 2015.

[51] M. d. C. Fonseca, B. H. S. Araujo, C. S. B. Dias, N. L. Archilha, D. P. A. Neto, E. Cavalheiro, H. Westfahl, A. J. R. da Silva, and K. G. Franchini, "High-resolution synchrotron-based x-ray microtomography as a tool to unveil the three-dimensional neuronal architecture of the brain," *Scientific reports*, vol. 8, no. 1, pp. 1–13, 2018.

[52] C. C. Scott, M. Farrier, Y. Li, S. Laxer, P. Ravi, P. Kenesei, M. J. Wojcik, A. Miceli, and K. S. Karim, "High-energy micrometre-scale pixel direct conversion x-ray detector," *Journal of Synchrotron Radiation*, vol. 28, no. 4, pp. 1081–1089, 2021.

[53] A. Pil-Ali, S. Adnani, C. C. Scott, and K. S. Karim, "Evaluation of edge-illumination and propagation-based x-ray phase contrast imaging methods for high resolution imaging application," in *Medical Imaging 2021: Physics of Medical Imaging*, vol. 11595, pp. 441–452, SPIE, 2021.

[54] J. Andrejewski, F. De Marco, K. Willer, W. Noichl, A. Gustschin, T. Koehler, P. Meyer, F. Kriner, F. Fischer, C. Braun, *et al.*, "Whole-body x-ray dark-field radiography of a human cadaver," *European Radiology Experimental*, vol. 5, no. 1, pp. 1–9, 2021.

[55] M. Viermetz, N. Gustschin, C. Schmid, J. Haeusele, M. von Teuffenbach, P. Meyer, F. Bergner, T. Lasser, R. Proksa, T. Koehler, *et al.*, "Dark-field computed tomography reaches the human scale," *Proceedings of the National Academy of Sciences*, vol. 119, no. 8, p. e2118799119, 2022.

[56] A. Astolfo, M. Endrizzi, F. A. Vittoria, P. C. Diemoz, B. Price, I. Haig, and A. Olivo, "Large field of view, fast and low dose multimodal phase-contrast imaging at high x-ray energy," *Scientific reports*, vol. 7, no. 1, pp. 1–8, 2017.

[57] C. Hauke, P. Bartl, M. Leghissa, L. Ritschl, S. Sutter, T. Weber, J. Zeidler, J. Freudenberger, T. Mertelmeier, M. Radicke, *et al.*, "A preclinical talbot–lau prototype for x-ray dark-field imaging of human-sized objects," *Medical physics*, vol. 45, no. 6, pp. 2565–2571, 2018.

[58] K. Willer, A. A. Fingerle, L. B. Gromann, F. De Marco, J. Herzen, K. Achterhold, B. Gleich, D. Muenzel, K. Scherer, M. Renz, *et al.*, "X-ray dark-field imaging of the human lung—a feasibility study on a deceased body," *PLoS One*, vol. 13, no. 9, p. e0204565, 2018.

[59] A. Bravin, P. Coan, and P. Suortti, "X-ray phase-contrast imaging: from pre-clinical applications towards clinics," *Physics in Medicine & Biology*, vol. 58, no. 1, p. R1, 2012.

[60] M. Marenzana, C. K. Hagen, P. D. N. Borges, M. Endrizzi, M. B. Szafraniec, K. Ignatyev, and A. Olivo, "Visualization of small lesions in rat cartilage by means of laboratory-based x-ray phase contrast imaging," *Physics in Medicine & Biology*, vol. 57, no. 24, p. 8173, 2012.

[61] R. L. Lohr, C. C. Scott, A. Pil-Ali, and K. S. Karim, "A comparison of phase retrieval methods for propagation-based contrast x-ray imaging with polychromatic sources," in *Medical Imaging 2020: Physics of Medical Imaging*, vol. 11312, p. 1131251, International Society for Optics and Photonics, SPIE, 2020.

[62] A. Burvall, U. Lundström, P. A. Takman, D. H. Larsson, and H. M. Hertz, "Phase retrieval in x-ray phase-contrast imaging suitable for tomography," *Optics express*, vol. 19, no. 11, pp. 10359–10376, 2011.

[63] P. J. Withers, C. Bouman, S. Carmignato, V. Cnudde, D. Grimaldi, C. K. Hagen, E. Maire, M. Manley, A. Du Plessis, and S. R. Stock, "X-ray computed tomography," *Nature Reviews Methods Primers*, vol. 1, no. 1, pp. 1–21, 2021.

[64] L. M. Lohse, A.-L. Robisch, M. Töpperwien, S. Maretzke, M. Krenkel, J. Hagemann, and T. Salditt, "A phase-retrieval toolbox for x-ray holography and tomography," *Journal of Synchrotron Radiation*, vol. 27, no. 3, pp. 852–859, 2020.

[65] A. Olivo and R. Speller, "Image formation principles in coded-aperture based x-ray phase contrast imaging," *Physics in Medicine & Biology*, vol. 53, no. 22, p. 6461, 2008.

[66] K. S. Karim and C. C. Scott, "Method and system for high-resolution x-ray detection for phase contrast x-ray imaging," apr 18 2019. US Patent App. 16/050,354.

[67] A. Parsafar, C. C. Scott, A. El-Falou, P. M. Levine, and K. S. Karim, "Direct-conversion cmos x-ray imager with 5.6 μm $\times$ 6.25 μm pixels," *IEEE Electron Device Letters*, vol. 36, no. 5, pp. 481–483, 2015.

[68] C. C. Scott, S. Abbaszadeh, S. Ghanbarzadeh, G. Allan, M. Farrier, I. A. Cunningham, and K. S. Karim, "Amorphous selenium direct detection cmos digital x-ray imager with 25 micron pixel pitch," in *Medical Imaging 2014: Physics of Medical Imaging*, vol. 9033, p. 90331G, International Society for Optics and Photonics, SPIE, 2014.

[69] T. Millard, M. Endrizzi, K. Ignatyev, C. Hagen, P. Munro, R. Speller, and A. Olivo, "Method for automatization of the alignment of a laboratory based x-ray phase contrast edge illumination system," *Review of Scientific Instruments*, vol. 84, no. 8, p. 083702, 2013.

[70] C. Scott, "Hybrid semiconductor detectors for high spatial resolution phase-contrast x-ray imaging," 2019.

[71] F. A. Vittoria, P. C. Diemoz, M. Endrizzi, L. Rigon, F. C. Lopez, D. Dreossi, P. R. Munro, and A. Olivo, "Strategies for efficient and fast wave optics simulation of coded-aperture and other x-ray phase-contrast imaging methods," *Applied optics*, vol. 52, no. 28, pp. 6940–6947, 2013.

[72] U. Lundström, *Phase-contrast x-ray carbon dioxide angiography*. PhD thesis, KTH Royal Institute of Technology, 2014.

[73] J. Siewerdsen, A. Waese, D. Moseley, S. Richard, and D. Jaffray, "Spektr: A computational tool for x-ray spectral analysis and imaging system optimization," *Medical physics*, vol. 31, no. 11, pp. 3057–3067, 2004.

[74] A. Pil-Ali, S. Adnani, C. C. Scott, and K. S. Karim, "Direct conversion x-ray detector with micron-scale pixel pitch for edge-illumination and propagation-based x-ray phase-contrast imaging," *Sensors*, vol. 22, no. 15, p. 5890, 2022.

[75] F. Palermo, N. Pieroni, L. Maugeri, G. B. Provinciali, A. Sanna, L. Massimi, M. Catalano, M. P. Olbinado, I. Bukreeva, M. Fratini, *et al.*, "X-ray phase contrast tomography serves preclinical investigation of neurodegenerative diseases," *Frontiers in Neuroscience*, vol. 14, p. 584161, 2020.

[76] K. S. Karim and C. C. Scott, "Method and system for high-resolution x-ray detection for phase contrast x-ray imaging," feb 9 2021. US Patent 10,914,689.

[77] G. Kallon, P. Diemoz, F. Vittoria, D. Basta, M. Endrizzi, and A. Olivo, "Comparing signal intensity and refraction sensitivity of double and single mask edge illumination lab-based x-ray phase contrast imaging set-ups," *Journal of Physics D: Applied Physics*, vol. 50, no. 41, p. 415401, 2017.

[78] A. Zamir, P. C. Diemoz, F. A. Vittoria, C. K. Hagen, M. Endrizzi, and A. Olivo, "Edge illumination x-ray phase tomography of multi-material samples using a single-image phase retrieval algorithm," *Optics express*, vol. 25, no. 10, pp. 11984–11996, 2017.

[79] S. Vespucci, C. Lewis, C. S. Park, and M. Das, "Examining phase contrast sensitivity to signal location and tissue thickness in breast imaging," in *Medical Imaging 2018: Physics of Medical Imaging*, vol. 10573, p. 1057324, International Society for Optics and Photonics, 2018.

[80] G. Kallon, F. Vittoria, I. Buchanan, M. Endrizzi, and A. Olivo, "An experimental approach to optimising refraction sensitivity for lab-based edge illumination phase contrast set-ups," *Journal of Physics D: Applied Physics*, vol. 53, no. 19, p. 195404, 2020.

[81] G. Havariyoun, F. A. Vittoria, C. K. Hagen, D. Basta, G. K. Kallon, M. Endrizzi, L. Massimi, P. Munro, S. Hawker, B. Smit, *et al.*, "A compact system for intraoperative specimen imaging based on edge illumination x-ray phase contrast," *Physics in Medicine & Biology*, vol. 64, no. 23, p. 235005, 2019.

[82] L. Massimi, G. K. Kallon, I. Buchanan, M. Endrizzi, P. Dobrosz, R. Brooks, D. Brau, E. Bullard, and A. Olivo, "Replacing the detector mask with a structured scintillator in edge-illumination x-ray phase contrast imaging," *Journal of Applied Physics*, vol. 131, no. 20, p. 204501, 2022.

[83] L. Romano, J. Vila-Comamala, H. Schift, M. Stampanoni, and K. Jefimovs, "Hot embossing of au-and pb-based alloys for x-ray grating fabrication," *Journal of Vacuum Science & Technology B, Nanotechnology and Microelectronics: Materials, Processing, Measurement, and Phenomena*, vol. 35, no. 6, p. 06G302, 2017.

[84] L. Romano, J. Vila-Comamala, M. Kagias, K. Vogelsang, H. Schift, M. Stampanoni, and K. Jefimovs, "High aspect ratio metal microcasting by hot embossing for x-ray optics fabrication," *Microelectronic Engineering*, vol. 176, pp. 6–10, 2017.

[85] M. Kagias, Z. Wang, V. A. Guzenko, C. David, M. Stampanoni, and K. Jefimovs, "Fabrication of au gratings by seedless electroplating for x-ray grating interferometry," *Materials Science in Semiconductor Processing*, vol. 92, pp. 73–79, 2019.

[86] J. Mohr, T. Grund, D. Kunka, J. Kenntner, J. Leuthold, J. Meiser, J. Schulz, and M. Walter, "High aspect ratio gratings for x-ray phase contrast imaging," in *AIP Conference proceedings*, vol. 1466, pp. 41–50, American Institute of Physics, 2012.

[87] W. Ehrfeld and H. Lehr, "Deep x-ray lithography for the production of three-dimensional microstructures from metals, polymers and ceramics," *Radiation Physics and Chemistry*, vol. 45, no. 3, pp. 349–365, 1995.

[88] H. Guckel, "High-aspect-ratio micromachining via deep x-ray lithography," *Proceedings of the IEEE*, vol. 86, no. 8, pp. 1586–1593, 1998.

[89] J. Kenntner, V. Altapova, T. Grund, F. J. Pantenburg, J. Meiser, T. Baumbach, and J. Mohr, "Fabrication and characterization of analyzer gratings with high aspect ratios for phase contrast imaging using a talbot interferometer," in *AIP Conference Proceedings*, vol. 1437, pp. 89–93, American Institute of Physics, 2012.

[90] T.-E. Song, S. Lee, H. Han, S. Jung, S.-H. Kim, M. J. Kim, S. W. Lee, and C. W. Ahn, "Evaluation of grating realized via pulse current electroplating combined with atomic layer deposition as an x-ray grating interferometer," *Journal of Vacuum Science & Technology A: Vacuum, Surfaces, and Films*, vol. 37, no. 3, p. 030903, 2019.

[91] H. Miao, A. A. Gomella, N. Chedid, L. Chen, and H. Wen, "Fabrication of 200 nm period hard x-ray phase gratings," *Nano letters*, vol. 14, no. 6, pp. 3453–3458, 2014.

[92] D. Josell, Z. Shi, K. Jefimovs, V. Guzenko, C. Beauchamp, L. Peer, M. Polikarpov, and T. Moffat, "Bottom-up gold filling in new geometries and yet higher aspect ratio gratings for hard x-ray interferometry," *Journal of The Electrochemical Society*, vol. 168, no. 8, p. 082508, 2021.

[93] A. Szeghalmi, M. Arnold, A. Berger, N. Schammelt, K. Fuechsel, M. Knez, E. Kley, D. Zahn, and A. Tuennermann, "Atomic layer deposition of iridium thin films and their application in gold electrodeposition," in *Advances in Optical Thin Films IV*, vol. 8168, pp. 142–151, SPIE, 2011.

[94] B. C. Mallick, C.-T. Hsieh, K.-M. Yin, Y. A. Gandomi, and K.-T. Huang, "On atomic layer deposition: Current progress and future challenges," *ECS Journal of Solid State Science and Technology*, vol. 8, no. 4, p. N55, 2019.

[95] G. N. Parsons and R. D. Clark, "Area-selective deposition: Fundamentals, applications, and future outlook," *Chemistry of Materials*, vol. 32, no. 12, pp. 4920–4953, 2020.

[96] M. Ahn, R. K. Heilmann, and M. L. Schattenburg, "Fabrication of ultrahigh aspect ratio freestanding gratings on silicon-on-insulator wafers," *Journal of Vacuum Science & Technology B: Microelectronics and Nanometer Structures Processing, Measurement, and Phenomena*, vol. 25, no. 6, pp. 2593–2597, 2007.

[97] A. Bruccoleri, P. Mukherjee, R. K. Heilmann, J. Yam, M. L. Schattenburg, and F. DiPiazza, "Fabrication of nanoscale, high throughput, high aspect ratio freestanding gratings," *Journal of Vacuum Science & Technology B, Nanotechnology and Microelectronics: Materials, Processing, Measurement, and Phenomena*, vol. 30, no. 6, p. 06FF03, 2012.

[98] X. Li, "In macetch: Anisotropic metal-assisted chemical etching defies the textbooks," *SPIE Newsroom*, 2012.

[99] L. Romano and M. Stampanoni, "Microfabrication of x-ray optics by metal assisted chemical etching: A review," *Micromachines*, vol. 11, no. 6, p. 589, 2020.

[100] R. C. Tiberio, M. J. Rooks, C. Chang, C. F. Knollenberg, E. A. Dobisz, and A. Sakdinawat, "Vertical directionality-controlled metal-assisted chemical etching for ultrahigh aspect ratio nanoscale structures," *Journal of Vacuum Science & Technology B, Nanotechnology and Microelectronics: Materials, Processing, Measurement, and Phenomena*, vol. 32, no. 6, p. 06FI01, 2014.

[101] K. Li, M. J. Wojcik, R. Divan, L. E. Ocola, B. Shi, D. Rosenmann, and C. Jacobsen, "Fabrication of hard x-ray zone plates with high aspect ratio using metal-assisted chemical etching," *Journal of Vacuum Science & Technology B, Nanotechnology and Microelectronics: Materials, Processing, Measurement, and Phenomena*, vol. 35, no. 6, p. 06G901, 2017.

[102] S. Rutishauser, M. Bednarzik, I. Zanette, T. Weitkamp, M. Börner, J. Mohr, and C. David, "Fabrication of two-dimensional hard x-ray diffraction gratings," *Microelectronic Engineering*, vol. 101, pp. 12–16, 2013.

[103] M. Drost, S. Marschmeyer, M. Fraschke, O. Fursenko, F. Bärwolf, I. Costina, M. K. Mahadevaiah, and M. Lisker, "Etch mechanism of an al2o3 hard mask in the bosch process," *Micro and Nano Engineering*, vol. 14, p. 100102, 2022.

[104] F. Aydinoglu, F. Saffih, R. K. Dey, and B. Cui, "Chromium oxide as a hard mask material better than metallic chromium," *Journal of Vacuum Science & Technology B, Nanotechnology and Microelectronics: Materials, Processing, Measurement, and Phenomena*, vol. 35, no. 6, p. 06GB01, 2017.

[105] F. Marty, L. Rousseau, B. Saadany, B. Mercier, O. Français, Y. Mita, and T. Bourouina, "Advanced etching of silicon based on deep reactive ion etching for silicon high aspect ratio microstructures and three-dimensional micro-and nanostructures," *Microelectronics journal*, vol. 36, no. 7, pp. 673–677, 2005.

[106] Y. Tang, A. Sandoughsaz, K. J. Owen, and K. Najafi, "Ultra deep reactive ion etching of high aspect-ratio and thick silicon using a ramped-parameter process," *Journal of Microelectromechanical Systems*, vol. 27, no. 4, pp. 686–697, 2018.

[107] J. Parasuraman, A. Summanwar, F. Marty, P. Basset, D. E. Angelescu, and T. Bourouina, "Deep reactive ion etching of sub-micrometer trenches with ultra high aspect ratio," *Microelectronic engineering*, vol. 113, pp. 35–39, 2014.

[108] M. Huff, "Recent advances in reactive ion etching and applications of high-aspect-ratio microfabrication," *Micromachines*, vol. 12, no. 8, p. 991, 2021.

[109] J. Rieger, P. Meyer, F. Horn, G. Pelzer, T. Michel, J. Mohr, and G. Anton, "Optimization procedure for a talbot-lau x-ray phase-contrast imaging system," *Journal of Instrumentation*, vol. 12, no. 04, p. P04018, 2017.

[110] W. Haas, P. Bartl, F. Bayer, J. Durst, T. Grund, J. Kenntner, T. Michel, A. Ritter, T. Weber, G. Anton, *et al.*, "Performance analysis of x-ray phase-contrast interferometers with respect to grating layouts," in *IEEE Nuclear Science Symposuim & Medical Imaging Conference*, pp. 3176–3178, IEEE, 2010.

[111] M. Zakharova, V. Vlnieska, H. Fornasier, M. Börner, T. d. S. Rolo, J. Mohr, and D. Kunka, "Development and characterization of two-dimensional gratings for single-shot x-ray phase-contrast imaging," *Applied Sciences*, vol. 8, no. 3, p. 468, 2018.

[112] C.-K. Chung, "Geometrical pattern effect on silicon deep etching by an inductively coupled plasma system," *Journal of Micromechanics and Microengineering*, vol. 14, no. 4, p. 656, 2004.

[113] J. Meiser, M. Willner, T. Schröter, A. Hofmann, J. Rieger, F. Koch, L. Birnbacher, M. Schüttler, D. Kunka, P. Meyer, *et al.*, "Increasing the field of view in grating based x-ray phase contrast imaging using stitched gratings," *Journal of X-ray science and technology*, vol. 24, no. 3, pp. 379–388, 2016.

[114] T. J. Schröter, F. J. Koch, P. Meyer, D. Kunka, J. Meiser, K. Willer, L. Gromann, F. De Marco, J. Herzen, P. Noel, *et al.*, "Large field-of-view tiled grating structures for x-ray phase-contrast imaging," *Review of Scientific Instruments*, vol. 88, no. 1, p. 015104, 2017.

[115] S. M. P. Kalaiselvi, E. Tang, H. Moser, M. Breese, S. P. Turaga, H. Kasi, and S. P. Heussler, "Wafer scale manufacturing of high precision micro-optical components through x-ray lithography yielding 1800 gray levels in a fingertip sized chip," *Scientific reports*, vol. 12, no. 1, pp. 1–12, 2022.

[116] V. Nazmov, B. Goldenberg, A. Vasiliev, and V. Asadchikov, "Optimization of x-ray lithography conditions for fabrication of large arrays of high-aspect-ratio submicron pores," *Journal of Micromechanics and Microengineering*, vol. 31, no. 5, p. 055011, 2021.

[117] G. Genolet and H. Lorenz, "Uv-liga: From development to commercialization," *Micromachines*, vol. 5, no. 3, pp. 486–495, 2014.

[118] E. Fortunato, P. Barquinha, and R. Martins, "Oxide semiconductor thin-film transistors: a review of recent advances," *Advanced materials*, vol. 24, no. 22, pp. 2945–2986, 2012.

[119] Y. Kuo, "Thin film transistor technology—past, present, and future," *The Electrochemical Society Interface*, vol. 22, no. 1, p. 55, 2013.

[120] J. Daniel, A. Sawant, M. Teepe, C. Shih, R. Street, and L. Antonuk, "Fabrication of high aspect-ratio polymer microstructures for large-area electronic portal x-ray imagers," *Sensors and Actuators A: Physical*, vol. 140, no. 2, pp. 185–193, 2007.

[121] J.-h. Jeong, K.-d. Kim, D.-g. Choi, J. Choi, and E.-s. Lee, "Ultra-violet nanoimprint lithography applicable to thin-film transistor liquid-crystal display," in *Emerging Lithographic Technologies XI*, vol. 6517, pp. 370–377, SPIE, 2007.

[122] H. Lorenz, M. Despont, N. Fahrni, N. LaBianca, P. Renaud, and P. Vettiger, "Su-8: a low-cost negative resist for mems," *Journal of Micromechanics and Microengineering*, vol. 7, no. 3, p. 121, 1997.

[123] A. Llobera, V. Seidemann, J. A. Plaza, V. J. Cadarso, and S. Buttgenbach, "Su-8 optical accelerometers," *Journal of microelectromechanical systems*, vol. 16, no. 1, pp. 111–121, 2007.

[124] M. Jamal, A. M. Zarafshar, and D. H. Gracias, "Differentially photo-crosslinked polymers enable self-assembling microfluidics," *Nature communications*, vol. 2, no. 1, pp. 1–6, 2011.

[125] S. Ghosh and G. Ananthasuresh, "Single-photon-multi-layer-interference lithography for high-aspect-ratio and three-dimensional su-8 micro-/nanostructures," *Scientific reports*, vol. 6, no. 1, pp. 1–9, 2016.

[126] R. S. Lima, P. A. Leão, M. H. Piazzetta, A. M. Monteiro, L. Y. Shiroma, A. L. Gobbi, and E. Carrilho, "Sacrificial adhesive bonding: a powerful method for fabrication of glass microchips," *Scientific reports*, vol. 5, no. 1, pp. 1–15, 2015.

[127] D.-l. Li, Z.-y. Wen, Z.-g. Shang, and Y. She, "Thick su8 microstructures prepared by broadband uv lithography and the applications in mems devices," *Optoelectronics Letters*, vol. 12, no. 3, pp. 182–187, 2016.

[128] B. Li, M. Liu, and Q. Chen, "Low-stress ultra-thick su-8 uv photolithography process for mems," *Journal of Micro/Nanolithography, MEMS, and MOEMS*, vol. 4, no. 4, p. 043008, 2005.

[129] J. J. Kim, H. Al Thuwaini, and M. Almuslem, "Photolithography of su-8 microtowers for a 100-turn, 3-d toroidal microinductor," *Micro and Nano Systems Letters*, vol. 6, no. 1, pp. 1–9, 2018.

[130] J. Carlier, S. Arscott, V. Thomy, J. Fourrier, F. Caron, J. Camart, C. Druon, and P. Tabourier, "Integrated microfluidics based on multi-layered su-8 for mass spectrometry analysis," *Journal of micromechanics and Microengineering*, vol. 14, no. 4, p. 619, 2004.

[131] A. Mata, A. J. Fleischman, and S. Roy, "Fabrication of multi-layer su-8 microstructures," *Journal of micromechanics and microengineering*, vol. 16, no. 2, p. 276, 2006.

[132] M. C. Peterman, P. Huie, D. Bloom, and H. A. Fishman, "Building thick photoresist structures from the bottom up," *Journal of Micromechanics and Microengineering*, vol. 13, no. 3, p. 380, 2003.

[133] B. Bohl, R. Steger, R. Zengerle, and P. Koltay, "Multi-layer su-8 lift-off technology for microfluidic devices," *Journal of micromechanics and microengineering*, vol. 15, no. 6, p. 1125, 2005.

[134] K. Haq, K. Behrndt, and I. Kobin, "Adhesion mechanism of gold-underlayer film combinations to oxide substrates," *Journal of Vacuum Science and Technology*, vol. 6, no. 1, pp. 148–152, 1969.

[135] R. L. Barber, M. K. Ghantasala, R. Divan, D. C. Mancini, and E. C. Harvey, "Study of stress and adhesion strength in su-8 resist layers on silicon substrate with different seed layers," *Journal of Micro/Nanolithography, MEMS, and MOEMS*, vol. 6, no. 3, p. 033006, 2007.

[136] B. F. Matarèse, P. L. Feyen, A. Falco, F. Benfenati, P. Lugli, and J. C. deMello, "Use of su8 as a stable and biocompatible adhesion layer for gold bioelectrodes," *Scientific reports*, vol. 8, no. 1, pp. 1–12, 2018.

[137] H. Garoff and W. Ansorge, "Improvements of dna sequencing gels," *Analytical biochemistry*, vol. 115, no. 2, pp. 450–457, 1981.

[138] K. H. Rasmussen, S. S. Keller, F. Jensen, A. M. Jorgensen, and O. Hansen, "Su-8 etching in inductively coupled oxygen plasma," *Microelectronic engineering*, vol. 112, pp. 35–40, 2013.

[139] C. Lü, X. Yin, and M. Wang, "Fabrication of high aspect ratio metallic microstructures on ito glass substrate using reverse-side exposure of su-8," *Sensors and Actuators A: Physical*, vol. 136, no. 1, pp. 412–416, 2007.

[140] D. Geng, D. H. Kang, and J. Jang, "High-performance amorphous indium–gallium–zinc–oxide thin-film transistor with a self-aligned etch stopper patterned by back-side uv exposure," *IEEE Electron Device Letters*, vol. 32, no. 6, pp. 758–760, 2011.

[141] Y. Zhang, Z. Mei, W. Huo, T. Wang, H. Liang, and X. Du, "Self-aligned photolithography for the fabrication of fully transparent high-voltage devices," *Journal of Physics D: Applied Physics*, vol. 51, no. 17, p. 175102, 2018.

[142] Y.-K. Yoon, J.-H. Park, and M. G. Allen, "Multidirectional uv lithography for complex 3-d mems structures," *Journal of microelectromechanical systems*, vol. 15, no. 5, pp. 1121–1130, 2006.

[143] J. Vinje, K. S. Beckwith, and P. Sikorski, "Electron beam lithography fabrication of su-8 polymer structures for cell studies," *Journal of Microelectromechanical Systems*, vol. 29, no. 2, pp. 160–169, 2020.

[144] M. Kang, J. H. Byun, S. Na, and N. L. Jeon, "Fabrication of functional 3d multilevel microstructures on transparent substrates by one step back-side uv photolithography," *RSC advances*, vol. 7, no. 22, pp. 13353–13361, 2017.

[145] D. Noda, A. Tokuoka, and T. Hattori, "Fabrication of high aspect ratio x-ray grating using silicon dry etching method," in *AIP Conference Proceedings*, vol. 1466, pp. 187–192, American Institute of Physics, 2012.

[146] M. N. Wernick, O. Wirjadi, D. Chapman, Z. Zhong, N. P. Galatsanos, Y. Yang, J. G. Brankov, O. Oltulu, M. A. Anastasio, and C. Muehleman, "Multiple-image radiography," *Physics in Medicine & Biology*, vol. 48, no. 23, p. 3875, 2003.

[147] I. Zanette, T. Zhou, A. Burvall, U. Lundström, D. H. Larsson, M. Zdora, P. Thibault, F. Pfeiffer, and H. M. Hertz, "Speckle-based x-ray phase-contrast and dark-field imaging with a laboratory source," *Physical review letters*, vol. 112, no. 25, p. 253903, 2014.

[148] T. Partridge, A. Astolfo, S. Shankar, F. Vittoria, M. Endrizzi, S. Arridge, T. Riley-Smith, I. Haig, D. Bate, and A. Olivo, "Enhanced detection of threat materials by dark-field x-ray imaging combined with deep neural networks," *Nature communications*, vol. 13, no. 1, pp. 1–12, 2022.

[149] B. Vandenberghe, R. Jacobs, and H. Bosmans, "Modern dental imaging: a review of the current technology and clinical applications in dental practice," *European radiology*, vol. 20, no. 11, pp. 2637–2655, 2010.

[150] C. R. Inscoe, E. Platin, S. M. Mauriello, A. Broome, A. Mol, L. R. Gaalaas, M. W. R. Anderson, C. Puett, J. Lu, and O. Zhou, "Characterization and preliminary imaging evaluation of a clinical prototype stationary intraoral tomosynthesis system," *Medical physics*, vol. 45, no. 11, pp. 5172–5185, 2018.

[151] "American association of endodontists (aae)." https://www.aae.org/patients/wp-content/uploads/sites/3/2017/08/Root-Canals-Explained.jpg. Accessed: 2022-10-16.

[152] T. Weitkamp, D. Haas, D. Wegrzynek, and A. Rack, "Ankaphase: software for single-distance phase retrieval from inline x-ray phase-contrast radiographs," *Journal of synchrotron radiation*, vol. 18, no. 4, pp. 617–629, 2011.

[153] D. Paganin, S. C. Mayo, T. E. Gureyev, P. R. Miller, and S. W. Wilkins, "Simultaneous phase and amplitude extraction from a single defocused image of a homogeneous object," *Journal of microscopy*, vol. 206, no. 1, pp. 33–40, 2002.

[154] F. A. Vittoria, G. K. Kallon, D. Basta, P. C. Diemoz, I. K. Robinson, A. Olivo, and M. Endrizzi, "Beam tracking approach for single–shot retrieval of absorption, refraction, and dark–field signals with laboratory x–ray sources," *Applied Physics Letters*, vol. 106, no. 22, p. 224102, 2015.

[155] P. C. Diemoz and A. Olivo, "On the origin of contrast in edge illumination x-ray phase-contrast imaging," *Optics express*, vol. 22, no. 23, pp. 28199–28214, 2014.

[156] Y. Chen, C. K. Hagen, A. Olivo, and M. A. Anastasio, "A partial-dithering strategy for edge-illumination x-ray phase-contrast tomography enabled by a joint reconstruction method," *Physics in Medicine & Biology*, vol. 65, no. 10, p. 105007, 2020.

[157] P. Modregger, M. Kagias, S. C. Irvine, R. Brönnimann, K. Jefimovs, M. Endrizzi, and A. Olivo, "Interpretation and utility of the moments of small-angle x-ray scattering distributions," *Physical review letters*, vol. 118, no. 26, p. 265501, 2017.

[158] P. Modregger, F. Scattarella, B. Pinzer, C. David, R. Bellotti, and M. Stampanoni, "Imaging the ultrasmall-angle x-ray scattering distribution with grating interferometry," *Physical review letters*, vol. 108, no. 4, p. 048101, 2012.

[159] F. A. Vittoria, M. Endrizzi, and A. Olivo, "Retrieving the ultrasmall-angle x-ray scattering signal with polychromatic radiation in speckle-tracking and beam-tracking phase-contrast imaging," *Physical Review Applied*, vol. 7, no. 3, p. 034024, 2017.

[160] M.-C. Zdora, "State of the art of x-ray speckle-based phase-contrast and dark-field imaging," *Journal of Imaging*, vol. 4, no. 5, p. 60, 2018.

[161] H. Wang, S. Berujon, J. Herzen, R. Atwood, D. Laundy, A. Hipp, and K. Sawhney, "X-ray phase contrast tomography by tracking near field speckle," *Scientific reports*, vol. 5, no. 1, pp. 1–6, 2015.

[162] I. Zanette, M.-C. Zdora, T. Zhou, A. Burvall, D. H. Larsson, P. Thibault, H. M. Hertz, and F. Pfeiffer, "X-ray microtomography using correlation of near-field speckles for material characterization," *Proceedings of the National Academy of Sciences*, vol. 112, no. 41, pp. 12569–12573, 2015.

[163] S. Berujon and E. Ziegler, "Near-field speckle-scanning-based x-ray imaging," *Physical Review A*, vol. 92, no. 1, p. 013837, 2015.

[164] S. Z. Shi, N. Shapira, P. B. Noël, and S. Meyer, "Displacement retrieval for speckle-based x-ray phase-contrast imaging using a convolutional neural network," in *Medical Imaging 2022: Image Processing*, vol. 12032, p. 1203225, SPIE, 2022.

Appendix A

MATLAB® Algorithm for Simulating PB and EI-XPCi

```
 for j=60 %this is the tube potential (kVp)
%%
% R1 = 0.2899999; %try for 0.0899999    and    0.1799999    and     ...
    0.539999    and   1.079999    and    2.159999    and    4.319999
Modality = "EI";
material = "PEEK";
R1=(0.18);
    for R1=R1
        R_Total = (R1+0.000001)*1.25;
        n=1;
%       for R_sd=R_Total:-(R_Total-R1-0.000001)/1:R1+0.000001
        for R_sd=R_Total
            disp(n);

            %%%%     Imaging geometry
            %R1 = .179999; %[m] source to object distance
            Rtot = R_sd; %[m] source to detector distance
            R2 = Rtot-R1; %[m] object to detector distance
            M = Rtot/R1; %magnification
            z2 = R2/M; %[m] effective propagation distance
            z1 = R1/M;
            NN = 1.0;
            pixelSizeX = 7.8e-6 *NN ; pixelSizeY = 7.8e-6 *NN;

            FOV = 3*15.9*7.8e-6; %field of view for simulation
            %%
```

```
26              %%%%     Simulation resolution and field of view
27              dx = pixelSizeX/50/M; %[m] simulation pixel size in x ...
                    direction in object plane
28              dy = pixelSizeY/1/M; %[m] simulation pixel size in y ...
                    direction in object plane
29              xmin = -FOV; xmax = FOV; %[m] x range of field of view in ...
                    obj plane
30              ymin = -0.05*FOV; ymax = 0.05*FOV; %[m] y range of field ...
                    of view in obj plane
31              x = xmin:dx:xmax; y = ymin:dy:ymax; %[m] coordinate vectors
32              [X, Y] = meshgrid(x,y); %[m] coordinate matrices
33              %%
34              % % Spatial frequencies
35              nx = length(x); ny = length(y); %number of pixels in x ...
                    and y direction
36
37              %[1/m] frequency in the x and y directions, respectively
38              u = ifftshift((-floor(nx/2):floor((nx-1)/2))/(nx*dx));
39              v = ifftshift((-floor(ny/2):floor((ny-1)/2))/(ny*dy));
40              [U, V] = meshgrid(u,v); %[1/m] frequency grid
41              w2 = U.^2 + V.^2; %frequency magnitude squared
42
43              %%
44              % Physical constants
45
46              c = 299792458; %[m/s] speed of light in vacuum
47              h = 6.6260689633e-34; %[Js] Plack constant
48              eV = 1.6022e-019; %[J/eV] unit conversion constant
49              re = 2.82e-15; %[m] classical electron radius
50              Na = 6.022e23; %[atoms/mol] Avogradro's number
51              me = 9.10938356e-31; %[kg] mass of an electron
52              N = 6.022E23; % [atoms/mol] Avogadro's number
53
54  %     gain = 7e-5; %[counts/eV] the detector sensitivity
55      exposureTime = 20; %[s] exposure time
56
57      %% X-ray energy
58      E = (1:150)*1e3'; % [eV]
59      inherent_filtration = [spektrElement2Z('Be'), 0.127]; % [mm Be]
60      added_filtration = [[spektrElement2Z('Al'), 0.5]]; % [mm Al]
61      kVp = j; % [kVp]
62      Phi_tube = spektrSpectrum(kVp, inherent_filtration); % spectrum ...
            with inherent filtratio
63      spectrum = spektrBeers(Phi_tube, added_filtration); % spectrum ...
            with filtration
64      spectrum = spectrum(1:150);
```

```
65
66      %%%%   selecting a material   %%%%
67      % material = "PTFE";
68      % % Density of the elements
69      % rhoC = 2.214392*100^3; %[g/m^3] Density of Carbon
70      % rhoH = 8.987E-5*100^3; %[g/m^3] Density of Hydrogem
71      % rhoN = 1.165E-3*100^3; %[g/m^3] Density of Nitrogen
72      % rhoO = 1.330E-3*100^3; %[g/m^3] Density of Oxygen
73      % rhoF = 1696;           %[g/m^3] Density of Fluorine
74
75      % Atomic number of the elements in the periodic table
76      ZH = 1;
77      ZC = 6;
78      ZN = 7;
79      ZO = 8;
80      ZF = 9;
81      ZTi= 22;
82
83
84      if material=="Kapton"
85          % Kapton compostion is C_(22)H_(10)N_(2)O_(5)
86          rho = 1.42*10^6; %[g/m^3] Density of Kapton Polyimide film
87          mu = spektrMuRhoCompound([6 22; 1 10; 7 2; 8 5])*rho*10^-7; % ...
                [1/m] attenuation
88          mu = interp1((1:150), mu, E/1000); % interpolate for all energies
89          %Number of elements in the selectrd material
90          Num_of_C = 22;
91          Num_of_H = 10;
92          Num_of_O = 5;
93          Num_of_N = 2;
94          Num_of_F = 0;
95          Num_of_Ti= 0;
96
97      elseif material=="PTFE" || material=="Teflon"
98          % PTFE compostion is C_(4)F(4); The best known PTFE-based ...
                formula is Teflon by Chemours
99          [mu,rho] = spektrMuRhoCompound(18); % mu(E) is in mm^-1 and ...
                rho is in g/cm^3
100         mu = mu(1:150)*10^3; % mu in m^-1
101         rho =rho*100^3; %[g/m^3] Density of PEEK
102     %     rho = 2.2*100^3; %[g/m^3] Density of PTFE
103         %Number of elements in the selectrd material
104         Num_of_C = 4;
105         Num_of_H = 0;
106         Num_of_O = 0;
107         Num_of_N = 0;
```

```
108         Num_of_F = 4;
109         Num_of_Ti= 0;
110
111     elseif material=="Polystyrene"
112         % Polystyrene compostion is C_(8)H_(8)
113         [mu,rho] = spektrMuRhoCompound(17); % mu(E) is in mm^-1 and ...
                rho is in g/cm^3
114         mu = mu(1:150)*10^3; % mu in m^-1
115         rho =rho*100^3; %[g/m^3] Density of PEEK
116     %     rho = 1.04*100^3; %[g/m^3] Density of Polystyrene
117         %Number of elements in the selectrd material
118         Num_of_C = 8;
119         Num_of_H = 8;
120         Num_of_O = 0;
121         Num_of_N = 0;
122         Num_of_F = 0;
123         Num_of_Ti= 0;
124
125     elseif material=="Titanium"
126         % Titanium compostion is Ti
127         [mu,rho] = spektrMuRhoElement(22);
128         mu = mu(1:150)*10^3;
129         mu = mu';
130         rho = rho*100^3; %[g/m^3] Density of Titanium
131         %Number of elements in the selectrd material
132         Num_of_C = 0;
133         Num_of_H = 0;
134         Num_of_O = 0;
135         Num_of_N = 0;
136         Num_of_F = 0;
137         Num_of_Ti= 1;
138
139     elseif material=="PEEK"
140         % PEEK (PolyEther Ether Ketone) compostion is C_(19)H_(12)O_(3)
141         rho = 1.26*10^6; %[g/m^3] Density of PEEK
142         mu = spektrMuRhoCompound([6 19; 1 12; 8 3])*rho*10^-7; % ...
                [1/m] attenuation
143         mu = interp1((1:150), mu, E/1000); % interpolate for all energies
144         % coefficient of PTFE
145     %     mu = interp1([1:5:150], mu, E/1000); % interpolate for all ...
            energies
146     %     mu = mu(1:150);
147         mu = mu';
148         %Number of elements in the selectrd material
149         Num_of_C = 19;
150         Num_of_H = 12;
```

```
151         Num_of_O = 3;
152         Num_of_N = 0;
153         Num_of_F = 0;
154         Num_of_Ti= 0;
155 
156     elseif material=="PMMA"
157         % PMMA Poly(methyl methacrylate) compostion or chemical ...
               formula is C_(5)O_(2)H_(8)
158         [mu,rho] = spektrMuRhoCompound(6); % mu(E) is in mm^-1 and ...
               rho is in g/cm^3
159         mu = mu(1:150)*1000; % mu in m^-1
160         rho =rho*100^3; %[g/m^3] Density of PEEK
161         %Number of elements in the selectrd material
162         Num_of_C = 5;
163         Num_of_H = 8;
164         Num_of_O = 2;
165         Num_of_N = 0;
166         Num_of_F = 0;
167         Num_of_Ti= 0;
168     end
169 
170     MMC = 12.011*Num_of_C; %[g/mol]
171     MMH = 1.008*Num_of_H; %[g/mol]
172     MMO = 15.9994*Num_of_O; %[g/mol]
173     MMN = 14.00670*Num_of_N; %[g/mol]
174     MMF = 18.9984*Num_of_F; %[g/mol]
175     MMTi= 47.867*Num_of_Ti; %[g/mol]
176 
177     MM_total = MMC + MMH + MMO + MMN + MMF + MMTi;
178     nz_total = rho*1/MM_total*N; %atoms/m^3
179     Z = ZC*Num_of_C +ZH*Num_of_H + ZO*Num_of_O + ...
180         ZN*Num_of_N + ZF*Num_of_F + ZTi*Num_of_Ti;
181 
182     %Delta calculated using detla = re*h^2*c^2/(2*pi*E) sum over all ...
           z(n_z*f^0_1z(E)) from thesis
183     ∆ = re*h^2*c^2./(2*pi*(E*eV).^2).*(nz_total.*Z);
184     % mu = mu_Teflon(E)*100;
185 
186     %Detector
187     rho_Se = 4.819; %[g/cm^3] density of selenium
188     mu_Se = spektrMuRhoElement(34)*rho_Se*100; %[1/m] attenuation
189     E_mu = (1:150)*1e3; %Spektr energies [eV]
190     mu_Se = interp1(E_mu, mu_Se, E);
191     thickness_Selenium = 100e-6; % [m] thickness of selenium ...
           deposited on the detector
192     eta = 1-exp(-mu_Se.*thickness_Selenium);
```

```
193      % spectrum = spectrum'.*eta;
194
195      lambda = c*h./(E*eV); %[m] wavelength
196      k = 2*pi./lambda; %[1/m] angular wave number
197  %%
198                nos = 100;   %number of steps
199
200          Contrast = NaN(nos,1);
201          Edge_Enhancement_percentage = NaN(nos,1);
202          Visibility = NaN(nos,1);
203          misalignment_x = NaN(nos,1);
204
205          trans = 0; % between 0 and 1
206          for misalignment_fraction = -0.18:0.03:1.0
207
208              %     misalignment_fraction=0;
209                  %                 %%%%%%%%%%%%%%%%%%
210                  %      GRATINGS
211                  %                 %%%%%%%%%%%%%%%%%%
212                  MM2 = zeros(ny,nx);
213                  % MM2 = ones(ny,nx);
214                  period2 = (1*pixelSizeX /M) / dx;
215                  opening_fraction = 0.15;
216                  misalignment_fraction_2 = 0.0;
217                  misalignment_2 = (misalignment_fraction_2 .* ...
218                      pixelSizeX /M) / dx;
219                  opening2 = (pixelSizeX * opening_fraction /M) / dx ;
220                  blocking2 = period2 - opening2  ;
221                  number2 = floor((nx)/period2);
222                  for xx = 1:number2-1
223                      xx21 = (2*xx-1)*(blocking2)/2 + ...
224                          (xx-1)*opening2 + misalignment_2;
225                      xx22 = (2*xx-1)*(blocking2)/2 + ...
226                          xx   *opening2 + misalignment_2;
227                      MM2 (:,xx21:xx22)=1;
228                  end
229      %             MM2 = ones(ny,nx);
230              %     figure
231              %     imagesc(MM2)
232                  T_M2 = MM2;
233                  T_M2(T_M2==0) = trans;
234                  %------------------------------
235                  MM1 = zeros(ny,nx);
236                  % MM1 = ones(ny,nx);
237                  fraction_M1 = 0.25;
238                  opening1 = (pixelSizeX * fraction_M1 /M)/dx;
```

```
239                 period1 = (1*pixelSizeX /M)/dx;
240                 blocking1 = period1 - opening1;
241 %                 misalignment_fraction = 0.15;
242
243                 misalignment = (misalignment_fraction .* ..
244                 pixelSizeX /M) / dx;
245                 number = floor((nx)/period1);
246                 for xx = 1:number-1
247                     xx11 = (blocking1 - (blocking2 / 2 - opening1 / ...
                            2)) ...
248                          + (xx-1)*opening1 +(xx-1)*blocking1 + ...
                                misalignment;
249                     xx12 = (blocking1 - (blocking2 / 2 - opening1 / ...
                            2)) ...
250                          + (xx)  *opening1 +(xx-1)*blocking1 + ...
                                misalignment;
251                     MM1 (:,xx11:xx12)= 1;
252                 end
253     %             MM1 = ones(ny,nx);
254                 T_M1 = MM1;
255             %     figure
256             %     imagesc(MM1)
257                 T_M1(T_M1==0) = trans;
258             %%
259                 % Specify the source spatial distribution
260                 sourceWidth = 9e-6; %[m] FWHM of Gaussian source
261                 %[m] source standard deviation scaled to sample plane
262                 sourceSigma = sourceWidth/(2*sqrt(2*log(2)))*(M-1)/M;
263                 %source contribution to the system MTF
264                 sourceMTF = exp(-w2*pi^2*2*sourceSigma^2);
265             %%
266                 %%%%     Sum-up contributions to the image from all ...
                        energies of the spectrum
267                 img = zeros(ny,nx); %[detector counts] the image to ...
                        be calculated
268                 img_w = zeros(ny,nx); %[detector counts] the image to ...
                        be calculated
269                 noiseVariance = zeros(ny,nx); %[detector counts^2] ...
                        the noise variance
270
271                 if Modality == "PB"
272                     T_M1 = ones(ny,nx);
273                     T_M2 = ones(ny,nx);
274                 elseif Modality == "EI"
275
276                 end
```

```
277
278                 for i = 1:5:60
279                     %the transmission function of the object at ...
                           energy E(i)
280                     thickness = 2*real(sqrt((37.44*7.8e-6)^2 - ...
281                         (X+1e-6).^2 )); % cylinder
282                     transmission = exp(-thickness*(mu(i) ...
283                         +1i*k(i)*Δ(i))); % mu is multiplied by 2 to ...
                               match experimental data
284
285                     %fourier filter corresponding to free space ...
                           propagation (Eq 5.12)
286                     propagator2 = exp(-1i*pi*z2*lambda(i)*w2);
287                     propagator1 = exp(-1i*pi*R1*lambda(i)*w2);
288                     %propagate field for current photon energy
289
290                     img0 =    abs(T_M2).^2 .*  ...
291                         ifft2(sourceMTF.* ...
292                         fft2(abs(ifft2(fft2(T_M1.*transmission) ...
293                         .* propagator2)).^2))       ;
294                     img_w0 =  abs(T_M2).^2 .*  ...
295                         ifft2(sourceMTF.*fft2(abs(ifft2(fft2(T_M1) ...
296                         .*propagator2)).^2))             ;
297                     %[counts] scaling of the normalized signal to get ...
                           detector counts
298                     %scaling = ...
                           spectrum(i)*dx*dy/R1^2*exposureTime*E(i)*gain;
299                     scaling = spectrum(i)*dx*dy/R1^2*E(i);
300                     %add contribution of this energy to the image
301                     img = img + img0*scaling;
302                     img_w = img_w + img_w0*scaling;
303
304                     %add contribution to the variance of the noise
305                 %   noiseVariance = noiseVariance + ...
                        img0*scaling*E(i)*gain;
306                 end
307             %%
308             % Specify the detector resolution
309
310                 dPSFWidth =7.8e-6 *NN ; %[m] FWHM of Gaussian ...
                       detector point spread function
311                 %[m] detector PSF standard deviation in sample plane
312                 dPSFSigma = dPSFWidth/(2*sqrt(2*log(2)))/M;
313                 %detector contribution to system MTF
314                 detectorMTF = exp(-w2*pi^2*2*dPSFSigma^2);
315
```

```
316
317                 %[m] distance between pixels in x and y direction
318                 %definition of the sinc function (sin(x)/x)
319                 sinc = inline(['sin(max(1e-9,abs(x)))./ ...' ...
320                     'max(1e-9,abs(x))'],'x');
321                 %MTF corresponding to integration over the area of a ...
                       pixel
322                 pixelMTF = sinc(pi*pixelSizeX/M*U).* ...
323                     sinc(pi*pixelSizeY/M*V);
324
325                 % Blur the image (filter with the MTF)
326                 img = ifft2(fft2(img).*detectorMTF.*pixelMTF);
327                 img_w = ifft2(fft2(img_w).*detectorMTF.*pixelMTF);
328
329 %%
330
331             %Interpolate from simulation pixels to detector pixels
332             %define pixel coordinates
333             Dx = pixelSizeX/M; Dy = pixelSizeY/M; %[m] pixel size in ...
                    sample plane
334             xp = min(x)-dx/2+Dx/2:Dx:max(x)+dx/2-Dx/2; %[m]
335             yp = min(y)-dy/2+Dy/2:Dy:max(y)+dy/2-Dy/2; %[m]
336             %[m] create pixel coordinate matrices
337             [Xp, Yp] = meshgrid(xp,yp);
338             %interpolate and scale signal with pixel size
339             img = interp2(X,Y,img,Xp,Yp) ...
340                 *pixelSizeX/M*pixelSizeY/M/(dx*dy);
341             img_w= interp2(X,Y,img_w,Xp,Yp) ...
342             *pixelSizeX/M*pixelSizeY/M/(dx*dy);
343
344                     img_final_CA = (img) ./ img_w; %normalized intensity
345
346         if n==1
347                 %xx is the number of rows in the image  %yy is the ...
                       number of columns in the image
348                 [xx, yy]=size(img_final_CA);
349                 img_PB_XPCi(:,:) = img_final_CA(round(xx/2),1:yy);
350                 img_PB_XPCi = img_PB_XPCi.';
351                 test_matrix = [yy,2];
352                 test_matrix(1:yy,1) = (1:yy);
353                 test_matrix(:,2) = img_PB_XPCi;
354                 Contrast(n,1) = (max(test_matrix(:,2)) - ...
355                     min(test_matrix(:,2)));
356                 Edge_Enhancement_percentage(n,1) = ...
357                     (max(test_matrix(:,2)) - 1) *100;
358                 Visibility(n,1) = (max(test_matrix(:,2)) - ...
```

```
359                     min(test_matrix(:,2)))./(max(test_matrix(:,2)) + ...
                            min(test_matrix(:,2)));
360
361                 misalignment_x(n,1) = misalignment_fraction .* ...
362                     pixelSizeX /M *10^6;
363
364         else
365                 %xx is the number of rows in the image  %yy is the ...
                        number of columns in the image
366                 [xx, yy]=size(img_final_CA);
367                 img_PB_XPCi(:,:) = img_final_CA(round(xx/2),1:yy);
368                 img_PB_XPCi = img_PB_XPCi.';
369                 test_matrix = [yy,2];
370                 test_matrix(1:yy,1) = (1:yy);
371                 test_matrix(:,2) = img_PB_XPCi;
372                 Contrast(n,1) = (max(test_matrix(:,2)) - ...
373                     min(test_matrix(:,2)));
374                 Edge_Enhancement_percentage(n,1) = (max( ...
375                     test_matrix(:,2)) - 1) *100;
376                 Visibility(n,1) = (max(test_matrix(:,2)) - ...
377                     min(test_matrix(:,2)))./(max(test_matrix(:,2)) + ...
378                     min(test_matrix(:,2)));
379                 misalignment_x(n,1) = misalignment_fraction .* ...
380                     pixelSizeX /M *10^6;
381         end
382         disp(n);
383         n = n+1; %n counts the number of loops for object to detector ...
                distance changing
384         end
385         end
386     end
387 end
388 %%%%%%%%%%%%%%%%%%%%%%%%%%%%%%%%%%%%%%%%%%%%%%%%%%
389 %%% CONTRAST
390 %%%%%%%%%%%%%%%%%%%%%%%%%%%%%%%%%%%%%%%%%%%%%%%%%%
391 % [x y width height], where x and y define the distance from the ...
       lower-left corner of the screen to the lower-left corner of the ...
       figure.
392 Fig1=figure('Position', [500 200 700 600], 'Color', [1 1 1]);
393
394 plot(misalignment_x,Contrast,'o','Color','#008000','MarkerSize',...
395     15,'linewidth',2,'MarkerFaceColor','#77AC30');
396
397 title(['Transmission = ',num2str(trans*100),'%']);
398 xlabel('Masks Misalignment (\mum)');
399 ylabel('Contrast');
```

```
xlim([misalignment_x(4) misalignment_x(38)]);
ylim([0 0.68]);
set(findall(gcf,'-property','FontSize'),'FontSize',28);
set(findall(gcf,'-property','FontWeight'),'FontWeight','normal');
set(findall(gcf,'-property','FontName'),'FontName','Times New Roman');
set(findall(gcf,'-property','marker'),'markersize',12)

x_11=1.1;
x_22=1.9;
y11 = ylim;
patch([x_11 x_11 x_22 x_22], ...
    [y11(1) y11(2) y11(2) y11(1)],'k',...
    'facecolor',[.4 .6 .4], ...
    'edgecolor',[.4 .6 .4],'facealpha',0.2,'edgealpha',0.0)

x_1=2.2;
x_2=3.1;
yl = ylim;
patch([x_1 x_1 x_2 x_2], ...
    [yl(1) yl(2) yl(2) yl(1)],'k',...
    'facecolor','#ff4747','edgecolor' ...
    ,'#ff4747','facealpha',0.2,'edgealpha',0.0)

x_111=3.5;
x_222=4.3;
y111 = ylim;
patch([x_111 x_111 x_222 x_222], ...
    [y111(1) y111(2) y111(2) y111(1)],'k',...
    'facecolor',[.4 .6 .4],'edgecolor', ...
    [.4 .6 .4],'facealpha',0.2,'edgealpha',0.0)

saveas(gcf,['Fig_Contrast_',num2str(material),'_',num2str(Modality), ...
    '_With_Interpolation','_trans_',num2str(trans*100)],'png'); ...
       %Generates automatic .png file
% grid on
%%%%%%%%%%%%%%%%%%%%%%%%%%%%%%%%%%%%%%%%%%%%%%%%
%%% EDGE ENHANCEMENT
%%%%%%%%%%%%%%%%%%%%%%%%%%%%%%%%%%%%%%%%%%%%%%%%
% [x y width height], where x and y define the distance from the ...
    lower-left corner of the screen to the lower-left corner of the ...
    figure.
Fig2=figure('Position', [500 200 700 600], 'Color', [1 1 1]);
plot(misalignment_x,Edge_Enhancement_percentage,'o', ...
    'Color','#7E2F8E','MarkerSize',...
    15,'linewidth',2,'MarkerFaceColor','#9B59B6');

```

```
443 title(['Transmission = ',num2str(trans*100),'%']);
444 xlabel('Masks Misalignment (\mum)');
445 ylabel('Edge-Enhancement %');
446 xlim([misalignment_x(4) misalignment_x(38)]);
447 ylim([0 52]);
448 set(findall(gcf,'-property','FontSize'),'FontSize',28);
449 set(findall(gcf,'-property','FontWeight'),'FontWeight','normal');
450 set(findall(gcf,'-property','FontName'),'FontName','Times New Roman');
451 set(findall(gcf,'-property','marker'),'markersize',12)
452
453 x_11=1.1;
454 x_22=1.9;
455 y11 = ylim;
456 patch([x_11 x_11 x_22 x_22],[y11(1) y11(2) y11(2) y11(1)],'k',...
457     'facecolor',[.4 .6 .4],'edgecolor', ...
458     [.4 .6 .4],'facealpha',0.2,'edgealpha',0.0)
459
460 x_1=2.2;
461 x_2=3.1;
462 yl = ylim;
463 patch([x_1 x_1 x_2 x_2],[yl(1) yl(2) yl(2) yl(1)],'k',...
464     'facecolor','#ff4747','edgecolor', ...
465     '#ff4747','facealpha',0.2,'edgealpha',0.0)
466
467 x_111=3.5;
468 x_222=4.3;
469 y111 = ylim;
470 patch([x_111 x_111 x_222 x_222],[y111(1) y111(2) y111(2) y111(1)],'k',...
471     'facecolor',[.4 .6 .4],'edgecolor', ...
472     [.4 .6 .4],'facealpha',0.2,'edgealpha',0.0)
473
474 saveas(gcf,['Fig_EdgeEnhancement_',num2str(material), ...
475     '_',num2str(Modality),'_With_Interpolation','_trans_', ...
476     num2str(trans*100)],'png'); %Generates automatic .png file
477
478 % grid on
479 %%%%%%%%%%%%%%%%%%%%%%%%%%%%%%%%%%%%%%%%%%%%%%%%
480 %%% VISIBILITY
481 %%%%%%%%%%%%%%%%%%%%%%%%%%%%%%%%%%%%%%%%%%%%%%%%
482
483  % [x y width height], where x and y define the distance from the ...
        lower-left corner of the screen to the lower-left corner of the ...
        figure.
484 Fig3=figure('Position', [500 200 700 600], 'Color', [1 1 1]);
485 plot(misalignment_x,Visibility,'o','Color','#0072BD','MarkerSize',...
486     15,'linewidth',2,'MarkerFaceColor','#4DBEEE');
```

```
487
488 title(['Transmission = ',num2str(trans*100),'%']);
489 xlabel('Masks Misalignment (\mum)');
490 ylabel('Visibility');
491 xlim([misalignment_x(4) misalignment_x(38)]);
492 ylim([0 0.28]);
493 set(findall(gcf,'-property','FontSize'),'FontSize',28);
494 set(findall(gcf,'-property','FontWeight'),'FontWeight','normal');
495 set(findall(gcf,'-property','FontName'),'FontName','Times New Roman');
496 set(findall(gcf,'-property','marker'),'markersize',12)
497
498 x_11=1.1;
499 x_22=1.9;
500 y11 = ylim;
501 patch([x_11 x_11 x_22 x_22],[y11(1) y11(2) y11(2) y11(1)],'k',...
502     'facecolor',[.4 .6 .4],'edgecolor',[.4 .6 .4], ...
503     'facealpha',0.2,'edgealpha',0.0)
504
505 x_1=2.2;
506 x_2=3.1;
507 yl = ylim;
508 patch([x_1 x_1 x_2 x_2],[yl(1) yl(2) yl(2) yl(1)],'k',...
509     'facecolor','#ff4747','edgecolor','#ff4747', ...
510     'facealpha',0.2,'edgealpha',0.0)
511
512 x_111=3.5;
513 x_222=4.3;
514 y111 = ylim;
515 patch([x_111 x_111 x_222 x_222],[y111(1) y111(2) y111(2) y111(1)],'k',...
516     'facecolor',[.4 .6 .4],'edgecolor',[.4 .6 .4], ...
517     'facealpha',0.2,'edgealpha',0.0)
518
519 saveas(gcf,['Fig_Visibility_', num2str(material),'_', ...
520     num2str(Modality),'_With_Interpolation','_trans_', ...
521     num2str(trans*100)],'png'); %Generates automatic .png file
```

Appendix B

Python Algorithm for Single-Mask EI-XPCi Information Retrieval

B.1 1D Grating Information Retrieval

```
%matplotlib notebook

from ipywidgets import interact, interactive, fixed, interact_manual
import ipywidgets as widgets
import cv2
import matplotlib.pyplot as plt
import matplotlib.image as mpimg
import numpy as np
from scipy.optimize import curve_fit
import pandas as pd
from PIL import *
from scipy.interpolate import interp1d
from tqdm.notebook import tqdm


def gauss(x, H, A, x0, sigma):
    return H + A * np.exp(-(x - x0)**2 / (2 * sigma**2))


def gauss_fit(x, y):
    mean = sum(x * y) / sum(y)
    sigma = np.sqrt(sum(y * (x - mean)**2) / sum(y))
```

```
    popt, pcov = curve_fit(gauss,
                           x,
                           y,
                           p0=[min(y), max(y), mean, sigma],
                          )
    return popt


def get_segments(x):
    idx = np.concatenate(([0], np.flatnonzero(x[:-1] != x[1:]) + 1, ...
       [x.size]))
    return np.array(
        list(zip(x[idx[:-1]], np.diff(idx), idx,
                 np.roll(idx, shift=-1) - 1)))


def reject_outliers(data, m=4):
    try:
        outliers = abs(data - np.mean(data)) > m * np.std(data)
        data[outliers] = np.nan
    except ValueError:
        pass
    return data


def maprange(a, b, s):
    (a1, a2), (b1, b2) = a, b
    return b1 + ((s - a1) * (b2 - b1) / (a2 - a1))


# ----- load the raw image
image_before = np.reshape(np.fromfile("before.raw", dtype='int16', ...
   sep=""), (1000, 1000))
image_after = np.reshape(np.fromfile("after.raw", dtype='int16', ...
   sep=""), (1000, 1000))
THRESHOLD_DARK = 32
THRESHOLD2 = 80
MIN_WIDTH = 10

# shift the after image by -2 pixels horizontally
PIXEL_SHIFT = -2
image_after = np.roll(image_after, PIXEL_SHIFT, axis=1)

# crop to remove dead pixels
OFFSET = 20
image_before = image_before[OFFSET:-OFFSET, OFFSET:-OFFSET]
```

```
66 image_after = image_after[OFFSET:-OFFSET, OFFSET:-OFFSET]
67
68 FIT_GAUSS = True
69 #------
70
71 plt.figure()
72 plt.imshow(image_after, cmap='gray', aspect='auto')
73 plt.show()
74
75 #------
76 # find the right THRESHOLD_DARK
77 ydata_proj = np.median(image_before, axis=0)
78 ydata_proj = np.median(image_before[100:101, :], axis=0)
79
80
81 plt.figure()
82 plt.plot(range(len(ydata_proj)), ydata_proj, '-o', markersize=0.5, ...
       linewidth=1)
83 plt.axhline(THRESHOLD_DARK)
84 plt.show()
85 segments_med = [segment for segment in ...
       get_segments(ydata_proj>THRESHOLD_DARK) if (segment[0]==1 and ...
       segment[1]>MIN_WIDTH)]
86
87
88 # find the right THRESHOLD2
89 segments_tmp = [segment for segment in ...
       get_segments(ydata_proj>THRESHOLD_DARK) if (segment[0]==1 and ...
       segment[1]>MIN_WIDTH)]
90 plt.figure()
91 yproj = [np.mean([np.max(row[segment[2]:segment[3]]) for segment in ...
       segments_tmp]) for row in image_before]
92 plt.plot(range(image_before.shape[0]), yproj)
93 plt.axhline(THRESHOLD2)
94 plt.show()
95
96 #------
97
98 #find the right PIXEL_SHIFT
99 PIXEL_SHIFT = 0
100 def check_pixel_shift(shift):
101     plt.figure()
102     r = (image_before-np.roll(image_after, shift, axis=1) )[100, :]
103     plt.plot(range(len(r)), r)
104     plt.show()
105
```

```
106 interact(check_pixel_shift, shift=widgets.IntSlider(min=-5, max=5, ...
    step=1, value=PIXEL_SHIFT, continuous_update=False))
107
108 #------
109
110 %%time
111
112 cols = ['image','x_min', 'x_max', 'y', 'peak' , 'H', 'A', 'x0', ...
    'sigma', 'peak_x']
113 results = []
114 skipped_rows = []
115 for image_i, image in enumerate([image_before, image_after]):
116     print(f'image {image_i}')
117     ydata_proj = np.median(image, axis=0)
118     for row in tqdm(range(image[:, :].shape[0]), total=image[:, ...
        :].shape[0]):
119
120         ydata_all = image[row, :]
121         # ignore the row if there is not enough stripes detected
122         if row in skipped_rows:
123             continue
124         if image_i == 0:
125 #             segments = [segment for segment in ...
    get_segments(ydata_proj>THRESHOLD_DARK) if (segment[0]==1 and ...
    segment[1]>MIN_WIDTH)]
126             segments = [segment for segment in ...
                get_segments(ydata_all>THRESHOLD_DARK) if ...
                (segment[0]==1 and segment[1]>MIN_WIDTH)]
127
128             if len(segments) < (len(segments_med) / 2):
129                 skipped_rows.append(row)
130                 continue
131             if np.mean([np.max(ydata_all[segment[2]:segment[3]]) for ...
                segment in segments_med]) < THRESHOLD2:
132                 skipped_rows.append(row)
133                 continue
134
135         for segment in segments_med:
136             x_min = segment[2]
137             x_max = segment[3]
138             ydata = ydata_all[x_min:x_max]
139 #             xdata = range(len(ydata)) + segment[2]\
140             xdata = np.arange(x_min, x_max)
141
142             H, A, x0, sigma = np.nan, np.nan, np.nan, np.nan
143             if FIT_GAUSS:
```

```
                try:
                    H, A, x0, sigma = gauss_fit(xdata, ydata)
                except RuntimeError:
                    print(f'Fitting a error at (x=[{x_min}-{x_max}], ...
                        y = {row})')

            results.append([image_i, x_min,x_max,row,np.max(ydata), ...
                H, A, x0, sigma, x_min+np.argmax(ydata)])

results = pd.DataFrame({k: v for k,v in zip(cols, np.array(results).T)})
results['amplitude'] = gauss(results.x0, results.H, results.A, ...
    results.x0, results.sigma)

#------

%matplotlib notebook
def plot_inputs(y):
    fig, axs = plt.subplots(2,2,figsize=(6, 6),sharex=True)

    for image_i, image in enumerate([image_before, image_after]):

        axs[0, image_i].imshow(image, cmap='gray', aspect='auto')
        axs[0, image_i].axhline(y, color='r' if y in skipped_rows ...
            else 'g', linewidth=1)

        ydata = image[y, :]
        xdata = range(len(ydata))
        axs[1, image_i].plot(xdata, ydata, '-o', markersize=0.5, ...
            linewidth=1)
        axs[0, image_i].set_title(image_i)

        # show the gaussian fit results
        if FIT_GAUSS:
#             display(results[results.image==image_i])
            for count, (row_ind, profile) in ...
                enumerate(results[(results.image==image_i) & ...
                (results.y==y)].iterrows()):
                H, A, x0, sigma = profile[['H', 'A', 'x0', ...
                    'sigma']].values
                x_min = int(profile.x_min)
                x_max = int(profile.x_max)
                # plot raw samples
                xdata_single = np.arange(x_min, x_max)
                ydata_single = ydata[x_min:x_max]
                axs[1, image_i].plot(xdata_single, ydata_single, 'o', ...
                    color='g',  markersize=1, label='__nolegend__' if ...
```

```
                    count else 'raw')
                # plot the fit function
                xdata_single = np.linspace(x_min, x_max , 50)
                axs[1, image_i].plot(xdata_single, ...
                    gauss(xdata_single, H, A, x0, ...
                    sigma),color='r',linewidth=0.5, ...
                    label='__nolegend__' if count else 'fit')
                # plot the center of the profile
                axs[1, image_i].axvline(x0, color='c', linewidth=0.5)


    axs[1, 0].axhline(THRESHOLD_DARK, color='b', linewidth=1)
    axs[1, 1].axhline(THRESHOLD_DARK, color='b', linewidth=1)

    axs[1, 0].get_shared_y_axes().join(axs[1, 0], axs[1, 1])
    axs[0, 0].get_shared_y_axes().join(axs[0, 0], axs[0, 1])

    plt.show()


interact(plot_inputs, y=widgets.IntSlider(min=0, ...
    max=image_before.shape[0], step=1, value=100, ...
    continuous_update=False))

#------

# simple image diff method!
plt.figure()
a = pd.Series((image_before-image_after).flatten())
a[a.abs()<10] = 0
a.replace(0, np.NaN, inplace=True)
img = a.interpolate().values
plt.imshow(img.reshape(image_before.shape), vmin=np.nanmean(img) - ...
    np.nanstd(img), vmax=np.nanmean(img) + np.nanstd(img))
plt.show()

#------

# dummy way of reconstructing the image
%matplotlib notebook
results_combined = results.loc[results.image==0, ['x_min', 'x_max', ...
    'y', 'x0']]
if FIT_GAUSS:
    results_combined['peak_amp_dif'] = ...
        results[results.image==1].amplitude.values / ...
        results[results.image==0].amplitude.values
```

```
    results_combined['peak_shift'] = ...
        results[results.image==1].x0.values - ...
        results[results.image==0].x0.values
    results_combined['sigma_dif'] = ...
        results[results.image==1].sigma.values - ...
        results[results.image==0].sigma.values
else:
    results_combined['peak_amp_dif'] = ...
        results[results.image==1].peak.values - ...
        results[results.image==0].peak.values
    results_combined['peak_shift'] = ...
        results[results.image==1].peak_x.values - ...
        results[results.image==0].peak_x.values
    results_combined['sigma_dif'] = 0

img_res = np.full((len(results_combined.y.unique()), ...
    len(segments_med), 3), np.nan, dtype=float)
for ind, (row, g) in enumerate(results_combined.groupby('y')):
    img_res[ind, :, 0] = reject_outliers(g['peak_amp_dif'].values)
    img_res[ind, :, 1] = reject_outliers(g['peak_shift'].values )
    img_res[ind, :, 2] = reject_outliers(g['sigma_dif'].values )

# img_res = np.full((*image_before.shape, 3), np.nan, dtype=float)
# for row, g in results_combined.groupby('y'):
#     pixel_y = int(row)
#     img_res[pixel_y, g['x0'].astype(int).values, 0] = ...
    reject_outliers(g['peak_amp_dif'].values)
#     img_res[pixel_y, g['x0'].astype(int).values, 1] = ...
    reject_outliers(g['peak_shift'].values)
#     img_res[pixel_y, g['x0'].astype(int).values, 2] = ...
    reject_outliers(g['sigma_dif'].values)


for ch in range(img_res.shape[2]):
    mean = np.nanmean(img_res[:, :, ch])
    std = np.nanstd(img_res[:, :, ch])
    img_res[:, :, ch] = [maprange((mean-std, mean+std), (0, 1), s) ...
        for s in img_res[:, :, ch]]


fig,axs = plt.subplots(1, 3, sharex=True, sharey=True)
for chi, ch in enumerate(['peak_amp_dif', 'peak_shift', 'sigma_dif']):
    axs[chi].imshow(img_res[:,:,chi], cmap='gray', aspect='auto', ...
        vmin=0, vmax=1, interpolation='nearest')
    axs[chi].set_title(ch)
plt.show()
```

```
249 fig.savefig('test.png')
250
251 plt.figure()
252 plt.imshow(img_res,aspect='auto', vmin=0, vmax=1, ...
       interpolation='nearest')
253 plt.show()
254
255 #------
```

B.2 2D Grating Information Retrieval

```
    # imports and helper functions

import math
import pickle

import cv2
import ipywidgets as widgets
import matplotlib
import matplotlib.image as mpimg
import matplotlib.pyplot as plt
import numpy as np
import pandas as pd
from ipywidgets import fixed, interact, interact_manual, interactive
from matplotlib.patches import Ellipse
from numpy import interp
from peakdetect import peakdetect
from PIL import *
from scipy import ndimage, optimize, spatial
from scipy.interpolate import interp1d
from scipy.optimize import curve_fit
from tqdm.notebook import tqdm


def map_range(src_range, new_range, val, allow_extrapolation=False):
    """map values to a different range"""
    if allow_extrapolation:
        return new_range[0] + ((val - src_range[0]) * (new_range[1] - ...
            new_range[0]) / (src_range[1] - src_range[0]))
    else:
        return interp(val,src_range,new_range)

def rotate_CV(image, angle , interpolation=cv2.INTER_LINEAR):
    #in OpenCV we need to form the tranformation matrix and apply ...
        affine calculations
    h,w = image.shape[:2]
    cX,cY = (w//2,h//2)
    M = cv2.getRotationMatrix2D((cX,cY),angle,1)
    rotated = cv2.warpAffine(image,M , (w,h),flags=interpolation)
    return rotated

def find_tilt(image, tilt_range=None):
    if tilt_range is None:
```

```
41          tilt_range= (-5, 5)
42      res=[]
43      for angle in tqdm(np.linspace(*tilt_range, 100)):
44          rotated =rotate_CV(image, angle)
45          proj = np.sum(rotated, axis=1)
46          res.append([angle, max(proj)])
47
48      res = np.array(res)
49      angle = res[np.argmax(res[:, 1])][0]
50
51      plt.figure( )
52      plt.plot(res[:, 0], res[:, 1], '-o')
53      plt.axvline(angle, color='r')
54      plt.title(f'tilt angle {angle} deg detected')
55      plt.xlabel('tilt angle (deg)')
56      plt.ylabel('proj count')
57      plt.show()
58
59      return angle
60
61  def get_peaks(values, lower_peaks=False, debug=True):
62      peaks = np.array(peakdetect(values, lookahead=2)[1 if lower_peaks ...
            else 0])
63      if debug:
64          plt.plot(values)
65          plt.plot(peaks[:,0], peaks[:,1], 'ko')
66          plt.show()
67      return peaks
68
69  def correct_tilt(image, debug = False, angle=None, tilt_range=None):
70      #rotation angle in degree
71      if not angle:
72          angle = find_tilt(image, tilt_range=tilt_range)
73
74      rotated =rotate_CV(image, angle)
75
76      if debug:
77          plt.figure()
78          plt.imshow(rotated)
79          plt.show()
80
81          plt.figure()
82          proj=np.sum(rotated, axis=0)
83          plt.plot(proj)
84          plt.show()
85
```

```
86      edges = []
87      for i in [0, 1]:
88          proj = np.sum(rotated, axis=i)
89          peaks = get_peaks(proj, lower_peaks=True, debug=debug)
90          edges.append([peaks[0,0], peaks[-1,0]])
91      edges = np.array(edges)
92      rotated_cropped = rotated[edges[1, 0]:edges[1, 1],
93                                edges[0, 0]:edges[0, 1]]
94      return angle, rotated_cropped
95
96  def gaussian(height, center_x, center_y, width_x, width_y):
97      """Returns a gaussian function with the given parameters"""
98      width_x = float(width_x)
99      width_y = float(width_y)
100     return lambda x,y: height*np.exp(
101                 -(((center_x-x)/width_x)**2+((center_y-y)/width_y)**2)/2)
102
103 def moments(data):
104     """Returns (height, x, y, width_x, width_y)
105     the gaussian parameters of a 2D distribution by calculating its
106     moments """
107     total = data.sum()
108     X, Y = np.indices(data.shape)
109     x = (X*data).sum()/total
110     y = (Y*data).sum()/total
111     col = data[:, int(y)]
112     width_x = ...
            np.sqrt(np.abs((np.arange(col.size)-x)**2*col).sum()/col.sum())
113     row = data[int(x), :]
114     width_y = ...
            np.sqrt(np.abs((np.arange(row.size)-y)**2*row).sum()/row.sum())
115     height = data.max()
116     return height, x, y, width_x, width_y
117
118 def fitgaussian(data):
119     """Returns (height, x, y, width_x, width_y)
120     the gaussian parameters of a 2D distribution found by a fit"""
121     params = moments(data)
122     errorfunction = lambda p: ...
            np.ravel(gaussian(*p)(*np.indices(data.shape)) -
123                                   data)
124     p, success = optimize.leastsq(errorfunction, params)
125     return p
126
127 def rotate(p, origin=(0, 0), degrees=0):
128     angle = np.deg2rad(degrees)
```

```
129     R = np.array([[np.cos(angle), -np.sin(angle)],
130                   [np.sin(angle),  np.cos(angle)]])
131     o = np.atleast_2d(origin)
132     p = np.atleast_2d(p)
133     return np.squeeze((R @ (p.T-o.T) + o.T).T)
134 
135 def get_range(vals):
136     # roughly return the range of the values in a given array
137     return (np.nanpercentile(vals, 1.8) , np.nanpercentile(vals, 98.2))
138 
139 
140     #---------
141 
142     # use debug mode on a smaller part of the image (set ...
            DEBUG_IMAGE_REGION) to test the algorithms. Debug mode ...
            generates extra plots as well.
143 DEBUG_MODE = False
144 DEBUG_MODE_IMAGE_REGION =  [[1300, 1400], [1500, 1650 ]]
145 NODEBUG_MODE_IMAGE_REGION =  [[100, -100], [100, -100 ]]  # ignore ...
        100 pixles from each side.
146 
147 path = r'C:\Users\apilali\Downloads'
148 IMAGE_BEFORE = f"{path}\\Sugar_Powder_ref.raw"
149 IMAGE_AFTER = f"{path}\\Sugar_Powder_sample.raw"
150 RAW_IMAGE_RESOLUTION = (4096, 4096)
151 CORRECT_TILT = True
152 SPECKLE_RADIUS = 5  # pixels
153 TILT_RANGE=(2, 4)  # provide an estimate of the tilt angle (in ...
        degrees) to limit the search
154 
155     #---------
156 
157 file_name = r'data_tilt_corrected.pkl'
158 
159 data = pickle.load(open(file_name, 'rb'))
160 DEBUG_MODE = False
161 CORRECT_TILT = 'tilt' in file_name
162 
163     #---------
164 
165 # ----- load the raw images
166 
167 image_before = np.reshape(np.fromfile(IMAGE_BEFORE, dtype='int16', ...
        sep=""),   RAW_IMAGE_RESOLUTION)
168 image_after = np.reshape(np.fromfile(IMAGE_AFTER, dtype='int16', ...
        sep=""), RAW_IMAGE_RESOLUTION)
```

```
data = {
    'before': {'image': image_before},
    'after': {'image': image_after}
       }
    #---------

angle = None

centers = []
for condition, datadic in data.items():
    print(f'pre-processing "{condition}" condition')
    if DEBUG_MODE:  # don't run on the full image in the deubg mode ... because it will be very slow and the debug images won't be any ... useful
        gray = datadic['image'][
        DEBUG_MODE_IMAGE_REGION[0][0]:DEBUG_MODE_IMAGE_REGION[0][1],
        DEBUG_MODE_IMAGE_REGION[1][0]:DEBUG_MODE_IMAGE_REGION[1][1]
            ].astype(np.uint8).T
    else:
        %matplotlib inline
        gray = datadic['image'][
        NODEBUG_MODE_IMAGE_REGION[0][0]:NODEBUG_MODE_IMAGE_REGION[0][1],
        NODEBUG_MODE_IMAGE_REGION[1][0]:NODEBUG_MODE_IMAGE_REGION[1][1]
            ].astype(np.uint8).T

    if CORRECT_TILT:
        print('finding the tilt angle ...')
        angle, gray = correct_tilt(gray, debug = False, angle = None ... if condition=='before' else angle, tilt_range=TILT_RANGE)
    data[condition]['image_processed'] = np.array(gray)

    gray_invert = 255-gray
    lower_bound = np.array([0])
    upper_bound = np.array([200]) # you may need to tune this ... ------------------------------------
    mask = cv2.inRange(gray_invert, lower_bound, upper_bound)

    print('detecting location of the speckles in the image ...')

    kernel = np.ones((3, 3), np.uint8)

    contours = cv2.findContours(mask.copy(), cv2.RETR_EXTERNAL,
            cv2.CHAIN_APPROX_SIMPLE)[0]
    contours.sort(key=lambda x:cv2.boundingRect(x)[0])

    if condition == 'after':
```

```
211         search_array = data['before']['centers']
212     for c in tqdm(contours):
213         (x,y),r = cv2.minEnclosingCircle(c)
214         r = int(r)
215         if r ≥ 1 and r≤2*SPECKLE_RADIUS:
216             if condition == 'before':
217                 centers.append([y, x])
218             else:  # find the corresponding speckle in the before image
219                 # very slow
220 #                 distance,index = ...
    spatial.KDTree(data['before']['centers']).query((y,x))
221 #                 if distance < 2*SPECKLE_RADIUS:
222 #                     item_index = index
223 #                     data['after']['centers'][item_index, :] = (y, x)
224                  # faster
225 #                 dist = lambda p, xy: math.hypot(p[0]-xy[0], p[1]-xy[1])
226 #                 item_index = centers.index(min(centers, key=lambda ...
    co: dist(co, (y, x))))
227 #                 data['after']['centers'][item_index, :] = (y, x)
228
229 #                 # even faster
230                 item_index = ...
                       np.argmin(np.linalg.norm(np.subtract(search_array, ...
                       np.array([y, x])), axis=1))
231                 data['after']['centers'][item_index, :] = (y, x)
232
233     if condition == 'before':
234         print(f'{len(centers)} speckle found')
235         data['before']['centers'] = np.array(centers)
236         data['after']['centers'] = np.array(centers) * np.nan
237
238
239     if DEBUG_MODE:
240         fig, axs = plt.subplots(1,3, sharex=True, sharey=True)
241         axs[0].imshow(gray_invert)
242         axs[0].set_title('original image')
243         axs[1].imshow(mask)
244         axs[1].set_title('threshold')
245         axs[2].imshow(gray_invert)
246         for center in data[condition]['centers']:
247             axs[2].scatter(center[1], center[0], s=5, c='r')
248         axs[2].set_title('speckles\n(rough locations)')
249         plt.show()
250     #---------
251 # process the images and fit a gaussian model on each speckle image
252
```

```
r = SPECKLE_RADIUS
for condition in data.keys():
    data[condition]['results'] = ...
       np.full((data['before']['centers'].shape[0], 5), np.nan)

    print(f'processing "{condition}" condition')
    gray = np.array(data[condition]['image_processed'])
    fit_results = []

    for item_index, (x,y) in enumerate(tqdm(data[condition]['centers'])):
        if np.any(np.isnan([x, y])):
            continue


        img_speckle = gray[max(int(x-r), 0):min(int(x+r), gray.shape[0]),
                           max(int(y-r), 0):min(int(y+r), gray.shape[1])]

        params = fitgaussian(img_speckle)
        fit = gaussian(*params)
        (height, x_local, y_local, width_x, width_y) = params
        x_abs = x_local + max(int(x-SPECKLE_RADIUS), 0)
        y_abs = y_local + max(int(y-SPECKLE_RADIUS), 0)

        if not (0<x_abs<gray.shape[0] and 0<y_abs<gray.shape[1]):
            continue

        # store the main measurements per speckle including: model ...
           height, center xy and width and height
        data[condition]['results'][item_index, :] = [height,
                                                     x_abs,
                                                     y_abs,
                                                     width_x,
                                                     width_y]

        # show fitting per cell (only do this if the grid size is small)
        if DEBUG_MODE and condition =='before' and ...
           len(data[condition]['centers']) < 50:
            print(x,y)
            print(height, x_local, y_local, width_x, width_y)
            print(img_speckle.shape)
            print(x_abs, y_abs)
            plt.figure()
            plt.imshow(img_speckle, vmin = 0, vmax=255, cmap='gray')
            plt.contour(fit(*np.indices(img_speckle.shape)), ...
                cmap=plt.cm.copper)
            plt.scatter(y_local,x_local, s=5, c='r')
```

```
            ax = plt.gca()
            plt.show()
if DEBUG_MODE:
    import random
    colors = color = ["#"+''.join([random.choice('0123456789ABCDEF') ... for j in range(6)]) for i in range(1000)]
    fig, axs = plt.subplots(1,2, sharex=True, sharey=True,figsize=(8, 6))

    for cond_i, condition in enumerate(data.keys()):
        axs[cond_i].imshow(data[condition]['image_processed'], ... cmap='gray')

        for res_i, res in enumerate(data[condition]['results']):
            if not np.any(np.isnan(res)):
                axs[cond_i].scatter(res[2], res[1], s=1, color='r')

                ellipse = Ellipse(xy=(res[2], res[1]), width=res[4], ... height=res[3],
                                  edgecolor=colors[res_i], fc='None', lw=1)
                axs[cond_i].add_patch(ellipse)

        axs[cond_i].set_title(condition)

    plt.show()

pickle.dump(data, open(f"data_{'tilt_corrected' if CORRECT_TILT else ... 'tilt_not_corrected'}{'_debug' if DEBUG_MODE else ''}.pkl", 'wb'), ... protocol=pickle.HIGHEST_PROTOCOL)
    #---------
# regardless of whether the raw images were tilt corrected above or ... not, here we need a tilt corrected version of the speckle candidates
# of the before image in order to show the results which is currently ... stored as a 1d array. We need to reshape the results into a 2d ... image, and for this
# we need to define a grid based on the centers in the before image ... (our reference). We cannot map the speckle coordinates to a grid
# without rotating the coordinates

origin=np.array(data['before']['image_processed'].shape)//2
angle = find_tilt(data['before']['image_processed'])
print(f'origin: {origin}, angle: {angle}')

new_points = rotate(data['before']['centers'], origin=origin, ... degrees=angle)

def detect_grid_lines(vals):
```

```
    vals = np.sort(vals)
    mask = np.diff(vals) > (np.max(np.diff(vals))/2)
    grid_vals = []
    breaks = np.where(mask)[0]
    vpre = 0
    for brk in breaks:
        grid_vals.append(np.median(vals[vpre:brk]))
        vpre = brk
    grid_vals=  grid_vals + [np.median(vals[vpre:])]
    return np.array(grid_vals)

xs = detect_grid_lines(new_points[:, 0])
ys = detect_grid_lines(new_points[:, 1])
n_grid_x  = len(xs)
n_grid_y  = len(ys)

xs = (xs[1:] + xs[:-1]) / 2
ys = (ys[1:] + ys[:-1]) / 2


def get_address(posx, posy):
    # this function will map a speckle position into a coordinates in ...
       the grid
    return len(xs) if xs[-1]≤posx else np.argmax(xs > posx), len(ys) ...
       if ys[-1]≤posy else np.argmax(ys > posy)


if DEBUG_MODE:
    fig=plt.figure()
    ax=plt.gca()
    for center in new_points:
        plt.scatter(center[1], center[0], s=5, c='r')
    ax.set_aspect('equal')
    ax.invert_yaxis()

    for l in ys:
        plt.axvline(l, alpha=0.5)

    for l in xs:
        plt.axhline(l, alpha=0.5)

    plt.show()

print(f'the grid size is {n_grid_x}x{n_grid_y}={n_grid_x * n_grid_y}')

    #---------
```

```
# The main results will come from the difference between the after and before images
diff = data['after']['results'] - data['before']['results']

# store whatever metric that may be interesting into the results array
results_dic = {}
results_dic['dHeight'] = diff[:, 0]
results_dic['dX'] = diff[:, 1]
results_dic['dY'] = diff[:, 2]
results_dic['dXY'] = np.linalg.norm(diff[:, 1:3], axis=1)
results_dic['dW'] = diff[:, 3]
results_dic['dH'] = diff[:, 4]
results_dic['dWH'] = np.linalg.norm(diff[:, 3:5], axis=1)

#  plot the histograms of each metric to give an idea about the range of the values
for k in results_dic:
    plt.figure()
    b, bins, patches = plt.hist(results_dic[k], 255, get_range(results_dic[k]))
    plt.show()

    #---------
# pick 3 main channles from the dictionary
THREE_MAIN_CHANNELS = ['dHeight', 'dXY', 'dWH']

def results_to_image(results_dic):
    image = np.full((n_grid_y , n_grid_x, len(results_dic)), np.nan)

    for channel_i, channel in enumerate(tqdm(results_dic)):
        rng = get_range(results_dic[channel])
        for item_i, center in enumerate(tqdm(data['before']['centers'], leave=False)):
            ind_y, ind_x = get_address(*rotate(center, origin=origin, degrees=angle))
            val =  map_range(rng,[0, 255],results_dic[channel][item_i])
            image[ind_x, ind_y, channel_i] =  0 if np.isnan(val) else val

    return image

image = results_to_image({k: results_dic[k] for k in THREE_MAIN_CHANNELS})


plt.figure()
plt.hist(image[:, :, 0].ravel(), bins = 256, color = 'red', alpha = 0.5)
```

```
415 plt.hist(image[:, :, 1].ravel(), bins = 256, color = 'Green', alpha = ...
        0.5)
416 plt.hist(image[:, :, 2].ravel(), bins = 256, color = 'Blue', alpha = 0.5)
417 plt.xlabel('Intensity Value')
418 plt.ylabel('Count')
419 plt.ylim(0, 3000)
420 plt.legend(THREE_MAIN_CHANNELS)
421 plt.show()
422
423     #---------
424 %matplotlib inline
425
426
427 DENOISE = False
428
429 img_tmp = np.array(image)
430
431 if DENOISE:
432     img_tmp = cv2.fastNlMeansDenoisingColored(np.uint8(img_tmp), ...
            None, 10, 10, 7, 9)
433
434 cv2.imwrite("image.png", img_tmp)
435
436
437 # for some reason matplotlib doesn't show the image when calling ...
        imshow directly
438 if 0:
439     plt.figure(figsize=(10, 10))
440     plt.imshow(img_tmp,
441                aspect='auto',
442                cmap='jet',
443                 interpolation='nearest',
444                vmin=0,
445                vmax=255
446               )
447     plt.show()
448 else:
449     plt.figure(figsize=(10, 10))
450     plt.imshow(mpimg.imread('image.png'))
451     plt.show()
452
453     #---------
454
455 image = data['after']['image'] - data['before']['image']
456 plt.figure(figsize=(10, 10))
```

```
457 plt.imshow(image, aspect='auto', ...
        cmap='gray',vmin=get_range(image.ravel())[0], ...
        vmax=get_range(image.ravel())[1])
458 plt.show()
```